Mass determination of supersymmetric particles in ATLAS

Børge Kile Gjelsten
Department of Physics
University of Oslo
Norway

Thesis submitted in partial fulfillment
of the requirements for the degree Doctor Scientiarum.

February 2005

Series of dissertations submitted to the
Faculty of Mathematics and Natural Sciences,University of Oslo.
No. 417

ISSN 1501-7710

Cover: Inger Sandved Anfinsen.
Printed in Norway: AiT e-dit AS, Oslo, 2005.

Produced in co-operation with Unipub AS.
The thesis is produced by Unipub AS merely in connection with the
thesis defence. Kindly direct all inquiries regarding the thesis to the copyright
holder or the unit which grants the doctorate.

Unipub AS is owned by
The University Foundation for Student Life (SiO)

Abstract

If supersymmetry is the solution to the hierarchy problem, supersymmetric partners of the Standard Model particles will exist near the TeV scale and be copiously produced at the LHC. With R-parity conserved to avoid proton decay, the sparticles produced in the collisions will decay in cascades, ending with the LSP. Neutral LSPs will not be seen in the detector, rendering impossible the full reconstruction of SUSY events and in particular complicating the measurement of sparticle masses. This thesis focuses on a method which uses endpoints of kinematic distributions to obtain sparticle masses. Its use for the decay chain $\tilde{q} \to \tilde{\chi}_2^0 q \to \tilde{l} l q \to \tilde{\chi}_1^0 l l q$ is investigated, including studies to delimit the region of applicability in the mSUGRA parameter space, studies of mass distributions and of complications related to the compositeness of the endpoint expressions. The method is extended to the situation where a gluino is added to the head of the chain. The new endpoint expressions are calculated and the performance of the method is estimated for a given SUSY scenario, yielding an accuracy for the gluino mass measurement competitive to other methods available. The impact of having the LSP mass determined by a Linear Collider is also considered.

Acknowledgements

During the years dedicated to this doctoral project my path has crossed with many people who have in one way or another contributed to my work. I am particularly grateful to my supervisor Prof. Per Osland. Without his continued support and encouragement, insight and ability to focus every discussion, this thesis would probably never have seen the light of day. I thank Prof. Steinar Stapnes, also supervisor, for taking me in and introducing me to ATLAS. I thank Dr. David J. Miller who has provided clarity and refinement through the many phases of the project. Furthermore, I am indebted to many members of the ATLAS collaboration whose achievements lay the foundation for this work, and in particular to Dr. Giacomo Polesello for his interest and advice.

This work has been conducted within the group of Experimental Particle Physics at the University of Oslo. I thank all staff members, current and previous doctoral and master students for their efforts in creating a friendly and scientifically rewarding setting. On the technical side the computer assistance of Trond Myklebust and Prof. Alex Read has been invaluable. Special thanks go to Dr. Sigve Haug whose physics intuition and extra-scientific perspectives have brought a little extra to everyday life in the corridor. Dr. Yurij Pylypchenkov and doctoral student Torkjell Huse also need mention, as do the master students, Marianne Johansen, Mustafa Hussain, Olav Mundal, Robindra Prahbu and more. Their enthusiasm must not be underestimated. Furthermore, I have appreciated the good spirits of Prof. Lars Bugge and Ass. Prof. Farid Ould-Saada, Prof. Torleiv Buran, Em. Prof. Tor Jacobsen, Cand. Scient. Kjell-Martin Danielsen and Dr. Samir Ferrag.

I thank family and friends, both parties largely neglected in this period, for their moral support when needed and an eagerness to see me through. Finally, I must express my gratitude to Cand. Philol. Silje M. Rosseland for bringing flavour and colour to these dedicated years.

Contents

Preface

This thesis is based on two papers written together with D. J. Miller and P. Osland [1, 2], and one work performed also in collaboration with E. Lytken and G. Polesello. The latter work is available as an ATLAS Note [3] and is part of the larger LHC/ILC Working Group report [4], where the benefits of having an overlap between the LHC and the next Linear Collider are studied.

The thesis is organised in the following way. In Chapter 1, after a short motivation, the structure of supersymmetry is described, ending in typical phenomenologies and current experimental limits. Chapter 2 gives a short description of the LHC, then treats the ATLAS detector in some detail focusing on general performance. Chapter 3 deals with the simulation tools used in this work. In Chapter 4 a brief introduction to supersymmetry measurements in ATLAS is given, describing in particular a few aspects of the 'endpoint method' of determining SUSY masses, which is the main focus of this thesis. A more complete presentation of the topic is given in the papers. Chapter 5 summarises the work, including results which have not been covered in Chapters 1–4 and are only available in the papers. Then follows the local bibliography, after which the papers [1] and [2] are reproduced.

Chapter 1

Theory

1.1 Standard Model

The Standard Model of particle physics is one of the most successful theories of science. At the energies tested by experiment this quantum field theory describes the sub-atomic world to high precision [5]. It includes three generations of fermion matter particles. In each generation there are two quarks with electric charge 2/3 and -1/3, respectively, and two leptons with electric charge 0 and -1, as well as their antiparticles. Interactions take place by the exchange of gauge bosons. The electroweak (EW) interactions are described by photons and the massive Z and W bosons. The strong interactions of Quantum Chromo Dynamics (QCD) are due to massless gluons. The only remaining part of the Standard Model which has not been confirmed experimentally is the Higgs boson. The limit from the experiments at the Large Electron Positron collider (LEP) [6], combined with unitarity arguments require the Higgs mass to lie in the range 114.4 GeV $< m_H \lesssim 1$ TeV, an energy range which will be fully explored by the next generation of experiments to be conducted at the Large Hadron Collider (LHC) starting in 2007.

While the Standard Model is in accordance with all experimental tests, it is not considered *the* fundamental theory, but rather an effective theory, valid at least up to the electroweak scale of 10^2 GeV, and which will be extended at higher energies. The 'circumstantial evidence' for this belief includes the lack of explanation for the specific gauge groups chosen, for the number of fermion families observed, for the symmetry between leptons and quarks, amongst others, not to forget the rather large number of free parameters in the theory. Furthermore, although outside of its primary domain and leaning on cosmological and astrophysical claims, the Standard Model does not provide all the elements needed to describe the evolution and state of the universe, such as e.g. the matter-antimatter asymmetry we observe or the dark matter component believed to fill the universe.

Another demonstration that the Standard Model cannot be viewed as the ultimate theory, comes from the fact that gravitational interactions are not included. From the experimental side of elementary particle physics this is no surprise. At the energies tested in high-energy experiments, gravitational interactions are so much weaker than the electroweak and strong interactions that no experimental observation is expected. From the theoretical side one would however like to have one common framework in which, at minimum, both gravity and the Standard Model are described. At energies of the reduced Planck scale, $\sim 10^{18}$ GeV, the gravitational force becomes comparable to the Standard Model forces. The enormous gap of 16 orders of magnitude between this scale and the electroweak scale is the basis for the 'hierarchy problem', which is the aesthetical unease of having two so different scales in one fundamental theory. There are other problems related to this scale difference. Since the Higgs is a scalar field, it receives quadratic quantum corrections to its mass. These corrections will be of the order of the largest mass in the theory or the cut off where new physics enter. If this is the Planck scale, then the Higgs mass is naturally driven towards the Planck scale, a problem dubbed the 'naturalness problem'. To avoid this and get the Higgs mass at the electroweak scale, where it must be, an extreme fine-tuning is required: The bare mass of the Higgs must be such that we get $[\mathcal{O}(10^{18})]^2 - [\mathcal{O}(10^{18})]^2 = [\mathcal{O}(10^2)]^2$. This is the 'fine-tuning problem'.

A key to one possible resolution of the fine-tuning problem lies in the observation that the quantum corrections to the Higgs mass due to boson loops have similar form as the corrections from fermion loops, but with different sign. A cancellation of the most dangerous terms is therefore possible, given that there is perfect balance between the fermions and the bosons in the theory. There exists a principle which can guarantee such a balance: supersymmetry.

1.2 Minimal Supersymmetric Standard Model

Supersymmetry is a symmetry between fermions and bosons. In a supersymmetric theory there are operators which transform fermions into bosons and vice versa. The particles of the theory fall into 'supermultiplets', each of which contains a balanced number of fermion and boson states – these are 'superpartners' of each other, and have the same gauge quantum numbers. If the supersymmetry is unbroken, they have the same masses too. The Minimal Supersymmetric Standard Model (MSSM) is the most economic supersymmetric extension of the Standard Model. Below, the main steps in going from the SM to the MSSM are described. The notation follows mostly that of [7], which is the main reference to the survey and in particular to all the formulas given in this chapter.

1.2.1 Exact supersymmetry

Field content

For each independent Standard Model field component (degree of freedom), a superpartner component is added. For the MSSM two types of supermultiplets are needed, 'matter multiplets', which contain the Standard Model fermions (spin-$\frac{1}{2}$) and their scalar (spin-0) superpartners, and 'gauge multiplets', which contain the Standard Model gauge fields (spin-1) and their fermionic superpartners (spin-$\frac{1}{2}$). In addition the Higgs sector needs to grow from the single Higgs doublet of the Standard Model to two Higgs doublets. Together with their fermionic superpartners (spin-$\frac{1}{2}$) the Higgs fields (spin-0) enter 'matter multiplets'.

Names	spin-0	spin-$\frac{1}{2}$	$SU(3)_C$	$SU(2)_L$	$U(1)_Y$
squarks, quarks	$\widetilde{Q} = (\tilde{u}_L\ \tilde{d}_L)$	$Q = (u_L\ d_L)$	**3**	**2**	1/6
	$\tilde{u}_R$	u_R	**3**	**1**	2/3
	$\tilde{d}_R$	d_R	**3**	**1**	-1/3
sleptons, leptons	$\widetilde{L} = (\tilde{\nu}\ \tilde{e}_L)$	$L = (\nu\ e_L)$	**1**	**2**	-1/2
	$\tilde{e}_R$	e_R	**1**	**1**	-1
Higgses, higgsinos	$H_u = (H_u^+\ H_u^0)$	$\widetilde{H}_u = (\widetilde{H}_u^+\ \widetilde{H}_u^0)$	**1**	**2**	1/2
	$H_d = (H_d^0\ H_d^-)$	$\widetilde{H}_d = (\widetilde{H}_d^0\ \widetilde{H}_d^-)$	**1**	**2**	-1/2

Table 1.1: Matter multiplets of the MSSM.

Names	spin-$\frac{1}{2}$	spin-1	$SU(3)_C$	$SU(2)_L$	$U(1)_Y$
gluino, gluon	$\tilde{g}$	g	**8**	**1**	0
winos, W	$(\widetilde{W}^+\ \widetilde{W}^0\ \widetilde{W}^-)$	$(W^+\ W^0\ W^-)$	**1**	**3**	0
bino, B	$\widetilde{B}^0$	B^0	**1**	**1**	0

Table 1.2: Gauge multiplets of the MSSM.

In Tables 1.1 and 1.2 the matter and gauge multiplets of the MSSM are shown. The superpartners of the Standard Model particles (where the extended Higgs sector is also taken as Standard Model particles) are written with a tilde. The names given to the superpartners are based on the names of the corresponding Standard Model particles. The spin-0 superpartners add an 's' in front: sfermion, squark, selectron. The spin-$\frac{1}{2}$ superpartners add 'ino' at the end (and adjust if necessary): higgsino, gaugino, gluino.

The requirement that the states within each multiplet have the same gauge quantum numbers naturally separates the left-handed ('L') quarks and leptons from the

right-handed ('R') ones. Their superpartners are scalars and have no handedness, but are nevertheless referred to as the 'left-handed selectron' etc. Only the matter multiplets of the first-generation quarks and leptons are shown.

In both tables the rightmost column shows the gauge representation of the supermultiplet. In the two middle columns the $SU(2)_L$ status is explicit. The weak isospin $[SU(2)_L]$ values of triplet/doublet/singlet fields are $T_3 = (1, 0, -1)/(1/2, -1/2)/0$. In the convention used for the hypercharge Y $[U(1)_Y]$, the electric charge of a field can be read off from the formula $Q = T_3 + Y$.

Interactions

The requirement of invariance under both supersymmetry and the gauge symmetries of the Standard Model, severely restricts the form of allowed interactions. Still, with the large number of fields available, the number of possible interactions is considerable. It is convenient to classify them according to origin.

The interactions between the members of the matter multiplets are guaranteed to satisfy supersymmetry if they are defined in terms of a 'superpotential' W in the following way:

$$\mathcal{L}_{\text{int}} = -(\frac{1}{2}W^{ij}\psi_i\psi_j + W^i W_i^* + \text{c.c.}) \tag{1.1}$$

$$W^i = \frac{\delta W}{\delta \phi_i}, \quad W^{ij} = \frac{\delta^2 W}{\delta\phi_i\delta\phi_j} \tag{1.2}$$

Here ψ_i and ϕ_i are fermion and scalar fields, respectively, of the matter multiplets. The superpotential contains scalar fields only. For the MSSM it is given by

$$W_{\text{MSSM}} = \tilde{u}_R^* \mathbf{y_u} \widetilde{Q} H_u - \tilde{d}_R^* \mathbf{y_d} \widetilde{Q} H_d - \tilde{e}_R^* \mathbf{y_e} \widetilde{L} H_d + \mu H_u H_d \tag{1.3}$$

Indices are suppressed. The two squark/slepton fields in each of the three first terms run over the three generations and are combined by dimensionless 3×3 matrices ($\mathbf{y}$) which are nothing but the well known Yukawa matrices of the Standard Model. The squark/slepton $SU(2)_L$ doublets are appropriately combined with the Higgs doublets. In the last term an unknown dimensionful parameter μ enters with the Higgs fields.

The Lagrangian (1.1) produces many interactions. In a notation where q, l and H denote quark and lepton (particle and antiparticle) and Higgs (neutral and charged), with a tilde for their superpartners, we get the following couplings: qqH, $q\tilde{q}\widetilde{H}$, llH, $l\tilde{l}\widetilde{H}$, $\tilde{q}\tilde{q}\tilde{q}\tilde{q}$, $\tilde{q}\tilde{q}\tilde{l}\tilde{l}$, $\tilde{l}\tilde{l}\tilde{l}\tilde{l}$, $\tilde{q}\tilde{q}HH$, $\tilde{l}\tilde{l}HH$, all of which are given by the Yukawa couplings, then $\widetilde{H}\widetilde{H}$ (higgsino mass term), HH (Higgs potential) given by μ, and $\tilde{q}\tilde{q}H$, $\tilde{l}\tilde{l}H$ set by a combination of μ with the Yukawa matrices. The number of couplings is significantly reduced if, in the Yukawa matrices, only the third-generation diagonal elements are kept. For many purposes this is a good approximation since the elements are proportional to the corresponding quark/lepton mass. Some of the field

combinations listed above become mass terms for higgsinos, and for (s)quarks and (s)leptons after the symmetry is spontaneously broken.

A second set of interactions are those formed by members of the same gauge multiplet. These count the Standard Model self-interaction of gauge fields, AAA and $AAAA$, where A denotes the gauge boson, as well as $A\widetilde{A}\widetilde{A}$, all with gauge-coupling strength.

Next, when matter and gauge multiplets are combined, the gauge couplings to the Standard Model fermions appear in the usual way through the covariant derivatives. In the same manner we get $\tilde{q}\tilde{q}A$ and $\widetilde{l}\widetilde{l}A$, but also $\tilde{q}\tilde{q}AA$ and $\widetilde{l}\widetilde{l}AA$. Finally, a few more terms are found to satisfy the symmetries and are added to the full Lagrangian. These turn out to have gauge strength, and include some phenomenologically important couplings, $q\tilde{q}\widetilde{A}$ and $l\widetilde{l}\widetilde{A}$, as well as quartic scalar couplings. In fact, most of the phenomenology of the theory is determined by the interactions of gauge-coupling strength. From the superpotential, only the interactions which involve the third-generation Yukawa couplings or the μ parameter will normally play a role.

R-parity

In model building one usually likes to adhere to the principle of including all terms which are allowed under the considered symmetries. However, in choosing the superpotential of the MSSM, Eq. (1.3), this principle was not followed. An additional set of terms also respects the symmetries:

$$W_{\substack{\Delta L=1\\ \Delta B=1}} = \frac{1}{2}\lambda\widetilde{L}\widetilde{L}\tilde{e}_R^* + \lambda'\widetilde{L}\widetilde{Q}\tilde{d}_R^* + \mu'\widetilde{L}H_u + \frac{1}{2}\lambda''\tilde{u}_R^*\tilde{d}_R^*\tilde{d}_R^* \tag{1.4}$$

(Family indices for the sfermion fields and for the coupling constants are suppressed.) The problem with the terms in Eq. (1.4) is that they have the undesirable feature of violating either baryon number (B) or total lepton number (L). Since these processes, which e.g. give rapid proton decay, have not been observed, their couplings would have to be very strongly suppressed. (In the Standard Model, B/L violating terms are naturally absent under the rule of accepting only renormalisable terms.)

One solution could be to simply discard these types of terms. That would however conflict with the principle above of allowing all possible interactions which respect the symmetries. Instead an additional symmetry is introduced in order to disallow the terms in Eq. (1.4). First, a new multiplicative quantum number dubbed R-parity is defined:

$$P_R = (-1)^{3(B-L)+2s} \tag{1.5}$$

Here B/L is the baryon/lepton number of the field and s is the spin. It is easy to see that all Standard Model fields, including the additional Higgs fields, have $P_R = 1$, while all the superpartners get $P_R = -1$. The symmetry to be imposed is then

that the MSSM conserves R-parity, which means that for any interaction vertex the product of P_R for all participating fields must be 1. Hence, only vertices with an even number of sparticles are allowed. While all the interactions discussed earlier satisfy this requirement, the interactions of Eq. (1.4) do not and so can be discarded.

Conservation of R-parity has other very important consequences, which will become apparent later.

1.2.2 Broken supersymmetry

Soft SUSY breaking

If supersymmetry was an exact symmetry, then all particles within a supermultiplet would have identical mass. However, no supersymmetric partners of the Standard Model particles have been observed. Supersymmetry must therefore be broken. Furthermore, the breakdown should be 'spontaneous', caused by a vacuum state which does not respect supersymmetry. Many models have been proposed for this, but there is no consensus on the exact implementation, which should not come as a surprise, as this step involves the unknown, more fundamental theory.

There is however some guidance from the opposite side of the scale. In order for the SUSY breaking terms not to ruin the solution of the fine-tuning problem, they must be 'soft', i.e. the couplings must have positive mass dimension. Furthermore, the scale of the massive couplings should lie around 1 TeV, which also means approximately 1 TeV for the sparticle masses. In the MSSM the symmetry breaking is implemented by simply adding to the Lagrangian (nearly) all possible 'soft terms', involving the superpartners only, and which satisfy the gauge symmetries of the Standard Model and conserve R-parity,

$$\begin{aligned}
\mathcal{L}_{\text{soft}} \;=\; & -\frac{1}{2}(M_1\widetilde{B}\widetilde{B} + M_2\widetilde{W}\widetilde{W} + M_3\tilde{g}\tilde{g} + \text{c.c.}) \\
& -(\tilde{u}_R^*\mathbf{a_u}\widetilde{Q}H_u - \tilde{d}_R^*\mathbf{a_d}\widetilde{Q}H_d - \tilde{e}_R^*\mathbf{a_e}\widetilde{L}H_d + \text{c.c.}) \\
& -\widetilde{Q}^\dagger\mathbf{m_Q^2}\widetilde{Q} - \widetilde{L}^\dagger\mathbf{m_L^2}\widetilde{L} - \tilde{u}_R^*\mathbf{m_{\tilde{u}}^2}\tilde{u}_R - \tilde{d}_R^*\mathbf{m_{\tilde{d}}^2}\tilde{d}_R - \tilde{e}_R^*\mathbf{m_{\tilde{e}}^2}\tilde{e}_R \\
& -m_{H_u}^2 H_u^* H_u - m_{H_d}^2 H_d^* H_d - (bH_u H_d + \text{c.c.})
\end{aligned} \tag{1.6}$$

The mass dimensions of gaugino and scalar fields are 3/2 and 1, respectively. From the requirement that each term in the Lagrangian must have mass dimension 4, the dimensions of the coupling constants can be read out. Line 1 provides additional mass terms for the gauginos; M_1, M_2 and M_3 have mass dimension 1. The terms in line 2 have form similar to the Yukawa terms of the superpotential W_{MSSM} (1.3). The matrices $\mathbf{a_u}$, $\mathbf{a_d}$ and $\mathbf{a_e}$ are complex 3×3 matrices in flavour space of mass dimension 1. They play a role similar to $\mathbf{y_u}$, $\mathbf{y_d}$ and $\mathbf{y_e}$ of W_{MSSM} (but are not dimensionless). In line 3 additional mass and mixing terms are given to the sfermions.

The parameters $\mathbf{m}_Q^2$ etc. are hermitian 3×3 matrices in flavour space with dimension of mass squared. The terms in line 4 give SUSY breaking contributions to the Higgs sector. The parameters $m_{H_u}^2$, $m_{H_d}^2$, both real, and b all have mass dimension 2. Below we will see that these last terms are crucial for the electroweak symmetry breaking.

Electroweak symmetry breaking

Due to the stricter symmetry conditions of the MSSM compared to the SM, the same Higgs doublet cannot give masses to both up-type and down-type fields. The $SU(2)_L$ doublet $H_u = (H_u^+ \; H_u^0)$ gives masses to up-type fields, while $H_d = (H_d^0 \; H_d^-)$ gives masses to the down-type field. As in the Standard Model this happens if the Higgs potential is such that the minimum value is obtained for non-zero values of some of the Higgs fields. Only electrically neutral components can have non-zero vacuum expectation values (VEVs). In the MSSM we have

$$\langle H_u^0 \rangle = v_u, \quad \langle H_d^0 \rangle = v_d \tag{1.7}$$

The two VEVs must add up to give the appropriate electroweak symmetry breaking,

$$v_u^2 + v_d^2 = v^2 = 2m_Z^2/(g^2 + g'^2) \approx (174 \text{ GeV})^2 \tag{1.8}$$

where g' and g are the gauge coupling constants of $U(1)_Y$ and $SU(2)_L$, and relate to the electric charge and the weak mixing angle by $e = g' \cos\theta_W = g \sin\theta_W$.

In the Standard Model three of the available four degrees of freedom of the complex Higgs doublet are spent to give mass to the electroweak gauge bosons W^+, W^- and Z. The last degree of freedom corresponds to the Higgs boson. In the MSSM there are eight degrees of freedom to start with, which ends in five Higgs bosons. Three are electrically neutral; h and H, which are CP even, A, which is CP odd, and two are charged; H^+ and H^-.

To investigate the conditions for spontaneous symmetry breaking, we look at those terms of the scalar potential which only involve the neutral Higgs components. All other fields have vanishing VEVs and are not relevant for these considerations. The stripped potential has the form

$$\begin{aligned} V &= (|\mu|^2 + m_{H_u}^2)|H_u^0|^2 + (|\mu|^2 + m_{H_d}^2)|H_d^0|^2 - (bH_u^0 H_d^0 + \text{c.c.}) \\ &\quad + \frac{1}{8}(g^2 + g'^2)(|H_u^0|^2 - |H_d^0|^2)^2 \end{aligned} \tag{1.9}$$

It is interesting to note that without the soft terms, $m_{H_u}^2$, $m_{H_d}^2$ and b, the potential would be positive-definite and no spontaneous breaking would be possible.

At the minimum both partial derivatives must vanish: $(\partial V/\partial H_u^0) = (\partial V/\partial H_d^0) = 0$. Applied to (1.9) this translates into the following equations,

$$|\mu|^2 + m_{H_u}^2 = b \cot\beta + \frac{m_Z^2}{2} \cos 2\beta \tag{1.10}$$

$$|\mu|^2 + m_{H_d}^2 = b \tan\beta - \frac{m_Z^2}{2} \cos 2\beta \tag{1.11}$$

where the much used VEV ratio parameter is introduced, $\tan\beta = v_u/v_d$. This allows for two of the involved parameters to be eliminated. The convention is to keep $\tan\beta$ (together with $m_{H_u}^2$ and $m_{H_d}^2$), and eliminate b and $|\mu|$. The sign of μ is however not addressed by the equations, and remains a free parameter.

SUSY breaking mechanisms

While the part of the MSSM which respects supersymmetry adds no new parameter, the supersymmetry-breaking part introduces 105 new parameters. Many of these are however strongly constrained by existing data, e.g. the lepton-flavour violating interactions given by the off-diagonal elements of $\mathbf{m_L^2}$ must be extremely small. Furthermore, many of the new interactions give unacceptably large contributions to CP-violation or flavour-changing neutral currents (FCNC), unless the relevant couplings are strongly suppressed. While such a suppression could happen 'by accident', it is more satisfactory to have it as a result of some symmetry which typically has its source in the details of the breaking mechanism. Below, the size of the MSSM parameter space is dramatically reduced and brought out of (the most apparent) conflict with existing data by a few simple assumptions.

First, the lepton-flavour violating couplings as well as dangerous FCNC contributions are removed by requiring complete flavour-blindness in the sfermion mass matrices:

$$\mathbf{m_Q^2} = m_Q^2 \mathbf{1}, \quad \mathbf{m_L^2} = m_L^2 \mathbf{1}, \quad \mathbf{m_{\tilde{u}}^2} = m_{\tilde{u}}^2 \mathbf{1}, \quad \mathbf{m_{\tilde{d}}^2} = m_{\tilde{d}}^2 \mathbf{1}, \quad \mathbf{m_{\tilde{e}}^2} = m_{\tilde{e}}^2 \mathbf{1} \tag{1.12}$$

Second, the trilinear couplings are set proportional to the corresponding Yukawa couplings which appear in the superpotential:

$$\mathbf{a_u} = A_{u0} \mathbf{y_u}, \quad \mathbf{a_d} = A_{d0} \mathbf{y_d}, \quad \mathbf{a_e} = A_{e0} \mathbf{y_e} \tag{1.13}$$

This forbids dangerous FCNC contributions in that only the third generation squarks and sleptons can have large trilinear couplings. Third, to avoid CP-violation far beyond what is measured, all the new complex phases are removed:

$$M_1, M_2, M_3, A_{u0}, A_{d0}, A_{e0} \in \mathbb{R} \tag{1.14}$$

In combination, Eqs. (1.12)–(1.14) constitute a mild version of what is called 'soft-breaking universality'.

While these assumptions are clearly convenient from an experimental point of view, i.e. when confronted with data, it would be nice if they were also theoretically reasonable. They should be a consequence of the breaking mechanism, and in fact

it turns out that many of the suggested SUSY breaking mechanisms naturally give some kind of universality to the soft terms. This means, however, that the conditions (1.12)–(1.14) should hold, not at the electroweak scale, but at some 'input scale' which typically lies much higher, and where such a universality is present. The parameter values at different scales are connected by the renormalisation group (RG) equations. Fortunately, the RG evolution from the high to the low scale has very little effect on the CP-violating and FCNC contributions as set at the input scale, so the assumptions hold approximately at the electroweak scale, thereby avoiding conflict with data.

As the input scale depends on the details of the SUSY breaking mechanism, it is in practice unknown. The parameters and structure of the Standard Model might however hold some clues. One puzzling result is found from RG evolving the three gauge couplings $\alpha_i = g_i^2/4\pi$ to higher energies. If done for the Standard Model, the couplings meet in the range 10^{13}–10^{17}, but only two at a time. For the MSSM with sparticle masses around 1 TeV, all three couplings meet at $\sim 2 \cdot 10^{16}$ GeV. This could be taken as a sign that the three forces meet to unite in a Grand Unified Theory (GUT) at these energies, in which case it is also a natural choice for the input scale. (The (reduced) Planck scale at $\sim 10^{18}$ GeV, where gravitational interactions become important, is another natural choice for the input scale.)

Common for most of the attempts to construct a satisfactory, spontaneous SUSY breaking mechanism, is the existence of a 'visible sector' where the MSSM lives, and a 'hidden sector' where other fields live and where supersymmetry is broken. The interaction between these two sectors is weak, and it is through this interaction that supersymmetry breaking is mediated to the MSSM. Two types of interactions are frequently considered for this purpose, gravity and gauge interactions. In both cases, to take into account gravity, the MSSM is promoted from a global to a local supersymmetric theory, turning it into a 'supergravity' theory which then contains a spin-2 graviton and a spin-3/2 gravitino, both massless. When supersymmetry is spontaneously broken, the gravitino acquires mass in the 'super-Higgs mechanism'.

In models where the SUSY breaking is mediated by gauge interactions, the mass of the gravitino is nearly always much smaller than the other SUSY masses. Being the lightest supersymmetric particle (LSP), it can play a role in collider experiments if it couples with sufficient strength. The minimal version of gauge-mediated supersymmetry breaking (GMSB) counts three parameters and a sign. Often one or two more model parameters are added in the versions used for phenomenological studies.

In the case of SUSY-breaking mediation by gravity, the mass of the gravitino is comparable to the other SUSY masses. With couplings roughly gravitational in strength, it plays no role in collider experiments (but can still have cosmological implications). The most popular model for phenomenological studies within supersymmetry, and the basis for the simulation studies in this thesis, is of this type. It is called 'minimal supergravity' or 'mSUGRA' and implements a strong version of the

soft-breaking universality assumptions (1.12)–(1.14),

$$M_1 = M_2 = M_3 = m_{1/2} \tag{1.15}$$

$$m_Q = m_L = m_{\bar{u}} = m_{\bar{d}} = m_{\bar{e}} = m_{H_u} = m_{H_d} = m_0 \tag{1.16}$$

$$A_{u0} = A_{d0} = A_{e0} = A_0 \tag{1.17}$$

in which all the gaugino masses have a common value at the input scale, as do all the scalar masses and the trilinear mass parameters. The model is completely defined by these three mass parameters, $m_{1/2}$, m_0 and A_0, together with $\tan\beta$ and $\mathrm{sign}(\mu)$, both from the Higgs sector, in total '$4\frac{1}{2}$' parameters.

1.2.3 Phenomenology

Renormalisation group evolution, masses and mixing

When the Lagrangian at the input scale has been set, either by Nature or by the curious physicist, in order to obtain the phenomenology relevant for our experiment all its parameters should be RG evolved down to the electroweak scale. Mass eigenstates, mixing angles, couplings etc. appropriate to the electroweak scale can then be found. Below, the various steps of the process are described in more detail for the mSUGRA model.

First the explicit RG equations of each parameter must be found. For the third-generation Yukawa coupling, y_b, the 1-loop β-function has the form

$$\frac{dy_b}{dt} = \frac{y_b}{16\pi^2}(6|y_b|^2 + |y_t|^2 + |y_\tau|^2 - \frac{16}{3}g_3^2 - 3g_2^2 - \frac{7}{15}g_1^2) \tag{1.18}$$

where $t = \ln(Q/Q_0)$ with Q the 'current' scale and Q_0 the input scale. (The gauge couplings of Eq. (1.8) are rewritten, $g_1 = \sqrt{5/3}g'$ and $g_2 = g$, and $g_3 = g_s$ is the gauge coupling of $SU(3)$.) Similar equations are found for the other parameters in the superpotential, y_t, y_τ and μ.

The 1-loop RG equations of the gaugino masses give, in combination with the gauge coupling RG equations and their unification condition at the GUT scale,

$$\frac{M_1}{g_1^2} = \frac{M_2}{g_2^2} = \frac{M_3}{g_3^2} \tag{1.19}$$

These relations hold at any scale. Since the gauge couplings are known, knowledge of one of the gaugino masses automatically gives the two others.

For $m_{H_u}^2$ we get

$$\frac{dm_{H_u}^2}{dt} = \frac{1}{16\pi^2}[3(2|y_t|^2(m_{H_u}^2 + m_{Q_3}^2 + m_{\bar{u}_3}^2) + 2|a_t|^2) - 6g_2^2|M_2|^2 - \frac{6}{5}g_1^2|M_1|^2] \tag{1.20}$$

The large Yukawa coupling of the top quark may drive $m_{H_u}^2$ negative near the electroweak scale, contributing to the spontaneous symmetry breaking, see Eq. (1.9). Similar RG equations are found for the remaining parameters; $m_{H_d}^2$ and b; a_t, a_b and a_τ; $\mathbf{m}_Q^2$, $\mathbf{m}_L^2$, $\mathbf{m}_{\bar{u}}^2$, $\mathbf{m}_{\bar{d}}^2$ and $\mathbf{m}_{\bar{e}}^2$. From Eq. (1.12) the five mass matrices are proportional to the identity matrix at the input level. As they are evolved down, they remain approximately diagonal, but the third-generation masses receive contributions from the large Yukawa (y_t, y_b, y_τ) and soft trilinear (a_t, a_b, a_τ) couplings. Consequently, we get at the weak scale the same values for the first and second-generation parameters $(m_{Q_1}^2, \dots)$ and a different one for the third generation $(m_{Q_3}^2, \dots)$.

Some features of the RG running are quite generic and hold also for less constrained models than mSUGRA: the relation (1.19) guarantees a gaugino mass hierarchy in accordance with the known coupling hierarchy, in particular giving a heavy gluino; squark/slepton mass parameters increase as the energy scale decreases; due to their SU(3) charge squarks become significantly heavier than the sleptons at the electroweak scale; third-generation sfermions get large contributions from the Yukawa couplings and differ from sfermions of the two first generations which get the same mass at the electroweak scale.

All considerations so far have been on the gauge eigenstates. Fields with the same electric charge, colour charge and spin will mix to form mass eigenstates, which are the physical, observable states. The gluino cannot mix with other fields and is both gauge and mass eigenstates. The bino and the neutral wino will mix with the neutral higgsinos to form four 'neutralinos'; $\tilde{\chi}_1^0$, $\tilde{\chi}_2^0$, $\tilde{\chi}_3^0$ and $\tilde{\chi}_4^0$, where $\tilde{\chi}_1^0$ is the lightest and very often the LSP. The charged winos and higgsinos give four 'charginos'; $\tilde{\chi}_1^\pm$ and $\tilde{\chi}_2^\pm$. In mSUGRA the mass of $\tilde{\chi}_1^0$ is close to M_1 and inherits essentially the bino-couplings, while both $m_{\tilde{\chi}_2^0}$ and $m_{\tilde{\chi}_1^\pm}$ are close to $M_2 \approx 2M_1$ and are predominantly winos. The remaining neutralinos and chargino are all of similar mass, considerably heavier than M_2, and are mostly higgsinos.

In the squark/slepton sector the two first generations have practically no mixing between the left and right-handed states, and so the mass eigenstates are the same as the gauge eigenstates. The third-generation squarks/sleptons, however, are mixed states, which also has the consequence that one of them, $\tilde{t}_1/\tilde{\tau}_1$, is the lightest of its type. This has important phenomenological consequences.

Finally, one very important feature of the MSSM is the quite low upper bound on the mass of the lightest Higgs boson,

$$m_h \lesssim 130 \text{ GeV} \tag{1.21}$$

a limit clearly open to experimental testing in an otherwise very flexible or evasive model. Still, by minor extensions of the model this limit may be increased to $m_h \lesssim 150$ GeV. The masses of the other Higgs bosons can be much larger, and typically lie close to each other.

Collider signatures

At a hadron collider the varying center of mass (CM) energies of the hard collision allow for a large spectrum of SUSY channels to be accessed. Pair production of gluinos and squarks, available at tree level and with $SU(3)$ coupling strength, will however dominate, unless their masses are too large. Each event will be characterised by two 'cascades' formed by the subsequent decay of the sparticles into lighter ones together with accompanying Standard Model particles, eventually ending with the LSP. Since the initial gluinos and squarks are usually heaviest, most of the other sparticles can be accessed in the cascades. For these intermediate and lower-mass sparticles the indirect production is much larger than the direct production.

In the case of gravity-mediated supersymmetry breaking, where $\tilde{\chi}_1^0$ is the LSP and leaves the detector without any trail, large $E_{\mathrm{T}}^{\mathrm{miss}}$ is one of the key signatures. Also hard jets and leptons are typical signatures, as in the cascade

$$\tilde{q} \rightarrow \tilde{\chi}_1^+ q \rightarrow \tilde{\tau}_1^+ \nu_\tau q \rightarrow \tilde{\chi}_1^0 \tau^+ \nu_\tau q \tag{1.22}$$

In GMSB scenarios the gravitino will be the LSP. Depending on the strength of its coupling, which decides whether it will be decayed into inside or outside the detector, as well as the identity of the next-to-lightest sparticle (NLSP), several phenomenologies will be available.

In an e^+e^- collider the CM energy is fixed, and normally at a value significantly lower than the reach of a hadron collider of the same generation. The heaviest sparticles, squarks and gluinos, may therefore not be kinematically accessible, and if they are, their production will not be favoured by the $SU(3)$ couplings as they are at a hadron machine. Consequently, the upper part of the cascade (1.22) is less relevant. Direct production of charginos, neutralinos and sleptons will dominate. The large benefit of e^+e^- collisions over e.g. pp collisions is the immense reduction in background, which will allow for precision measurements of a large number of sparticle properties.

Experimental bounds

The search for supersymmetry has been on the agenda of many experiments for quite a while, but no compelling evidence has yet been presented. These negative search results can then in principle be turned into exclusion limits. For the MSSM such a conversion is however not straightforward due to the size of the parameter space. If at all possible, absolute limits tend to be very conservative as it is nearly always possible to find a constellation of parameters which undermines the relevance of the measurements. The exclusion limits presented by the experiments are therefore valid for various constrained models only, and a limit found under one set of assumptions is not trivially translated to another set. Still, for a complex model like the MSSM it cannot be otherwise.

Searches can be divided into direct and indirect searches. Direct searches look at specific signatures, such as $e^+e^- + E_{\mathrm{T}}^{\mathrm{miss}}$, expected from $e^+e^- \to \tilde{e}^+\tilde{e}^- \to \tilde{\chi}_1^0\tilde{\chi}_1^0 e^+e^-$, and from the lack of signal above the background deduce limits on the masses and couplings of the sparticles involved. The strongest limits are those set by the experiments at LEP2 and at the Tevatron. Indirect searches look for sparticles (or any other non-standard particles) in loop contributions to various Standard Model processes. This requires that the theoretical and experimental status of the quantities in question, e.g. the muon anomalous magnetic moment or the decay width of $b \to s\gamma$, be sufficiently known that any deviation from a pure Standard Model hypothesis is recognised. Also figuring in this category are global fits to the entire collection of electroweak precision data. If a significant deviation from the Standard Model hypothesis should be found, these indirect searches are less suited to determine its origin, whether it is due to supersymmetry or some other new physics.

In recent years, measurements from outside of particle physics have started to play a role, in particular the more and more accurate determination of astrophysical parameters. The combination of the latest data from the Wilkinson Microwave Anisotropy Probe (WMAP) with other cosmological data gives a precise determination of the the amount of cold dark matter (CDM) in the universe. This puts stringent constraints on R-parity conserving SUSY scenarios, where the LSP will contribute to the CDM. (Still, it should be kept in mind that these new constraints rely on cosmological and astrophysical theories which in strict terms are outside the regime of direct testing as we are used to from the building and confirmation of the Standard Model.) In brief, the relic density depends mainly on the LSP annihilation cross-section into SM particles. In most mSUGRA scenarios the LSP annihilation process $\tilde{\chi}_1^0\tilde{\chi}_1^0 \to l^+l^-$ is too weak to bring the CDM contribution equal to or below the measured value. Only in the so-called 'bulk region', where sparticle masses are light, are the constraints naturally satisfied. Other allowed regions are defined by special circumstances which enhance the annihilation cross-section: the 'coannihilation region' where the NLSP is close to the LSP in mass, the 'focus point region' where $\tilde{\chi}_1^0$ has a large higgsino component, and the Higgs resonance regions where $2m_{\tilde{\chi}_1^0} \approx m_{h/H/A}$. In a less constrained MSSM there are more possibilities to produce the correct amount of relic density (or less), e.g. by having a wino-like $\tilde{\chi}_1^0$.

In Table 1.3 a very short and incomplete compilation of the current limits on sparticle masses is given. The numbers are taken from the Particle Data Group review [5] and come from searches at LEP2 and at the Tevatron. Minimal supergravity with $\tilde{\chi}_1^0$ LSP is assumed. Some central assumptions for each of the limits are given. For more detail, the source [5] and references therein must be consulted. In the next few years the Tevatron will keep pushing further some of these limits, or even start seeing signs of supersymmetry. Then the LHC will take over and eventually cover more or less the entire parameter space valid for low-energy supersymmetry.

m_h	$\gtrsim$	114 GeV	$\tan\beta \lesssim 7$–8, LEP $m_h^{\max}$ scenario
m_h	$\gtrsim$	90 GeV	$\tan\beta \gtrsim 7$–8, LEP $m_h^{\max}$ scenario
$m_{\tilde{\chi}_1^0}$	$\gtrsim$	46 GeV	
$m_{\tilde{\chi}_2^0}$	$\gtrsim$	62 GeV	
$m_{\tilde{\chi}_1^\pm}$	$\gtrsim$	85 GeV	$m_{\tilde{\nu}} > m_{\tilde{\chi}_1^\pm}$
$m_{\tilde{e}_R}$	$\gtrsim$	73 GeV	
$m_{\tilde{e}_R}$	$\gtrsim$	99 GeV	$m_{\tilde{e}_R} - m_{\tilde{\chi}_1^0} > 10$ GeV
$m_{\tilde{\mu}_R}$	$\gtrsim$	95 GeV	$m_{\tilde{\mu}_R} - m_{\tilde{\chi}_1^0} > 10$ GeV
$m_{\tilde{\tau}_1}$	$\gtrsim$	81 GeV	$m_{\tilde{\tau}_1} - m_{\tilde{\chi}_1^0} > 15$ GeV
$m_{\tilde{\nu}_e}$	$\gtrsim$	84 GeV	
$m_{\tilde{g}}$	$\gtrsim$	195 GeV	$m_{\tilde{q}} > m_{\tilde{g}}$
$m_{\tilde{q}}$	$\gtrsim$	270 GeV	$m_{\tilde{q}} > m_{\tilde{g}}$
$m_{\tilde{g}} + 2m_{\tilde{q}}$	$\gtrsim$	900 GeV	$m_{\tilde{g}} > m_{\tilde{q}}$, $m_{\tilde{g}} \in (300, 550)$ GeV
$m_{\tilde{t}_1}$	$\gtrsim$	95 GeV	$m_{\tilde{t}_1} - m_{\tilde{\chi}_1^0} \gtrsim 10$ GeV

Table 1.3: Rough survey of the current limits on the sparticle masses [5].

Chapter 2

Experiment

2.1 LHC

At the Large Hadron Collider (LHC) we will have proton-proton collisions at a center of mass (CM) energy of 14 TeV. At these energies the collisions will be not between the two protons as a whole, but rather between the constituent partons, e.g. between a gluon from one of the protons and an antiquark picked from the sea of the other proton. While the CM energy of the elementary parton collision will be less than 14 TeV and varying, it will be sufficient to probe conclusively on the most pressing problem of fundamental physics, the electroweak symmetry breaking, believed to be caused by the Higgs mechanism. Also, definite answers on most variants of low-energy supersymmetry, as described in the previous chapter, will be provided in the course of the LHC running period.

In order to arrive at energies of 7 TeV each, the protons are lead through several stages in the CERN accelerator setup, see Fig. 2.1. After the protons have been extracted from a hydrogen plasma in a duoplasmatron, a five-step acceleration process takes place. First, a linear accelerator (LINAC2) accelerates the protons to a kinetic energy of 50 MeV. Next, the Proton Synchrotron Booster (PSB) takes them up to a kinetic energy of 1.4 GeV and passes them into the Proton Synchrotron (PS). Here the LHC bunch-train structure is created, as well as a further increase of kinetic energy to 25 GeV. The Super Proton Synchrotron (SPS) then accelerates the protons to 450 GeV, and injects them in both directions into the LHC ring where they are pushed to the ultimate 7 TeV.

At design (high) luminosity each bunch contains $n_\mathrm{b} \approx 10^{11}$ protons. The spacing between bunches is 25 ns, corresponding to a bunch rate of $f_\mathrm{b} = 40$ MHz. A bunch will have a width of $\sigma_\mathrm{b} = 15.9$ μm in both transverse directions (and 7.5 cm in the

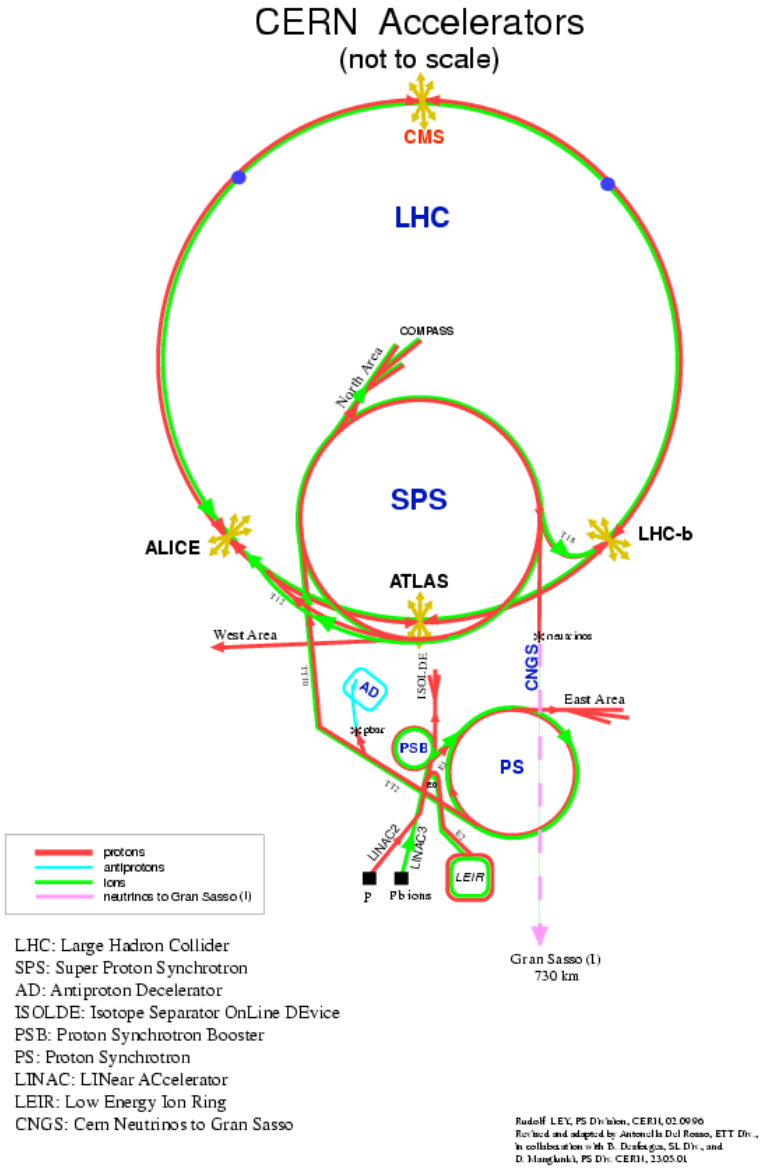

Figure 2.1: The CERN accelerator setup. (From the CERN web pages.)

longitudinal direction). Taken together these parameters give the luminosity:

$$\mathcal{L} = \frac{n_{\mathrm{b}}^2 f_{\mathrm{b}}}{4\pi\sigma_{\mathrm{b}}^2} \approx 10^{34}\mathrm{cm}^{-2}\mathrm{s}^{-1} \tag{2.1}$$

In the first three years of operation the LHC will run at low luminosity, which is one order of magnitude less.

At four selected points along the ring the beams are made to cross. A Toroidal LHC ApparatuS (ATLAS) and the Compact Muon Solenoid (CMS) are general-purpose experiments which cover two of these collision points. The other two are occupied by LHC-b, a dedicated B-physics experiment, and A Large Ion Collider Experiment (ALICE), a heavy-ion experiment which will primarily investigate Pb-Pb collisions, an alternative LHC operation mode.

2.2 ATLAS

2.2.1 Introduction

The purpose of a detector complex like ATLAS [8] is to describe with sufficient accuracy the outcome of what are considered interesting particle collisions, and in doing so allowing for their reconstruction and subsequent comparison with theory. Usually the particles initially produced are not the ones measured by the detector. When a heavy particle like a Z or a Higgs boson is created, it decays instantly into lighter particles like quarks or leptons. Next, due to colour confinement, quarks and gluons, being coloured objects, fragment into colour neutral ones; baryons and mesons. Many of the baryons and mesons immediately decay further by the weak force, producing the (quasi)stable particles which then start their journey outwards, into the detector. Most of this happens at a time scale not detectable by the experimental setup. Consequently the stable particles will all point back to the collision point. Important exceptions to this description are intermediate tauons and B-hadrons (and to a lesser extent D-hadrons) which will typically move a few hundred micrometers before decaying. The particles which are stable on the time scale of the detector, and which are the ones the detector will measure as they interact with the detector material, are muons, electrons, photons and hadronic jets (consisting of $p/\bar{p}$, $n/\bar{n}$, $\pi^{\pm}$, $K^{\pm}$ and K_L^0 as well as μ, e and γ). Neutrinos will not leave any trace in the detector. However, since the total transverse momentum of an event should approximately sum up to zero, the combined transverse momentum of neutrinos (and any other invisible particles, like the SUSY LSPs) can be deduced from $\mathbf{p}_{\mathrm{T}}^{\mathrm{miss}}$, the missing-transverse-momentum vector.

The task of the detector is then to measure some or all of the momenta, energies and positions of these particles, as well as identifying them. The momenta of charged

particles are found from the track curvatures in a known magnetic field. Energy is determined in a calorimeter. Since calorimeters are based on simply stopping the particle, they are placed outside of tracking devices. The exception is for muons, since they are not stopped in calorimeters. Tracking devices and calorimeters also naturally give information on the position and direction of the particles. Particle identification is accomplished by various often overlapping techniques; particle-specific interactions, dE/dx, impact parameter, shower structure in calorimeter, amongst others.

The specific implementation of these tasks for a given detector complex depends on the experimental situation, here the harsh LHC environment, in combination with the physics one is interested in studying. In some sense these correspond to background and signal, respectively. At a hadron collider there is always an intrinsic background from the 'underlying event', the parts of the hadrons which do not participate in the hard interaction. Furthermore, in addition to the very high bunch crossing rate of 40 MHz, at design luminosity each bunch crossing is expected to give on average 23 minimum bias events. The hadronic activity will therefore be considerable, and it is with this as background that interesting signatures will be searched for. For instance, the huge QCD background will largely disqualify the traditional $H \to b\bar{b}$ as a discovery channel for a low-mass Higgs ($\lesssim 130$ GeV), even though it is by far the dominant decay mode with a branching ratio of $\sim$90%. Since Higgs discovery is one of the main objectives of ATLAS, it is crucial to have discovery channels throughout the theoretically allowed mass range. It has therefore been necessary to ensure that the low-rate $H \to \gamma\gamma$ will be detectable in this mass region, resulting in stringent requirements on the electromagnetic calorimeter in terms of resolution and identification capabilities.

Some other requirements, partly motivated by existing theories beyond the Standard Model, are excellent capabilities in lepton momentum/energy measurements and identification, accurate jet and missing transverse energy ($E_{\mathrm{T}}^{\mathrm{miss}}$) measurement ensured by full hadronic calorimeter coverage, efficient b-tagging and τ-tagging.

2.2.2 Detector layout

The ATLAS detector is shown in Fig. 2.2, partly dismantled to reveal its inner parts. Proton bunches enter from left and right through the beam pipe, which defines the z-axis. Closest to the collision point lies the inner detector (ID) [orange]. It stretches to $(R, |z|) \approx (1.15, 3.5)$ m,[1] where R is the radius. Outside is the central solenoid (CS) [red] which provides a magnetic field essentially along the z-axis in the ID cavity. Next comes the electromagnetic (EM) calorimeter [green] which goes out to $(R, |z|) \approx (2.25, 4.3)$ m. The hadronic calorimeters [red] including the

[1]Except for the part on the pixel detector, the detector description which follows is based on the ATLAS Technical Design Report (TDR) [8]. Numbers may have changed slightly.

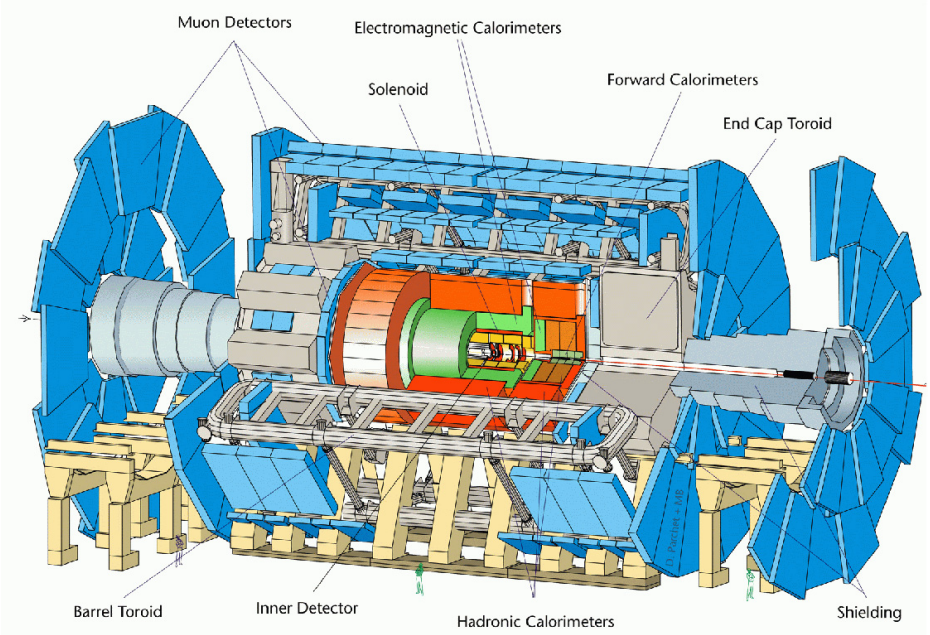

Figure 2.2: The ATLAS detector. (From the ATLAS TDR.)

forward calorimeter (FCAL) [green] then cover out to $(R, |z|) \approx (4.25, 6.65)$ m. Finally, the muon detectors [blue] define the total size of the ATLAS detector with $(R, |z|) \approx (11, 23)$ m. The barrel toroid (BT) and end cap toroids (ECT) [grey], provide the magnetic field in the muon system. A cooling system keeps the different subdetectors at optimised working temperatures. In addition there are mechanical support structures which keep the detector parts in place, cold walls between different subdetectors which operate at different temperatures and services which provide data read out and powering. These all add to the amount of dead material in the detector, potentially degrading the performance, and are kept at a minimum.

For constructional reasons most detector systems consist of a barrel section at low $|z|$ values and an end cap section at high $|z|$ values, as can be seen in the figure. The barrel parts have full coverage in the azimuth angle ϕ at fixed radii while the end cap parts have full ϕ coverage at fixed $|z|$ from the collision point. Except for a small cone around the beam pipe on each side, the full solid angle is covered, although with some degradation of the detector performance in the overlap region between the barrel and the end caps.

In cylindrical coordinates the position of detector parts and the original momenta

of particles coming from the hard process can be put on equal footing, which is practical. For both, the direction out from the collision point is given in terms of ϕ and the polar coordinate θ, which is traded for the pseudorapidity $\eta = -\ln\tan(\theta/2)$. A complete position in the detector system is then given by an additional z or R value, while a particle momentum usually is completed by giving the p_{T} value.

Inner detector

The main purpose of the inner detector is to measure the position of the interaction vertex together with any secondary vertices from long-lived particles like τ's or B-hadrons, and to measure the momenta of charged particles from the curvature of their trajectories in the magnetic field. The ID is shown in Fig. 2.3 [yellow and interior, the brown part is the EM calorimeter] and consists of three subdetectors, each having several layers.

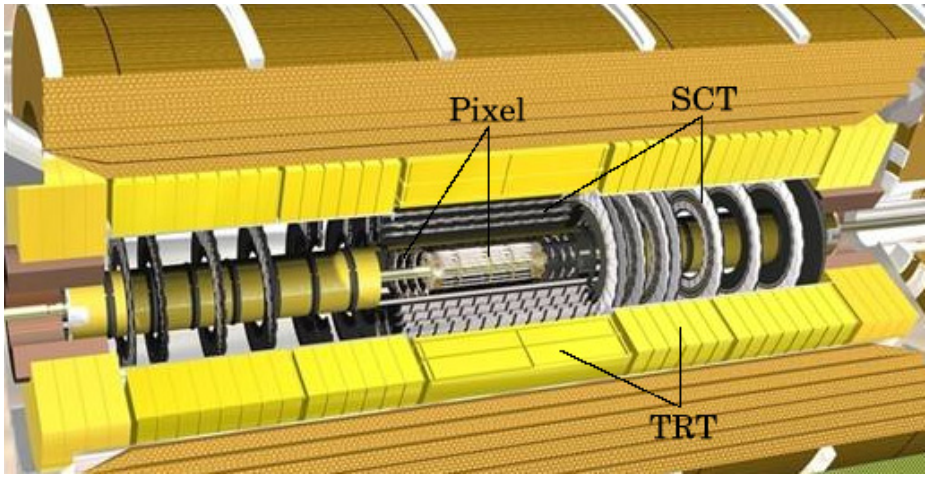

Figure 2.3: The inner detector. (Post-TDR geometry.)

Closest to the beam pipe lies the pixel detector. Both the barrel and the end cap parts have three pixel layers, ensuring three hits over the full acceptance defined by $|\eta| < 2.5$ (corresponding to $9.4^{\mathrm{o}} < \theta < 170.6^{\mathrm{o}}$), which amounts to 98.7% of the solid angle. The layers of the barrel part are situated at radii of 5, 9 and 12 cm. Due to its proximity to the beam pipe, the innermost barrel layer will be experiencing a very tough radiation climate and is scheduled to be replaced after 4-5 years.

Outside, in radial range between 30 and 52 cm, lies the semiconductor tracker (SCT). Four barrel layers together with end cap layers appropriately distributed on

nine wheels on each side in the $|z|$ range 80–280 cm ensure four hits over the full acceptance. Together the pixel detector and the SCT are referred to as the precision tracker. Their silicon-based technologies give discrete measurements and will be run at low temperatures of approximately -7 °C to reduce the radiation damage.

Outside the precision tracker lies the transition radiation tracker (TRT), a continuous tracking device. It is based on straw detectors with a diameter of 4 mm. Each straw consists of a cylinder serving as the cathode filled with a Xenon-based gas mixture and with a central anode wire. When a charged particle traverses a straw, the gas is ionised and charges drift towards the anode/cathode. In the barrel at radii 56–107 cm, and in the end cap at $|z| \in (80, 340)$ cm a total amount of 420 000 straw channels ensure approximately 36 hits per track. The TRT also has electron identification capabilities. A radiator material interspaced between and on the straws stimulates transition radiation (TR) as charged particles go from one medium to another. The Xenon-based gas in the straw volumes detects well TR photons in the energy range given by initiator electrons. TR hits are distinguished from ordinary track hits by their higher energy deposit in the straws. Since transition radiation starts to become important at a Lorentz factor $\gamma \gtrsim 1000$, the effect can be used to separate electrons from charged pions up to momenta of about 100 GeV.

ATLAS calorimetry

The purpose of the ATLAS calorimetry, shown in Fig. 2.4, is to measure the energy of electrons, photons and jets, as well as provide identification. While the depth of electromagnetic showers, initiated by electrons and photons, scales with the radiation length X_0, the depth of hadronic showers scales with the nuclear interaction length λ_I. Since $X_0 \ll \lambda_I$ for most detector materials, a calorimeter structure usually consists of two main parts, the electromagnetic (EM) calorimeter (inner layer) and the hadronic calorimeter (outer layer). Electrons and photons are measured and stopped in the EM calorimeter which is tuned for electromagnetic showers. Hadrons usually continue to the hadronic calorimeter where they eventually stop. Shower development is a stochastic process. While the widths and depths of electromagnetic showers are relatively stable for incident electrons and photons of a certain energy, the shape and size of hadronic showers show large variations for identical initial conditions.

All the ATLAS calorimeters are of the 'sampling' type, which means that they are made up of alternating layers of active and passive material. Only the energy collected in the active material is measured. Furthermore, the ATLAS calorimeters are 'non-compensating', which means that the response to an electron or photon of a certain energy is different (larger) than the response to hadrons of the same energy.

The energy resolution in a calorimeter can be parametrised by

$$\frac{\sigma(E)}{E} = \frac{a}{\sqrt{E}} \oplus b \oplus \frac{c}{E} \tag{2.2}$$

The first term is called the stochastic term and is mostly due to the stochastic nature, pronounced by the sampling principle, of measuring energy by 'counting charges'. Since the energy is proportional to N, the number of charges collected, and Poisson statistics is appropriate, we get $\sigma(E) \propto \sqrt{E}$. The second term is the constant term reflecting the 'mechanical precision' of the construction, and the third term is the noise term which takes into account the effect of electronic noise and pile up. The relation (2.2) shows that the resolution of the energy measurement increases with the energy of the particle.

Electromagnetic calorimeter

The electromagnetic calorimeter [olive] is placed just outside the inner detector, separated only by the solenoid. Both the barrel and the end cap parts are liquid argon (LAr) based with accordion-shaped electrodes and lead absorber plates. The showers are developed from the incident particle in the absorber plates The liquid argon is then ionised by the secondaries leaving the absorber, and the signal detected by the electrode. The accordion geometry provides faster readout and better hermeticity.

The total thickness of the calorimeter is approximately 25 radiation lengths (X_0) over the full acceptance. While muons will pass and leave only an ionising trail, electrons and photons will shower and stop entirely by consecutive bremsstrahlung and pair production processes. Hadrons will deposit part of their energy in the EM calorimeter, then arrive at the hadronic calorimeters which lie outside. At $|\eta| < 2.5$ the EM calorimeter consists of three sampling layers with different granularities ($\Delta\eta \times \Delta\phi$), optimised to give high precision angular measurement. At $2.5 < |\eta| < 3.2$ two layers and a coarser granularity are sufficient.

Before reaching the EM calorimeter, material amounting to $\sim 2X_0$ has to be crossed. A presampler placed in front of the calorimeter is used to correct for energy losses of electrons and photons. In the transition region between the barrel and the end cap, $1.37 < |\eta| < 1.52$, which corresponds to 3.0% of the full solid angle, the amount of material in front of the calorimeter is particularly large (5–$7X_0$), disqualifying this region for precision measurement involving photons. Due to the high granularity of the EM calorimeter, the two showers from primary $\pi^0 \rightarrow \gamma\gamma$ will rarely be interpreted as one, resulting in a good γ/π^0 separation vital to Higgs discovery through the $H \rightarrow \gamma\gamma$ channel.

Hadronic calorimetry

The hadronic calorimetry consists of three subsystems situated outside the EM calorimeter, see Fig. 2.4. In the barrel region the tile calorimeter [white], a sampling calorimeter with scintillating plastic plates as the active material and iron as the absorber, covers $|\eta| < 1.7$. Like the EM calorimeter it has three sampling lay-

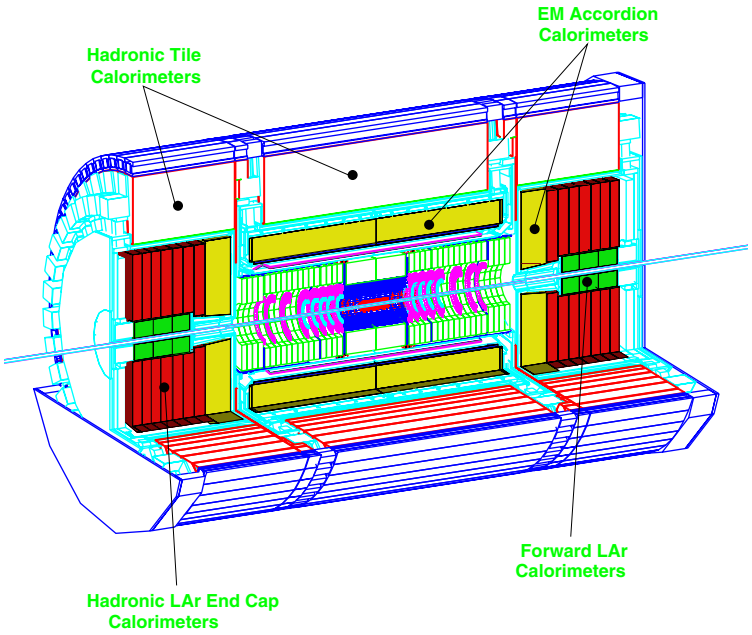

Figure 2.4: The ATLAS calorimetry. (From the ATLAS TDR.)

ers, although with a somewhat lower granularity. The hadronic end cap calorimeter (HEC) [red] at $1.5 < |\eta| < 3.2$ is based on the LAr technology, now with copper as the absorber material. It has four sampling layers. The forward calorimeter (FCAL) [green] extends the coverage to $|\eta| = 4.9$, thereby increasing the precision of the $E_{\mathrm{T}}^{\mathrm{miss}}$ measurement which is particularly important for SUSY studies. It is LAr based with three sampling layers, one with copper as the absorber material, the other two with tungsten, which due to its higher density provides the required material amount in the limited space allocated to the FCAL.

The total detector thickness in front of the muon system is ∼11–15 interaction lengths (λ_I), most of which is in the calorimeters and predominantly provided by the hadronic calorimeters. This is sufficient for measuring high-energetic jets with good resolution, as well as keeping punch-through into the muon system at controllable rates.

Muon spectrometer

The outermost subdetector in the ATLAS complex is the muon spectrometer. Its main task is to measure the momenta of the muons. As in the inner detector this is done by measuring how particle trajectories are bent in a magnetic field. Three barrel stations at radii of 5, 7.5 and 10 m and four end cap stations on each side at $|z|$ equal to 7, 10, 14 and 21–23 m ensure each muon to traverse three stations. Two technologies are in use to measure the tracks. For the barrel region and the outer end cap wheels, where rates are lower and background conditions milder, monitored drift-tube (MDT) chambers are sufficiently fast. They are based on aluminium tubes of 3 cm diameter filled with an Argon-based gas mixture at 3 bar and with a central anode wire. A total of 370 000 tubes is needed, with the length of the tubes varying from 70 to 630 cm. In the more demanding regions close to the interaction point, cathode strip chambers (CSC) are used. These are multiwire proportional chambers with shorter response-time and higher granularity.

The MDT and CSC measure the track positions in the R-z plane with high precision. In the idealised case where the magnetic field set up by the toroids is directed along ϕ, the bent muon tracks lie in the R-z plane, which means that in principle no ϕ-coordinates are required and the MDT/CSC measurements suffice to obtain the muon momenta.

The muon system is also equipped with a second set of detector chambers, again implemented with two different technologies and covering $|\eta| < 2.4$. These serve as trigger chambers, as well as provide measurements in ϕ, albeit at lower resolution, for use in the off-line pattern recognition.

Magnetic fields

The superconducting magnetic system of ATLAS consists of the central solenoid and the barrel and end cap toroids, see Fig. 2.2. For use in the inner detector tracking system the central solenoid provides a magnetic field at a nominal value of 2.0 T. The direction of the field is mainly along the z-direction, which is perpendicular to the transverse component of the particles. Due to its positioning in front of the EM calorimeter, the amount of material is kept at a minimum to disturb the energy measurements as little as possible.

The barrel and end cap toroids provide a magnetic field of peak value close to 4 T for use in the muon tracking system. Each of the three toroids are made up of eight coils and contained in aluminium alloy casings. The resulting magnetic field is mainly in the ϕ-direction, perpendicular to the muon momenta.

All the superconductors are cooled by helium at 4.5 K.

Trigger

While the bunch crossing rate is at 40 MHz, for permanent storage and later analysis only a rate of ∼100 Hz can be handled. The necessary reduction by a factor $\sim 4 \cdot 10^5$ is made by a three-level online trigger and data-acquisition (DAQ) system, programmed to select the interesting events.

First, by use of reduced-granularity information from the muon trigger system and all the calorimeters, and looking for high-p_{T} measurements as well as large total E_{T} or $E_{\mathrm{T}}^{\mathrm{miss}}$, the hardware-based level-1 trigger reduces the rate to ∼75 kHz. The total information on each selected event is read out from the electronics of the detectors and put into a buffer memory where it is eventually accessed by the software-based level-2 trigger. By refining and combining information, e.g. by applying isolation cuts for muons and matching between calorimeter and ID information for electrons, the level-2 trigger reduces the rate to ∼1 kHz. Finally the event filter (EF) uses off-line algorithms for further refinement, and arrives at the required ∼100 Hz, which means a storage rate of ∼100 MB/s.

2.2.3 Particle reconstruction

As stated at the beginning of the previous section, the objects which need to be reconstructed are muons, electrons, photons and jets. In the following more details are given on each of the types; how they interact with the detector, which subdetectors are active, specific challenges as well as the overall performance. Resolutions and efficiencies are given for design luminosity unless otherwise stated.

Muons

In addition to having a long lifetime ($c\tau_\mu = 659$ m), muons have great penetration power. From the center of the detector and outwards muons give hits in the ID, deposit only some energy in the calorimeters, then give hits in the muon spectrometer before leaving the detector to decay later.

In the determination of momentum from the track curvature [and assuming a uniform magnetic field], the relevant track parameter relates linearly not to p_{T} but to $1/p_{\mathrm{T}}$. If other effects are discarded, appropriate error propagation therefore gives

$$\frac{\sigma(p_{\mathrm{T}})}{p_{\mathrm{T}}} \propto p_{\mathrm{T}} \tag{2.3}$$

Hence, momentum resolution from tracking systems deteriorates as the energy grows, quite contrary to the energy resolution from calorimeter readings, see Eq. (2.2).

The muon momentum is measured both in the ID and in the muon system. The two systems complement each other in that they have different regions of sensitivity.

At low energies the precision is dominated by the ID, at high energies by the muon system, with a transition around $p_{\mathrm{T}} \approx 30$–$50$ GeV. For $p_{\mathrm{T}} = 10/100/1000$ GeV the expected resolution is $\sigma(p_{\mathrm{T}})/p_{\mathrm{T}} \approx 1.5/2.5/8\%$, showing the reduced precision as the energy is increased. The track reconstruction efficiency also reduces at higher energies. For $p_{\mathrm{T}} = 10/100/1000$ GeV the expected efficiency is $\epsilon \approx 97/95/85\%$. Furthermore, studies using single muons from the leptonic decay of a heavy vector boson, $W' \to \mu\nu_\mu$, show that the muon charge can be determined with a wrong-sign fraction of 0.2–0.9/3–4% for $m_{W'} = 1/6$ TeV. (For the numbers above, pile-up is not included.)

While we are usually most interested in muons which come directly from the hard process, typically as decay products of heavy particles like a Z or a SUSY particle, there are other sources, which need to be controlled. One is the muonic decay of $\pi^{\pm}/K^{\pm}$ ($c\tau = 7.8/3.6$ m) produced in the fragmentation into hadrons with subsequent decay. They have a good chance of decaying, typically to low-p_{T} muons, somewhere in the inner parts of the detector. The way to recognise these non-prompt muons is by combining the information from the ID with that of the muon spectrometer. The momentum from the ID measurement will be larger by an amount which cannot be explained by the limited energy loss in the calorimeters. Furthermore, the ID track will have a kink at the position of the decay which usually spoils the χ^2 for the combined track.

The other 'background' source of muons is semi-leptonic decay of B/D-hadrons resulting from fragmentation. These muons, which usually have higher p_{T}, can be distinguished from 'signal muons' by the larger energy deposited in the calorimeter cells close to the muon passage from the accompanying hadrons.

Electrons

The passage of electrons through the ID can be tracked through their hits in the precision detector and the TRT. While the same applies to muons, electrons have some additional features: They give special TR hits in the TRT, good for identification. Next, they are more affected by the noticeable amount of matter, $\sim 0.5 X_0$, in the ID and steadily lose energy by bremsstrahlung. This degrades the track quality and thereby the momentum measurement. Finally, when they reach the EM calorimeter, a showering procedure takes place through bremsstrahlung and pair production which effectively results in a full stop for the electrons.

In the same way the muon reconstruction takes advantage of two separate tracking systems, allowing for consistency checks, electron reconstruction is based on the combined ID and calorimeter readings. In accordance with the logic of Eqs. (2.2) and (2.3) the best energy measurement is obtained by the calorimeter at high energies and by the ID at low energies. The transition region is around $p_{\mathrm{T}} \approx 15$ GeV. For $E = 20/50/200$ GeV the expected resolution is roughly $\sigma(E)/E \approx 3/2/1\%$. Charge

identification is achieved with a wrong-sign fraction below 1.4% for $p_{\mathrm{T}} < 500$ GeV and increasing to 4.4% for $p_{\mathrm{T}} = 1$ TeV.

In the LHC environment one of the necessities of electron reconstruction is a high rejection factor against jets. From the calorimeter alone; by looking at how energy is shared between the different samplings, as well as the shower width and possible substructures within the shower, strong rejection is already achieved. Then, additional separation power is provided by combining the calorimeter and the ID information; looking at the calorimeter energy over the momentum, E/p, which for electrons is very close to 1, requiring consistency between the track and the position of calorimeter deposit, and asking for TR hits. All put together, the required jet rejection ($\sim 10^5$) is achieved with an electron efficiency close to 70%.

Photons

In principle photons leave no tracks in the ID. They are then detected in the EM calorimeter only, and are reconstructed with an energy resolution similar to that of electrons. However, due to the amount of material in the ID, around 30% of the photons convert to e^+e^- pairs before reaching the calorimeter. By reconstructing oppositely-charged tracks and requiring that they meet in a common vertex with no opening angle, and that the reconstructed photon points back to the beam-line, conversions can be recovered with an overall efficiency of about 60%. The energy resolution for converted photons is somewhat less than for unconverted photons.

While the converted photons are reconstructed from combined ID and EM calorimeter information, which also naturally gives the direction of the photon, the reconstruction of unconverted photon relies solely on the EM calorimeter. Driven by the requirements of the $H \to \gamma\gamma$ channel, the calorimeter is constructed to determine with sufficient precision the direction of an incoming photon. Since the z-position of the primary vertex is not known unambiguously, the directional capabilities of the calorimeter is essential to the mass resolution of the reconstructed Higgs mass. The ability of the calorimeter to determine the direction of a photon is also crucial in some versions of GMSB-type SUSY scenarios, where the next-to-lightest SUSY particle may be sufficiently long-lived to fly a distance of the order of the ID before decaying to an invisible gravitino and a photon. The evidence for having a GMSB-like scenario of this type, as well as the important measurement of the NLSP lifetime which relates to the SUSY breaking mechanism, will rely on the measurement of the photon direction.

Rejection against jets is important in the LHC environment, in particular for the $H \to \gamma\gamma$ channel. By investigating the shower shape, leakage into the hadron compartment, as well as vetoing tracks, the sufficient rejection ($\sim 10^3$) is achieved at about 80% photon efficiency.

Jets; b-jets, τ-jets

The path from the initially produced partons of the hard process to the reconstructed jets goes first via non-trivial and inescapable physics effects like the coexistence with the underlying event, initial and final state radiation, fragmentation and subsequent decay of unstable hadrons. When the (quasi)stable colourless objects have been formed, usually gathered into more or less narrow jet structures, they continue outwards through the ID where the charged ones give hits, enter the EM calorimeter where some amount of energy is deposited and end their journey in the hadronic calorimeter (if not already in the EM calorimeter). Since any charged components of a jet are deflected in the magnetic field, calorimeter clusters at different positions may be part of the same jet. From the ID tracking they can be appropriately combined, also with the neutral part.

Hadronic showers are dominated by successive inelastic hadronic interactions involving multiparticle production, but contain also an electromagnetic part from the frequent creation of π^0's which decay into two photons. The stochastic nature of π^0 production in combination with a non-compensating calorimeter, as well as the general LHC pile-up situation degrade the energy resolution of jets significantly compared to muons, electrons and photons. The resolution follows Eq. (2.2), but with larger coefficients than for electrons and photons. For $E = 50/100/200/1000$ GeV the expected resolution is $\sigma(E)/E \approx 15/9/7/3\%$.

While the identity of the initiating parton in most cases is lost, b-jets and jets from hadronically decaying τ's can be fairly efficiently tagged. For the former the tagging is due to the noticeable lifetime of B-hadrons ($c\tau \approx 450$ μm), allowing the observation of the secondary vertex. At design luminosity tagging efficiencies of 50% can be obtained with rejection factors of $\sim$10 against c-jets, which also have a noticeable lifetime, and $\sim$100 against gluon and light-quark jets.

Hadronic decay of τ's ($c\tau = 87$ μm) is characterised by few tracks, either one from $\pi^\pm$ or three from $\pi^\pm\pi^\pm\pi^\mp$, which take 50% and 15%, respectively, of the total branching width. This track information, together with the shower shape, allows for useful τ-tagging efficiencies, which become better with increasing p_{T}.

In conclusion, the ATLAS detector is well equipped to tackle supersymmetry. The high precision and efficiency of lepton and photon reconstruction, the good jet reconstruction including high b-tagging efficiency, and the large coverage to control the missing transverse energy address the most prominent SUSY features. In fact, beside the obligatory Higgs search, due to its rich phenomenology SUSY has been the most important source of benchmarks during the planning of the ATLAS detector.

Chapter 3

Simulation

In all the phases of an experiment like ATLAS, from the drawing board through the long period of building the machine, during the entire data taking and well into the aftermath, Monte Carlo simulations in different and continuously refined forms are invaluable tools to understand what actually happens in the detector. They guide the planning and building and form the basis for the conclusions that ultimately are to be drawn from the experiment. Most simulations, in particular those that aim to study certain physics channels (before, during or after the running period), are naturally divided into three parts.

The first step is the 'event generation'. The interactions at the beam crossing including production and decay of new particles, any additional radiation and hadronisation, all of which is called an event, are described by a Monte Carlo event generator. This is usually a general program, applicable to a multitude of experiments and which, apart from obvious variables like the energy of the colliding beams, is only slightly tuned to the experimental setup.

The next step is the 'detector simulation'. It consists of two parts, and is usually based on the general detector description and simulation tool `GEANT` [11]. First, the outgoing particles are transported through the detector with which they interact in a probabilistic manner. For this, full account of the most important processes for interaction with matter in the relevant energy range is required, as well as a detailed map of the detector. The transport of particles, especially the shower development in the calorimeters, is the most time-consuming part of the entire simulation. Next, from the hits in the tracking devices and the energy deposit in the calorimeters, the detector response is simulated. This is called the digitisation, and produces information in the same form as will be read out from the electronics in a real event.

The final step in the simulation chain is the 'reconstruction' of the original event from the detector read-out. This involves pattern recognition of tracker hits to determine particle tracks and momenta, the combining of calorimeter cells to form jets, inclusion of correction factors, particle identification etc., first locally in each

subdetector, then combined. Optimally, the reconstructed event corresponds well with the hard interaction of the generated event.

While the first step is quickly done with today's processor speeds, the two others, in particular the detector simulation, are very time-consuming. Depending on the needs of the particular study, various levels of detector detail can be incorporated in the simulation. Usually two versions are in use, a 'full simulation', which uses a detailed detector description thereby making it slow, and a 'fast simulation' in which the detector simulation and the reconstruction are merely parametrised to capture the overall behaviour of the detector.

Below follows a brief description of `PYTHIA` [12], the event generator used for the simulation, and `ATLFAST` [13], the ATLAS fast simulation program. No full simulation was performed for this thesis.

3.1 PYTHIA

3.1.1 Event generation

The natural starting point of the event generation process is the hard interaction: In its standard form two incoming partons, selected in a probabilistic manner according to parton distribution functions (PDFs), produce one or more heavy particles which immediately decay into lighter particles. If the underlying event is neglected for now, this will produce a $2 \to n$ event topology, where n is the number of outgoing particles.

However, it turns out that if coloured (charged) objects are present in the hard interaction, which is inevitable in a pp-collision, gluon (photon) radiation typically gives large corrections to the event topology suggested by the lowest-order hard interaction, and must be incorporated in some way. Two methods are in use for this. In the matrix-element method the appropriate Feynman-diagrams are calculated. While this is the theoretically appreciated method, it becomes very hard to carry through due to computational difficulties for higher order diagrams, especially loop diagrams. In general, hard gluon emission is well described by the matrix-element method, while multiple soft emissions are not. `PYTHIA` uses the somewhat less ambitious parton-shower method in which the more complicated topologies are generated by allowing each incoming and outgoing parton to initiate a set of subsequent branchings $a \to bc$. The parton-shower method performs well for multiple soft gluon emission and not so well for hard emissions.

In the parton-shower picture radiation is divided into initial state radiation (ISR) and final state radiation (FSR). The starting point of the ISR are two massless partons, one from each of the protons. When a massless parton branches, energy-momentum conservation requires at least one of the daughters to be space-like. In

PYTHIA the other is either on-shell or else it is time-like, in which case subsequent branchings will bring all the particles of this 'side branch' on-shell. The space-like daughter, now a mother, then branches into one daughter which is even more space-like and another one which is on-shell or time-like. In this way a 'main chain' of partons with increasing space-like virtuality is constructed, together with many side branches of on-shell partons. The side branches constitute the ISR. The final daughter of each of the two main chains meet in the hard process. [In PYTHIA the ISR evolution is actually carried through the other way around. The partons which enter the hard process are selected from 'evolved' PDFs where the effect of ISR is already included. Then a backward-evolution is performed which takes the two selected partons back to the initial partons of the proton.]

The FSR starts from the partons which leave the hard interaction. These have time-like virtualities to start with, otherwise branchings to on-shell particles would not be possible. The set of branchings then reduces the initial virtuality step by step until all the partons are on-shell. Since the branchings are predominantly soft, most of the energy in a branching is given to one of the daughters. Each parton leaving the hard process therefore gives rise to one main chain whose final daughter carries most of the initial momentum, and many softer side branches which contribute to the FSR.

When ISR and FSR have been brought to an end, the event consists of the following: one or more hard partons from the FSR main chains, ISR and FSR, mostly in terms of softer gluons and possibly some quarks and photons, and the beam remnants, all going out in different directions from the collision point. As these different parts separate more and more and start climbing the linear potential of QCD, their interconnections through colour charge become apparent and fragmentation eventually takes place.

Since fragmentation occurs in the non-perturbative regime of QCD, it is not understood from first principles. Two main types of phenomenological models are in use for this purpose. PYTHIA is based on the Lund Model, the most celebrated of the 'string fragmentation' (SF) models. Here the partons are first gathered logically into colourless objects called strings. In the simplest case a string is made up of a quark-antiquark pair $q\bar{q}$, moving away from each other with a uniform colour flux tube between them. Such a construction gives rise to a linear potential, which is exactly what the QCD confinement potential is believed to be. Eventually, as the quark and the antiquark move further apart, the string will break with the creation of a new quark-antiquark pair, $\bar{q}'q'$, resulting in two strings, $q\bar{q}'$ and $q'\bar{q}$. This process will continue until the strings have sufficiently low masses and convert into hadrons. The other main type, 'cluster fragmentation' (CF), is used e.g. in the Monte Carlo generator HERWIG [14]. Here all final gluons from the parton showers are first forced to split into $q\bar{q}$ pairs, then each quark combines with a nearby antiquark into a colourless cluster which finally decays into one or more hadrons.

The last step in the event generation chain is the decay of any unstable particles. In particular, the many hadrons produced in the fragmentation are usually unstable and decay immediately to lighter particles. The following (quasi)stable particle types are the ones that will be seen by the detector: $p/\bar{p}$, $n/\bar{n}$, $\pi^{\pm}$, $K^{\pm}$, K^0_L, γ, $e^{\pm}$, $\mu^{\pm}$. (A typical SUSY event may count ∼300 (quasi)stable particles, most of which are γ and $\pi^{\pm}$.)

3.1.2 SUSY

A wide range of hard processes are available in PYTHIA. In addition to most Standard Model processes of practical interest, many scenarios beyond the Standard Model are included. In particular SUSY is well represented. A large part of the full MSSM parameter space can be accessed. Also lepton-violating processes, see Eq. (1.4), which are discarded from the ordinary MSSM by R-parity conservation, have been coded.

The simulations performed for this thesis are within the mSUGRA scenario. While the full MSSM parameter space is determined by only $4\frac{1}{2}$ parameters in this scenario, RG evolution from the GUT scale to the EW scale is required. PYTHIA does not include this RG running. As a compensation, approximate formulas which in most cases get the parameters right by ∼10% are available. However, for studies in which the RG evolution is important, the idea is rather to interface PYTHIA with one of the programs which perform the evolution from the high scale. A fully standardised interface is available for ISASUSY [15], and is the one used for the simulations here. From the $4\frac{1}{2}$ GUT parameters ISASUSY evolves the relevant parameters down to the EW scale, calculates from these the mass parameters and passes them to PYTHIA which in turn finishes by calculating decay widths and cross-sections.

In PYTHIA all decays of SUSY particles are spin-averaged. For most studies, including the ones undertaken in this thesis, this has no consequence. However, spin effects are of course interesting in complete SUSY investigations, and must be incorporated for certain studies. At the time of writing only in HERWIG have spin-correlations in SUSY cascade decays been implemented.

3.1.3 LHC energies

The LHC will operate at presently unstudied energies. While we are able to predict quite precisely how the electroweak sector will behave at these energies, although with the obvious uncertainty of the Higgs mass, our predictions for QCD have large error bars. The extrapolation involved in the PDFs is significant. Also the adequacy of the current fragmentation models remains uncertain. Like the PDFs they are fitted to the available data, and it is not obvious that the current tunings work equally well at LHC energies. In total, one must reckon with considerable uncertainties

in the QCD background predicted by the event generators. This makes 'counting experiments' a particularly daunting exercise, and invites in general to caution in predicting discovery and measurement potential.

3.2 ATLFAST

The aims of the ATLAS fast simulation package, as given in the documentation, are to reproduce as well as possible the full-simulation results on the mass resolution for all important physics channels, to reproduce accurately the expected jet reconstruction efficiencies, especially for b-jets, as well as obtain the expected $E_{\mathrm{T}}^{\mathrm{miss}}$ resolution. In contrast, the package has not been optimised to reproduce the full-simulation efficiencies of lepton and photon isolation. The main application of the fast simulation is studies where it is reasonable to trade the accuracy of the simulation for speed. Resolution or reconstruction efficiency studies should always be confirmed with full simulation.

In the fast simulation algorithm the detector is represented by a grid of 'calorimetric cells' in η and ϕ with coverage and resolution similar to an approximate average over all the subdetectors ($\Delta\eta \times \Delta\phi$ equal to 0.1×0.1 for $|\eta| < 3$ and 0.2×0.2 for $|\eta| > 3$). The complicated affair of transporting the particles obtained from the event generator *through* the detector is simplified to depositing the E_{T} of each stable, visible final-state particle in the event, except muons, *onto* the detector grid of calorimetric cells.

Then reconstruction starts, where clusters are formed by a simple cone algorithm. Cells with $E_{\mathrm{T}} > 1.5$ GeV are allowed to act as cluster initiators, and are scanned in order of decreasing E_{T}. If the deposited E_{T} within $\Delta R \equiv \sqrt{(\Delta\eta)^2 + (\Delta\phi)^2} = 0.4$ of the initiator cell exceeds 10 GeV, a cluster is formed. The cells which make up a cluster are marked so as not to participate in the formation of another cluster. (Throughout the detector there will be cells where some energy is deposited, but which do not belong to a cluster.)

`ATLFAST` then goes on to identify the clusters. The list of final particles is scanned for muons, electrons and photons, in that order. When one of these are found, its four-vector is smeared according to the resolution expected for the given particle type. [In the language of the full simulation, this step belongs to the detector simulation rather than the reconstruction.] The smeared momenta are then required to be within the acceptance, $|\eta| < 2.5$ and $p_{\mathrm{T}} > 6/5/5$ GeV for $\mu/e/\gamma$, or else the particle is lost. While muons have no cluster associated to them, as they deposit no energy onto the detector grid, electrons and photons do, and the associated cluster is now identified.

Then isolation criteria are imposed. First, there must be no other (yet unidentified) cluster within $\Delta R = 0.4$. Second, the E_{T} deposited in a cone $\Delta R < 0.2$,

excluding the contribution of the particle itself, must not exceed 10 GeV. If these cuts are satisfied, the particle is regarded as reconstructed. If not, a muon will be marked as non-isolated while an electron/photon will be lost. The cluster stays though.

The energies of the remaining, unidentified clusters are then smeared according to the expected hadronic resolution, including pile-up effects at design luminosity, and the energy of any non-isolated muons within the cluster cone is added. A cluster is identified as a jet if $E_{\mathrm{T}} > 15$ GeV. Furthermore, as a first step of b/τ-tagging, the jets are 'labelled' as b, c or τ-jets if a particle of this type is found nearby and satisfying certain criteria relevant to the tagging in real life.

Finally, $\mathbf{p}_{\mathrm{T}}^{\mathrm{miss}}$ is constructed by summing the $\mathbf{p}_{\mathrm{T}}$ of all identified particles, all unidentified clusters, any non-isolated muons not attached to a jet, as well as all cells not belonging to a cluster (after first smearing them with hadronic resolution), then changing the sign.

The identification of μ, e, γ and b/τ-jets, as described above, is not complete. Additional efficiencies need to be included, and these are not constant, but depend on the rate of misidentification deemed acceptable for a given purpose. The higher the identification/tagging efficiency, the lower the rejection factor against misidentification/mistagging. For μ, e and γ realistic efficiencies need to be put in by hand, which for the two latter should be considered in combination with the possibility of misidentifying a jet for e/γ, which is lacking in the fast simulation. For b/τ-tagging dedicated routines are provided in the `ATLFAST-B` package.

There are two main sources of uncertainties in the simulation studies performed for this thesis. One is the unknown behaviour of physics at LHC energies, in particular of QCD. In the SUSY scenarios investigated here the sparticle masses are rather light and the collected signal samples large. Changes in the QCD cross-section and typical event topology will then not change the conclusions significantly. The other source of uncertainties is the simplifications involved in replacing the full simulation with the parametrised one, and this is probably more important. The reconstruction efficiencies and precisions both of leptons and jets are most likely slightly different for fast and full simulation. More pressing is however the lack of possibility to study realistic detector effects with the fast simulation. For the particular studies undertaken here, the detector behaviour is rather important for the final results. Therefore, in order to understand the detector effects and correct for them, large-scale full simulation must eventually be performed.

Chapter 4

SUSY measurements in ATLAS

In this chapter the prospects for SUSY discovery and subsequent parameter measurements is first briefly discussed. Then the endpoint method, which is the main theme of this thesis, is introduced and discussed. A few techniques for the endpoint calculations are shown, then some of the mass distributions themselves are discussed. Only to a very small degree does the presentation account for the contents of the papers. It is meant to be introductory as well as somewhat complementary.

4.1 Introduction

In order for SUSY to successfully address the hierarchy problem, the sparticle masses must lie within $\sim$1 TeV. This means that they will be fully accessible at the LHC and hence either discovered or excluded. If low-mass SUSY does indeed exist, the aims of ATLAS is first to make the discovery, which normally should happen quite fast (months or even weeks), depending on how quickly the detector is sufficiently understood, then, for the rest of the running period, to measure as many signatures as possible as accurately as possible. This will be vital in understanding the structure of the new sector. Is it compatible with e.g. mSUGRA, with MSSM, or is a less minimal structure required? Furthermore, one would like to look beyond, to the mechanisms for SUSY breaking and the physics residing there.

Given the number of free parameters in the more 'realistic' class of non-minimal models, this is a very ambitious goal. However, with a collection of central measurements in hand, such as cross-sections, masses, couplings and branching ratios, one may hope that the parameter space would be drastically reduced (although still considerable). Without such measurements, and this is the situation for preparatory studies, the available parameter space is overwhelming. It is simply impossible to envisage and study all viable phenomenologies. There are however some experimental constraints and theoretical hints, as discussed in Sects. 1.2.2–1.2.3. While these

serve to put strong limits on certain types of interactions, it is clear that the simplest implementations of these constraints, and which almost exclusively are the ones used for test analyses, do not capture the wealth of phenomenologies still allowed. A relevant example here is the mass degeneracy of the two first sfermions generations, present both in mSUGRA and in GMSB. It has a direct impact on many studies, but need not at all be realised in a less minimal model.

Nevertheless, the impact of restricting the analyses to e.g. mSUGRA, is probably less confining on the phenomenologies, which still are fairly generic, than on the next step, that of going from the measured quantities to the SUSY parameters. Although a complicated task even for the $4\frac{1}{2}$-parameter mSUGRA, obtaining the SUSY parameters and RG evolving them back to the GUT scale to find good correspondence with the initial parameters, is probably taking mSUGRA too seriously. Still, it is a starting point for learning how to cope with more realistic models. As the SUSY parameters are RG evolved towards higher scales, their errors increase. The prospects to constrain GUT scale physics rely therefore strongly on accurate measurements.

The standard signature of mSUGRA-like scenarios, to which we limit ourselves at this stage, is considerable $E_{\mathrm{T}}^{\mathrm{miss}}$ from the two escaping LSPs, many hard jets from the decay of gluinos and squarks, and leptons, either e or μ or the experimentally less attractive τ. By simply counting the number of events which pass certain selection cuts based on the typical signature, the SUSY signal can be observed on top of the SM background quite clearly for a large region of the $m_{1/2}$-m_0 plane already within months, and ultimately for squark and gluino masses of several TeV [16].

An estimate of the SUSY mass scale

$$m_{\mathrm{SUSY}} \approx \min(m_{\tilde{g}}, m_{\tilde{u}}) \tag{4.1}$$

and cross-section can be obtained from the 'effective mass' constructed from $E_{\mathrm{T}}^{\mathrm{miss}}$ and the p_{T} of the 4 hardest jets [17]

$$M_{\mathrm{eff}} = E_{\mathrm{T}}^{\mathrm{miss}} + \sum_{i=1}^{4} p_{\mathrm{T},i}^{\mathrm{jet}} \tag{4.2}$$

To get more precise information and in doing so also establish that what has been discovered really is SUSY, one needs to turn to exclusive analyses, i.e. try to isolate certain useful decay chains. With this change of perspective the remaining part of the SUSY sample suddenly becomes background, and as it turns out, a more dangerous background than the Standard Model one, for most SUSY scenarios and most analyses.

Some decay chains are more useful than others. Particularly interesting are decays which involve e or μ, since they provide a natural trigger and have very accurate momentum reconstruction. Due to the escaping LSP of each chain, no mass peaks

can be reconstructed as one would e.g. for the Z mass. Instead, indirect measurement through the endpoints of mass distributions has risen to become the canonical way of obtaining sparticle masses in such scenarios. Some details of the method are explained in the following sections.

In SUSY analyses so far, emphasis has been on determining sparticle masses. Then, within the framework of mSUGRA one has from this information alone been able to regain the GUT scale parameters. For more 'realistic' scenarios, masses alone will not suffice. Cross-sections, branching ratios, couplings etc.; all information must be combined, both to obtain the SUSY parameters, and to test for inconsistencies. Although the LHC experiments will be able to measure a lot of these quantities, in order to have a chance of fulfilling such a programme, a Linear Collider will most likely be required to provide complementary information of high accuracy.

4.2 Endpoints

4.2.1 Introduction

The endpoint method of obtaining masses is based on the following: if we are able to select events containing a certain decay chain and in each of these events isolate the correct branch, then from the visible decay products ('visibles') mass distributions can be constructed whose kinematic endpoints depend on the masses of the intermediate SUSY particles in a quantifiable way. Measurements of these endpoints can then be turned into measurements of the SUSY masses.

A decay chain particularly apt for this kind of analysis, is

$$\tilde{q} \to \tilde{\chi}_2^0 q \to \tilde{l} l q \to \tilde{\chi}_1^0 l l q \tag{4.3}$$

which is realised for considerable parts of the mSUGRA parameter space. The longer a decay chain is, the more mass distributions can be constructed. For a decay chain of this 'sequential type' with n SUSY particles, there are in principle $2^{n-1} - n$ mass distributions. This formula can be found by representing the combinations of visibles by a binary number where each of the $n-1$ visibles fills up a digit. The total number of combinations is then trivially 2^{n-1}, but since invariant masses cannot be constructed by combinations with 0 or 1 visible, n combinations must be subtracted.

4.2.2 Relativistic kinematics

Some useful results of relativistic kinematics, to be used later, can be obtained by investigating the first step of (4.3), $\tilde{q} \to \tilde{\chi}_2^0 q$. Align the coordinate system so as to have the quark go in the $+z$-direction ('up') and $\tilde{\chi}_2^0$ in the $-z$-direction ('down').

Since all movement is in the z-direction, the x and y-coordinates can be suppressed. In the rest frame of $\tilde{q}$ we then have

$$ {}^{\{\tilde{q}\}}p_q = \left({}^{\{\tilde{q}\}}E_q, {}^{\{\tilde{q}\}}p_q^z\right) = \left(\frac{m_{\tilde{q}}^2 - m_{\tilde{\chi}_2^0}^2}{2m_{\tilde{q}}}, \frac{m_{\tilde{q}}^2 - m_{\tilde{\chi}_2^0}^2}{2m_{\tilde{q}}}\right) \tag{4.4} $$

$$ {}^{\{\tilde{q}\}}p_{\tilde{\chi}_2^0} = \left({}^{\{\tilde{q}\}}E_{\tilde{\chi}_2^0}, {}^{\{\tilde{q}\}}p_{\tilde{\chi}_2^0}^z\right) = \left(\frac{m_{\tilde{q}}^2 + m_{\tilde{\chi}_2^0}^2}{2m_{\tilde{q}}}, -\frac{m_{\tilde{q}}^2 - m_{\tilde{\chi}_2^0}^2}{2m_{\tilde{q}}}\right) \tag{4.5} $$

where the squark rest frame is indicated with a 'pre'-superscript. The quark is taken to be massless which is a very appropriate approximation considering the large SUSY masses. The quarks, and later the leptons, can thus kinematically be pictured as photons. In particular, no Lorentz transformation can flip their direction.

The four-vectors (4.4)–(4.5) are seen to satisfy ${}^{\{\tilde{q}\}}p_q^2 = 0$, ${}^{\{\tilde{q}\}}p_{\tilde{\chi}_2^0}^2 = m_{\tilde{\chi}_2^0}^2$ and $({}^{\{\tilde{q}\}}p_p + {}^{\{\tilde{q}\}}p_{\tilde{\chi}_2^0})^2 = m_{\tilde{q}}^2$, as they should. For these relations to also hold in the rest frame of $\tilde{\chi}_2^0$, we need to have

$$ {}^{\{\tilde{\chi}_2^0\}}E_q = {}^{\{\tilde{\chi}_2^0\}}p_q^z = \frac{m_{\tilde{q}}^2 - m_{\tilde{\chi}_2^0}^2}{2m_{\tilde{\chi}_2^0}} \tag{4.6} $$

For the massless particle (quark) the energies in the two rest frames are seen to be related by the ratio $m_{\tilde{q}}/m_{\tilde{\chi}_2^0}$. This turns out to be a generic relation for rest frames defined by the decay of a particle into a massive and a massless one: If the momentum of a massless particle is parallel or antiparallel to the relative speed of two such rest frames, then its momenta in the two frames are related by the ratio of the two masses involved.

This 'mass-ratio rule', which will turn out to be very useful, can be deduced in a more conventional language. In the above example the relation between the rest frames of $\tilde{q}$ and $\tilde{\chi}_2^0$ can be given uniquely in terms of the Lorentz factor

$$ \gamma = \frac{{}^{\{\tilde{q}\}}E_{\tilde{\chi}_2^0}}{m_{\tilde{\chi}_2^0}} = \frac{m_{\tilde{q}}^2 + m_{\tilde{\chi}_2^0}^2}{2m_{\tilde{q}}m_{\tilde{\chi}_2^0}} \tag{4.7} $$

From γ the relative speed is found,

$$ \beta = \frac{m_{\tilde{q}}^2 - m_{\tilde{\chi}_2^0}^2}{m_{\tilde{q}}^2 + m_{\tilde{\chi}_2^0}^2} \tag{4.8} $$

and the two useful quantities

$$ \gamma(1+\beta) = m_{\tilde{q}}/m_{\tilde{\chi}_2^0}, \quad \gamma(1-\beta) = m_{\tilde{\chi}_2^0}/m_{\tilde{q}} \tag{4.9} $$

Consider now the appropriate parallel/antiparallel Lorentz transformation (boost) of a massless particle:

$$\begin{pmatrix} \gamma & \pm\gamma\beta \\ \pm\gamma\beta & \gamma \end{pmatrix} \begin{pmatrix} p_q^z \\ p_q^z \end{pmatrix} = \gamma(1 \pm \beta) \begin{pmatrix} p_q^z \\ p_q^z \end{pmatrix} \tag{4.10}$$

From Eq. (4.9) we see that the boost is given by multiplication with the mass ratios, confirming the mass-ratio rule.

Further understanding can be obtained by rewriting the factors γ and β in terms of rapidity ζ,

$$\gamma = \cosh\zeta, \quad \gamma\beta = \sinh\zeta \tag{4.11}$$

which also gives the relation

$$\gamma(1 \pm \beta) = e^{\pm\zeta} \tag{4.12}$$

Rapidity is an additive quantity under boosts. This means that two consecutive Lorentz boosts, characterised by ζ_1 and ζ_2, respectively, correspond to one boost with $\zeta = \zeta_1 + \zeta_2$.

Now, from Eq. (4.12) we can write

$$e^{\zeta} = e^{\zeta_1+\zeta_2} = e^{\zeta_1}e^{\zeta_2} = \gamma_1(1+\beta_1)\gamma_2(1+\beta_2) \tag{4.13}$$

The factor $\gamma(1 \pm \beta)$, which for a decay into one massive and one massless particle is simply given by the mass ratio, see Eq. (4.9), is therefore the multiplicative equivalent of rapidity. For massless particles consecutive boosts between the relevant frames in a decay chain like (4.3) are therefore easily performed by consecutive multiplications with the corresponding mass ratios.

4.2.3 Endpoint calculations

In the following the usefulness of the mass-ratio rule will be explicit in a calculation which generalises Eq. (2.11) of [2] to a (sequential) decay chain with an arbitrary number of SUSY particles. Consider the decay chain

$$\tilde{a}_n \to \tilde{a}_{n-1}b_{n-1} \to \tilde{a}_{n-2}b_{n-2}b_{n-1} \to \cdots \to \tilde{a}_1 b_1 b_2 \cdots b_{n-1} \tag{4.14}$$

where $\tilde{a}_i$ represents the (massive) SUSY particles and b_i are the visibles, the massless SM particles which are typically quarks, leptons and/or photons. In this subsection we will calculate the kinematic maximum value of the 'inclusive mass distribution', i.e. the mass distribution formed by combining all the visibles,

$$m^2_{b_1 b_2 \cdots b_{n-1}} = (p_1 + p_2 + \cdots + p_{n-1})^2 \tag{4.15}$$

where the four-momentum of b_i is given as p_i (instead of p_{b_i}). For $n = 2$ only one visible is available, so no invariant mass can be constructed. For $n = 3$ the maximum value is obtained when b_1 and b_2 are back-to-back in the rest frame of $\tilde{a}_2$, giving

$$m^2_{b_1 b_2} = \frac{(m_3^2 - m_2^2)(m_2^2 - m_1^2)}{m_2^2} \tag{4.16}$$

For $n \geq 4$ the decay configuration which gives the maximum value will depend on the masses, thereby giving multiple expressions for the endpoint. It is this situation we will investigate here.

Following the reasoning in Sect. 2.2 of [2], which applies equally well to our situation with n SUSY particles, we find that if the combination of SUSY masses are such that it is possible to bring $\tilde{a}_1$ to rest in the rest frame of $\tilde{a}_n$, then the endpoint will be given by $m_n - m_1$, where m_i is the mass of $\tilde{a}_i$. If this cannot be done, it will be because the masses are such that one of the $n-1$ decays in the chain is sufficiently dominant, meaning that the massive daughter of the dominant decay is emitted with momentum so large that not even optimal alignment of all the other $n-2$ decays will bring $\tilde{a}_1$ to rest in the rest frame of $\tilde{a}_n$.

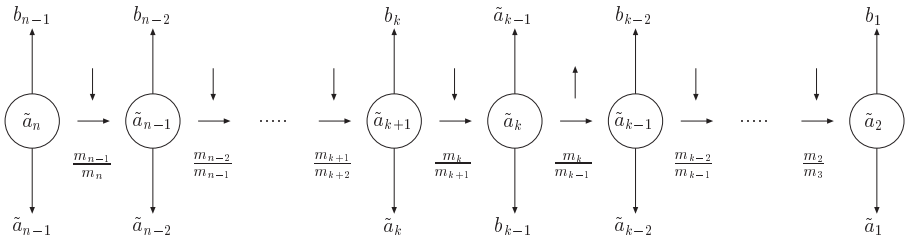

Figure 4.1: Sequential decay chain with n sparticles. See the text for details.

To quantify further, assume we have the decay configuration shown in Fig. 4.1. As before, the (massive and invisible) SUSY particles and the (massless and visible) SM particles are denoted $\tilde{a}_i$ and b_i, respectively. First, at the very left, $\tilde{a}_n$ decays, emitting b_{n-1} upwards and $\tilde{a}_{n-1}$ downwards. We then boost (the reference system) downwards to the rest frame of $\tilde{a}_{n-1}$, illustrated by the vertical arrow. (The horizontal arrow takes us to the next step in time.) Next, we let $\tilde{a}_{n-1}$ decay in the same way, emitting the visible upwards, the sparticle downwards, then boost anew to the rest frame of the sparticle etc. We assume the dominant mother to be $\tilde{a}_k$. The extreme configuration, which will allow us to find the appropriate formulas, occurs when the visible is emitted upwards in every decay except the dominant one where b_{k-1} is emitted downwards.

In the rest frame of $\tilde{a}_n$ conservation of momentum gives

$$|p^z_{k-1}| = \sum_{i\neq k-1} p^z_i + p^z_{\tilde{a}_1} \tag{4.17}$$

where, as earlier, particle names are suppressed for the visibles. If, in the given configuration where all the other visibles 'join forces against b_{k-1}', $p^z_{\tilde{a}_1}$ points upwards, i.e. has direction opposite to p^z_{k-1}, then the decay of $\tilde{a}_k$ is sufficiently dominant. (In the opposite case, if $p^z_{\tilde{a}_1}$ was directed downwards (and no other decay was dominant), then a sufficient mis-alignment of the $n-2$ non-dominant decays would allow $p^z_{\tilde{a}_1}$ to vanish, and we would have the maximum at $m_n - m_1$.) The criterion for the decay of $\tilde{a}_k$ to be dominant is therefore, in the rest frame of $\tilde{a}_n$:

$$|p^z_{k-1}| > \sum_{i\neq k-1} p^z_i \tag{4.18}$$

In the mother rest frame the energy of b_{i-1} is $(m_i^2 - m_{i-1}^2)/(2m_i)$. To find the energy in the rest frame of $\tilde{a}_n$, starting from $\tilde{a}_i$ go leftwards in Fig. 4.1 and for each decay boost (the reference system) in the opposite direction of the vertical arrow. As discussed earlier, for massless particles this corresponds to multiplying by a mass ratio for each boost. The appropriate mass ratios for $p^z_{i\neq k-1}$ (which all point upwards) are given in the figure, below the horizontal arrows. For p^z_{k-1} the inverse ratios should be used, since it is pointing downwards. This will give the following results for the momenta in the rest frame of $\tilde{a}_n$:

$$\begin{aligned}
p^z_{n-1} &= \frac{(m_n^2 - m_{n-1}^2)}{2m_n} &&= \frac{(m_n^2 - m_{n-1}^2)}{2m_n} \\
p^z_{n-2} &= \frac{(m_{n-1}^2 - m_{n-2}^2)}{2m_{n-1}}\frac{m_{n-1}}{m_n} &&= \frac{(m_{n-1}^2 - m_{n-2}^2)}{2m_n} \\
&\vdots && \vdots \\
p^z_k &= \frac{(m_{k+1}^2 - m_k^2)}{2m_{k+1}}\frac{m_{k+1}}{m_{k+2}}\cdots\frac{m_{n-2}}{m_{n-1}}\frac{m_{n-1}}{m_n} &&= \frac{(m_{k+1}^2 - m_k^2)}{2m_n} \\
-p^z_{k-1} &= \frac{(m_k^2 - m_{k-1}^2)}{2m_k}\frac{m_{k+1}}{m_k}\cdots\frac{m_{n-1}}{m_{n-2}}\frac{m_n}{m_{n-1}} &&= \frac{(m_k^2 - m_{k-1}^2)}{2m_n}\Big(\frac{m_n}{m_k}\Big)^2 \\
p^z_{k-2} &= \frac{(m_{k-1}^2 - m_{k-2}^2)}{2m_{k-1}}\frac{m_k}{m_{k-1}}\cdots\frac{m_{n-2}}{m_{n-1}}\frac{m_{n-1}}{m_n} &&= \frac{(m_{k-1}^2 - m_{k-2}^2)}{2m_n}\Big(\frac{m_k}{m_{k-1}}\Big)^2 \\
&\vdots && \vdots \\
p^z_2 &= \frac{(m_3^2 - m_2^2)}{2m_3}\frac{m_3}{m_4}\cdots\frac{m_{n-2}}{m_{n-1}}\frac{m_{n-1}}{m_n} &&= \frac{(m_3^2 - m_2^2)}{2m_n}\Big(\frac{m_k}{m_{k-1}}\Big)^2 \\
p^z_1 &= \frac{(m_2^2 - m_1^2)}{2m_2}\frac{m_2}{m_3}\cdots\frac{m_{n-2}}{m_{n-1}}\frac{m_{n-1}}{m_n} &&= \frac{(m_2^2 - m_1^2)}{2m_n}\Big(\frac{m_k}{m_{k-1}}\Big)^2
\end{aligned}$$

Summation of the $n-2$ non-dominant ones gives

$$\begin{aligned}\sum_{i\neq k-1} p_i^z &= \sum_{i=k}^{n-1} p_i^z + \sum_{i=1}^{k-2} p_i^z = \frac{(m_n^2 - m_k^2)}{2m_n} + \frac{(m_{k-1}^2 - m_1^2)}{2m_n}\left(\frac{m_k}{m_{k-1}}\right)^2 \\ &= \frac{(m_n^2 m_{k-1}^2 - m_k^2 m_1^2)}{2m_n m_{k-1}^2} \end{aligned} \tag{4.19}$$

Then, imposing Eq. (4.18) results in the following defining inequality

$$m_k^2 m_1 > m_{k-1}^2 m_n \tag{4.20}$$

or equivalently

$$\frac{m_k}{m_{k-1}} > \prod_{i\neq k-1}^{n-1} \frac{m_{i+1}}{m_i} = \frac{m_n}{m_{n-1}}\frac{m_{n-1}}{m_{n-2}} \cdots \frac{m_{k+1}}{m_k}\frac{m_{k-1}}{m_{k-2}} \cdots \frac{m_3}{m_2}\frac{m_2}{m_1} \tag{4.21}$$

Finally, from p_{k-1}^z and $\sum_{i\neq k-1} p_i^z$ the maximum value for the endpoint is obtained:

$$(m_{b_1\cdots b_{n-1}}^{\max})^2 = \frac{(m_k^2 - m_{k-1}^2)(m_n^2 m_{k-1}^2 - m_k^2 m_1^2)}{m_k^2 m_{k-1}^2} \tag{4.22}$$

This formula applies in the case of a dominant $\tilde{a}_k$, as defined by Eq. (4.21), and is valid for all $n-1$ dominance regions, $k \in \{2, \ldots, n\}$, $n \geq 4$. If no decay is dominant, the endpoint value is given by

$$(m_{b_1\cdots b_{n-1}}^{\max})^2 = (m_n - m_1)^2 \tag{4.23}$$

For $n = 4$ and $n = 5$ Eqs. (4.21)–(4.23) reproduce the previously obtained formulas for the squark and the gluino chain, see [9, 1] and [2]. With appropriate substitutions the same formulas also apply to a subchain of (4.14), provided, of course, that the effective n is larger than 3.

'Non-inclusive' mass distributions like $m_{b_1 b_2 b_4}$ will also be available experimentally, so their endpoints must be found. For $n \leq 5$ this programme is accomplished, see [2]. (A procedure analogous to the one applied for the inclusive distribution, although somewhat more complicated, might allow for the general solution to non-inclusive endpoints to be calculated.)

In the calculation performed above it is assumed that we can distinguish the b_i's from each other. This is not always the case. Consider e.g. the decay chain (4.3). It will usually be impossible to know which of the two leptons is b_1/b_2. Assuming that we have selected the correct jet (quark) and the leptons, two m_{ql} values can be constructed, but it is not possible to say which is $m_{b_3 b_1}$ and which is $m_{b_3 b_2}$.

The conventional solution to this problem is the construction of 'secondary distributions'. In this case these are defined by

$$m_{ql(\text{high})} = \max(m_{ql_1}, m_{ql_2}), \quad m_{ql(\text{low})} = \min(m_{ql_1}, m_{ql_2}) \tag{4.24}$$

on an event by event basis, where l_1 and l_2 denote the two leptons in an arbitrary labelling. While the endpoint of $m_{ql(\text{high})}$ is obtainable straightforward from the ('primary') ones already known, the endpoint of $m_{ql(\text{low})}$ and its equivalent for other distributions can in general be quite difficult to find [2].

4.3 Mass distributions

4.3.1 Endpoints from mass distributions

One ingredient to the method of finding the masses from the mass distributions is to calculate the endpoint expressions. The idea is then to match these with the experimentally obtained endpoints. In order for this matching to make any sense, there must of course be a correspondence between the two. However, given even the most optimal resolution and background situations, with limited statistics such a correspondence is not necessarily realised. The reason is that phase space for the highest mass values may be too small for experimental detection. It is not the one event with the largest mass value which gives the experimental measurement, but the collection of high-mass events. The endpoint is in practice determined from the higher 'edge' of the distribution by some fit.

A second ingredient to the method of obtaining masses from endpoints is therefore the knowledge of how edges relate to endpoints. For this the various mass distributions must be studied. Such studies have been performed for both the squark and the gluino distributions [1, 2]. Although most of the shapes depend on the masses involved, some generic behaviour can be stated for each. As a first step the distributions were classified into usable and unusable ones, based on how well the edge points towards the endpoint. On these grounds some of the gluino distributions were discarded due to the smallness of the phase space at high values. A second step would be to seek appropriate (mass-dependent) functions to describe the edges. These would then be used in the fitting procedure, in combination with prescriptions (found from full simulation studies) to describe detector and background effects. So far, in studies of this type, the edges have usually been described with a straight line, only to assess the statistical precision which can be obtained and without addressing the considerable systematic uncertainty of the fitting procedure. A third step might be perceived in which not only the edge is fitted, but the entire distribution. However, while the edge region is usually quite free of background, the intermediate and low-mass region is not. The original shape is therefore considerably distorted

at lower values, limiting the usefulness of such a procedure. In some cases there is however information to be retrieved from looking somewhat below the very edge, as will be demonstrated in the next subsection.

4.3.2 Shapes

The invariant mass of a certain combination of visibles in a decay chain containing n sparticles can be written formally as $m_{b_j \cdots b_m} = f(\mathbf{m}; \theta_i, \phi_i)$, where (θ_i, ϕ_i) are the $n-1$ sets of angles describing the given decay configuration and $\mathbf{m}$ denotes the n masses involved. If the matrix element of the decay contains no angular dependence (see Sect. 4.1 of [1]), then the rate is simply proportional to the solid angle, $\mathrm{d}N \propto \prod_i \mathrm{d}\theta_i \mathrm{d}\cos\phi_i$. To find the functional shape of the invariant mass distribution, it must be possible to express the rate in terms of the invariant mass. This has only been achieved in the near-trivial case of a sequential decay with $n = 3$, where the freedom to choose the coordinate system in each event reduces the number of parameters (angles) describing the decay configuration from 2×2 to 1. The rate is found to be proportional to the invariant mass, resulting in the well known triangular shape with a vertical high edge of e.g. m_{ll} in (4.3). The same triangular shape is also realised for m_{ql_n}, where l_n ('n' for 'near') denotes the lepton nearest to the squark, i.e. emitted by $\tilde{\chi}_2^0$. The other lepton is denoted l_f ('f' for 'far'). For m_{ql_f} the situation is different. An arbitrary configuration, and hence an arbitrary m_{ql_f}, is described by $3 \times 2 - 3 = 3$ angles, which already seems to be too much freedom to allow for a simple relation between the rate and the invariant mass.

We will now investigate in some detail the m_{ql} distributions, both to address very briefly the issue of appropriate fitting functions, but also to note that there is more to a distribution than its endpoint. In Fig. 4.2 m_{ql_n} and m_{ql_f} are shown along with their experimentally applicable substitutes, $m_{ql(\mathrm{low})}$ and $m_{ql(\mathrm{high})}$, for a representative selection of mass scenarios. The scenarios are classified according to three mass regions, as in Eq. (4.5) of [1], depending on which primary endpoint, if any, determines which of the secondary endpoints. To the left in the figure the specific relations are given. (The occurrence of the expression $m^{\max}_{ql(\mathrm{eq})}$ is explained in [10] and is available in Sect. 3.1 of [2] in this thesis.) The two primary distributions are both plotted in dashed black, and are distinguished from each other by the triangular shape of m_{ql_n} with a vertical high edge. The red curve shows the $m_{ql(\mathrm{high})}$ distribution, while $m_{ql(\mathrm{low})}$ is shown in blue. At higher invariant masses a secondary distribution may become identical to a primary one, resulting in overlapping curves. In these situations the dashed style of the primary distributions allows for both to be seen.

The secondary distributions have a rich variety of shapes which must be understood in relation to their origin as composite distributions, partly m_{ql_n}, partly m_{ql_f}. The $m_{ql(\mathrm{low})}$ distribution either inherits the vertical edge of m_{ql_n} (region 1), or else

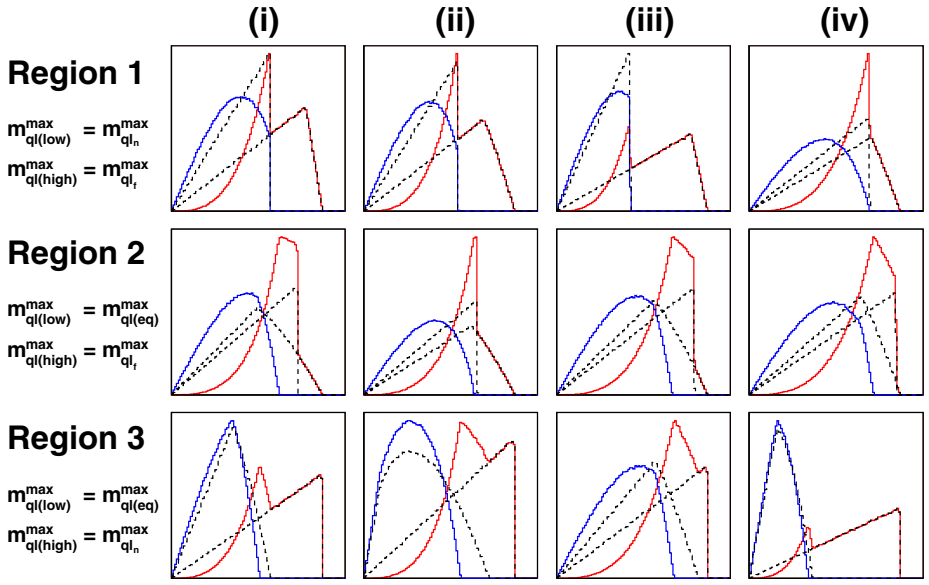

Figure 4.2: Four m_{ql} distributions. The primary distributions $m_{ql_{\rm n}}$ and $m_{ql_{\rm f}}$ are plotted in dashed black (two in each panel). The secondary distributions $m_{ql({\rm low})}$ and $m_{ql({\rm high})}$ are plotted in blue and red, respectively. See the text for further details.

descends towards the $m^{\rm max}_{ql({\rm eq})}$ value in an approximately linear (non-vertical) way. In some cases, e.g. scenario (ii) of region 2, the deviation from linearity is significant, suggesting that a better fit function should be sought. In the case of $m_{ql({\rm high})}$ the shapes are more varied. For invariant masses beyond the endpoint of the smaller of the primary distributions, $m_{ql({\rm high})}$ takes on the exact shape of the larger, and hence should in principle be fitted accordingly. However, $m_{ql({\rm high})}$ is also very interesting below this region, where it connects to and therefore contains information on the primary distribution with the lower endpoint. In region 1 the vertical fall in the interior of the $m_{ql({\rm high})}$ distribution, is caused by the end of $m_{ql_{\rm n}}$. Since this endpoint can already be measured by $m_{ql({\rm low})}$, no new information is obtained by fitting the 'endpoint' in the interior of $m_{ql({\rm high})}$, but a good consistency check is provided. For the other regions more is gained. In region 2 $m^{\rm max}_{ql_{\rm n}}$ is not measured in the conventional analysis but can again be found from the vertical fall in the interior of $m_{ql({\rm high})}$. In region 3 the secondary distributions leave $m^{\rm max}_{ql_{\rm f}}$ unaddressed, but it can be found from the now non-vertical fall in the interior of $m_{ql({\rm high})}$.

This short discussion demonstrates that not just the endpoints, but also the shapes of at least some of the distributions contain 'exact' information, i.e. which

can be quantitatively related to the masses. Although the theoretical shapes of Fig. 4.2 will become somewhat distorted by the inclusion of detector and background effects, their original structure will usually shine through, especially at higher invariant masses. This is at least the case for SPS 1a (α) and (β), the two scenarios investigated in [1] and shown in Fig. 4.2 as scenario (iv) of regions 1 and 2, respectively. At (α), although not really used in the analysis, the composite nature of the $m_{ql(\text{high})}$ edge is quite visible in the 'experimental' plot. At (β) the identification of the vertical fall in $m_{ql(\text{high})}$ with $m_{ql_{\text{n}}}^{\text{max}}$ becomes crucial when it is realised from consistency checks that the $m_{ql(\text{high})}^{\text{max}}$ measurement is unreliable.

4.3.3 Improvements

Should SUSY be detected at the LHC, the study of shapes will become very important, both for consistency tests and to find appropriate fitting functions. Detailed studies of shapes must include physics effects like radiation and fragmentation, distortions due to precuts, and pure detector effects. Furthermore, most scenarios studied so far have been within mSUGRA, where all first and second-generation squarks are near-degenerate. If this feature should be absent in the realisation chosen by Nature, substructures would be added to the mass distributions, complicating the measuring process. Future shape studies should therefore also include the possibility of non-degenerate squarks. A further extension could be to investigate correlations between mass distributions.

4.4 Masses from endpoints

Finally, when experimental values for the endpoints have been obtained, they can be turned into values for the masses. If the number of endpoints coincides with the number of masses, as in a sequential decay chain with four invisibles, then it is usually possible to solve for the masses analytically [1]. If more endpoints are available, a numerical approach is however required in order to weight the endpoints according to measurement uncertainty. The best-fit masses are the ones which minimise the appropriate least-squares function.

Two important features are discussed at length in [1, 2]. One is that the inversion of the endpoint expressions, be it analytical or numerical, is not a one-to-one operation. The endpoints are in general composite functions of the masses, so different sets of masses may give the same set of endpoint values. Multiple solutions for masses are therefore inherent to the endpoint method of determining masses, unfortunately. The other feature is also generic. The endpoint method determines mass differences with much higher accuracy than the masses. This opens for a strong desire to cooperate with a Linear Collider which fixes the mass scale by a precise measurement of the LSP mass.

Chapter 5

Summary

In R-parity conserving TeV-scale supersymmetry, sparticles will be produced in pairs at the LHC, then decay in cascades which end with the lightest supersymmetric particle. If the LSP is neutral it will not be detected, and decay chains cannot be fully reconstructed, complicating the mass determination of the sparticles. In this thesis the endpoint method of determining SUSY masses has been thoroughly investigated, both theoretically and experimentally. For the sequential four-sparticle squark decay chain, inversion formulas have been calculated which give the masses explicitly in terms of the endpoints. Ambiguities and complications in the mass determination caused by the composite endpoint expressions have been carefully investigated. For the sequential five-sparticle gluino decay chain, all the new endpoint expressions were calculated in full generality, thereby opening for a new and competitive way of determining the gluino mass. The shape variety of the mass distributions was studied in some detail since endpoint measurement through edge fitting relies strongly on the specific edge behaviour. More remains to be done in this area. In two specific mSUGRA scenarios the performance of the endpoint method was estimated with a fast simulation of the ATLAS detector. Finally, as the LHC will not be the last particle accelerator, the impact of combining the LHC measurements with a Linear Collider measurement of the LSP mass was assessed.

Bibliography

[1] B. K. Gjelsten, D. J. Miller, P. Osland, JHEP **12** (2004) 003 [arXiv:hep-ph/0410303].

[2] B. K. Gjelsten, D. J. Miller, P. Osland, ATL-PHYS-2005-001 [arXiv:hep-ph/0501033].

[3] B. K. Gjelsten, E. Lytken, D. J. Miller, P. Osland, G. Polesello, ATL-PHYS-2004-007.

[4] G. Weiglein *et al.* [LHC / ILC Study Group], hep-ph/0410364.

[5] S. Eidelman *et al.* [Particle Data Group Collaboration], Phys. Lett. B **592** (2004) 1.

[6] R. Barate *et al.* Phys. Lett. B **565** (2003) 61 [arXiv:hep-ex/0306033].

[7] S. P. Martin, arXiv:hep-ph/9709356.

[8] ATLAS Collaboration, *ATLAS Detector and Physics Performance Technical Design Report, 1 and 2*, CERN-LHCC-99-014, CERN-LHCC-99-015, 1999.

[9] B. C. Allanach, C. G. Lester, M. A. Parker and B. R. Webber, JHEP **0009** (2000) 004 [arXiv:hep-ph/0007009].

[10] C. G. Lester, *Model independent sparticle mass measurements at ATLAS*, Ph. D. thesis, http://www.slac.stanford.edu/spires/find/hep/www?r=cern-thesis-2004-003.

[11] R. Brun *et al.*, GEANT3, CERN/DD/EE/84-1 (1996).

[12] T. Sjöstrand, P. Edén, C. Friberg, L. Lönnblad, G. Miu, S. Mrenna, E. Norrbin, Comput. Phys. Commun. **135** (2001) 238; T. Sjöstrand, L. Lönnblad and S. Mrenna, "PYTHIA 6.2: Physics and manual", arXiv:hep-ph/0108264.

[13] E. Richter-Was, D. Froidevaux and L. Poggioli, "ATLFAST 2.0: a fast simulation package for ATLAS", Tech. Rep. ATL-PHYS-98-131 (1998)

[14] G. Marchesini, B. R. Webber, G. Abbiendi, I. G. Knowles, M. H. Seymour and L. Stanco, Comput. Phys. Commun. 67 (1992) 465;
G. Corcella, I.G. Knowles, G. Marchesini, S. Moretti, K. Odagiri, P. Richardson, M. H. Seymour, B. R. Webber, JHEP **0101** (2001) 010 [arXiv:hep-ph/9912396]

[15] H. Baer, F. E. Paige, S. D. Protopopescu and X. Tata, arXiv:hep-ph/9305342, arXiv:hep-ph/0001086.

[16] H. Baer, C. h. Chen, F. Paige and X. Tata, Phys. Rev. D **52** (1995) 2746 [arXiv:hep-ph/9503271], Phys. Rev. D **53** (1996) 6241 [arXiv:hep-ph/9512383].

[17] I. Hinchliffe, F. E. Paige, M. D. Shapiro, J. Soderqvist and W. Yao, Phys. Rev. D **55** (1997) 5520 [arXiv:hep-ph/9610544], D. R. Tovey, Phys. Lett. B **498** (2001) 1 [arXiv:hep-ph/0006276].

List of papers

This thesis is based on the following papers:

1. B. K. Gjelsten, D. J. Miller, P. Osland,
   Measurement of SUSY Masses via Cascade Decays for SPS 1a
   JHEP **12** (2004) 003 [ATL-PHYS-2004-029, arXiv:hep-ph/0410303]

2. B. K. Gjelsten, D. J. Miller, P. Osland
   Measurement of the Gluino Mass via Cascade Decays for SPS 1a
   (Submitted to JHEP) [ATL-PHYS-2005-001, arXiv:hep-ph/0501033]

Preprint typeset in JHEP style - HYPER VERSION

ATL-PHYS-2004-029
Edinburgh 2004/12

Measurement of SUSY Masses via Cascade Decays for SPS 1a

B. K. Gjelsten

Department of Physics, University of Oslo, P.O.B. 1048, Blindern, N-0316 Oslo, Norway
E-mail: B.K.Gjelsten@fys.uio.no

D. J. Miller

Department of Physics and Astronomy, University of Glasgow, Glasgow G12 8QQ, U.K.
and
School of Physics, University of Edinburgh, Edinburgh EH9 3JZ, U.K.
E-mail: D.Miller@physics.gla.ac.uk

P. Osland

Department of Physics, University of Bergen, N-5007 Bergen, Norway
E-mail: Per.Osland@ift.uib.no

Abstract: If R-parity conserving supersymmetry exists below the TeV-scale, new particles will be produced and decay in cascades at the LHC. The lightest supersymmetric particle will escape the detectors, thereby complicating the full reconstruction of the decay chains. In this paper we expand on existing methods for determining the masses of the particles in the cascade from endpoints of kinematical distributions. We perform scans in the mSUGRA parameter space to delimit the region where this method is applicable. From the examination of theoretical distributions for a wide selection of mass scenarios it is found that caution must be exerted when equating the theoretical endpoints with the experimentally obtainable ones. We provide analytic formulae for the masses in terms of the endpoints most readily available. Complications due to the composite nature of the endpoint expressions are discussed in relation to the detailed analysis of two points on the SPS 1a line. Finally we demonstrate how a Linear Collider measurement can improve dramatically on the precision of the masses obtained.

Keywords: SUSY, BSM, MSSM.

Contents

1. Introduction

The Standard Model (SM) of particle physics has been remarkably successful in describing the physics probed by modern day particle accelerators. No deviation from the SM has thus far been confirmed by experiment and only the Higgs mechanism, the SM's instrument for the breaking of the electroweak symmetry, remains to be discovered. Nevertheless, the SM suffers from considerable theoretical difficulties, not least of which is the *hierarchy problem* [1], the extreme sensitivity of the electroweak scale to new physics. Such difficulties imply that the SM is only an *effective low-energy theory* (albeit a highly successful one) applicable only up to a few hundred GeV or so, and will need to be extended in order to describe physics at higher scales.

One extension which has attracted a lot of attention is supersymmetry [2, 3, 4, 5]. Supersymmetry not only solves the hierarchy problem but has many other attractive features: it is the only non-trivial extension to the Poincaré symmetry of space-time [6]; it is essential to the formulation of superstring theories [7]; it provides a low-energy theory which is more amenable to the unification of the fundamental forces into a Grand Unified Theory (GUT) at some high energy scale [8]; it provides a *natural* mechanism for generating the Higgs potential which breaks the electroweak symmetry [9, 10, 11, 12, 13, 14]; and it supplies a good candidate for cold dark matter [15]. Furthermore, if it is to be relevant in solving the hierarchy problem it must exhibit experimental consequences at the TeV-scale, and therefore can be tested by experiment at the Large Hadron Collider (LHC). For an overview of supersymmetry searches at LEP, the Tevatron and HERA, see Ref. [16].

If supersymmetric particles are produced at the LHC, thus confirming supersymmetry, it will become important to identify them and accurately measure their masses. This will be essential for identifying the low energy model and hopefully distinguishing the Minimal Supersymmetric Standard Model (MSSM) from other non-minimal extensions. Furthermore, since no supersymmetric particles have so far been discovered, supersymmetry must be broken by some as yet unknown mechanism. Only an accurate determination of the supersymmetric particle masses and couplings will allow us to determine the low energy soft supersymmetry breaking parameters. It is hoped that extrapolation of these masses and couplings to high energies using the renormalisation group equations will provide an insight into the mechanism of supersymmetry breaking and, more generally, physics at the GUT scale [17]. Since errors in the mass measurements will be magnified by the renormalisation group running it is absolutely essential that these masses be determined as accurately as possible.

Here we will discuss supersymmetric mass measurements with reference to one particular model of supersymmetry breaking, minimal super-gravity (mSUGRA) [18, 12, 9, 13, 14]. In this model, the supersymmetry is broken by the interaction of new particles at high energy which are only linked to the usual particles by gravitational interactions; this new sector of physics is often referred to as the *hidden sector*. These gravitational interactions transmit the supersymmetry breaking from the hidden sector to our own sector, producing TeV scale effective soft supersymmetry breaking terms in the GUT scale Lagrangian, quantified by parameters which run logarithmically down to the probed TeV scale. At the

GUT scale, the scalar supersymmetric particles are assumed to have a common mass, m_0, while the gauginos have a common mass $m_{1/2}$. The trilinear couplings are also taken to be universal at the GUT scale and denoted A_0.

Mass measurements in the MSSM are complicated by R-parity conservation, which is introduced to prevent unphysical proton decay. R-parity conservation requires that supersymmetric particles are produced in pairs and causes the lightest supersymmetric particle (LSP) to be stable. Consequently the LSP is inevitably the end product of every supersymmetric decay and, if electrically neutral, will escape the detector leaving no track or energy deposit. While this provides a very distinctive *missing energy* signature, it makes it very difficult to measure masses at the LHC since one cannot fully reconstruct decays.

Instead, mass measurements rely on continuous mass distributions of decay products which attain extrema for certain configurations of the particle momenta that are unambiguously determined by the masses of initial, intermediate and final particles involved. These relations may often be inverted to give the masses of unstable particles. This is analogous to the way a bound on the neutrino mass can be obtained from the end-point of the beta-decay spectrum of ^{3}H [19], but is usually more complex, since a long decay chain is often involved.

In this study we will consider supersymmetric mass measurements made by examining the mass distribution endpoints or 'edges' of the long decay chain[1] $\tilde{q} \to \tilde{\chi}_2^0 q \to \tilde{l} l q \to \tilde{\chi}_1^0 l l q$ in the ATLAS detector [20]. In particular, we will focus on the Snowmass mSUGRA benchmark line SPS 1a [21], but will also include other mSUGRA parameters in a general discussion. In addition to the usual SPS 1a point, which we will denote SPS 1a (α), we will also consider another point on the SPS 1a line, denoted SPS 1a (β), which has a reduced branching ratio for the decay. This will provide a counterpoint to the study of SPS 1a (α) where the branching ratio is rather high. This study differs from previous reports [22, 23, 24, 25, 26] by (i) discussing theoretical distributions which arise for different mass scenarios, (ii) providing inversion formulas, (iii) discussing ambiguities and complications related to the composite nature of the endpoint expressions. Furthermore, we provide an overview of the mSUGRA parameter space, and consider a new point on the SPS 1a line. Finally, we discuss the effects of including Linear Collider data in the analysis.

In Sect. 2 we will discuss general mSUGRA scenarios, paying attention to supersymmetric decay branching ratios to gain some understanding of how generally applicable these kinematic endpoint measurements are. We will identify mass hierarchies for which these mass measurements are possible and show that they occur over a large portion of the mSUGRA parameter space. In Sect. 3 we will outline the properties and mass spectra of the Snowmass benchmark line SPS 1a and the associated points SPS 1a (α) and SPS 1a (β). After defining the decay chain under investigation, we go on in Sect. 4 to discuss the theoretical framework of cascade endpoint measurements, and present analytic expressions for masses in terms of these endpoints. In Sect. 5 the experimental situation at the ATLAS detector will be studied, including event generation and reconstruction, the removal of backgrounds, and results for the measurement of the kinematic endpoints will

[1]Throughout the text the notions lepton/slepton as well as $l/\tilde{l}$ will refer to the particles of the first and second generation. The third generation particles will be called tau/stau and denoted $\tau/\tilde{\tau}$.

be presented. The extraction of masses from the kinematic endpoints will be described in Sect. 6. Finally, the remarkable improvement of the accuracy of the mass measurements obtained by using inputs from an e^+e^- collider [27, 28] will be studied in Sect. 7, before drawing our conclusions in Sect. 8.

2. Cascade decays in mSUGRA scenarios

In this paper we will be examining the decay chain $\tilde{q} \to \tilde{\chi}_2^0 q \to \tilde{l}lq \to \tilde{\chi}_1^0 llq$ in the Snowmass scenario SPS 1a for the purpose of the extraction of the supersymmetric particle masses. However, it is extremely unlikely that SPS 1a is exactly the parameter choice of reality, and there would be little point to the study if our methods were only applicable at SPS 1a, or a small region around it. Therefore, in this section we will take a more general look at mSUGRA scenarios to determine whether or not these methods may be used more generally, over a wide parameter range.

At the LHC the main supersymmetric production will be sparticle pairs $\tilde{g}\tilde{g}$, $\tilde{g}\tilde{q}$ and $\tilde{q}\tilde{q}$, as long as these are not too heavy. Each sparticle immediately decays into a lighter sparticle, which in turn decays further, until, at the end of the chain, an LSP will be produced. Since there are two parent supersymmetric particles, each event will typically have two such chains, complicating their reconstruction.

What route is taken from the initial gluino or squark down to the LSP depends on which decay channels are open, as well as their branching fractions. Therefore there are two criteria which must be met in order to use the cascade kinematic endpoint methods: firstly the sparticle mass hierarchy must be such that the analysed decay chain is allowed; and secondly, the cross-section for the entire decay chain must be large enough to allow analysis.

2.1 The mSUGRA mass hierarchy

In a general MSSM model there are few constraints on the sparticle masses, so little can be assumed about their relative mass hierarchy. However, if universal boundary conditions are imposed on the mass parameters at the GUT scale, some mass orderings at the TeV scale are natural, and some are even necessary.

For example, in mSUGRA scenarios squarks and sleptons have a common mass at the GUT scale, m_0, but when the masses are evolved down to the TeV scale, QCD interactions affect only the evolution of the squarks and not the colourless sleptons. Consequently, squarks are always heavier than sleptons at LHC energies. For the same reasons, although they may start off with different masses at the GUT scale, running induced by QCD interactions is usually enough to result in the squarks of the first two generations being heavier than the neutralinos and charginos at the TeV scale. (Large mixing can however bring $\tilde{t}_1$, and to a lesser extent $\tilde{b}_1$, quite low in mass.)

At the opposite end of the spectrum, there are a number of possible candidates for the LSP: the lightest neutralino, $\tilde{\chi}_1^0$, the lightest chargino $\tilde{\chi}_1^\pm$, or the lightest slepton (in mSUGRA models, the gravitino is usually rather heavy). Which of these is the LSP depends on the relative sizes of m_0, $m_{1/2}$ and the derived low-energy Higgs-higgsino mass

parameter μ. However, the assumption of gauge unification at the GUT scale explicit in mSUGRA models leads to the relation

$$M_1 \approx \frac{5}{3} \tan^2 \theta_W M_2 \tag{2.1}$$

between the $U(1)$ and $SU(2)$ gaugino masses, M_1 and M_2 respectively. As a result, M_1 tends to be rather low, significantly lower than $m_{1/2}$. Furthermore, the derived quantity μ is often required to be much larger than M_1 in order to give the correct electroweak symmetry breaking (at the SPS 1a (α) reference point $\mu = 357.4$ GeV). For the majority of parameter choices this implies that the LSP will be $\tilde{\chi}_1^0$, with $\tilde{\tau}_1$ being the LSP only if $m_0 \ll m_{1/2}$, and $\tilde{\chi}_1^\pm$ only for a small region where $m_{1/2} \to 0$. The left-handed sneutrino, by virtue of its $SU(2)$ interactions, is usually heavier than $\tilde{\tau}_1$, and is anyway ruled out by direct searches [29]. It is indeed fortunate that $\tilde{\chi}_1^0$ is the LSP for most of the parameter space since it is clear that only an electrically neutral LSP can play the role of the dark matter constituent which is believed to fill the universe. Finally, the gaugino mass relation, Eq. (2.1), implies that the LSP is usually bino-like.

The first requirement for the decay chain $\tilde{q} \to \tilde{\chi}_2^0 q \to \tilde{l}lq \to \tilde{\chi}_1^0 llq$ is that the gluino should be comparable to or heavier than the squark initiating the decay chain. If the gluino is sufficiently light, then the squark will almost always choose to decay via its strong interaction $\tilde{q} \to \tilde{g}q$ rather than by the electroweak decay $\tilde{q} \to \tilde{\chi}_2^0 q$. Of course, one does not need all of the squarks to be lighter than the gluino; as long as one squark, for example $\tilde{b}_1$, is lighter than the gluino, useful information can potentially be obtained from its subsequent decay chain. The second important characteristic is that $\tilde{\chi}_2^0$ should be heavier than $\tilde{l}$, thereby allowing the lower part of the chain to proceed, $\tilde{\chi}_2^0 \to \tilde{l}l \to \tilde{\chi}_1^0 ll$. Otherwise $\tilde{\chi}_2^0$ will decay to $\tilde{\chi}_1^0 Z$ or $\tilde{\chi}_1^0 h$, or to $\tilde{\chi}_1^0 f\bar{f}$ via a three-body decay, and the useful kinematic endpoints are lost.

In order to understand where in the mSUGRA parameter space these hierarchy requirements are realised, we have performed a scan over the $m_{1/2}$–m_0 plane for four different choices of A_0 and $\tan\beta$ (with $\mu > 0$), and identified the different hierarchy regions with different colours in Fig. 1. The renormalisation group running of the parameters from the GUT scale to the TeV scale has been done using version 7.58 of the program `ISAJET` [30], which is inherent to the definition of the 'Snowmass Points and Slopes' (see Sect. 3).

The upper left plot shows the $m_{1/2}$–m_0 plane with $A_0 = -m_0$ and $\tan\beta = 10$ and includes the SPS 1a line and points (labeled (α) and (β)). The upper right plot has $A_0 = 0$ and $\tan\beta = 30$ and contains the benchmark point SPS 1b. The lower left plot also has $A_0 = 0$ but $\tan\beta = 10$ and contains the SPS 3 benchmark line and point. Finally the lower right plot has $A_0 = -1000$ GeV and $\tan\beta = 5$ and contains SPS 5.

The different hierarchies themselves are combinations of the hierarchy between the gluino and the squarks important to the upper part of the decay chain, and that of $\tilde{\chi}_2^0$ and the sleptons relevant to the later decays. Since $m_{\tilde{l}_R} < m_{\tilde{l}_L}$ for any set of mSUGRA parameters, we here use $\tilde{l}_R$. The seven numbered regions are defined by:

$$\text{(i)} \qquad \tilde{g} > \max(\tilde{d}_L, \tilde{u}_L, \tilde{b}_1, \tilde{t}_1) \qquad \text{and} \quad \tilde{\chi}_2^0 > \max(\tilde{l}_R, \tilde{\tau}_1)$$

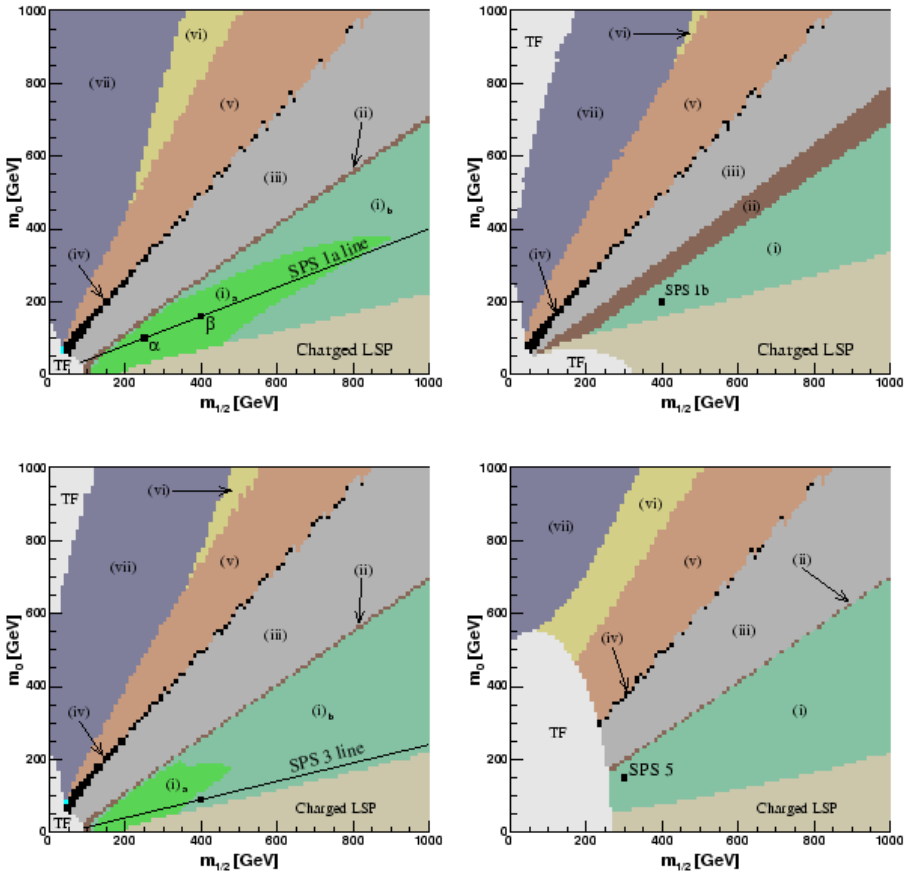

Figure 1: Classification of different hierarchies, labeled (i)–(vii), for four combinations of $\tan\beta$ and A_0, such that the four panels contain respectively the SPS 1a line, the SPS 1b point, the SPS 3 line, and the SPS 5 point. The regions marked 'TF' are theoretically forbidden. (See text for details.)

$$
\begin{array}{lllll}
\text{(ii)} & \tilde{g} > \max(\tilde{d}_L, \tilde{u}_L, \tilde{b}_1, \tilde{t}_1) & \text{and} & \tilde{l}_R > \tilde{\chi}_2^0 > \tilde{\tau}_1 & \\
\text{(iii)} & \tilde{g} > \max(\tilde{d}_L, \tilde{u}_L, \tilde{b}_1, \tilde{t}_1) & \text{and} & \min(\tilde{l}_R, \tilde{\tau}_1) > \tilde{\chi}_2^0 & \\
\text{(iv)} & \tilde{d}_L > \tilde{g} > \max(\tilde{u}_L, \tilde{b}_1) & \text{and} & \min(\tilde{l}_R, \tilde{\tau}_1) > \tilde{\chi}_2^0 & \\
\text{(v)} & \min(\tilde{d}_L, \tilde{u}_L) > \tilde{g} > \tilde{b}_1 & \text{and} & \min(\tilde{l}_R, \tilde{\tau}_1) > \tilde{\chi}_2^0 & \\
\text{(vi)} & \min(\tilde{d}_L, \tilde{u}_L, \tilde{b}_1) > \tilde{g} > \tilde{t}_1 & \text{and} & \min(\tilde{l}_R, \tilde{\tau}_1) > \tilde{\chi}_2^0 & \\
\text{(vii)} & \min(\tilde{d}_L, \tilde{u}_L, \tilde{b}_1, \tilde{t}_1) > \tilde{g} & \text{and} & \min(\tilde{l}_R, \tilde{\tau}_1) > \tilde{\chi}_2^0 & (2.2)
\end{array}
$$

where for fermions a particle's symbol represents its mass, while for scalars a particle's sym-

bol represents the sum of the masses of the scalar and its SM partner. Also shown (mauve) is a region where the LSP is charged and therefore ruled out, as well as a theoretically forbidden (TF) region (gray) for low $m_{1/2}$.

It is interesting to note that there are *no* regions where a squark is heavier than the gluino *and* $\tilde{\chi}_2^0$ is heavier than one of the sleptons. This is simply because the gluino and [the gaugino part of] the neutralino have a common mass, $m_{1/2}$, at the high scale, so if the gluino is light, the neutralinos will also be light.

However, for more general non-mSUGRA unification scenarios one could still expect hierarchies of the type $m_{\tilde{q}_L} > m_{\tilde{g}} > m_{\tilde{\chi}_2^0} > m_{\tilde{l}} > m_{\tilde{\chi}_1^0}$ to be realised. It would then be important to be able to distinguish one hierarchy from the other; this should be possible using the kinematic endpoints, number of b-quarks in the final state, etc. Also it is possible to distinguish $\tilde{\chi}_2^0 \to \tilde{l}l \to \tilde{\chi}_1^0 ll$ ($m_{\tilde{\chi}_2^0} > m_{\tilde{l}}$) from $\tilde{\chi}_2^0 \to \tilde{\chi}_1^0 ll$ ($m_{\tilde{l}} > m_{\tilde{\chi}_2^0}$). The first has the well-known triangular shape of m_{ll} while the second has a typical 3-body shape. All in all it should therefore be possible to distinguish the various hierarchies (2.2) before continuing to determine the masses themselves.

Region (i) is the only one that has a 'useful' squark decay together with a decay of $\tilde{\chi}_2^0$ to a slepton, and is shown in light and dark green in Fig. 1. We see that there is therefore a large region where the mass hierarchy is compatible with the methods presented here, and even though we will only perform the analysis for the points (α) and (β) on the SPS 1a line, one would expect these methods to be widely applicable.

However, these plots of the mass hierarchies really only show the regions in which the masses are such that the decay chain *may* occur. If the full decay chain is to be useful, it must have a sufficiently large branching ratio to be seen above the many backgrounds. We will therefore go on to examine the branching ratios of the pertinent decays over (a restricted range of) the mSUGRA parameter space. As a first taste, we have highlighted in a brighter green (and denoted (i)$_a$) the part of region (i) corresponding to where the overall branching ratio for the decay chain $\tilde{q} \to \tilde{\chi}_2^0 q \to \tilde{l}lq \to \tilde{\chi}_1^0 llq$ exceeds a tenth of that at the SPS 1a (α) reference point. Although the decay chain is available over a rather large region of the parameter space, using this decay for large values of $m_{1/2}$ and m_0 will be extremely challenging due to the small branching ratio.

2.2 Gluino and squark decays: the upper part of the chain

The decay branching ratios of the gluino are shown in Fig. 2 over the $m_{1/2}$–m_0 plane for two different scenarios. The representation is such that the branching ratio of a given decay channel in a small neighbourhood of the $m_{1/2}$–m_0 plane is equal to the fraction which the corresponding colour occupies in that neighbourhood. Since the gluino only feels the strong force, it has to decay into a quark and a squark. If no squark is light enough, a three-body decay through an off-shell squark will take place; this is what happens in the green/white region of Fig. 2 at small $m_{1/2}$.

For the rest of the $m_{1/2}$–m_0 plane the gluino decays fairly democratically into the accessible squarks. In considerable parts of the plane only one two-body decay is open, $\tilde{b}_1 b$ (red) or $\tilde{t}_1 t$ (yellow), in which case the allowed decay takes close to the full decay width. Although one can in principle obtain information about the gluino mass by analysing its

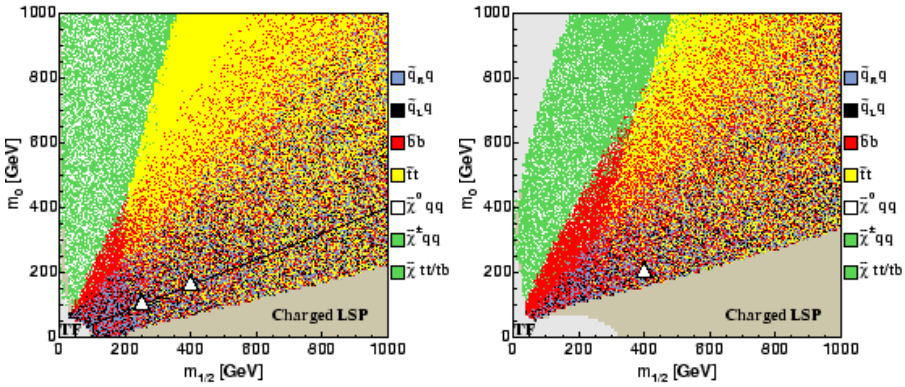

Figure 2: Decay channels of $\tilde{g}$ with $A_0 = -m_0$, $\tan\beta = 10$ (left) and $A_0 = 0$, $\tan\beta = 30$ (right). In the left panel the SPS 1a line is shown together with the two points (α) and (β) marked with triangles. In the right panel the triangle marks the SPS 1b point. The branching ratio of a given decay channel in a small neighbourhood of the $m_{1/2}$–m_0 plane is equal to the fraction which the corresponding colour occupies in that neighbourhood. The region where $\tilde{\chi}_1^0$ is not the LSP is denoted 'Charged LSP' and is discarded. Some regions are also forbidden theoretically, in that e.g. it is not possible to obtain electroweak symmetry breaking (labeled 'TF').

decay chain, we will only consider here the decay chain starting from a parent squark, and leave the gluino case for a separate publication [33].

As already intimated, squarks may decay by the strong force into a quark and a gluino (if the gluino is lighter), or decay by weak interactions into a quark and a chargino or neutralino, or via a loop into a gluon and a lighter squark. If kinematically allowed, the strong interaction takes a large fraction of the branching ratio, but since the (lighter) charginos and neutralinos are typically much lighter than the gluino, there will always be some neutralino production.

Within mSUGRA models, the squarks $\tilde{d}_L$ and $\tilde{u}_L$ are very close in mass and behaviour. Furthermore, the second generation squarks, $\tilde{s}_L$ and $\tilde{c}_L$, are almost identical copies of the former two. It is therefore useful to have the common notation, $\tilde{q}_L$, for these four squarks. In a similar manner $\tilde{q}_R$ is used for $\tilde{d}_R$, $\tilde{u}_R$ and their second generation copies. The right-handed squarks differ from the left-handed ones in that they do not feel weak interactions, which again makes their decay pattern different. In Fig. 3 the decay branching ratios of $\tilde{u}_L$ and $\tilde{u}_R$ are shown in the $m_{1/2}$–m_0 plane for two different scenarios.

For $m_{1/2} \ll m_0$, when the gluino mass is smaller than the squark mass, both $\tilde{q}_L$ and even more so $\tilde{q}_R$ have strong-interaction decays. In the rest of the $m_{1/2}$–m_0 plane, when the strong decay is forbidden or suppressed by phase space, their decay patterns are very different: while $\tilde{q}_R$ decays directly into the LSP, $\tilde{q}_L$ prefers $\tilde{\chi}_2^0$ and $\tilde{\chi}_1^\pm$.

For both low and high $\tan\beta$, the $\tilde{\chi}_1^0$ is predominantly bino, with only a tiny admixture of wino and higgsino, while $\tilde{\chi}_2^0$ and $\tilde{\chi}_1^\pm$ are mainly wino. For quite low mass parameters,

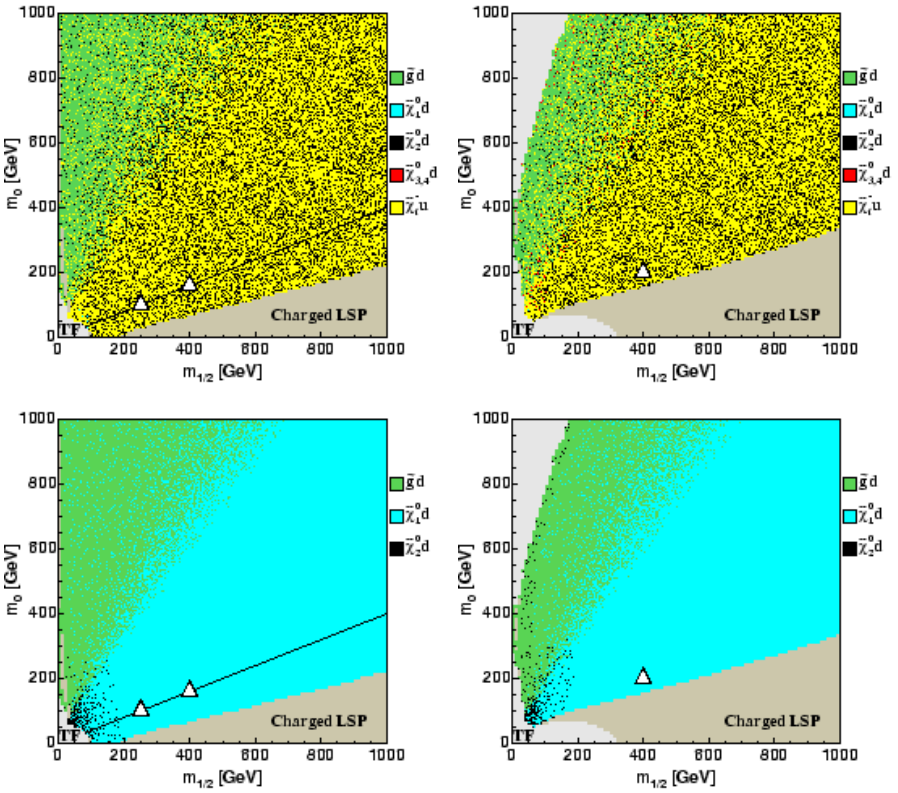

Figure 3: Decay channels of $\tilde{u}_L$ (top) and $\tilde{u}_R$ (bottom) with $A_0 = -m_0$, $\tan\beta = 10$ (left) and $A_0 = 0$, $\tan\beta = 30$ (right). (See the caption of Fig. 2.) Note that the branching ratios for all first and second-generation squarks are assumed to be essentially the same.

$m_{1/2} \lesssim 100$ GeV, they become more mixed. Since $\tilde{q}_L$ generally has a much larger SU(2) coupling than U(1) coupling, decays to $\tilde{\chi}_1^\pm$ and $\tilde{\chi}_2^0$ will be preferred unless the difference in phase space makes the decay to the lighter $\tilde{\chi}_1^0$ competitive. In contrast, since the $\tilde{q}_R$ has no SU(2) interaction it will decay predominantly to the bino $\tilde{\chi}_1^0$, except at quite low mass parameters where the neutralinos change character.

The third generation squarks differ from the others in two aspects. First, the mass eigenstates can have more even admixtures of both handedness components. For $\tilde{b}$ this is the case for low mass parameters, $m_0, m_{1/2} \lesssim 200$ GeV, where the branching ratios into $\tilde{\chi}_1^0$ and $\tilde{\chi}_2^0$ are of comparable size. At higher masses $\tilde{b}_1 \approx \tilde{b}_L$ and $\tilde{b}_2 \approx \tilde{b}_R$, giving a $\tilde{b}_1$ which prefers to go to $\tilde{\chi}_2^0$ rather than $\tilde{\chi}_1^0$. Second, due to large splitting, the third generation squarks can decay into other third generation squarks together with a weak gauge boson. The drastic change observed in figure 4 as $m_0, m_{1/2}$ become less than ~ 200 GeV, is due

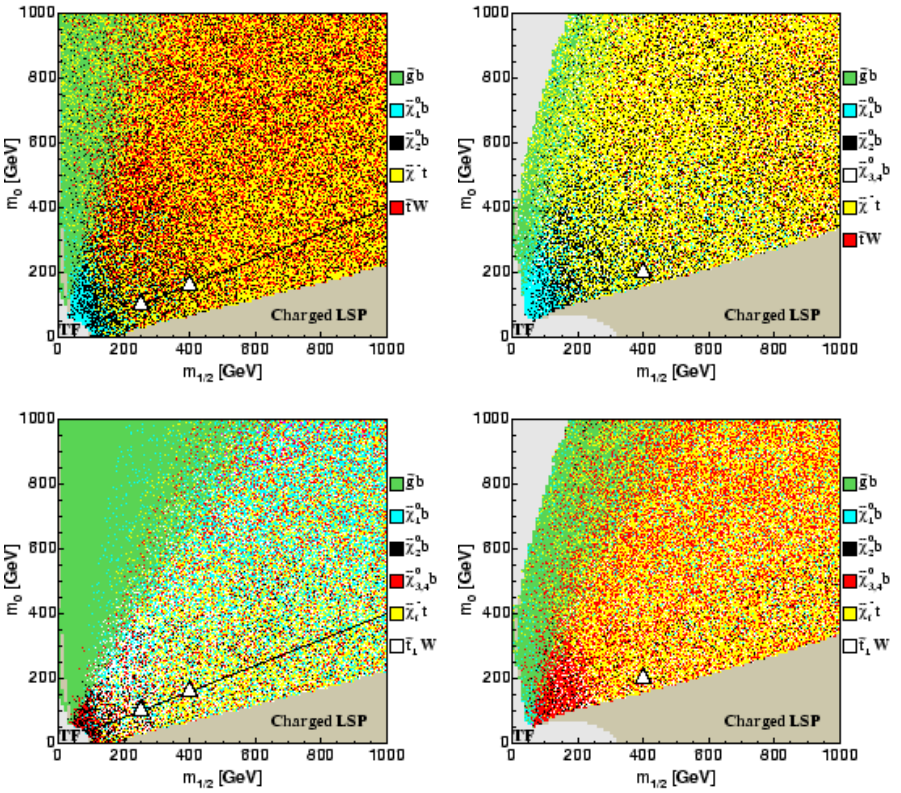

Figure 4: Decay channels of $\tilde{b}_1$ (upper panels) and $\tilde{b}_2$ (lower panels) with $A_0 = -m_0$, $\tan\beta = 10$ (left) and $A_0 = 0$, $\tan\beta = 30$ (right). (See the caption of Fig. 2.)

both to the more mixed mass eigenstates for lower masses, and to the closing of certain channels involving t or a heavy gauge boson.

While $\tilde{b}_1$ has a large branching ratio into $\tilde{\chi}_2^0$ throughout the entire plane, $\tilde{b}_2$ produces $\tilde{\chi}_2^0$ at a much smaller rate, except for small mass parameters.

To summarize, the squark decays that are 'useful' for kinematic endpoint analyses, are those of left-handed first and second-generation squarks, as well as those of $\tilde{b}_1$ and to a lesser extent $\tilde{b}_2$. These occur in the entire $m_{1/2}$–m_0 plane, except for extreme values $m_{1/2} \ll m_0$, and for both low and high $\tan\beta$ values. For quite low mass parameters also $\tilde{q}_R$ contributes.

2.3 Neutralino and slepton decays: the lower part of the chain

The reasons why $\tilde{\chi}_2^0$ often plays an important role in the reconstruction of SUSY events are many. Kinematically situated midway between the initially produced gluinos/squarks and

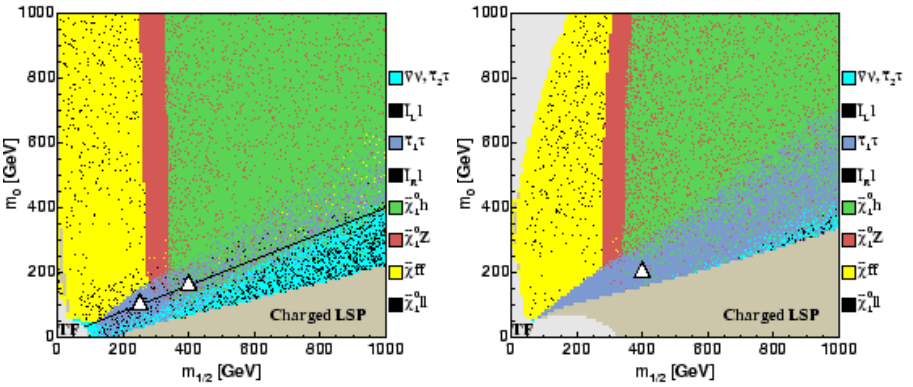

Figure 5: Decay channels of $\tilde{\chi}_2^0$ with $A_0 = -m_0$, $\tan\beta = 10$ (left) and $A_0 = 0$, $\tan\beta = 30$ (right). (See the caption of Fig. 2.)

the LSP, it is abundantly decayed into, as we have seen. What makes it so useful, usually more so than the $\tilde{\chi}_1^\pm$, which is produced in similar ways and amounts, is the fact that its decay products, in addition to easily setting off the trigger, also reconstruct well.

In Fig. 5 the main decay channels of $\tilde{\chi}_2^0$ are shown for two values of $\tan\beta$. A two-body decay is preferred over a three-body decay, and the coupling to $\tilde{l}$, $\tilde{\tau}$ or $\tilde{\nu}$ is usually stronger than the coupling to $\tilde{\chi}_1^0$.

For $m_0 \gtrsim 0.5 m_{1/2}$ all of $\tilde{l}$, $\tilde{\tau}$ and $\tilde{\nu}$ are heavier than $\tilde{\chi}_2^0$, so only the decay into the LSP is possible. In yellow, to the very left, no two-body channel is open, and $\tilde{\chi}_2^0$ undergoes a three-body decay, proceeding through an off-shell squark or stau/slepton, or involving an off-shell Z, W or h. As $m_{1/2}$ increases, also $m_{\tilde{\chi}_2^0} - m_{\tilde{\chi}_1^0}$ increases and more decay channels become available. First the Z channel opens and takes the full decay width, then the h channel opens to dominate. The mass difference between $\tilde{\chi}_1^0$ and $\tilde{\chi}_2^0$ is mostly independent of m_0, which is why, to a good approximation, the yellow, red and green regions are stacked horizontally.

In the blue regions decays into $\tilde{l}/\tilde{\tau}/\tilde{\nu}$ are kinematically allowed. Following a clockwise movement, the scalar masses are reduced relative to $\tilde{\chi}_2^0$. The right-handed scalars are lighter and become available first (dark blue region). In the light blue region the left-handed scalars have become available and, despite less phase space, take most of the width due to their SU(2) coupling. The black part of the blue regions shows the decay into $\tilde{l}_R$ (dark blue region) and $\tilde{l}_L$ (light blue region). These are the decays of interest to us. At low $\tan\beta$ (left panel) the slepton channels can be used in most of the blue regions. At high $\tan\beta$ the situation is less optimistic. The $\tilde{\tau}_1$ channel totally dominates the $\tilde{l}_R$ channel, and only in a small region is the $\tilde{l}_L$ channel open.

Decay products which involve tau particles are more difficult to use since their reconstruction is always incomplete due to undetected neutrinos. However, in some parts of the parameter space, especially at high $\tan\beta$, these channels take the full decay width, so one

must be prepared to use them. In any case, whatever the MSSM parameters should turn out to be, in order to measure the stau mass itself, tau particles must be reconstructed.

In the non-blue regions of the plane, information on the sparticle masses can still be retrieved, although to a lesser extent. From an experimental point of view final states involving two leptons are preferable. In the yellow region this fraction is marked in black. In the red region Z decays leptonically in 7% of the cases. In the green region, no leptonic decay is available. Here the $b\bar{b}$ final state of the Higgs can be used. This channel may even serve as a discovery channel for the Higgs boson.

Returning once more to our chosen decay chain, $\tilde{q} \to \tilde{\chi}_2^0 q \to \tilde{l} l q \to \tilde{\chi}_1^0 l l q$, it is clear from Figs. 2–4 that the initiating squark must be $\tilde{q}_L$ or $\tilde{b}$. Furthermore Fig. 5 shows that for low $\tan\beta$ the sleptonic decay of $\tilde{\chi}_2^0$ is open in a large fraction of the $m_{1/2}$–m_0 plane.

2.4 Other constraints

Much of these parameter planes considered in Figs. 1–5 are actually excluded or disfavoured by observations. The left part (small $m_{1/2}$) is typically excluded by the lower bound on the Higgs mass, and the region of 'large' $m_0 + m_{1/2}$ is excluded by the WMAP data [39, 40], since a too high contribution to the Cold Dark Matter (relic LSP) density is produced. Such bounds have been explored in considerable detail for the so-called 'Post-LEP' SUSY benchmark points [34, 35]. For the SPS points, see Ref. [36]. Also, there are constraints from the non-emergence of unphysical vacua during the renormalisation-group running from the high scale [37]. These typically rule out a sector at low m_0 and high $m_{1/2}$ that may extend beyond that excluded by charged LSP. We shall here ignore such additional constraints, since they depend somewhat on the assumptions which are adopted. In particular, tunneling into them may take longer than the age of the Universe.

3. Summary of SPS 1a

We have shown that the squark and gluino initiated cascade decays seen at the benchmark point and slope SPS 1a are not atypical of a large portion of the parameter space. In this section we will go on to explore SPS 1a in more detail, and introduce our second SPS 1a point on the line.

3.1 The SPS 1a line and points

The SPS 1a benchmark *line* is defined as the masses and couplings of supersymmetric particles at the TeV scale as evolved from the GUT scale mSUGRA inputs

$$\begin{aligned} m_0 = -A_0 &= 0.4\, m_{1/2}, \\ \tan\beta &= 10, \qquad \mu > 0, \end{aligned} \tag{3.1}$$

by version 7.58 of the program `ISAJET` [30]. Elsewhere in this report when the mSUGRA GUT scale parameters are referred to it is to be understood that the low energy parameters are obtained in this way.

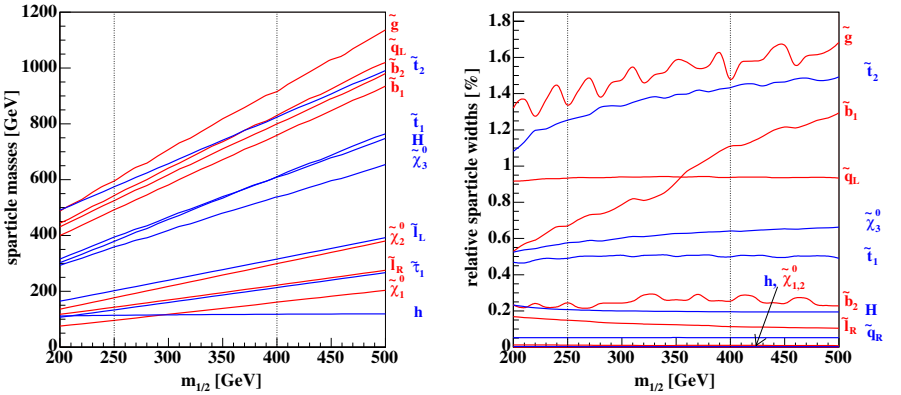

Figure 6: Masses (left) and relative widths (right) of relevant sparticles as $m_{1/2}$, m_0 and A_0 are varied along the SPS 1a slope, defined by Eq. (3.1). The vertical dotted lines represent SPS 1a points (α) and (β).

In addition, we define two points (α) and (β) on the SPS 1a line according to:

$$\begin{aligned} (\alpha): \quad & m_0 = 100 \text{ GeV}, \qquad m_{1/2} = 250 \text{ GeV}, \\ (\beta): \quad & m_0 = 160 \text{ GeV}, \qquad m_{1/2} = 400 \text{ GeV}. \end{aligned} \tag{3.2}$$

The first point (α) is the 'basic' SPS 1a point of Ref. [21] and studied in Ref. [27, 28], while the second (β) is a new, less optimistic scenario with a reduced cross-section for the decay chain.

The masses of particles relevant for our analysis are shown in Fig. 6 (left), moving along the SPS 1a line by varying $m_{1/2}$. The values of the masses at points (α) and (β) can be seen from the vertical dotted lines. As expected, all the masses except the lightest Higgs boson mass increase linearly with $m_{1/2}$. Neither the heaviest neutralino mass nor the chargino masses are shown; to a good approximation, $m_{\tilde{\chi}_2^\pm} \simeq m_{\tilde{\chi}_3^0} \simeq m_{\tilde{\chi}_4^0}$ and $m_{\tilde{\chi}_1^\pm} \simeq m_{\tilde{\chi}_2^0}$. Similarly, the masses of $H^\pm$ and A are not shown, but $m_{H^\pm} \simeq m_A \simeq m_H$.

For the points (α) and (β), these masses are further detailed in Table 1, with the masses of the particles in our chosen decay chain displayed in bold.

The relative widths (width divided by the mass) of the decaying sparticles are shown in Fig. 6 (right), and are everywhere less than 2% of the mass. The wiggles in some of these curves (as well as in some of the branching ratio curves below) are due to limited precision in `ISAJET` [38]. As will be discussed, these widths contribute to a blurring of the kinematical endpoints, and will thus be reflected in the mass determination.

3.2 Sparticle production

The cross-sections for producing supersymmetric particles at the LHC are for moderate values of $m_{1/2}$ rather high. This can be seen in Fig. 7 which shows the dominating sparticle

Point	$\tilde{g}$	$\tilde{d}_L$	$\tilde{d}_R$	$\tilde{u}_L$	$\tilde{u}_R$	$\tilde{b}_2$	$\tilde{b}_1$	$\tilde{t}_2$	$\tilde{t}_1$
(α)	**595.2**	**543.0**	520.1	**537.2**	520.5	**524.6**	**491.9**	574.6	379.1
(β)	**915.5**	**830.1**	799.5	**826.3**	797.3	**800.2**	**759.4**	823.8	610.4
	$\tilde{e}_L$	$\tilde{e}_R$	$\tilde{\tau}_2$	$\tilde{\tau}_1$	$\tilde{\nu}_{e_L}$	$\tilde{\nu}_{\tau_L}$		$H^{\pm}$	A
(α)	202.1	**143.0**	206.0	133.4	185.1	185.1		401.8	393.6
(β)	315.6	**221.9**	317.3	213.4	304.1	304.1		613.9	608.3
	$\tilde{\chi}_4^0$	$\tilde{\chi}_3^0$	$\tilde{\chi}_2^0$	$\tilde{\chi}_1^0$	$\tilde{\chi}_2^{\pm}$	$\tilde{\chi}_1^{\pm}$		H	h
(α)	377.8	358.8	**176.8**	**96.1**	378.2	176.4		394.2	114.0
(β)	553.3	538.4	**299.1**	**161.0**	553.3	299.0		608.9	117.9

Table 1: Masses [GeV] for the considered SPS 1a points (α) and (β) of Eq. (3.2).

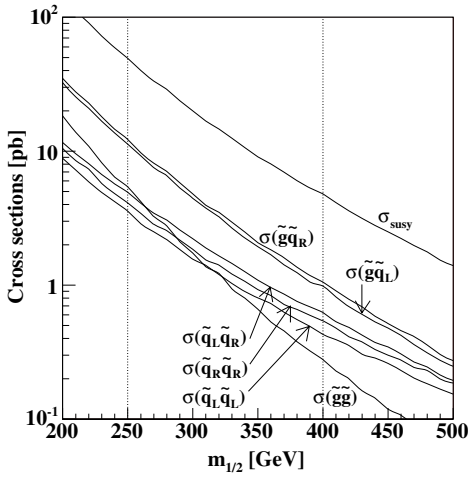

Figure 7: Cross-sections as $m_{1/2}$, m_0 and A_0 are varied along the SPS 1a slope, defined by Eq. (3.1). The vertical dotted lines represent SPS 1a points (α) and (β).

pair production cross-sections, as $m_{1/2}$ is varied along the SPS 1a line. Notice that these cross-sections fall very rapidly as $m_{1/2}$ is increased, which will cause repercussions in the analysis of SPS 1a (β).

The cross-sections for gluino–gluino, gluino–squark and squark–squark pair productions are detailed in Table 2 for the two chosen analysis points, together with the SUSY total rate. Of course since other supersymmetric particle pairs may contribute to the total SUSY rate it is *not* simply a sum of the other numbers in the table.

These supersymmetric particle pairs are predominantly produced by QCD interactions of quarks and gluons in the colliding protons. For gluino pairs this is mainly due to $gg \to \tilde{g}\tilde{g}$ via t-channel gluino exchange and s-channel gluons, and at a much smaller rate $q\bar{q} \to \tilde{g}\tilde{g}$ via s-channel gluons. Squark pairs with the same handedness have the dominant production

process $qq \to \tilde{q}_{L/R}\,\tilde{q}_{L/R}$ with a t-channel gluino exchange, but can also be produced via $gg \to \tilde{q}_{L/R}\,\tilde{q}_{L/R}$ with an s-channel gluon, or via $q\bar{q} \to \tilde{q}_{L/R}\,\tilde{q}_{L/R}$ with both t-channel gluino and s-channel gluons. For opposite handedness, $\tilde{q}_L\tilde{q}_R$ production, the s-channel gluon exchange processes [and thus $gg \to \tilde{q}_L\,\tilde{q}_R$ at tree-level] are disallowed. Lastly, the $\tilde{g}\tilde{q}$ final states are produced by the process $gq \to \tilde{g}\tilde{q}$ mediated by t-channel squark or gluino exchanges and s-channel quarks.

	σ(SUSY)	$\sigma(\tilde{g}\tilde{g})$	$\sigma(\tilde{g}\tilde{q}_L)$	$\sigma(\tilde{g}\tilde{q}_R)$	$\sigma(\tilde{q}_L\tilde{q}_L)$	$\sigma(\tilde{q}_L\tilde{q}_R)$	$\sigma(\tilde{q}_R\tilde{q}_R)$
(α)	49.3	5.3	11.4	12.3	3.5	4.8	4.1
(β)	4.76	0.29	0.97	1.06	0.44	0.61	0.53

Table 2: Selected supersymmetry cross-sections in pb.

However, these particle pair cross-sections are not the production cross-sections that are relevant to our analysis of the decay chain, since it does not matter from where the parent squark originates. Therefore we should also be counting, for example, gluinos which decay into squarks as possible sources of the decay chain. In Table 3 we divide the sparticle productions rates into 'direct' and 'indirect' contributions, reflecting production rates from sparticles in the 'initial' supersymmetric state as opposed to their generation from the decay of a parent sparticle. Furthermore, if the 'initial' supersymmetric state contains two possible parents then the chance of generating the desired decay chain is doubled[2]. Therefore the pair-production rates with two possible parent particles are counted twice. Again, one cannot simply add the various contributions from Table 2 to obtain the 'direct' rates of Table 3, since they include contributions from squarks or gluinos produced in association with other supersymmetric particles.

		$\Sigma(\tilde{g})$	$\Sigma(\tilde{q}_L)$	$\Sigma(\tilde{q}_R)$	$\Sigma(\tilde{b}_1)$	$\Sigma(\tilde{b}_2)$	$\Sigma(\tilde{t}_1)$	$\Sigma(\tilde{\chi}_2^0)$
(α)	Direct	35.4	24.6	25.8	1.4	0.9	3.4	1.8
	Indirect	-	8.2	14.6	6.3	3.5	5.6	16.0
	Total	35.4	32.8	40.4	7.7	4.3	9.0	17.8
(β)	Direct	2.71	2.64	2.80	0.10	0.06	0.23	0.23
	Indirect	-	0.58	1.00	0.40	0.25	0.64	1.44
	Total	2.71	3.21	3.79	0.50	0.31	0.87	1.67

Table 3: Selected sparticle production rates in pb.

For low $m_{1/2}$ values $\tilde{\chi}_2^0$ will decay dominantly to a stau and a tau, see Fig. 8. Here, the decay mode of interest is to a right-handed slepton, $\tilde{l}_R$, and a lepton, and is at the level of 10%. For higher values of $m_{1/2}$, the mass difference between $\tilde{\chi}_1^0$ and $\tilde{\chi}_2^0$ grows sufficiently to allow the decay $\tilde{\chi}_2^0 \to \tilde{\chi}_1^0 h$. At ($\beta$), even though the Higgs channel takes a significant 30% of the decay width, it was not used in this study. Due to the accuracy of lepton reconstruction compared to jet reconstruction, only in the case of very low lepton channel statistics can the Higgs channel improve on the results obtained with the slepton channel.

[2]The total branching ratio for the decay is sufficiently small that the chance of generating *two* of the desired decay chains is tiny.

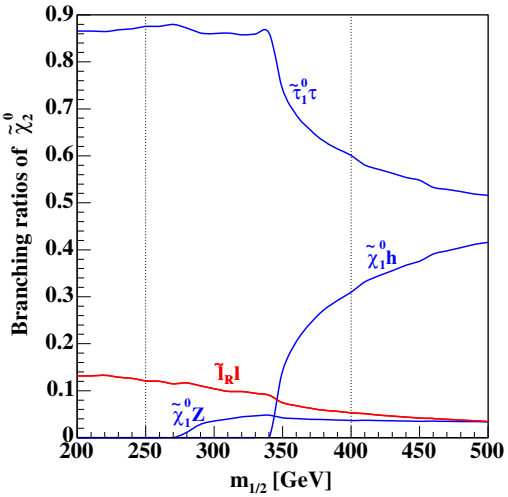

Figure 8: Branching ratios of $\tilde{\chi}_2^0$ as $m_{1/2}$, m_0 and A_0 are varied along the SPS 1a slope. The vertical dotted lines represent SPS 1a points (α) and (β).

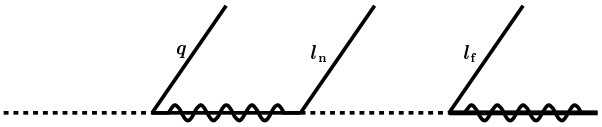

(α)	σ = 32.8 pb	$\tilde{q}_L$	31.4%	$\tilde{\chi}_2^0$	12.1%	$\tilde{l}_R$	100%	$\tilde{\chi}_1^0$	1245 fb
	σ = 7.7 pb	$\tilde{b}_1$	35.5%						329 fb
	σ = 4.3 pb	$\tilde{b}_2$	18.0%						94 fb
									1669 fb
(β)	σ = 3.21 pb	$\tilde{q}_L$	31.9%	$\tilde{\chi}_2^0$	5.3%	$\tilde{l}_R$	100%	$\tilde{\chi}_1^0$	54.3 fb
	σ = 0.50 pb	$\tilde{b}_1$	23.6%						6.3 fb
	σ = 0.31 pb	$\tilde{b}_2$	8.8%						1.5 fb
									62.0 fb

Figure 9: The SPS 1a cascade decay chain.

3.3 The cascade

The cross-sections and branching ratios of our chosen decay chains

$$\tilde{q}_L \to \tilde{\chi}_2^0 q \to \tilde{l}_R^{\mp} l_n^{\pm} q \to \tilde{\chi}_1^0 l_f^{\mp} l_n^{\pm} q \tag{3.3}$$

$$\tilde{b}_1 \to \tilde{\chi}_2^0 b \to \tilde{l}_R^{\mp} l_n^{\pm} b \to \tilde{\chi}_1^0 l_f^{\mp} l_n^{\pm} b \tag{3.4}$$

$$\tilde{b}_2 \to \tilde{\chi}_2^0 b \to \tilde{l}_R^{\mp} l_n^{\pm} b \to \tilde{\chi}_1^0 l_f^{\mp} l_n^{\pm} b \tag{3.5}$$

are summarized in Fig. 9 for the two SPS 1a points. Since the left-handed up and down squarks, $\tilde{u}_L$ and $\tilde{d}_L$, have very similar masses (at 537.2 GeV and 543.0 GeV respectively), for (α), they are in the above jointly referred to as $\tilde{q}_L$, and for this analysis will be grouped

together. For the fraction of decay chains which commence from a sbottom, $\tilde{b}_1$ is responsible for 78% or so, leaving us rather insensitive to the contribution from $\tilde{b}_2$.

4. Mass distributions

The longer a decay chain is, the more information it contains. To extract the masses of the supersymmetric particles in the decay we require at least as many kinematic endpoint measurements as unknown masses. In the lower part of the decay chain, where the second-lightest neutralino decays via $\tilde{\chi}_2^0 \to \tilde{l}_R l \to \tilde{\chi}_1^0 ll$, there are three unknown masses: $m_{\tilde{\chi}_2^0}$, $m_{\tilde{l}_R}$ and $m_{\tilde{\chi}_1^0}$. However, only two particle momenta are measured, those of the two leptons, from which only one mass distribution can be constructed, m_{ll}. The system is highly underdetermined; one cannot extract the three masses, only a relation between them.

When a squark is added to the head of the decay chain, $\tilde{q} \to \tilde{\chi}_2^0 q \to \tilde{l}_R l_{\rm n} q \to \tilde{\chi}_1^0 l_{\rm f} l_{\rm n} q$, three particles can be collected, and one can construct four mass distributions, m_{ll}, $m_{ql_{\rm n}}$, $m_{ql_{\rm f}}$ and m_{qll}, where following the notation of Refs. [31, 32], we denote the first emitted lepton $l_{\rm n}$ ('n' for 'near') and the second $l_{\rm f}$ ('f' for 'far'). In principle this is just sufficient for extracting the four unknown masses: $m_{\tilde{q}}$, $m_{\tilde{\chi}_2^0}$, $m_{\tilde{l}_R}$ and $m_{\tilde{\chi}_1^0}$. However, in order to use the distributions $m_{ql_{\rm n}}$ and $m_{ql_{\rm f}}$, we need to be able to distinguish $l_{\rm n}$ from $l_{\rm f}$. Since this is usually not possible, two alternative distributions are defined, $m_{ql(\text{high})}$ and $m_{ql(\text{low})}$ [31], constructed by selecting for each event the largest and smallest values of m_{ql} respectively.

As will be detailed later in this section, the expressions for these kinematic endpoints are not always linearly independent, so these four endpoints are not always sufficient to determine the masses in the decay chain. In this circumstance one must look for other endpoint measurements.

Correlations between different mass distributions can provide further measurements. For example, one may define the mass distribution $m_{qll(\theta>\frac{\pi}{2})}$ identically to the m_{qll} distribution but with the additional constraint

$$m_{ll}^{\max}/\sqrt{2} < m_{ll} < m_{ll}^{\max}. \tag{4.1}$$

This cut on m_{ll} translates directly into a cut on the angle θ between the two leptons in the rest frame of $\tilde{l}_R$ [41]. In terms of this angle, m_{ll} is given by

$$m_{ll} = m_{ll}^{\max}\sqrt{(1-\cos\theta)/2} \tag{4.2}$$

so a constraint of the form (4.1) directly corresponds to $\theta > \frac{\pi}{2}$. The simplicity of this constraint allows one to find an analytic expression for the minimum of the $m_{qll(\theta>\frac{\pi}{2})}$ distribution.

In principle, other correlations between mass distributions could be used, but they are limited by the lack of analytic expressions for the associated extrema. It is no doubt possible to construct simple constraints for which analytic expressions for minima or maxima of mass distributions are possible, but this will not be investigated further in this study.

If we were to also include a parent gluino at the head of the decay chain, $\tilde{g} \to \tilde{q}q \to \tilde{\chi}_2^0 qq \to \tilde{l}_R lqq \to \tilde{\chi}_1^0 llqq$, we would have an extra quark momentum at our disposal and could construct with it seven more ('primary') mass distributions.

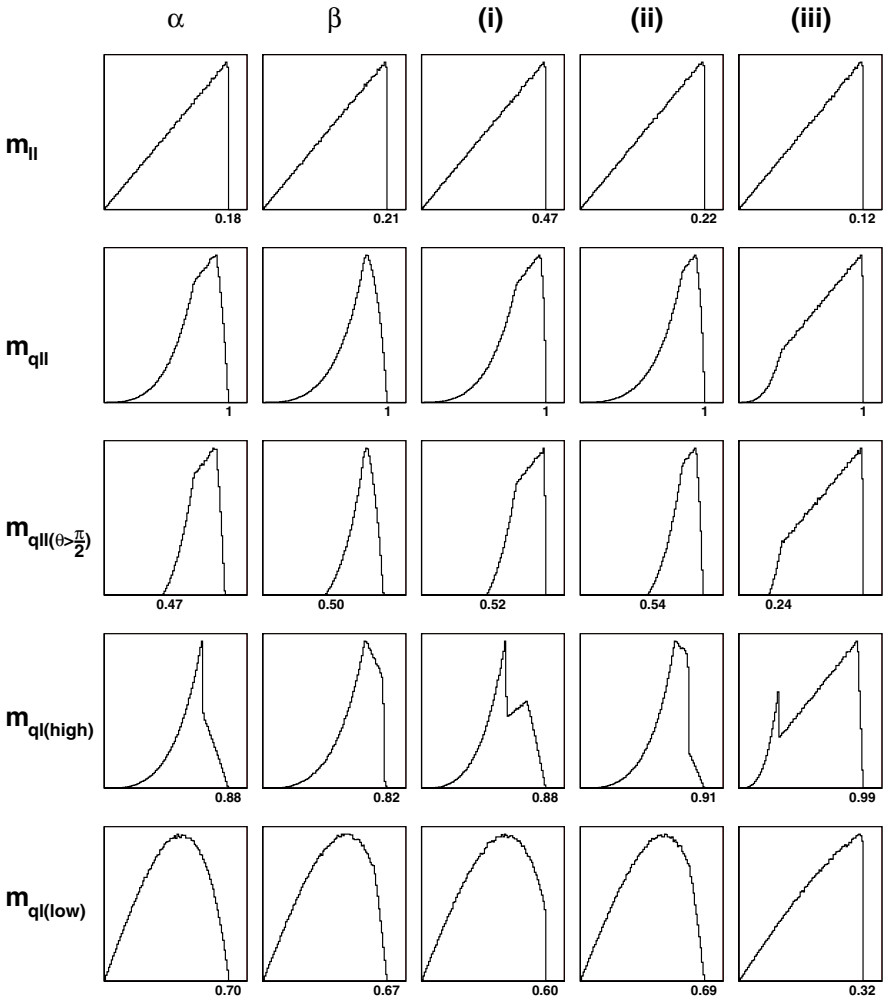

Figure 10: Theoretical mass distributions for SPS 1a (α) and (β), as well as for three other mass scenarios, denoted (i), (ii) and (iii). Kinematic endpoints are given in units of $m_{qll}^{\max}$. (More details will be given in [42].)

4.1 Theory curves of invariant mass distributions

In Fig. 10 we show 'theory' versions of the five mass distributions discussed above for SPS 1a (α) and (β), and three other mass scenarios. These distributions reflect the parton level only, where the quark and leptons are assumed to be perfectly reconstructed, and particle widths have been neglected, suppressing a mild smearing of the distributions. Leptons and

quarks are assumed massless; at worst, i.e. for an endpoint involving a 4.8 GeV b-quark, this approximation gives a value for $m_{qll}^{\max}$ which is wrong by 5.7 MeV at SPS 1a (α), which is negligible. Furthermore a common squark mass is used; in reality, the experimental distributions would be a sum of several similar distributions shifted typically by a few percent, depending on the differences between the squark masses.

These theory curves have been generated from the phase space only, with no matrix elements inserted. For the two-body decay of scalar particles this is not a problem; the daughter particles are always emitted back-to-back in the rest frame of the parent and since a scalar particle provides no intrinsic direction the decay will be isotropic. The m_{ll} distribution, for example, is very well described by phase-space considerations alone since the scalar $\tilde{l}_R$ removes any spin-correlations between the two leptons. For the decays of fermions this is not so clear; the parent's spin picks out a particular direction so the decay need not be isotropic. One would expect that spin-correlations must be fully taken into account by calculating the full matrix elements for the decay chain. In practice, while these spin-correlations are indeed very significant in individual processes, when one sums up final states containing leptons with positive and negative charge (which are produced in equal proportion) these spin correlations cancel out [43]. We have confirmed this assertion analytically.

Most of the distributions of Fig. 10 show a strong dependence on the scenario. Only the m_{ll} distribution is independent of the masses involved, which is easily understood from (4.2) together with the isotropic decay of $\tilde{l}_R$. The shape is easy to fit, and since only leptons are involved, the experimental resolution is high. The presence of the quark reduces the precision with which the other distributions may be measured. For m_{qll} there is a clear dependence on the masses involved, the main feature being the length of the straight section, ranging from infinitesimal to the entire distribution. However, the maximum edge itself is quite well described by a straight line, at least for the latter part. Next, the constrained m_{qll} distribution differs from m_{qll} for smaller invariant masses. Its rise from threshold is not very well described by a straight line making the measurement of the minimum value rather imprecise. Both m_{ql} distributions are 'composite' distributions, based on entries from m_{ql_n} and m_{ql_t}. This double nature is readily apparent for $m_{ql(\mathrm{high})}$, which has a wide variety of shapes. Particularly dangerous are mass scenarios like (β) or (ii), where the 'foot' which forms the last part of the edge can be hidden by backgrounds, giving a false maximum. In Sections 5–6 these considerations will come up in relation to (β). For $m_{ql(\mathrm{low})}$ a similar danger arises in cases like (i) where what appears to be an approximately linear descent to zero suddenly turns into a vertical drop towards the end.

These theory curves must serve as guidance for our determination of the endpoints. As a first stage they should be the basis for the choice of functions with which the edges of the different distributions are fitted. As a second stage the more ambitious goal may be to fit not only the endpoint, but the entire distribution.

4.2 Formulae for kinematic endpoints

The invariant masses of various subsets of particles can be determined from kinematical endpoints and thresholds, as discussed in [31]. We confirm the results relevant for our

analysis:

$$\left(m_{ll}^{\max}\right)^2 = \left(m_{\tilde{\chi}_2^0}^2 - m_{\tilde{l}_R}^2\right)\left(m_{\tilde{l}_R}^2 - m_{\tilde{\chi}_1^0}^2\right)/m_{\tilde{l}_R}^2 \tag{4.3}$$

$$\left(m_{qll}^{\max}\right)^2 = \left\{ \begin{array}{lll} \dfrac{\left(m_{\tilde{q}_L}^2 - m_{\tilde{\chi}_2^0}^2\right)\left(m_{\tilde{\chi}_2^0}^2 - m_{\tilde{\chi}_1^0}^2\right)}{m_{\tilde{\chi}_2^0}^2} & \text{for} \quad \dfrac{m_{\tilde{q}_L}}{m_{\tilde{\chi}_2^0}} > \dfrac{m_{\tilde{\chi}_2^0}}{m_{\tilde{l}_R}} \dfrac{m_{\tilde{l}_R}}{m_{\tilde{\chi}_1^0}} & (1) \\ \dfrac{\left(m_{\tilde{q}_L}^2 m_{\tilde{l}_R}^2 - m_{\tilde{\chi}_2^0}^2 m_{\tilde{\chi}_1^0}^2\right)\left(m_{\tilde{\chi}_2^0}^2 - m_{\tilde{l}_R}^2\right)}{m_{\tilde{\chi}_2^0}^2 m_{\tilde{l}_R}^2} & \text{for} \quad \dfrac{m_{\tilde{\chi}_2^0}}{m_{\tilde{l}_R}} > \dfrac{m_{\tilde{l}_R}}{m_{\tilde{\chi}_1^0}} \dfrac{m_{\tilde{q}_L}}{m_{\tilde{\chi}_2^0}} & (2) \\ \dfrac{\left(m_{\tilde{q}_L}^2 - m_{\tilde{l}_R}^2\right)\left(m_{\tilde{l}_R}^2 - m_{\tilde{\chi}_1^0}^2\right)}{m_{\tilde{l}_R}^2} & \text{for} \quad \dfrac{m_{\tilde{l}_R}}{m_{\tilde{\chi}_1^0}} > \dfrac{m_{\tilde{q}_L}}{m_{\tilde{\chi}_2^0}} \dfrac{m_{\tilde{\chi}_2^0}}{m_{\tilde{l}_R}} & (3) \\ \left(m_{\tilde{q}_L} - m_{\tilde{\chi}_1^0}\right)^2 & \text{otherwise} & (4) \end{array} \right\} \tag{4.4}$$

$$\left(m_{ql(\text{low})}^{\max}, m_{ql(\text{high})}^{\max}\right) = \left\{ \begin{array}{lll} \left(m_{ql_{\text{n}}}^{\max}, m_{ql_{\text{f}}}^{\max}\right) & \text{for} \quad 2m_{\tilde{l}_R}^2 > m_{\tilde{\chi}_1^0}^2 + m_{\tilde{\chi}_2^0}^2 > 2m_{\tilde{\chi}_1^0} m_{\tilde{\chi}_2^0} & (1) \\ \left(m_{ql(\text{eq})}^{\max}, m_{ql_{\text{f}}}^{\max}\right) & \text{for} \quad m_{\tilde{\chi}_1^0}^2 + m_{\tilde{\chi}_2^0}^2 > 2m_{\tilde{l}_R}^2 > 2m_{\tilde{\chi}_1^0} m_{\tilde{\chi}_2^0} & (2) \\ \left(m_{ql(\text{eq})}^{\max}, m_{ql_{\text{n}}}^{\max}\right) & \text{for} \quad m_{\tilde{\chi}_1^0}^2 + m_{\tilde{\chi}_2^0}^2 > 2m_{\tilde{\chi}_1^0} m_{\tilde{\chi}_2^0} > 2m_{\tilde{l}_R}^2 & (3) \end{array} \right\} \tag{4.5}$$

$$\left(m_{ql_{\text{n}}}^{\max}\right)^2 = \left(m_{\tilde{q}_L}^2 - m_{\tilde{\chi}_2^0}^2\right)\left(m_{\tilde{\chi}_2^0}^2 - m_{\tilde{l}_R}^2\right)/m_{\tilde{\chi}_2^0}^2 \tag{4.6}$$

$$\left(m_{ql_{\text{f}}}^{\max}\right)^2 = \left(m_{\tilde{q}_L}^2 - m_{\tilde{\chi}_2^0}^2\right)\left(m_{\tilde{l}_R}^2 - m_{\tilde{\chi}_1^0}^2\right)/m_{\tilde{l}_R}^2 \tag{4.7}$$

$$\left(m_{ql(\text{eq})}^{\max}\right)^2 = \left(m_{\tilde{q}_L}^2 - m_{\tilde{\chi}_2^0}^2\right)\left(m_{\tilde{l}_R}^2 - m_{\tilde{\chi}_1^0}^2\right)/\left(2m_{\tilde{l}_R}^2 - m_{\tilde{\chi}_1^0}^2\right) \tag{4.8}$$

$$\begin{aligned} \left(m_{qll(\theta>\frac{\pi}{2})}^{\min}\right)^2 = \Big[& \left(m_{\tilde{q}_L}^2 + m_{\tilde{\chi}_2^0}^2\right)\left(m_{\tilde{\chi}_2^0}^2 - m_{\tilde{l}_R}^2\right)\left(m_{\tilde{l}_R}^2 - m_{\tilde{\chi}_1^0}^2\right) \\ & - \left(m_{\tilde{q}_L}^2 - m_{\tilde{\chi}_2^0}^2\right)\sqrt{\left(m_{\tilde{\chi}_2^0}^2 + m_{\tilde{l}_R}^2\right)^2\left(m_{\tilde{l}_R}^2 + m_{\tilde{\chi}_1^0}^2\right)^2 - 16m_{\tilde{\chi}_2^0}^2 m_{\tilde{l}_R}^4 m_{\tilde{\chi}_1^0}^2} \\ & + 2m_{\tilde{l}_R}^2\left(m_{\tilde{q}_L}^2 - m_{\tilde{\chi}_2^0}^2\right)\left(m_{\tilde{\chi}_2^0}^2 - m_{\tilde{\chi}_1^0}^2\right)\Big]/\left(4m_{\tilde{l}_R}^2 m_{\tilde{\chi}_2^0}^2\right) \end{aligned} \tag{4.9}$$

where 'low' and 'high' on the left-hand side in Eq. (4.5) refer to minimising and maximising with respect to the choice of lepton. Furthermore 'min' in Eq. (4.9) refers to the threshold in the subset of the m_{qll} distribution for which the angle between the two lepton momenta (in the slepton rest frame) exceeds $\pi/2$, corresponding to the mass range (4.1).

Notice that the different cases listed in Eq. (4.4) are distinguished by *mass ratios* of neighbouring particles in the hierarchy, $m_{\tilde{q}_L}/m_{\tilde{\chi}_2^0}$, $m_{\tilde{\chi}_2^0}/m_{\tilde{l}_R}$ and $m_{\tilde{l}_R}/m_{\tilde{\chi}_1^0}$. Since each decay in the chain involves two massive particles and one massless one, the boosts from one rest frame to another are conveniently expressed in terms of such mass ratios.

4.3 Inversion formulae

Once the endpoints of the distributions have been measured, the masses may be extracted. In principle, this can be done in two ways. If the number of endpoint measurements coincides with the number of unknown masses, one may analytically invert the expressions for the endpoints to give explicit formulae for the masses in terms of the endpoints. If more endpoints are known, the system becomes overconstrained and the measurements must be weighted according to their uncertainties. The analytic method cannot easily handle such a situation. Instead the more flexible approach of numerical fit must be used.

However, the analytic inversion is more transparent than the numerical treatment, and reveals some interesting features of how the masses are related to the endpoints. It is also practical to use the analytical method in combination with the numerical method to provide initial values for the fits. Consequently we will discuss the inversion of the endpoint formulae in some detail in this subsection.

The four principal endpoints $m_{ll}^{\max}$, $m_{qll}^{\max}$, $m_{ql(\mathrm{low})}^{\max}$ and $m_{ql(\mathrm{high})}^{\max}$ are given by Eqs. (4.3)–(4.5). While $m_{ll}^{\max}$ is given by one unique expression, the others have different representations for different mass spectra. To perform the inversion, each combination of the endpoint expressions must be considered separately. There are four representations of $m_{qll}^{\max}$ and three representations of $(m_{ql(\mathrm{low})}^{\max}, m_{ql(\mathrm{high})}^{\max})$. Each overall combination corresponds to a unique region in mass space $(m_{\tilde{q}_L}, m_{\tilde{\chi}_2^0}, m_{\tilde{l}_R}, m_{\tilde{\chi}_1^0})$ and can be labeled by *(i,j)*, where i and j denote the region of applicability of the m_{qll} and m_{ql} endpoints, respectively, as given in Eqs. (4.4)–(4.5).

However, not all of the 4×3 combinations are physical. In particular the regions *(2,1)*, *(2,2)* and *(3,3)* are not possible. For *(2,1)* this can be seen by simultaneously trying to satisfy the mass constraints *(2)* of Eq. (4.4) and *(1)* of Eq. (4.5).

Additionally, for the regions *(2,3)*, *(3,1)* and *(3,2)* the endpoint expressions are not linearly independent. In each of these three regions, one of the mass ratios is dominant, and a lepton (rather than a quark) is emitted from the vertex involving the dominant mass ratio. The maximum of m_{qll} occurs when this lepton travels in one direction and the other lepton together with the quark travels in the opposite direction, all observed from the rest frame of any one of the sparticles in the decay. For massless quarks and leptons one can always write

$$m_{qll}^2 = 2p_q p_{l_{\mathrm{n}}} + 2p_q p_{l_{\mathrm{f}}} + 2p_{l_{\mathrm{n}}} p_{l_{\mathrm{f}}} = m_{ql(\mathrm{high})}^2 + m_{ql(\mathrm{low})}^2 + m_{ll}^2 \tag{4.10}$$

In the three regions mentioned above, for maximum values this equation reduces to

$$(m_{qll}^{\max})^2 = (m_{ql(\mathrm{high})}^{\max})^2 + (m_{ll}^{\max})^2 \tag{4.11}$$

Since one of the endpoints can be expressed in terms of two others, the four endpoint measurements only transform into three independent conditions. Hence, in order to determine the masses an additional endpoint would be required for these three regions. The endpoint of $m_{qll(\theta>\frac{\pi}{2})}$ is therefore particularly important in such cases. However, the complicated nature of Eq. (4.9) leads to exceptionally cumbersome inversion formulae and will not be studied here.

For the remaining six regions the inversion of the four endpoint expressions Eqs. (4.3)–(4.5) is possible. Coincidentally these are actually the regions most likely to be realised in SUSY scenarios with sparticle mass unifications at the GUT scale. Inversion formulae for these regions are detailed below. For simplicity of notation we will write:

$$a = m_{ll}^{\max},\ b = m_{qll}^{\max},\ c = m_{ql(\mathrm{low})}^{\max},\ d = m_{ql(\mathrm{high})}^{\max}. \tag{4.12}$$

Region (1,1):

$$m_{\tilde{\chi}_1^0}^2 = \frac{(b^2-d^2)(b^2-c^2)}{(c^2+d^2-b^2)^2}a^2 \tag{4.13}$$

$$m_{\tilde{l}_R}^2 = \frac{c^2(b^2-c^2)}{(c^2+d^2-b^2)^2}a^2 \tag{4.14}$$

$$m_{\tilde{\chi}_2^0}^2 = \frac{c^2d^2}{(c^2+d^2-b^2)^2}a^2 \tag{4.15}$$

$$m_{\tilde{q}_L}^2 = \frac{c^2d^2}{(c^2+d^2-b^2)^2}(c^2+d^2-b^2+a^2) \tag{4.16}$$

Region (1,2):

$$m_{\tilde{\chi}_1^0}^2 = \frac{(b^2c^2-b^2d^2+c^2d^2)(2c^2-d^2)}{(d^2-c^2)^2(b^2-d^2)}a^2 \tag{4.17}$$

$$m_{\tilde{l}_R}^2 = \frac{(b^2c^2-b^2d^2+c^2d^2)c^2}{(d^2-c^2)^2(b^2-d^2)}a^2 \tag{4.18}$$

$$m_{\tilde{\chi}_2^0}^2 = \frac{(2c^2-d^2)c^2d^2}{(d^2-c^2)^2(b^2-d^2)}a^2 \tag{4.19}$$

$$m_{\tilde{q}_L}^2 = \frac{c^2d^2}{(d^2-c^2)^2(b^2-d^2)}[a^2(2c^2-d^2)+(d^2-c^2)(b^2-d^2)] \tag{4.20}$$

Region (1,3):

$$m_{\tilde{\chi}_1^0}^2 = \frac{(d^2-c^2)(b^2-d^2)(b^2-2c^2)}{(c^2+d^2-b^2)^2d^2}a^2 \tag{4.21}$$

$$m_{\tilde{l}_R}^2 = \frac{(d^2-c^2)^2(b^2-d^2)}{(c^2+d^2-b^2)^2d^2}a^2 \tag{4.22}$$

$$m_{\tilde{\chi}_2^0}^2 = \frac{(2d^2-b^2)(d^2-c^2)c^2}{(c^2+d^2-b^2)^2d^2}a^2 \tag{4.23}$$

$$m_{\tilde{q}_L}^2 = \frac{(2d^2-b^2)c^2}{(c^2+d^2-b^2)^2d^2}[a^2(d^2-c^2)+d^2(c^2+d^2-b^2)] \tag{4.24}$$

Region (4,1):

$$m_{\tilde{\chi}_1^0}^2 = m_{\tilde{\chi}_2^0}^2 - (da/c+ac/d)m_{\tilde{\chi}_2^0} + a^2 \tag{4.25}$$

$$m_{\tilde{l}_R}^2 = m_{\tilde{\chi}_2^0}^2 - (ac/d)m_{\tilde{\chi}_2^0} \tag{4.26}$$

$$m_{\tilde{\chi}_2^0} = \frac{\left[(a^2+b^2)c^2d^2-(b^2-a^2)a^2(c^2+d^2)+2abcd\sqrt{(a^2+c^2-b^2)(a^2+d^2-b^2)}\right]}{\left[(a^2c^2+a^2d^2+c^2d^2)^2-4a^2b^2c^2d^2\right]/(acd)} \tag{4.27}$$

$$m_{\tilde{q}_L} = m_{\tilde{\chi}_1^0} + b \tag{4.28}$$

Region (4,2):

$$m_{\tilde{\chi}_1^0} = \frac{2c^2 - d^2}{d^2 - c^2}\left(b - c\sqrt{\frac{b^2 - a^2 - d^2}{2c^2 - d^2}}\right) \tag{4.29}$$

$$m^2_{\tilde{l}_R} = \frac{c^2}{2c^2 - d^2} m^2_{\tilde{\chi}_1^0} \tag{4.30}$$

$$m^2_{\tilde{\chi}_2^0} = \frac{c^2}{2c^2 - d^2} m^2_{\tilde{\chi}_1^0} + \frac{a^2 c^2}{d^2 - c^2} \tag{4.31}$$

$$m_{\tilde{q}_L} = m_{\tilde{\chi}_1^0} + b \tag{4.32}$$

Region (4,3):

$$m^2_{\tilde{\chi}_1^0} = m^2_{\tilde{l}_R} + a\left[a(d^2 - c^2) - \sqrt{a^2(d^2 - c^2)^2 + 4c^2 d^2 m^2_{\tilde{l}_R}}\right]/(2d^2) \tag{4.33}$$

$$\begin{aligned} m^2_{\tilde{l}_R} = {} & a^2\{-(d^4 - c^4)^2 a^8 + (d^2 - c^2)[c^6(2d^2 - 3b^2) + 7c^4 b^2 d^2 + d^4(c^2(3b^2 - 2d^2) + b^2 d^2)]a^6 \\ & + c^2 d^2[(5c^4 - 6c^2 d^2 - 3d^4)b^4 + (7c^2 d^4 + 5c^6 - 5c^4 d^2 + d^6)b^2 + 4d^4 c^4]a^4 \\ & + d^4 c^4[4d^2 c^2 b^2 - 10c^2 b^4 + 2c^2 d^4 + 2c^4 d^2 + c^4 b^2 + 4b^6 - 2d^2 b^4 - d^4 b^2]a^2 \\ & + c^6 d^6 (b^2 - d^2)(b^2 - c^2) \pm 2abc\sqrt{(b^2 - a^2 - d^2)(b^2 d^2 - 2a^2 d^2 - 2c^2 d^2 + 2a^2 c^2)} \\ & \times[(d^2 + c^2)(d^2 - c^2)^2 a^4 + 2c^2 d^2(c^2 b^2 - b^2 d^2 + c^4 + d^4)a^2 + c^4 d^4(d^2 + c^2 - 2b^2)]\} \\ & /[a^4 d^4 + (a^2 + d^2)^2 c^4 + 2a^2 c^2 d^2(a^2 + d^2 - 2b^2)]^2 \end{aligned} \tag{4.34}$$

$$m^2_{\tilde{\chi}_2^0} = m^2_{\tilde{l}_R}(a^2 + m^2_{\tilde{l}_R} - m^2_{\tilde{\chi}_1^0})/(m^2_{\tilde{l}_R} - m^2_{\tilde{\chi}_1^0}) \tag{4.35}$$

$$m_{\tilde{q}_L} = m_{\tilde{\chi}_1^0} + b \tag{4.36}$$

For a given set of endpoint measurements the inversion formulae of most regions will return unacceptable masses. In some regions the masses returned will be in contradiction with the presupposed hierarchy, $m_{\tilde{q}_L} > m_{\tilde{\chi}_2^0} > m_{\tilde{l}_R} > m_{\tilde{\chi}_1^0}$, in some there will even be negative or imaginary masses. Such solutions must be discarded. If the masses returned by the inversion formulae of a region *(i,j)* do obey the hierarchy, they constitute a physical solution if they themselves belong to *(i,j)*. Solutions which do not satisfy this last constraint will be referred to as 'unphysical'. In principle it should be possible to construct for each region a number of conditions on the endpoint values which, beforehand, would tell if the inversion formulae would return a physical solution or not. Such conditions will however become quite complicated, and have not been sought in this study. Instead the more straightforward approach is taken: try the inversion formulae of each region, then discard any unacceptable solutions.

Originating from realisation *(4)* of $m_{qll}^{\max}$, see Eq. (4.4), where masses appear unsquared, the inversion formulae of region *(4,j)* in principle come in two versions, the difference being a sign within one of the mass expressions. In regions *(4,1)* and *(4,2)* it turns out that only one of the signs returns masses in the appropriate region. In Eqs. (4.27) and (4.29) the physical sign is therefore chosen. For *(4,3)* both versions must be considered.

Once the required endpoints are measured and the inversion formulae used to determine the masses, we encounter a delicate feature of the entire method of obtaining masses from

endpoints. While the endpoints are given by single-valued functions of the masses, albeit with different expressions for different mass regions, the inverse is not true. A given set of endpoint values can in principle correspond to several sets of mass values. This is equally true for the numerical fit method, and has not received much attention previously (see, however, Ref. [32]). This complication will be faced in Section 6.

5. 'Data' generation and reconstruction

5.1 Event generation

The SPS points are defined by the low-energy MSSM parameters produced by ISAJET 7.58 [30], given a set of high-energy input parameters. In our analysis PYTHIA 6.2 [44] with CTEQ 5L [45] is used to generate the Monte Carlo sample.[3] To allow for this the low-energy parameters from ISAJET are fed into PYTHIA via the standard interface. PYTHIA in turn calculates the decay widths and cross-sections. Each event produced is passed through ATLFAST 2.60 [47], a fast simulation of the ATLAS detector. In ATLFAST the output particles of PYTHIA are mapped onto a grid of 'calorimetric cells' of a given spacing in pseudorapidity η and azimuth angle ϕ. Next, the cells are combined into clusters, after which particle identification takes place, including smearing of the four-momenta according to particle type. Jets are built by a cone algorithm with $\Delta R = 0.4$, where $\Delta R = \sqrt{(\Delta\eta)^2 + (\Delta\phi)^2}$. Acceptance requirements are imposed: $|\eta| < 2.5$ for e/μ and $|\eta| < 5$ for jets as well as $p_T > 5/6/10$ GeV for e/μ/jets. Leptons are marked as isolated if there is no other cluster within a distance $\Delta R = 0.4$ of the lepton, and if additional energy inside a cone $\Delta R = 0.2$ is below 10 GeV. While ATLFAST captures quite well the main features of the full simulation, some important effects are left out. Lepton identification efficiencies are not parametrized. A conventional 90% efficiency per lepton is therefore included by hand in the analysis. Also, the possibility of misidentifying a jet as a lepton is absent in the fast simulation, and has not been included in our analysis. The effect of pile-up on the jet energy resolution is accounted for in ATLFAST when run at high luminosity, as in this analysis, but pile-up events have not been simulated, and the underlying event is probably too 'slim'. However, as the selection criteria on jets and leptons are quite hard, we do not expect a more realistic detector simulation to change the results very much. Nevertheless, the numbers quoted at the end of this section should be validated with these effects included.

The signature of a signal event is two opposite-sign same-flavour (SF) leptons, considerable missing p_T from the escaping LSPs, and at least two hard jets, one from the signal chain, the other from the decay of the squark nearly always present in the other decay chain. The most important Standard Model process to have the same features as the signal, is $t\bar{t}$ production. Also W/Z together with jets, one of which is a b-jet, can mimic the signal, and in combination with the underlying event, pile-up and detector effects, other processes will also now and then result in the given signature. Together with $t\bar{t}$ we therefore include QCD, Z/W+jet as well as $ZZ/ZW/WW$ production. No K-factors have been used.

[3] The main parts of the analysis have been confirmed with HERWIG [46], see [28].

The precuts (not tuned) used to isolate the chain are the following,

- At least three jets, satisfying: $p_T^{\rm jet} > 150, 100, 50$ GeV
- $E_{T,\rm miss} > \max(100 \text{ GeV}, 0.2 M_{\rm eff})$ with $M_{\rm eff} \equiv E_{T,\rm miss} + \sum_{i=1}^{3} p_{T,i}^{\rm jet}$
- Two isolated opposite-sign same-flavour leptons (e or μ), satisfying $p_T^{\rm lep} > 20, 10$ GeV

The QCD background is cut away by the requirement of two leptons and of considerable missing p_T. For the processes involving Z and W the requirement of high hadronic activity together with the missing p_T removes nearly all events. After the rather hard cuts listed above, the Standard Model background consists of approximately 95% $t\bar{t}$.

5.2 Different Flavour (DF) subtraction

At this stage the main background events, in addition to $t\bar{t}$, will come from other SUSY processes which have two opposite-sign same-flavour leptons. It is useful to distinguish between two types. The first, which will also be referred to as 'lepton-correlated', produces correlated leptons, e.g. leptonic decay of Z. In these processes the leptons always have the same flavour. The other type produces uncorrelated leptons which need not be of the same flavour. Typically the uncorrelated leptons are produced in different decay branches within the same event. Lepton universality implies that electrons and muons are produced in equal amounts (apart from negligible mass effects). This means that for events which produce uncorrelated leptons, there should be as many opposite-sign different-flavour (DF) lepton pairs produced as there are opposite-sign same-flavour lepton pairs, and their event characteristics should be the same. The same-flavour leptons are already part of the selected events. If one then subtracts the different-flavour events from the total same-flavour sample, this corresponds statistically to removing the non-signal same-flavour events which come from uncorrelated leptons. The residual of the subtraction is a larger statistical uncertainty in the new signal distribution. Clearly the different-flavour subtraction is a very effective tool which takes care of both $t\bar{t}$ and most of the SUSY background. Only processes with correlated leptons remain.

In a more detailed study one would need to correct for the different acceptances of electrons and muons as functions of (p_T, η, ϕ) in the different-flavour subtraction. Here we have assumed equal acceptance for electrons and muons, which even for a fast simulation is only approximately true. Also we have assumed that the efficiencies for reconstructing two same-flavour and two different-flavour leptons are the same. For close leptons this is not the case in the ATLFAST reconstruction. This will have some visible effects in the different-flavour-subtracted distributions, see below.

Fig. 11 shows the different-flavour subtraction for the m_{ll} (top) and m_{qll} (bottom) distributions at points (α) (left) and (β) (right). (The jet used in the m_{qll} distribution is the one of the two p_T-hardest jets which gives the smaller value of m_{qll}.) All the plots have the same colour code. In red the same-flavour ('SF') distribution is shown by solid curve, the different-flavour ('DF') one by dashed curve. Their difference, the different-flavour-subtracted distribution ('SF-DF'), is shown in black with errors. The curve in blue

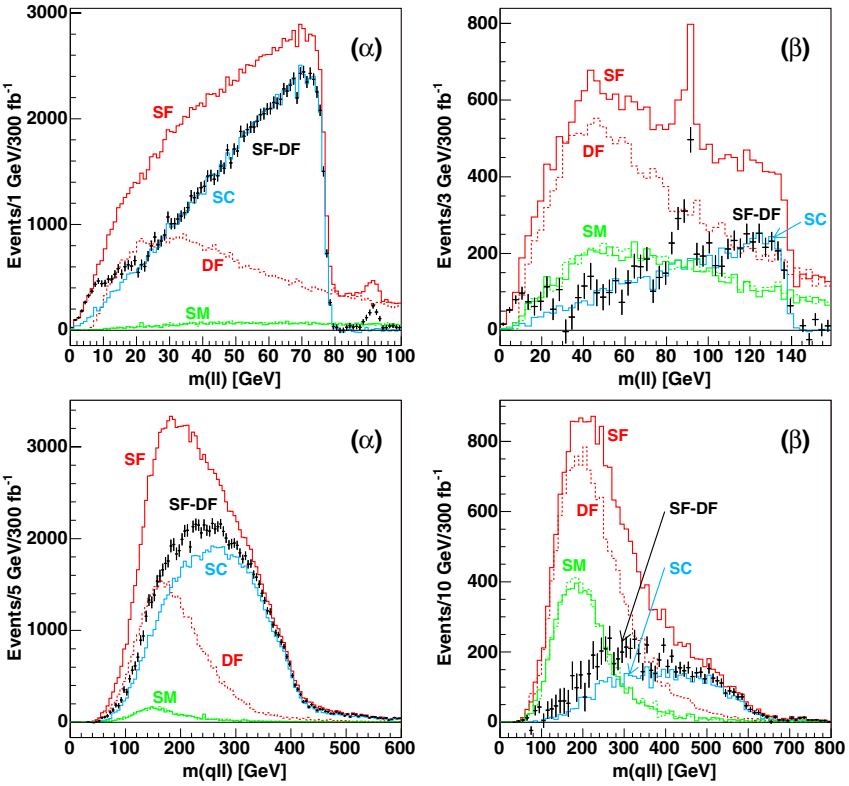

Figure 11: Different-flavour subtraction for m_{ll} and m_{qll} at (α) (left) and (β) (right). The solid/dashed red curves are the same-flavour ('SF')/different-flavour ('DF') distributions. In black, their difference, the different-flavour-subtracted distribution ('SF-DF'), is shown with error bars. The blue curve shows the part of the subtracted distribution which contains a signal chain ('SC'). The solid/dashed green curves ('SM') give the Standard Model part (completely dominated by $t\bar{t}$) of the same-flavour/different-flavour distributions. They are statistically equal and will cancel each other.

shows the part of the different-flavour-subtracted distribution which contains a signal chain ('SC'). The reason why the blue distribution of m_{qll} does not have the form of the theory distribution in Fig. 10, is that the jet is only correctly selected in roughly half of the cases. In solid/dashed green the Standard Model contributions to the same-flavour/different-flavour distributions are shown ('SM'). They are statistically identical and will cancel each other through the different-flavour subtraction.

If the samples contained only background events with uncorrelated leptons (and the different-flavour-subtraction procedure removed all of these), the different-flavour-subtracted distribution should fall exactly on top of the blue line. When this does not happen, it implies that the sample also contains background events with correlated leptons. The

Z-peaks in the m_{ll} distribution at both (α) and (β) are obviously of this type. The Z's stem predominantly from the decay of heavier gauginos into lighter ones. At (α) $\sim 80\%$ of the peak comes from the heavy gauginos $\tilde{\chi}_3^0$, $\tilde{\chi}_4^0$ and $\tilde{\chi}_2^{\pm}$. At (β) $\tilde{\chi}_2^0$ is sufficiently heavy to decay into $\tilde{\chi}_1^0 Z$ and is responsible for $\sim 40\%$ of the peak. The rest involves the heavy gauginos.

For $m_{ll} \lesssim 20$ GeV a bump is visible in the different-flavour-subtracted distribution. This excess turns out to come mainly from lepton-uncorrelated events, predominantly of the type $\tilde{\chi}_2^0 \to \tilde{\tau}_1 \tau$ which is abundant in the two scenarios, and where the taus decay leptonically. Since a pair of taus produce same-flavour and different-flavour leptons in identical amounts, the different-flavour subtraction should take care of this background. When it does not, it is because of an asymmetry in the reconstruction algorithm of ATLFAST which accepts close same-flavour leptons at a higher rate than close different-flavour leptons. Since small ΔR between the leptons means small m_{ll} values, the bump appears at low m_{ll}. Such a reconstruction asymmetry may also have noticeable effects in other distributions, e.g. m_{qll}, for which the maximum values in our two mass scenarios appear for parallel leptons. A dedicated study of the impact detector effects of this type may have on the endpoint determinations may be worthwhile.

In the m_{qll} distributions there is an excess of events (compared with the blue line) at lower masses. Some of this excess comes from the lepton-uncorrelated events in the m_{ll} bump. Typically these land at low m_{qll} values. The main contribution to the excess is however from $\tilde{\chi}_2^0$'s which decay sleptonically, but which originate from $\tilde{q}_R$, $\tilde{t}_1$, $\tilde{g}$ or the heavier gauginos.

At (β) two effects complicate the endpoint measurements. One is a reduction of the SUSY cross-section by one order of magnitude relative to (α). This allows for the Standard Model background to have a larger impact, see the green curves in Fig. 11. Since this background (practically only $t\bar{t}$) consists of uncorrelated leptons, it is dealt with by the different-flavour subtraction. It leaves however an increased statistical uncertainty in the resulting distribution. The other effect at (β) is a reduction in the signal branching ratio, mainly from a reduced BR($\tilde{\chi}_2^0 \to \tilde{l}_R l$), see Fig. 9. As a result also the SUSY background becomes larger relative to the signal.

While the Standard Model background is practically negligible at (α), it is of similar size as the SUSY background at (β). For the m_{qll} distribution both background types are important only at low values, a fair distance away from the kinematical maximum value. The same is true for the m_{ql} distributions. The endpoint measurements are therefore only minimally affected by the background. An exception is the $m_{qll(\theta > \frac{\pi}{2})}$ distribution, where a minimum is measured.

5.3 Selection cuts

A fair fraction of the events which pass the precuts, $\sim 30\%$ for (α) and $\sim 20\%$ for (β), have more than two leptons. Each opposite-sign lepton pair which satisfies $p_T > 20, 10$ GeV is used, either in the same-flavour or the different-flavour distribution. As usual, the different-flavour subtraction takes care of the incorrect combinations.

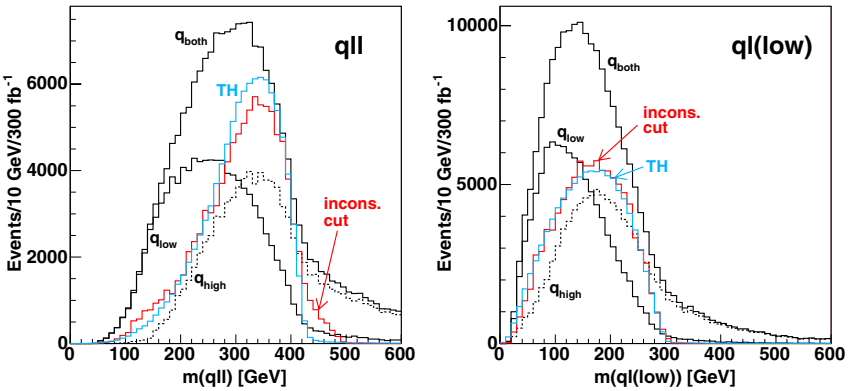

Figure 12: Quark selection cuts for m_{qll} (left) and $m_{ql(\mathrm{low})}$ (right). Left: The two lower black curves in solid and dashed show the $m_{q_{\mathrm{low}}ll}$ ('q_{low}') and $m_{q_{\mathrm{high}}ll}$ ('q_{high}') distributions. The highest black curve shows the sum of the two, $m_{q_{\mathrm{both}}ll}$ ('q_{both}'). Notation is defined in the text. Blue: theory distribution ('TH'). Red: inconsistency cuts ('incons. cut') have been applied on $m_{ql(\mathrm{low})}$ and $m_{ql(\mathrm{high})}$ (the resulting distribution is scaled up). Right: An inconsistency cut is applied on m_{qll}. The jet chosen for $m_{q_{\mathrm{low}}ll}$ is the one used in $m_{q_{\mathrm{low}}l(\mathrm{low})}$ etc. The inconsistency cut is seen to work very well for the $m_{ql(\mathrm{low})}$ distribution.

The selection of the jet to go with the two leptons is more difficult. In the precuts at least three jets are required. If the squarks are considerably heavier than $\tilde{\chi}_2^0$, and the gluinos are not very much heavier than the squarks, then the two p_T-hardest jets are expected to come from the decay of the two squarks present in nearly all events. (More specifically we need $m_{\tilde{q}}^2 - m_{\tilde{\chi}_2^0}^2$ somewhat larger than $m_{\tilde{g}}^2 - m_{\tilde{q}}^2$.) Along the entire SPS 1a line this is the case. The third jet is then expected to come from a gluino decay. Specifically, both for (α) and (β) the correct quark is one of the two p_T hardest in 94% of the cases at the parton level. It is therefore reasonable to consider only these two jets.

In a realistic setting all possible combinations will be investigated, along with all kinds of precuts. However, whatever the mass situation, one will not be able to select the correct jet by some simple cut. Combinatorial background from the jet selection procedure is something one will have to live with.

In Fig. 12 (left) the different-flavour-subtracted m_{qll} distribution at (α) is shown for various jet selections. The two lower black curves are obtained by selecting from the two p_T-hardest jets the one which gives the smaller (solid) and larger (dashed) value of m_{qll}, for simplicity referred to as $m_{q_{\mathrm{low}}ll}$ ('q_{low}') and $m_{q_{\mathrm{high}}ll}$ ('q_{high}'), respectively. The highest black curve shows the sum of the two, $m_{q_{\mathrm{both}}ll}$ ('q_{both}'). In blue and marked 'TH', with the same normalisation as $m_{q_{\mathrm{low}}ll}$, is the parton level theory distribution, as generated by PYTHIA so that it contains widths, production biases etc.

It is possible to get a reasonable first estimate of the endpoint both from $m_{q_{\mathrm{low}}ll}$ and $m_{q_{\mathrm{both}}ll}$. The shape of the theory distribution is however not reproduced by any of the three experimental distributions (in black), which is quite natural since they all contain

both combinatorial and lepton-correlated background, and two of them are also biased by the jet selection procedure. For (α) the lepton-correlated background comes mainly from sleptonically decaying $\tilde{\chi}_2^0$'s that do not have a $\tilde{q}_L$ or $\tilde{b}$ as a parent. As can be seen from Table 3 together with Fig. 9, $\tilde{\chi}_2^0$ comes from $\tilde{q}_L$ or $\tilde{b}$ in 78% of the times. If, for a signal event, we assume 50% chance of picking the correct jet, a different-flavour-subtracted distribution will consist of 39% signal, 39% combinatorics and 22% lepton-correlated background. For (β) the fractions are 35%, 35% and 30%. For these numbers $\tilde{\chi}_2^0$ is assumed to be the only source of lepton-correlated background.

We have investigated methods to remove or model this combinatorial background. For example, the sample may be purified [25] by using events where only one of the jets can reasonably be assigned to the signal quark. Consider the case where a measurement of $m_{qll}^{\max}$ has been made, and one wants to now measure $m_{ql(\mathrm{low})}^{\max}$. In constructing the $m_{ql(\mathrm{low})}$ distribution we must choose one of the two highest p_T jets, and with no other input will choose the wrong jet 50% of the time, giving a combinatorial background. However, in some events, one of the jets will be such that its intepretation as the signal quark would contradict the previous measurement of $m_{qll}^{\max}$, i.e. using it to construct m_{qll} would give $m_{qll} > m_{qll}^{\max}$. In these events, we can be reassured that in choosing the *other* jet we have chosen correctly. If neither of the jets in the event gives m_{qll} in contradiction with the previous measurement, then we cannot be certain that we have the correct jet, and therefore discard the event. In other words, we only use events where only one choice of signal quark is consistent with other endpoint measurements. This allows one to build a purified sample where for signal events the wrong jet is only chosen if the correct jet is not one of the two p_T-hardest jets. There will however still be background events in the sample.

The red curve of Fig. 12 (left) is constructed from the m_{qll} distribution by means of 'inconsistency cuts' on $m_{ql(\mathrm{low})}$ and $m_{ql(\mathrm{high})}$ where we insist that only one of the two highest p_T jets has $m_{ql(\mathrm{low})} < 310$ GeV and $m_{ql(\mathrm{high})} < 390$ GeV. Approximately 1/4 of the events pass these cuts; the resulting curve is normalised to have the same number of events as the $m_{q_{\mathrm{low}}ll}$ distribution. The similarity with the blue theory curve has improved, but is still not excellent. In particular there is a large tail towards higher values, which in practice makes it less useful for accurate endpoint determination.

In this respect a better result is obtained for the $m_{ql(\mathrm{low})}$ distribution, shown in Fig. 12 (right) with an inconsistancy cut requiring only one jet with $m_{qll} < 440$ GeV, and normalisation as $m_{q_{\mathrm{low}}l(\mathrm{low})}$. The red curve matches quite well with the theory curve, and there is no disturbing tail. In fact the red curve is the one we later use to estimate the endpoint for this distribution.

While it is certainly reassuring to regain the theoretical distribution, it is still not clear what is the best way to obtain an accurate measurement of the endpoints. One would probably combine many different methods, looking for convergence as well as inconsistencies. For instance, even though we should choose not to fit the distribution from the inconsistency cut, since it has less statistics, it teaches us that a linear fit to $m_{q_{\mathrm{low}}l(\mathrm{low})}$ from 150 to 300 GeV, which might otherwise seem reasonable, would not at all be a fit to the signal since it is close to linear only in the region 240–300 GeV.

Another approach to obtaining a distribution closer to the original one relies not on purification of the actual sample, but on finding an estimate for the background, combinatorial and/or lepton-correlated, and then subtracting it from the original distribution. Statistics may be better preserved in this way, but systematics are introduced. Some attempts have been made with 'mixed events', i.e. the combination of the lepton pair from one event with jets from other events. The idea is that since the lepton and the jet sectors of mixed events are necessarily uncorrelated, they may mimic both types of background, lepton-correlated and combinatorial, where also the lepton pair is only weakly correlated with the jet.

A first complication of this method is encountered when the four-vectors of different events are to be combined into mixed events. What rest frame is the appropriate one? This already points to the inexact nature of such a method. Its performance is however promising, although somewhat variable, as will be demonstrated later in this section.

The mixed event sample is constructed from the events which make up the distributions, i.e. those which pass the precuts listed in Sect. 5.1. An additional requirement of having exactly two opposite-sign leptons is imposed to avoid ambiguities in the lepton sector. No major differences are however expected from leaving out this constraint. Each event then provides two leptons, uniquely defined because of the additional cut, and its two p_T-hardest jets. The four-vectors of the selected leptons and jets are here taken in the rest frame of the lepton pair. Due to the prominent role of the lepton pair, this choice is not unreasonable. On the other hand it is not unique. Both the laboratory frame, the rest frame of the entire event or the rest frame of the leptons together with the two p_T-hardest jets are viable candidates. A dedicated study of the characteristics of these different possibilities would be worthwhile.

The mixed sample is then constructed by consecutively combining the lepton sector of one event with the jet sector of another. In our study each lepton sector was combined with the jet sector of five other events. By increasing this number, very high statistics can be obtained for the mixed sample. For each combination of events all relevant masses were constructed, $m_{q_{\mathrm{low}}ll}$, $m_{q_{\mathrm{high}}ll}$, $m_{q_{\mathrm{both}}ll}$, $m_{q_{\mathrm{low}}l(\mathrm{low})}$ etc.

Mixed samples for same-flavour and different-flavour events are constructed separately. In the end their difference is taken, in line with the previously described different-flavour subtraction. The resulting mixed distributions are the ones used later in this section.

5.4 Multiple squark masses

The theory distributions shown in Fig. 10 are only for one squark mass per scenario. In reality four different squark masses, $m_{\tilde{d}_L}/m_{\tilde{s}_L}$, $m_{\tilde{u}_L}/m_{\tilde{c}_L}$, $m_{\tilde{b}_1}$ and $m_{\tilde{b}_2}$ will contribute to the distribution. The blue theory distribution of Fig. 12 is therefore the sum of four separate distributions, each with a different endpoint, different normalisation and similar though not identical shapes.

While jets from the three lightest quarks, and for most purposes also from the c-quark, will be indistinguishable in ATLAS, jets from b-quarks will be identified with a certain probability. The expected rejection factors for incorrectly identifying jets from lighter quarks and gluons as b-jets, are for high luminosity operation given in the ATLAS TDR

[20], Fig. 10-41. Low/high b-tagging efficiencies come with high/low rejection factors and allow for high-purity b/non-b-samples, respectively. The higher the purity, the smaller the sample. In this analysis we have used the following simplistic b-tagging prescription for both purposes: For a b-tagging efficiency of 50% the rejection factors against jets from gluons/three lightest jets and from c-jets are set to 100 and 10, respectively.

With b-tagging one can to a certain extent separate the $\tilde{q}_L$ and the $\tilde{b}$ distributions, thus opening for a disentanglement of the squark masses. Nevertheless, even though a high purity separation has been accomplished, each of the two distributions will still contain contributions from two squark masses. Typically a kink can be observed at the position of the lowest endpoint. For mSUGRA scenarios $\tilde{d}_L/\tilde{s}_L$ and $\tilde{u}_L/\tilde{c}_L$ only differ by a few GeV, so the kink will appear very near the end of the distribution. Since the proton contains more u than d-quarks, $\tilde{u}_L$ will be produced at a higher rate than the heavier $\tilde{d}_L$. This reduces further the visibility of the kink. Then with the general smearing due to physics and detector effects in addition to background near the endpoint, it may be very difficult to identify such a kink. In case of the two b-squarks the separation will be larger. Whether it is possible to identify it or not depends on the rate of $\tilde{b}$ production as well as the level of impurity from $\tilde{q}_L$-events in the b-tagged distribution.

5.5 Invariant mass distributions

SUSY processes for (α) and (β) as well as the Standard Model background have been produced for 300 fb^{-1}. This corresponds to 3 years at design (high) luminosity. The mass distributions of the available edges for SPS 1a (α) and (β) are shown in Figs. 13–14.

For all plots the black points with errors show the total different-flavour-subtracted distribution ('SF-DF'). Solid green marks the SUSY background ('SUSY'), and in green with error bars the Standard Model background ('SM') is shown. The solid blue curve then shows the original theory distribution ('TH'), normalised to the different-flavour-subtracted distribution. The fitted function appears in red. In cases where mixed events are used to model the background, the smooth function fitted to the high-statistics mixed-event sample is shown in dashed red. When additional distributions are plotted, they will be described in the accompanying discussion.

For each distribution the endpoint estimation will be discussed. In most cases the edges are fitted to a straight line in combination with a simple background hypothesis, and in some cases convoluted with a Gaussian distribution. At (α) this procedure gives numbers in reasonably good agreement with the nominal values. At (β), where the SUSY cross-section is much smaller and also the branching fraction of the signal is reduced, the estimated endpoint values depend more strongly on the fitting method chosen. To control and reduce this systematic effect, a better understanding of the whole chain is required; physics effects, detector effects, multiple masses at different rates, background, precuts. After some years of LHC operation one can expect these issues to be understood sufficiently that the systematics of endpoint estimation is controlled and corrected for in the fitting procedure, up to some small uncertainty.

If this is achieved, it is the statistical error of the endpoint values, in combination with the uncertainty on the absolute energy scale, expected to be 1% for jets and 0.1% for

leptons, which determine the precision at which masses can be obtained for the different scenarios.

In the discussion of the distributions we therefore have the main focus on the statistical uncertainty of the endpoint determination, but are also concerned with the present magnitude of the systematic uncertainty. For some of the distributions it may seem bold to state that the systematic fit uncertainty will be reduced far below the statistical one. One shall however remember that once such distributions become available, a great effort will go into investigating them.

SPS 1a (α)

m_{ll}: The m_{ll} distribution at (α) is shown in Fig. 13 (top left). It is very close to the expected triangular shape. To the right of the endpoint the Z peak is clearly visible. These Z's come from SUSY decays. The bump at low m_{ll} is discussed in Sect. 5.2.

The distribution is fitted with a straight line convoluted with a Gaussian,

$$g(m_{ll}) = \begin{cases} A\, m_{ll}, & m_{ll} < m_{ll}^{\max} \\ 0, & m_{ll} > m_{ll}^{\max} \end{cases} \quad , \quad f(m_{ll}) = \frac{1}{\sqrt{2\pi}\sigma} \int_0^\infty dm'_{ll}\, g(m'_{ll}) e^{-\frac{(m_{ll}-m'_{ll})^2}{2\sigma^2}} \qquad (5.1)$$

Both the endpoint, the width of the Gaussian and the normalisation are kept free in the fit, resulting in an endpoint value of 76.72 GeV at a statistical error of 0.04 GeV. Compared to the nominal value this is 0.35 GeV too low. When a more appropriate model for loss of lepton energy is implemented in the fit function, such a systematic shift is expected to be reduced to the level of the statistical error or below. The fit results are quite stable with respect to variations in bin size and range of fit. We thus arrive at the well-known result that the m_{ll} endpoint is expected to be estimated to high precision.

m_{qll}: As for all cases where jets are involved, the m_{qll} distribution comes in many versions, depending on the jet selection procedure as well as the use of b-tagging information. Plotted in Fig. 13 (top right) is $m_{q_{\rm low}ll}$ (see Sect. 5.3) with no b-veto. Mixed events have been used in an attempt to model the background. A $6^{\rm th}$ degree polynomial was first fitted to the high statistics mixed event sample. Then, with the normalisation kept free, the polynomial was combined with a straight line for the signal part. This procedure returns $m_{qll}^{\max} = 427.7(0.9)$ GeV, statistical error in parenthesis. The nominal value is 425.9/431.1 GeV for $\tilde{u}_L/\tilde{d}_L$. Alterations to the bin size and fit range has a 1–2 GeV effect on the fit value, but the statistical error remains the same.

The dashed red line shows the shape of the mixed event sample. It matches the $m_{q_{\rm low}ll}$ distribution very well at values beyond the endpoint, justifying its use, and is sufficient to obtain a reasonable endpoint fit. Similar results can be found by modeling the background tail with an exponential or a polynomial. If, at some later stage, the entire distribution is to be compared with the theory distribution, the size of the background must be known for any m_{qll} value. An exponential or a polynomial based on the upper tail can never be a good background model for values somewhat below the edge. It is here the mixed events may have a role to play. In the particular case of the $m_{q_{\rm low}ll}$ distribution, the mixed sample actually appears to be a good background estimate at all values. For $m_{q_{\rm both}ll}$ and some

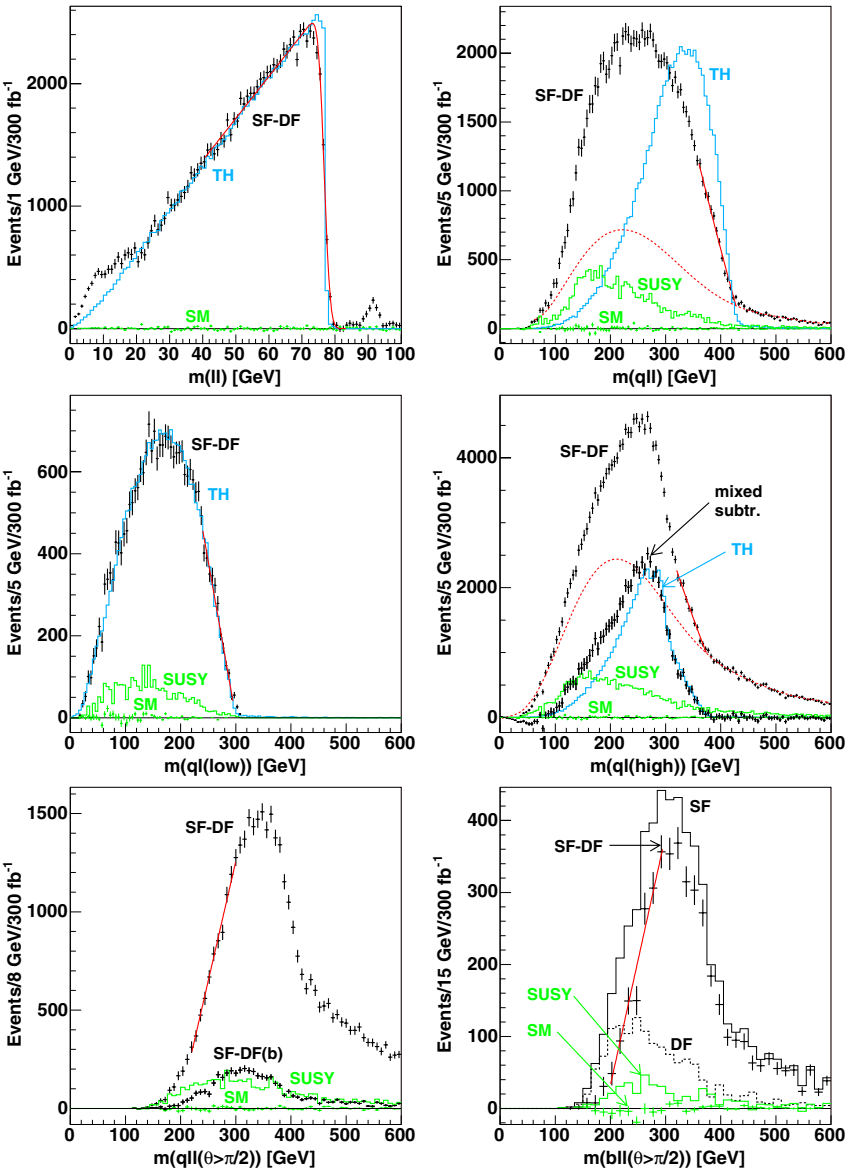

Figure 13: Invariant mass distributions for SPS 1a (α). See the text for details.

other distributions, it does not do so well. Nevertheless, there are many ways to construct the mixed sample. Further study of the method seems worthwhile.

It is tempting to suggest that it is mainly the $\tilde{u}_L/\tilde{c}_L$ endpoint we measure, and that the extra events just above the endpoint (see the figure), make up the hard-to-detect kink from the $\tilde{d}_L/\tilde{s}_L$ edge. At the present level of detail it is impossible to say if such an effect could be isolated to give an additional measurement for the heaviest mass. It does seem difficult, though, as the kink will be washed out by other effects, e.g. sparticle widths. At (α) the intrinsic width of $\tilde{u}_L$ is 5.3 GeV, see Fig. 6 (right), to be compared with $m_{\tilde{d}_L} - m_{\tilde{u}_L} = 5.8$ GeV. Also detector effects will result in a general smoothing of the distributions.

$m_{ql(\mathrm{low})}$: For $m_{ql(\mathrm{low})}$ the mixed sample is fine above the endpoint, but overestimates for lower masses. While the edge can be fitted and the endpoint measured by a mixed sample subtraction, due to its good behaviour in the edge region, we have here instead used the inconsistency cut $m_{q_{\mathrm{high}}ll} > 440$ GeV to purify the sample, Fig. 13 (middle left). The ability of the inconsistency cut to bring the distribution very close to the original one, was already discussed in relation to Fig. 12.

For a zero background hypothesis a straight line fit gives $m^{\mathrm{max}}_{ql(\mathrm{low})} = 300.7(0.9)$ GeV, to compare with the nominal 298.5/302.1 GeV for $\tilde{u}_L/\tilde{d}_L$. If the few bins around the endpoint are also included, the value increases by 1–2 GeV. Whether these high-mass events are signal or background is not easy to tell from the given distribution, since there is virtually no background structure to extrapolate from. This is because a 'consistency cut' has been imposed which requires $m_{q_{\mathrm{low}}ll} < 440$ GeV, in accordance with the already measured m_{qll} endpoint. From Eq. (4.10) this implies $m_{ql(\mathrm{low})} < 440/\sqrt{2}$ GeV $= 311.1$ GeV. The consistency cut takes away a large part of the background, but also has the effect that it becomes difficult to see what structure the $m_{ql(\mathrm{low})}$ background has. If the consistency cut is dropped, the usual background tail appears and can be modeled, although at the cost of a slight increase in the statistical error.

$m_{ql(\mathrm{high})}$: Following the same procedure as for m_{qll} the background of the $m_{ql(\mathrm{high})}$ distribution was modeled by the mixed event sample. In Fig. 13 (middle right) the relevant distributions are shown. Also the result from subtracting the mixed sample is shown ('mixed subtr.'); the lower black points with error bars. This subtracted distribution follows the original theory distribution (blue) closely in the edge region, but overestimates at lower values.

In the range $m_{ql(\mathrm{high})} \in (320, 550)$ GeV the endpoint was estimated to 374.0(2.0) GeV. The nominal value is 375.8/380.3 GeV for $\tilde{u}_L/\tilde{d}_L$. At (α) the $m_{ql(\mathrm{high})}$ edge consists of two parts. This is clear from the theory distribution (blue), but also in the reconstructed distributions (black). In the fit only the lowest near-linear stretch was used. It is clearly incorrect to apply a straight line for the whole edge, but if done, the statistical error would be reduced to ~ 1 GeV. When a good signal function is at hand, the whole edge will be described. It may therefore be reasonable to expect a statistical error of 1 GeV rather than 2 GeV.

$m_{qll(\theta>\frac{\pi}{2})}$: The $m_{qll(\theta>\frac{\pi}{2})}$ distribution differs from the previous ones in that a minimum is to be measured. This has two important consequences. One can be seen from Fig. 11

(bottom left), even though this plot is for the unconstrained m_{qll} distribution. The lepton-uncorrelated background, modeled by the different-flavour distribution (dashed red), sits mostly at low values, far away from any maximum edge, but quite near the $m_{qll(\theta>\frac{\pi}{2})}$ threshold. While this background type is removed (statistically) by the different-flavour subtraction, the price is an increased statistical uncertainty which directly will affect the statistical precision of the $m^{\min}_{qll(\theta>\frac{\pi}{2})}$ estimation.

The other consequence of measuring a minimum is related to the multiple squark masses. As noted earlier, the distributions can be purified using b-tagging information. For the measurements discussed so far we have considered the total sample. This is because the $\tilde{q}_L$-squarks are so much heavier than the $\tilde{b}$-squarks that the upper edge regions are practically free of $\tilde{b}$-events anyway. A b-veto has therefore no effect, at least not at our level of precision. For the threshold measurement it is the other way around. Here the threshold related to the lightest squark, $\tilde{b}_1$, will be the threshold for the total distribution. A b-veto may therefore be important in order to obtain the threshold for the non-$\tilde{b}$-events.

A third complication is that the edge is very non-linear, as can be seen from the theory distributions in Fig. 10. Also, the fact that this non-linearity is of the concave type, could make it very difficult to see where the edge ends and where smearing from various sources takes over. This is all the more relevant since the $\tilde{b}$-events come at a significantly smaller rate than $\tilde{q}_L$-events (ratio $\sim 25\%$), and may therefore appear as just another contribution to the lower tail, not easily distinguishable from other effects.

The $m_{qll(\theta>\frac{\pi}{2})}$ distribution is shown in Fig. 13 (bottom left). The upper distribution ('SF-DF') shows the non-b-tagged $m_{qll(\theta>\frac{\pi}{2})}$ sample. The lower black points ('SF-DF(b)') mark the b-tagged sample. Only approximately 50% of the events which contain a b are actually b-tagged. This means that the non-b-tagged distribution contains a 'hidden' b-sample, statistically similar to the 'visible' b-sample both in size and shape. (There would be a shift to the left, though, since in the reconstruction b-tagged jets have larger recalibration factors. This is not accounted for here.) Analogous to the different-flavour subtraction it is therefore possible to get the non-b-tagged distribution closer to the original q-distribution by subtracting the visible b-sample, possibly scaled up or down according to the b-tagging efficiency applied. A slightly different approach would be to use a much harder b-veto and no subtraction. The price would be a significant reduction in sample size.

However, the main problem in the threshold region is not the b-contamination, but the lepton-correlated SUSY background shown in solid green. It comes primarily from events where $\tilde{\chi}^0_2$ decays sleptonically but does not descend from $\tilde{q}_L$ or $\tilde{b}$. It is this background which needs appropriate modeling. The difficulty with having a concave theory distribution together with an unknown background is evident from the figure. It is really difficult to separate the background from the signal.

As a simple estimate of the statistical uncertainty of the edge position, a straight line fit somewhat away from the threshold was performed on the non-subtracted sample ('SF-DF'), returning a statistical error on the endpoint around 1.8 GeV. If the subtracted sample (subtracting 'SF-DF(b)') is used, the error increases. The actual endpoint obtained from such a simple zero-background hypothesis is of course incorrect. At present it seems a

bit optimistic to expect the systematics of the fit to be dominated by the statistical error.

$m_{bll(\theta>\frac{\pi}{2})}$: The $m_{bll(\theta>\frac{\pi}{2})}$ distributions are shown in Fig. 13 (bottom right). The different-flavour-subtracted distribution ('SF-DF') is shown in black with error bars. The same-flavour ('SF') and different-flavour ('DF') curves are also plotted. In the threshold region the same-flavour and different-flavour distributions are considerably larger than their difference, which necessarily gives large statistical uncertainties in the different-flavour-subtracted samples.

As for $m_{qll(\theta>\frac{\pi}{2})}$ more studies are required to control and reduce the systematic error induced by the background and the nonlinear theory curve. A linear fit was performed in the near-linear region to measure the precision with which the position of the edge can be found. Variations in the bin size and the fit range yield systematic errors within 1 GeV and statistical error between 4 and 5 GeV.

m_{bll}, $m_{bl(\mathrm{low})}$, $m_{bl(\mathrm{high})}$: Given that the background can be controlled and a good signal function can be found, $m_{bll(\theta>\frac{\pi}{2})}$ is a good distribution since the lowest threshold is given by $\tilde{b}_1$, which also has a considerable rate. For the edges m_{bll}, $m_{bl(\mathrm{low})}$ and $m_{bl(\mathrm{high})}$ one problem is that it is $\tilde{b}_2$ which defines the outer endpoint for the b-distributions. Since this squark only contributes $\sim 22\%$ of the $\tilde{b}$-events, the edge above the $\tilde{b}_1$ endpoint may look like background. (However, since we expect the heavier $\tilde{b}$-squark to come at a considerably smaller rate as it has less phase space for production, and also a smaller branching ratio to the wino-like $\tilde{\chi}_2^0$, due to its larger right-handed component, we can explicitly look for such a small tail-like edge.)

A more serious problem is the background from other SUSY events. Typically these have the decay Eq. (3.3) in one chain, providing two leptons, and $\tilde{g} \to \tilde{b}b$ or $\tilde{g} \to \tilde{t}_1 t$ in the other, providing b-jets. The mass distributions of this background stretch sufficiently beyond the $\tilde{b}_1$ endpoints that the resulting edge structures become difficult to analyse. The positions of these three b-edges can typically be measured with a statistical precision of 3–4 GeV, but it remains unclear whether the systematics of the edge can be sorted out. Another approach could be to require a lower b-tagging efficiency for these distributions in order to get higher rejection factors and purer, although smaller, samples.

SPS 1a (β)

The mass distributions of (β) are shown in Fig. 14. Throughout, the total samples have been used. No b-veto has been applied.

m_{ll}: The m_{ll} distribution is shown in Fig. 14 (top left). It has the triangular shape with a Z-peak on top. Some datapoints in the Z-peak lie above the range of this plot, and can be viewed in Fig. 11 (top right).

As was also the case for (α) there is a bump at lower values. The distribution above the Z-peak was fitted with the same Gaussian-convoluted triangular shape as earlier, Eq. (5.1), giving $m_{ll}^{\mathrm{max}} = 137.4(0.5)$ GeV which is 0.5 GeV lower than the nominal value.

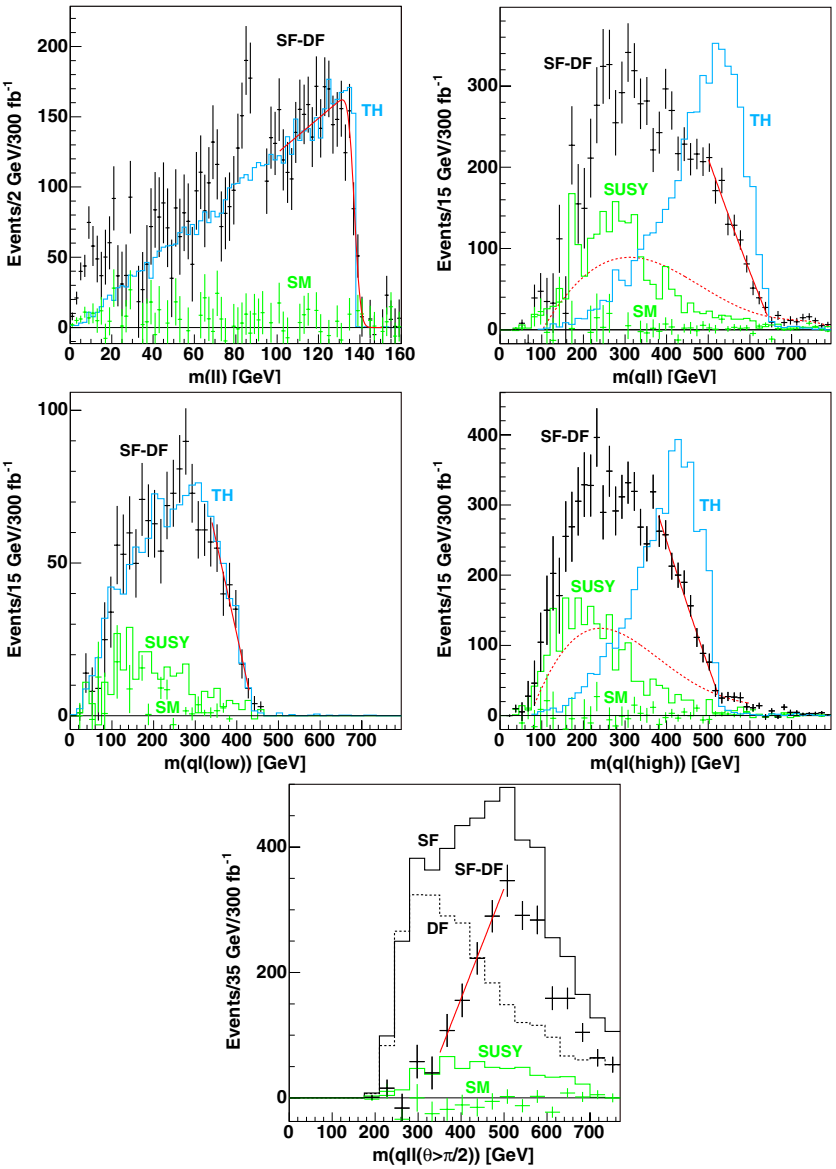

Figure 14: Invariant mass distributions for SPS 1a (β). See the text for details.

$\boldsymbol{m_{qll}}$**:** The $m_{q_{\rm low}ll}$ distribution is shown in Fig. 14 (top right). With the mixed sample as a rough background estimate a straight-line fit gives an endpoint at 640 GeV with a

systematic shift of 1 GeV from varying the bin size and fit range. The statistical error is 5 GeV. If, however, the same fitting procedure is applied to the $m_{q_{\rm both}ll}$ distribution, the endpoint value increases to 655 ± 2 GeV and the statistical error is 9 GeV.

Surely more study would bring these values closer, and optimally have them converge near the nominal value of 649.1/652.5 GeV for $\tilde{u}_L/\tilde{d}_L$. For later use we take an optimistic statistical error of 5 GeV, but also include a systematic fit error of 3 GeV for a more conservative estimate.

$m_{ql(\rm low)}$: The $m_{q_{\rm low}l(\rm low)}$ distribution is shown in Fig. 14 (middle left). Both a consistency cut $m_{q_{\rm low}ll} < 670$ GeV and an inconsistency cut $m_{q_{\rm high}ll} > 670$ GeV are used. A straight-line fit with no background hypothesis gives a statistical error around 6.3 GeV. The actual fit value is 443 GeV, which overshoots by a few GeV since the background plateau has not been included. The nominal value is 436.6/438.9 GeV for $\tilde{u}_L/\tilde{d}_L$.

$m_{ql(\rm high)}$: The $m_{q_{\rm low}l(\rm high)}$ distribution with the consistency and the inconsistency cut is shown in Fig. 14 (middle right). The mixed sample was again used to roughly model the background under the edge. A straight-line fit gives an average value of 520.5 GeV with systematics from binning and fit range of 3 GeV. The statistical error is at 5.5 GeV.

The nominal value is 529.9/532.7 GeV for $\tilde{u}_L/\tilde{d}_L$, some 10 GeV above our estimate. One could argue that the current endpoint measurement has considerable uncertainties and that this discrepancy is not dramatic at the present level of detail. However, such an underestimation is actually to be expected. In Fig. 10 the theoretical $m_{ql(\rm high)}$ distribution is shown for $\tilde{u}_L$ at (β). There is a long vertical fall towards 517 GeV (for $\tilde{d}_L$ it is at 519 GeV), then just before the bottom is reached, a small foot appears, as anticipated in Sect. 4.1, and takes us up by 11–13 GeV. To detect such a small foot would require more statistics than is available at (β). Experimentally it is therefore expected to get an endpoint near 517–519 GeV. The incorrect endpoint measurement will have important consequences for the determination of masses from the endpoints. This situation is further discussed in Section 6.

$m_{qll(\theta>\frac{\pi}{2})}$: The $m_{qll(\theta>\frac{\pi}{2})}$ distribution is shown in Fig. 14 (bottom). The same-flavour ('SF') and different-flavour ('DF') distributions are shown in solid and dashed black. Clearly, there are large uncertainties from the different-flavour subtraction. The statistical uncertainty of the different-flavour-subtracted sample was estimated with a straight-line fit, giving 13 GeV. In addition there will be a systematic error, here conservatively set to 10 GeV.

Endpoint measurement values

The results of the endpoint estimation for (α) and (β) are summarized in Table 4. The last column contains an estimate of the systematic error from different fitting techniques, ranges and bin widths. These values are not used in the following, but are included for completeness.

The column with the heading 'Energy Scale Error' shows the expected error on each endpoint estimation from the uncertainty on the absolute energy scale for jets and leptons.

Edge	Nominal Value [GeV]	Fit Value [GeV]	Energy Scale Error (σ^{scale}) [GeV]	Statistical Error (σ^{stat}) [GeV]	Syst. Fit Error [GeV]
(α)					
$m_{ll}^{\max}$	77.07	76.72	0.08	0.04	0.1
$m_{qll}^{\max}$	425.9	427.7	2.1	0.9	0.5
$m_{ql(\text{low})}^{\max}$	298.5	300.7	1.5	0.9	0.5
$m_{ql(\text{high})}^{\max}$	375.8	374.0	1.9	1.0	0.5
$m_{qll(\theta>\frac{\pi}{2})}^{\min}$	200.7	-	1.0	2.2	2.0
$m_{bll(\theta>\frac{\pi}{2})}^{\min}$	183.1	-	0.9	4.5	4.0
(β)					
$m_{ll}^{\max}$	137.9	137.4	0.14	0.5	0.1
$m_{qll}^{\max}$	649.1	647.0	3.2	5.0	3.0
$m_{ql(\text{low})}^{\max}$	436.6	443.0	2.2	6.3	4.0
$m_{ql(\text{high})}^{\max}$	529.9	520.5	2.6	5.5	3.0
$m_{qll(\theta>\frac{\pi}{2})}^{\min}$	325.7	-	1.6	13.0	10.0

Table 4: Endpoint values found from fitting the edges in Figs. 13–14, for 300 fb^{-1}. The nominal values correspond to the mass of $\tilde{u}_L$, which due to the proton content is produced at higher rates than the heavier $\tilde{d}_L$. For the thresholds no fit values are shown, only the errors. This reflects the fact that a reasonable fit function is lacking for this edge.

This effect has not been taken into account in the simulation. The uncertainties of the energy scales are here set to 1% for jets and 0.1% for electrons and muons, see Ch. 12 of [20]. For an invariant mass which consists of only jets or only leptons, this will give the same uncertainties, 1% and 0.1%, respectively. If the invariant mass is constructed from one jet and one lepton, the endpoint uncertainty is

$$\frac{\sigma(m_{ql})}{m_{ql}} = \frac{\sigma(m_{ql}^2)}{2m_{ql}^2} = \frac{1}{2}\sqrt{\left(\frac{\sigma(E_j)}{E_j}\right)^2 + \left(\frac{\sigma(E_l)}{E_l}\right)^2} = 0.50\% \tag{5.2}$$

where E_j and E_l are the jet and the lepton energies, respectively. For an invariant mass involving a higher number of jets and leptons, the error on the endpoint value from the energy scale uncertainty will be different for each event. The error of m_{qll} will depend on the relative size of the three terms on the right-hand side of Eq. (4.10). Since at (α) and (β) we are in the region where the mass ratio $m_{\tilde{q}_L}/m_{\tilde{\chi}_2^0}$ dominates the two other mass ratios, see Eq. (4.4)-*(1)*, the quark will usually be very energetic, leaving one or both m_{ql} terms to dominate. This is particularly true at large values, so near the edge of m_{qll} one can show that the energy scale error will result in an endpoint error between 0.35% and 0.5% for each event. For $m_{qll(\theta>\frac{\pi}{2})}$ the average energy scale error will be slightly lower in our two scenarios. For simplicity we have set the energy scale error to 0.5% for all endpoints involving jets.

6. Extraction of masses from edges

6.1 10,000 ATLAS experiments

In the simulation study described in Sect. 5 values for the endpoints and their statistical uncertainties were found, together with a 'systematic fit uncertainty'. Although not so far from the nominal endpoint values, the fit values in Table 4 are somewhat uncertain due to the as yet not-understood systematics of the fitting procedures. Also, the systematic error on the energy scale has not been addressed.

Assuming that one will eventually be able to control the systematics of the fitting, only the statistical errors together with the systematic error from the energy scale uncertainty will be what determine the LHC potential to measure the SUSY masses. To estimate this potential, consider an ensemble of typical LHC experiments, i.e. where the deviation of each endpoint measurement from the nominal value is based on a Gaussian distribution of width equal to the statistical error estimated for that endpoint, as well as a jet/lepton energy scale error picked from a Gaussian distribution for each experiment, in line with what is done in [31],

$$E_i^{\rm exp} = E_i^{\rm nom} + A_i\sigma_i^{\rm stat} + B\sigma_i^{\rm scale} \tag{6.1}$$

Here E_i denotes the position of the $i^{\rm th}$ endpoint. The coefficients A and B are picked from a Gaussian distribution of mean 0 and variance 1. Each experiment will pick as many A's as there are endpoint measurements as well as one B for the m_{ll} endpoint and one for the endpoints involving jets, thus neglecting the effect of the lepton energy scale error on the latter.

When a set of edges $\mathbf{E}^{\rm exp}$ has been found, the task is to find the masses $\hat{\mathbf{m}}$ which best correspond to the measurements. If only four endpoints are measured, the inversion formulae straight away return the possible mass combinations. If more endpoints are available, no mass combination will in general reproduce the edge measurements, and a numerical approach is required, where the measurements are weighted according to their uncertainties. Note that in this procedure we do not make use of the fit values given in Table 4.

It should also be emphasised that the systematics of the endpoint measurements are here assumed to be under control, i.e. the 'Syst. Fit Error' of Table 4 is neglected. The precision we will find in this section and the next for the determination of masses and mass differences at the LHC must be understood in this context. If the endpoint systematics turn out to be comparable to the combined statistical and energy scale errors, then the precision will be worse.

6.2 Mass estimation via Σ

In our case, where the jet energy scale error produces a correlation between the endpoint measurements, the method of least squares is appropriate. The best mass estimate $\hat{\mathbf{m}}$ is then the one which minimises the function

$$\Sigma = [\mathbf{E}^{\rm exp} - \mathbf{E}^{\rm th}(\mathbf{m})]^T \mathbf{W} [\mathbf{E}^{\rm exp} - \mathbf{E}^{\rm th}(\mathbf{m})] \tag{6.2}$$

where $\mathbf{E}^{\rm th}(\mathbf{m})$ contains the theoretical edge values for a set of masses $\mathbf{m}$. The weight matrix $\mathbf{W}$ is the inverse of the correlation matrix or error matrix of the observations, which is given by the variances and covariances of the endpoint measurements,

$$\begin{aligned}
(\mathbf{W}^{-1})_{ii} &= \sigma_{ii}^{\rm stat} + \sigma_{ii}^{\rm scale} = (\sigma_i^{\rm stat})^2 + (\sigma_i^{\rm scale})^2 \\
(\mathbf{W}^{-1})_{ij} &= \sigma_{ij}^{\rm scale} = \langle E_i^{\rm exp} E_j^{\rm exp} \rangle - \langle E_i^{\rm exp} \rangle \langle E_j^{\rm exp} \rangle = \sigma_i^{\rm scale} \sigma_j^{\rm scale}, \quad i \neq j \\
(\mathbf{W}^{-1})_{i1} &= 0, \quad i \neq 1
\end{aligned} \tag{6.3}$$

where $j = 1$ refers to $m_{ll}^{\rm max}$, which to a good approximation is uncorrelated with the other measurements. The covariances are similar to the variances in size, and so cannot be neglected. If the endpoint measurements were uncorrelated, $\mathbf{W}$ would become diagonal, and the least-squares method would reduce to the normal χ^2 minimum method.

The ensemble distributions obtained by such a procedure can be interpreted as probability density functions. From these the 'inverse probability problem' can be addressed, which is that of stating something about the true masses on the basis of the ones obtained in one experiment. We will be interested in the mean values of the ensemble distribution, their standard deviations, skewness, as well as the correlation between masses.

6.3 Minima of Σ

Because many endpoints are given by different expressions for different mass regions, see Eqs (4.4)–(4.5), the minimisation function Σ is a composite function. For the endpoint measurements used in this paper, Σ is made up of nine individual functions, $\Sigma_{(i,j)}$, one for each of the nine regions *(i,j)*. Considered separately each function $\Sigma_{(i,j)}$ has one or more minima. For these to also be minima of the composite function ('physical minima'), they need to be situated in the region of validity ('home region') *(i,j)* of the corresponding function. Physical minima can also occur on the borders between regions, in which case they will be referred to as 'border minima'.

If the threshold endpoints are left out, there are four measurements for four masses. The clear failure of the endpoint measurements of SPS 1a (α) and (β) to comply with Eq. (4.11) already discards the three regions where these four measurements are not sufficient to determine the masses. In each of the other six regions the minima can be sought by use of the inversion formulae. Such solutions correspond to $\Sigma = 0$. In cases where no physical solutions are found in this way, border minima exist at $\Sigma > 0$, and will have to be found by a least square minimisation.

When the threshold measurement is included, the system of equations becomes overconstrained. This will give a non-uniform increase in the value of Σ, which may destroy or create minima. Another effect will be to move the minima of Σ around in mass space, possibly moving them into or out of their home regions. One way to picture the effect is to 'tune in' the new measurement by letting its uncertainty go from infinity, in which case the measurement has no effect, to the value specified in Table 4. The masses and height of each Σ minimum will then move continuously from the old to the new position.

Even though composite, Σ is continuous, so its realisations in two neighbouring regions attain the same value at their common border. Assume that the endpoint measurements

are such that one of the realisations has a minimum at the border (not a so-called border minimum). Consider first the case of no threshold measurement. Since $\Sigma = 0$, also the other realisation must have a minimum at the border. If now one of the endpoint measurements is shifted up or down, the two minima will be driven off the border and also separated in mass space. To which side of the border they move, and whether they go to the same side or not, will depend on the actual parameters. If the minima are on the same side, as is the case at (β), only one of them will be a physical minimum. If they are on opposite sides, as is the case at (α), either both will be physical minima, or neither, in which case there will be a border minimum.

This means that if a mass scenario is situated close to one of the borders, the endpoints it produces may also have been produced by a set of masses from the neighbouring region, provided the minimum there is a physical minimum.

If the threshold measurement is added, this picture is no longer exact. Since Σ does not vanish at the minimum, the two regions will in general no longer have a common minimum at the border. However, the threshold measurement often has less weight than the other measurements, so the above picture still has some validity: Near a border two minima will be lurking. Both, one or none may be physical minima.

6.4 SPS 1a (α)

If we neglect the threshold measurements to start with, and thereby also wait with the $\tilde{b}_1$ mass, there are for each 'experiment' two solutions. One solution is in region *(1,1)*, which is the home region of the nominal masses, and one is in region *(1,2)*. This is an example of the situation described above: SPS 1a (α) has $2m^2_{\tilde{l}_R}/(m^2_{\tilde{\chi}^0_1} + m^2_{\tilde{\chi}^0_2}) = 1.01$. If this ratio becomes less than one, the region changes, as is seen from Eq. (4.5). A reduction of $m_{\tilde{l}_R}$ by 0.7 GeV would put the mass set on the border to region *(1,2)*. In both regions the mass distributions are close to Gaussian. The ensemble means of the home region solution essentially equal the nominal values. The *(1,2)* solution has central values some 15–20 GeV below the nominal ones. Without additional information both solutions are equally good and it would not be possible to determine which one to choose. One would have to state that the SUSY masses are summarized by either the *(1,1)* set or by the *(1,2)* set.

If the non-b threshold endpoint is included as a fifth measurement in a least square minimisation, the situation changes. While a *(1,1)* minimum exists for practically all the 'experiments', the occurence of a *(1,2)* minimum is now slightly reduced to 85–90%, but it is in the Σ value of the minima the effect is most apparent. The overconstraining fifth measurement lifts the two minima asymmetrically from zero. As could be expected, the *(1,1)* minimum is more often in accordance with the data, but there is always a non-negligible *(1,2)* contribution. The difference in Σ value between a given minimum and the global minimum, $\Delta\Sigma$, is a measure of the relevance of the minimum. Table 5 shows how many minima are available, on average, for various $\Delta\Sigma$ cuts, and how these are shared between regions *(1,1)* and *(1,2)*.

If only the lowest minimum is chosen, the wrong solution is returned in 10% of the experiments. However, if two minima exist and are close in Σ value, one would have to consider both. In a certain fraction of experiments, depending on the $\Delta\Sigma$ cut, there

would thus be two solution sets, e.g. for $\Delta\Sigma \leq 1$ we will have two solutions in 12% of the experiments. Whether or not it would be possible to select one of the solutions, and preferably the correct one, hinges on other measurements. In this case, where the masses of the two sets are quite close, they might be very difficult to distinguish, by e.g. cross-section considerations.

		(1,1)			*(1,2)*		
	Nom	$\langle m \rangle$	σ	γ_1	$\langle m \rangle$	σ	γ_1
$m_{\tilde{\chi}_1^0}$	96.1	96.3	3.8	0.2	85.3	3.4	0.1
$m_{\tilde{l}_R}$	143.0	143.2	3.8	0.2	130.4	3.7	0.1
$m_{\tilde{\chi}_2^0}$	176.8	177.0	3.7	0.2	165.5	3.4	0.1
$m_{\tilde{q}_L}$	537.2	537.5	6.1	0.1	523.2	5.1	0.1
$m_{\tilde{b}_1}$	491.9	492.4	13.4	0.0	469.6	13.3	0.1
$m_{\tilde{l}_R} - m_{\tilde{\chi}_1^0}$	46.92	46.93	0.28	0.0	45.08	0.72	-0.2
$m_{\tilde{\chi}_2^0} - m_{\tilde{\chi}_1^0}$	80.77	80.77	0.18	0.0	80.18	0.29	-0.1
$m_{\tilde{q}_L} - m_{\tilde{\chi}_1^0}$	441.2	441.3	3.1	0.0	438.0	2.7	0.0
$m_{\tilde{b}_1} - m_{\tilde{\chi}_1^0}$	395.9	396.2	12.0	0.0	384.4	12.0	0.1

Table 6: SPS 1a (α): Minima for $\Delta\Sigma \leq 1$ in regions *(1,1)* and *(1,2)*. Ensemble means, $\langle m \rangle$, and root-mean-square distances from the mean, σ, are in GeV. The three lightest masses are very correlated. The mass of $\tilde{q}_L$ is fairly correlated to the lighter masses, but $m_{\tilde{b}_1}$ is essentially uncorrelated. The distributions are very close to symmetric.

The upper part of Table 6 shows the ensemble means of the masses, $\langle m \rangle$, the root-mean-square distances from the mean, σ, and skewness γ_1[4] of the two solutions for $\Delta\Sigma \leq 1$. The values are relatively stable with respect to the $\Delta\Sigma$ cut: The same table for $\Delta\Sigma \leq 99$ would for *(1,1)* show a decrease in the masses by 0.1–0.2 GeV, and for *(1,2)* an increase by 1–1.3 GeV.

	# Minima	*(1,1)*	*(1,2)*
$\Delta\Sigma \leq 0$	1.00	90%	10%
$\Delta\Sigma \leq 1$	1.12	94%	17%
$\Delta\Sigma \leq 3$	1.30	97%	33%
$\Delta\Sigma \leq 99$	1.88	99%	88%

Table 5: Number of minima for various $\Delta\Sigma$ cuts and their whereabouts.

The inclusion of the threshold measurement has very little effect on the ensemble values of the *(1,1)* solution. For the *(1,2)* solution, to better comply with the additional measurement, the masses have increased, and are now 10–15 GeV below the nominal ones. Also the m_{bll} threshold was included in the fit which returned the values of Table 6. It is measured with much less precision than the other endpoints, so its inclusion has practically no effect on the other masses, only on $m_{\tilde{b}_1}$, for which it is the only measurement here.

The fact that the ensemble means of *(1,1)* reproduce the nominal values, relates to the good average performance of the ensemble of experiments. The probability of doing well with only one experiment relies in addition on the spread of the ensemble values, given by σ. For SPS 1a (α) the high precision of the endpoint measurements translates into rather small σ values. From the table we see e.g. that in $\sim 68\%$ of the experiments the mass of $\tilde{\chi}_1^0$ from the *(1,1)* solution will lie within 3.8 GeV of the nominal value. The root-mean-square

[4]Skewness is defined by $\gamma_1 = \mu_3/(\mu_2)^{3/2} = \mu_3/\sigma^3$, where $\mu_i = (x - \bar{x})^i$ is the i^{th} moment about the mean.

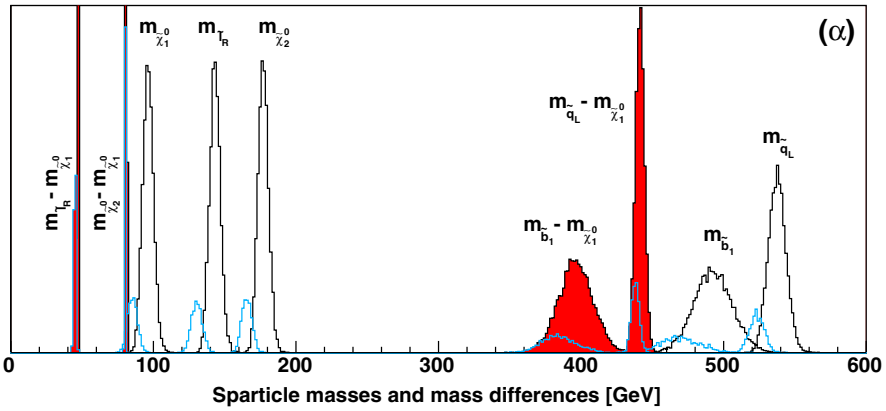

Figure 15: Sparticle masses and mass differences at SPS 1a (α) for solutions with $\Delta\Sigma \leq 1$. The unfilled distributions in black show from left to right $m_{\tilde{\chi}_1^0}$, $m_{\tilde{l}_R}$, $m_{\tilde{\chi}_2^0}$, $m_{\tilde{b}_1}$ and $m_{\tilde{q}_L}$ for solutions in the nominal region *(1,1)*. We will have such a solution in 94% of the experiments, see Table 5. The unfilled distributions in blue show the same masses for solutions in region *(1,2)*. Such a solution occurs in 17% of the experiments, and the masses returned are lower. The smaller rate of the *(1,2)* solutions is reflected in the smaller area under the blue curves. The ratio of probabilities between *(1,2)* and *(1,1)* solutions is $17\%/94\% = 18\%$. The area under one of the blue curves is 18% of the area under the corresponding black curve. The filled distributions show from left to right $m_{\tilde{l}_R} - m_{\tilde{\chi}_1^0}$, $m_{\tilde{\chi}_2^0} - m_{\tilde{\chi}_1^0}$, $m_{\tilde{b}_1} - m_{\tilde{\chi}_1^0}$ and $m_{\tilde{q}_L} - m_{\tilde{\chi}_1^0}$. Again, the most populated distributions (black curves) are for solutions in region *(1,1)*, the least populated (blue curves) for *(1,2)* solutions. For mass differences there is more overlap between the *(1,1)* and *(1,2)* solutions, in particular for $m_{\tilde{l}_R} - m_{\tilde{\chi}_1^0}$ and $m_{\tilde{\chi}_2^0} - m_{\tilde{\chi}_1^0}$, of which only the lower parts of the distributions are visible. Mass differences are better determined than the masses themselves, reflected here by the narrower distributions of the former. The exception is $m_{\tilde{b}_1}$ which largely decouples from the other masses.

distances from the ensemble means are in principle unknown, as seen from one experiment. They can however be approximated by the procedure of simulating 10^4 experiments, where the measured values play the role as 'nominal'. This will engender a systematic shift, but σ and any skewness should be fairly well approximated. The root-mean-square distances from the mean values also have their counterparts in the 1σ errors returned by the fit of each 'experiment'. To within a few percent they are found to be identical. This means that this information is available for the experiment actually performed. One can then make the inverse statement: For a given experiment one can with $\sim 68\%$ confidence state that the nominal value of $m_{\tilde{\chi}_1^0}$ lies within 3.8 GeV of the mass returned.

Due to the way masses enter in the endpoint expressions, the fit returns masses which have a strong positive correlation. If one mass is low at the minimum of the Σ function, so the others tend to be and by a similar amount. In the lower part of Table 6 ensemble mean and root-mean-square values of mass differences are shown. It is clear that the three lightest sparticles are very correlated. Fix one and the others are given very accurately. The

squark masses are less correlated. Also the results in region *(1,2)* are closer to *(1,1)* and the nominal ones when considering mass differences. Fig. 15 shows the ensemble distributions corresponding to Table 6.

Because of this strong correlation between the masses, not only the mean values and their 1σ uncertainties, but the entire error matrix should be considered if one wants to use the result obtained by this method as input for other analyses.

A less involved solution would be to use less dependent variables, e.g. $m_{\tilde{\chi}_1^0}$ to set the scale, then differences for the remaining masses, $m_{\tilde{l}_R} - m_{\tilde{\chi}_1^0}$, $m_{\tilde{\chi}_2^0} - m_{\tilde{\chi}_1^0}$, $m_{\tilde{q}_L} - m_{\tilde{\chi}_1^0}$ and $m_{\tilde{b}_1} - m_{\tilde{\chi}_1^0}$.

Due to the high cross-section, most of the endpoints are determined with high precision, which in turn gives narrow and approximately symmetric ensemble distributions. The masses are thus determined with quite high precision. As a result of the strong correlations between in particular the lighter masses, even better estimates can be obtained for other combinations of the variables, e.g. mass differences. At SPS 1a (α) there is however a fair chance that two sets of masses do equally well in the minimisation procedure. Other considerations must in that case be made in order to choose between them, or both must be kept.

6.5 SPS 1a (β)

In combination with the theory plots of Section 4 we found in Section 5 that the $m_{ql(\mathrm{high})}^{\mathrm{max}}$ value of (β) would most probably on the average be underestimated by 11–13 GeV. We will find that this has a dramatic effect on the masses returned. However, for easier comparison with nominal values we first consider the situation without such a systematic effect. Then, afterwards, the impact of the mismeasurement will be shown, together with a way to mend the situation.

As in the previous case we start out without the threshold measurement. Also here two solutions are available for all 'experiments', one in *(1,1)*, the other in either *(1,2)* or *(1,3)*. The nominal region for (β) is *(1,2)*, but it is quite close to *(1,3)*. This becomes clear from an inspection of the 'border parameter',

$$b = \frac{m_{\tilde{l}_R}^2}{m_{\tilde{\chi}_1^0}\, m_{\tilde{\chi}_2^0}}, \tag{6.4}$$

which is 1 on the border between these two regions. For (β) we have $b = 1.02$. If $m_{\tilde{l}_R}$ is reduced by 2.5 GeV, this ratio becomes unity and the the mass set sits on the border, see Eq. (4.5). The other point, (α), was near the border between *(1,1)* and *(1,2)*. There, both solutions (or none) were available. Here, the derivatives of Σ are such that only one of the two solutions is available. In 71% of the cases we get *(1,2)*, in 29% we get *(1,3)*. While the 'low-mass' solution, *(1,2)* or *(1,3)*, is in the vicinity of the nominal masses, the *(1,1)* solution, which is always present, usually sits at much higher masses, $\langle m_{\tilde{\chi}_1^0} \rangle = 514$ GeV. Because the two solutions are so separated one may hope that the incorrect one will be sufficiently disfavoured by other measurements, e.g. cross-sections, that it can be discarded.

For (α) the solution in the nominal region on the average reproduced the nominal values to within 0.2–0.5 GeV. Here the *(1,2)*/*(1,3)* solution has a mean of $m_{\tilde{\chi}_1^0}$ at 183 GeV,

some 22 GeV above the nominal value. The most probable value of the ensemble distribution is much closer to the nominal value. The distributions are infested with considerable skewness. On the way from endpoint measurement to mass determination a systematic effect which favours higher masses has been introduced. In statistical language our *estimators* of the true masses are not *consistent*: they do not converge to the nominal values. This of course has implications for the interpretation of the masses we obtain. What can be said about the true masses on the basis of the measured ones? We will return to the reasons for the skewness later.

When the threshold measurement is included, the *(1,1)* minimum usually yields a large Σ value. Only in a small fraction of the experiments does it challenge the other minima. In the other sector there is either one minimum, positioned in *(1,2)*, *(1,3)* or on the border (B), or there are two minima, in *(1,2)* and *(1,3)*. These minima are usually in good agreement with the threshold measurement and have low Σ values.

			1 sol			2 sol
	# Min	*(1,1)*	*(1,2)*	*(1,3)*	B	*(1,2)*&*(1,3)*
$\Delta\Sigma \leq 0$	1.0	3%	60%	25%	12%	0%
$\Delta\Sigma \leq 1$	1.2	5%	52%	18%	12%	16%
$\Delta\Sigma \leq 3$	1.4	13%	46%	14%	12%	28%
$\Delta\Sigma \leq 99$	2.3	99%	41%	13%	12%	34%

Table 7: SPS 1a (β): Average number of minima and the fraction of experiments with the specified solution types, for different $\Delta\Sigma$ cuts.

Table 7 shows the average number of minima for different Σ cuts. The three rightmost sections show the fraction of experiments which have the specified solution type. The two rightmost sections exclude one another. Either there is one solution in the low-mass sector, or there are two. For the one-solution case the whereabouts of the minimum is also shown. The home region of the nominal masses, *(1,2)*, is seen to dominate. As it may well be possible to discard the *(1,1)* minimum on the basis of other observations, it is logically separated from the low-mass minima. E.g. in 13% of the cases, regardless of the low-mass solution type, there is a *(1,1)* minimum at $\Delta\Sigma \leq 3$. To get the average number of minima shown in column 2, sum horizontally, adding twice the two-solution percentage. For small $\Delta\Sigma$ cuts the two rightmost sectors do not add up to 1. This simply means that in some cases the global minimum lies in *(1,1)*, and no low-mass minimum is available in the given $\Delta\Sigma$ range. For the current set of endpoint measurements the *(1,1)* contamination is seen to be very moderate. However, the systematic fit error (column 6 of Table 4) is here assumed to be zero. If it should become impossible to obtain the threshold value with such optimistic precision, the fraction of *(1,1)* solutions at low Σ will grow rapidly.

In Table 8 $\langle m \rangle$, σ and γ_1 of the ensemble masses and mass differences are shown for the different solution types and the cut $\Delta\Sigma \leq 1$. The masses of the *(1,1)* solution are much higher than what the low-mass minima give. Even though the distributions are broad, allowing for low values to occur, it is very rare that the masses stretch down to the low-mass sector. In section 4 of the table the low-mass one-solution values are shown. Since

					1 solution			2 solutions					
		(1,1)			*(1,2)*/*(1,3)*/B			*(1,2)*			*(1,3)*		
	Nom	$\langle m \rangle$	σ	γ_1	$\langle m \rangle$	σ	γ_1	$\langle m \rangle$	σ	γ_1	$\langle m \rangle$	σ	γ_1
$\tilde{\chi}_1^0$	161	438	88	0.9	175	35	1.0	161	22	0.3	166	27	0.6
$\tilde{l}_R$	222	518	85	0.7	236	37	0.8	221	24	0.3	223	28	0.5
$\tilde{\chi}_2^0$	299	579	85	0.7	313	35	1.0	299	22	0.3	304	27	0.6
$\tilde{q}_L$	826	1146	104	0.8	843	44	0.9	826	30	0.3	835	36	0.5
$\tilde{l}_R - \tilde{\chi}_1^0$	61	81	1.8	−0.3	61	4.4	0.4	61	1.9	−0.2	57	1.3	−0.2
$\tilde{\chi}_2^0 - \tilde{\chi}_1^0$	138	141	0.9	0.1	138	0.6	0.2	138	0.5	0.0	138	0.5	0.0
$\tilde{q}_L - \tilde{\chi}_1^0$	665	708	17	0.1	668	10	0.5	665	9	0.1	669	10	0.2

Table 8: SPS 1a (β): Nominal masses ('Nom') and $\Delta\Sigma \leq 1$ ensemble distribution values for the three solution types. High-mass sector: The *(1,1)* solutions return masses far beyond the nominal values. Low-mass sector: For the one-solution case the values are based on the common distribution of *(1,2)*, *(1,3)* and border (B) solutions. In the two-solution case the ensemble variables of both solutions are shown. Ensemble means, $\langle m \rangle$, and root-mean-square values, σ, are in GeV.

in such a case only one acceptable solution is available (discarding *(1,1)*), and since (β) anyway is situated close to the border, it makes sense to show the combined distribution of the *(1,2)*, *(1,3)* and border (B) minima. From Table 7 this situation is seen to occur in 52%+18%+12%=82% of the experiments. The mean values of the masses lie some 15 GeV above the nominal ones. This is an improvement compared to the non-threshold situation, but it remains an undesirable feature. The mass distributions are skewed and the most probable value is found close to the nominal value. The root-mean-square values of the ensemble distributions are large, nearly an order of magnitude larger than at (α).

The rightmost sections show the values for the two-solution type. The ensemble means of the two distributions do not differ too much, and they are much closer to the nominal values than is the case for the one-solution type. Since the values are rather close, it will probably be quite difficult to find other measurements which favours one of the sets. On the other hand, since the root-mean-square values are larger than the differences between the two solutions (also within one experiment), taking the average value, perhaps somehow weighted with the Σ value, might be a possible compromise.

Again, the mass correlation is very strong. This is evident from the lower part of Table 8, where the ensemble distributions of mass differences come with much smaller root-mean-square distance to the mean values than what the masses themselves do. They are also very close to the nominal values. Even more seems to be gained by using mass differences here than at (α). Fig. 16 shows the ensemble distributions for the masses of all solutions with $\Delta\Sigma \leq 1$ and which lie in the regions *(1,2)*, *(1,3)* or on their common border. See figure caption for details.

Skewness

The ensemble distributions are not symmetric. While the most probable values are close to the nominal values, the means lie above. For (α) the tendency of such an asymmetry is

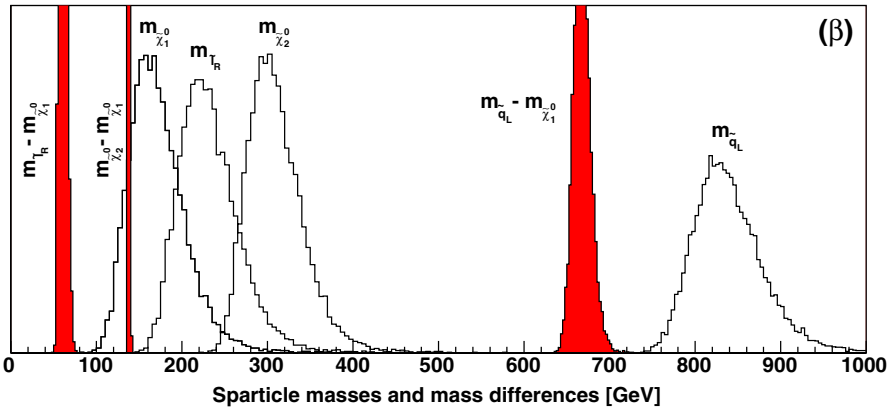

Figure 16: Sparticle masses and mass differences at SPS 1a (β). All masses of solutions with $\Delta\Sigma \leq 1$ which lie in regions *(1,2)*, *(1,3)* and on their common border are shown. From left to right the unfilled distributions show $m_{\tilde{\chi}_1^0}$, $m_{\tilde{l}_R}$, $m_{\tilde{\chi}_2^0}$ and $m_{\tilde{q}_L}$. The filled distributions show the narrower mass differences $m_{\tilde{l}_R} - m_{\tilde{\chi}_1^0}$, $m_{\tilde{\chi}_2^0} - m_{\tilde{\chi}_1^0}$ and $m_{\tilde{q}_L} - m_{\tilde{\chi}_1^0}$. Skewness of mass distributions is visible.

small, but for (β) the effect is large. The reason why we naively would expect a symmetric distribution around the nominal masses in the first place, is that the endpoint measurements are generated symmetrically. For complex functions like Eqs. (4.13)–(4.36) symmetric fluctuation of the endpoint arguments will produce near-symmetric variation of the function only for small fluctuations. As the arguments fluctuate more, the deviation from symmetry in the function values grows. At (α) the endpoint fluctuations are so small that the effect is negligible. For (β), where the endpoint fluctuations are larger, the effect of the 'asymmetric propagation' is a noticeable increase of 3–4 GeV for the ensemble means.

This is however not sufficient to explain the low-mass $\langle m_{\tilde{\chi}_1^0} \rangle$ of 183 and 173 GeV ($\Delta\Sigma \leq 99$) without and with the threshold measurement, respectively. 'Border effects' need to be considered. As described earlier, (β) lies in *(1,2)* but close to the border to *(1,3)*. First consider the situation without the threshold measurement. There is then always only one low-mass solution. If the *(1,2)* solution is physical, i.e. lies in *(1,2)*, then the true minimum of $\Sigma_{(1,3)}$ also lies in region *(1,2)* and so is unphysical, and vice versa, as described in Sect. 6.3.

In Fig. 17 the mass of $\tilde{\chi}_1^0$ is plotted as a function of the border parameter, b, of Eq. (6.4), for both physical and unphysical minima of $\Sigma_{(1,2)}$ and $\Sigma_{(1,3)}$. The minima of $\Sigma_{(1,2)}$ are shown in red, from upper right to lower left. The $\Sigma_{(1,3)}$ solutions are in blue. Filled boxes are physical solutions, i.e. $\Sigma_{(1,2)}$ (red) for $b > 1$ and $\Sigma_{(1,3)}$ (blue) for $b < 1$. Empty boxes are unphysical solutions. An asymmetry arises from the accidental fact that for both functions the lower masses tend to lie in the unphysical region. The average of the entire $\Sigma_{(1,2)}$ distribution, both physical and unphysical minima, returns 164 GeV, the nominal value plus the 3 GeV of the asymmetric propagation effect. It is then obvious that

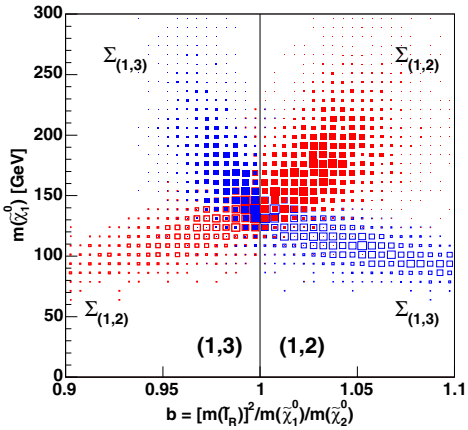

Figure 17: Border effect between region *(1,2)* and *(1,3)*; the mass of $\tilde{\chi}_1^0$ as a function of the border parameter b, see Eq. (6.4), demonstrating border effects. Filled boxes represent physical solutions, empty boxes represent unphysical solutions.

when the unphysical *(1,2)* solutions are replaced by the physical *(1,3)* solutions which lie at higher masses, the ensemble mean increases. Here, this effect brings the average value for $m_{\tilde{\chi}_1^0}$ to 183 GeV, an additional increase of nearly 20 GeV.

When the threshold measurement is added, the border effect is reduced, giving an average value of 173 GeV (for one solution). This is because a measurement will, unless there is any bias, on the average be conservative. It will try to keep the masses at their nominal values. Here, as the border effect is pushing the masses upwards, away from the nominal values, the threshold is holding back.

If, in a realistic situation, a set of endpoints has been measured, and the resulting set of masses is found to lie close to a border, caution should be exercised. Ad hoc procedures seem necessary for such a case. At least one is in a position to be aware of the danger. It is probably appropriate to consider unphysical minima as well.

Mismeasured $m_{ql\,(\mathrm{high})}^{\mathrm{max}}$

As pointed out at the start of this subsection it is very likely that, for (β), $m_{ql\,(\mathrm{high})}^{\mathrm{max}}$ will be understimated by 11–13 GeV. Without the threshold measurement, the effect of this as returned by the inversion formulae, is an increase of 50 GeV for the three lightest masses and 60 GeV for the squark! If the threshold measurement is included, the effect is reduced to 30–40 GeV for the lighter masses, depending on the solution type, and 40–55 GeV for the squark. The increase is still surprisingly large and represents a serious threat to the applicability of the method in the case where the nominal masses happen to sit near a border. (Not to be confused with the previously mentioned border effect.)

It may however be possible to discover afterwards that such a mismeasurement has or may well have been made. If the masses obtained are used to generate the corresponding theory distributions, one may spot the problem. A quick test showed that in our case the $m_{ql(\text{high})}$ theory distribution as generated with the obtained masses, did have a small foot. This is then a sign that the original $m^{\max}_{ql(\text{high})}$ measurement may have been wrong, since no such foot was seen and included in the fit. This test probably has quite wide applicability. The reason is that even though, as we have seen, the masses may change a lot in the case of a mismeasured $m^{\max}_{ql(\text{high})}$, mass *differences* are not so far off the nominal values. The main change is therefore in the overall scale. For theory distributions, the shapes are independent of the overall scale. Only mass ratios are relevant. The theory shapes based on the masses obtained from the partly mismeasured endpoints, will therefore usually not deviate too much from the nominal shapes.

If one is certain that a mismeasurement has been made, either from the test described above or from other considerations, not only does one know that the $m^{\max}_{ql(\text{high})}$ measurement is not to be trusted. There is also a way to pursue the matter further. It relies on the fact that the vertical fall we see and measure, is the endpoint of the $m_{ql_{\text{n}}}$ distribution. We have the explicit expression for this endpoint, and so we can just replace the $m^{\max}_{ql(\text{high})}$ expression and redo the least square minimisation.

At SPS 1a (β) many new aspects of the endpoint method have emerged. For a large fraction of the experiments a total of three minima were competing for a given set of endpoint values, some returning masses near the nominal values, some returning much higher masses. A generic characteristic is the skewness of the ensemble distributions. The problems and the causes of the asymmetry have been discussed, but a way to handle the asymmetry has not been proposed. The ensemble distributions are much broader than at SPS 1a (α). Mass differences are however quite precisely determined. The problem of mismeasuring $m^{\max}_{ql(\text{high})}$, which will be a danger in a large fraction of mass space, has been discussed and a solution proposed. Throughout, we have also seen that the inclusion of a fifth measurement in general improves on the results.

7. Linear Collider inputs

As compared with the LHC, the Linear Collider [48, 49] will more directly provide very precise measurements of the lightest neutralino mass (and possibly also the second lightest). Thus, the LC input fixes the scale, whereas the cascade decays primarily provide mass differences. This kind of input, if it becomes available during the analysis of LHC data, will have a dramatic influence on the over-all analysis [27].

To each LHC experiment a corresponding Linear Collider experiment is considered. The Linear Collider measurement of the LSP, $m^{\text{LC}}_{\tilde{\chi}^0_1}$, was for every experiment picked randomly from a Gaussian distribution of mean equal to $m^{\text{nom}}_{\tilde{\chi}^0_1}$, and standard deviation set by the expected uncertainty, $\sigma^{\text{LC}}_{m_{\tilde{\chi}^0_1}}$. We used $\sigma^{\text{LC}}_{m_{\tilde{\chi}^0_1}} = 0.05$ GeV, in accordance with [48]. Such a small uncertainty practically means fixing the mass at the nominal value. Still, for

completeness the measurement was appropriately included in the least square minimisation by adding the term $[(m_{\tilde{\chi}_1^0} - m^{\rm LC}_{\tilde{\chi}_1^0})/\sigma^{\rm LC}_{m_{\tilde{\chi}_1^0}}]^2$ to the Σ function, Eq. (6.2).

		1 sol			2 sol
	# Min	*(1,2)*	*(1,3)*	B	*(1,2)&(1,3)*
$\Delta\Sigma \leq 0$	1.0	65%	26%	9%	0%
$\Delta\Sigma \leq 1$	1.2	52%	18%	9%	21%
$\Delta\Sigma \leq 3$	1.4	36%	10%	9%	45%
$\Delta\Sigma \leq 99$	1.6	24%	7%	9%	59%

Table 9: Number of minima for SPS 1a (β) with LC input.

For (α) the fixing of $m_{\tilde{\chi}_1^0}$ reduces the occurrences of multiple minima to the per mille level for any usable minima, $\Delta\Sigma \leq 3$. In nearly all cases, 98-99%, it is the home region *(1,1)* minimum which survives. This seems reasonable since without the LC measurement the *(1,2)* minimum has $\langle m_{\tilde{\chi}_1^0} \rangle$ at some 10 GeV below the nominal value, see Table 6.

At (β) the high-mass minimum *(1,1)* is absent, disfavoured as it is by the Linear Collider measurement. The number of *(1,3)* minima has increased, which is reflected in an increase of the two-solution case, compare Tables 7 and 9. For small $\Delta\Sigma$ cuts this increase is not drastic. Fixing $m_{\tilde{\chi}_1^0}$ thus does not help us to uniquely determine one minimum, contrary to what one might have expected.

		(1,1)	
	Nom	$\langle m \rangle$	σ
$\tilde{\chi}_1^0$	96.05	96.05	0.05
$\tilde{l}_R$	142.97	142.97	0.29
$\tilde{\chi}_2^0$	176.82	176.82	0.17
$\tilde{q}_L$	537.25	537.2	2.5
$\tilde{b}_1$	491.92	492.1	11.7

Table 10: The SPS 1a (α) masses with LC input. All values in GeV. Region *(1,2)* solutions now occur only in $\sim 1\%$ of the cases and are left out.

The Tables 10–11 show the mean and root-mean-square values of the ensemble distributions at (α) and (β). For both SUSY scenarios the ensemble means fall very close to the nominal masses, even for minima not situated in the nominal home region. The uncertainty on the scale, which for the LHC alone is the main contribution to the spread of the ensemble distributions, is set to zero by the LC measurement. The root-mean-square values are therefore strongly reduced. Without Linear Collider measurements, the mass differences were more accurately determined in that they were less dependent on the mass scale. A comparison of the root-mean-square values of the masses in Tables 10–11 with the root-mean-square values of the mass differences in Tables 6–8 shows to which extent mass differences are scale independent variables. When a Linear Collider measurement is available, the mass differences no longer out-perform the masses themselves in terms of precision. With the fixing of the scale also the skewness of the distributions has vanished.

8. Conclusions

We have investigated the measurement of supersymmetric masses from the decay chain $\tilde{q} \to \tilde{\chi}_2^0 q \to \tilde{l}_R l q \to \tilde{\chi}_1^0 l l q$, in the Snowmass mSUGRA scenario SPS 1a. Since the lightest

		1 solution		2 solutions			
		(1,2)/(1,3)/B		*(1,2)*		*(1,3)*	
	Nom	$\langle m \rangle$	σ	$\langle m \rangle$	σ	$\langle m \rangle$	σ
$\tilde{\chi}_1^0$	161.02	161.02	0.05	161.02	0.05	161.02	0.05
$\tilde{l}_R$	221.86	221.15	3.26	222.22	1.32	217.48	1.01
$\tilde{\chi}_2^0$	299.05	299.15	0.57	299.11	0.53	299.05	0.52
$\tilde{q}_L$	826.29	826.1	6.3	825.9	5.8	828.6	5.5

Table 11: The SPS 1a (β) masses with LC input. Nominal, ensemble averages, $\langle m \rangle$, and root-mean-square deviations from the mean, σ, are all in GeV.

neutralino $\tilde{\chi}_1^0$ is the LSP in most interesting mSUGRA scenarios, it will escape detection and only the quark and two leptons are available for the construction of invariant mass distributions. Nevertheless, the kinematic endpoints of these distributions have a well defined dependence on the masses of the particles in the decay chain and their measurement allows the extraction of the masses either by analytic inversion or numerical fit. The analytic expressions for the endpoints in terms of the masses were confirmed and presented together with their analytic inversions.

In order to measure the endpoints of the invariant mass distributions pertaining to the chosen decay chain, one must have the correct mass hierarchies for the decay chain and a large enough cross-section. To ensure that this decay chain could be used over a wide range of scenarios, we performed a scan over the SUSY parameters. We found that as long as m_0 was not too large in comparison to $m_{1/2}$, a large proportion of the allowed parameter space would display the correct mass hierarchy. Furthermore, on examination of the sparticle production cross-sections and decay branching ratios we found that a large cross-section for the decay was available over much of this region. The Snowmass mSUGRA SPS 1a line/point falls into this region and is a good candidate for study. However, we noted that the cross-section for the decay chain is particularly high for the SPS 1a point, and it is instructive to examine a second point on the SPS 1a line with a less optimistic cross-section. We have denoted this new point as SPS 1a (β) while the original point became SPS 1a (α).

The LHC measurements of the endpoints were simulated using PYTHIA and ATLFAST. Hard kinematic cuts remove practically all Standard Model backgrounds, except $t\bar{t}$. Up to statistical fluctuations the powerful different-flavour subtraction then cancels the remaining $t\bar{t}$ as well as any lepton-uncorrelated background from other SUSY channels. The resulting distributions are however contaminated by lepton-correlated background from $\tilde{\chi}_2^0$'s not taking part in the decay chain under study and combinatorial background from choosing the wrong jet. The inconsistency cut was shown to address the latter part with great efficiency, giving distributions much closer to the theoretical ones. Also mixed events were studied, revealing their potential to describe the background. More study is however needed.

The endpoints were found by simplistic fitting of the edges, usually with a straight line together with a reasonable background estimate. A Gaussian smearing was sometimes included as a first approximation of the various smearing effects which take place. The

statistical precision of the edge was sought rather than an accurate determination of the endpoint. Still, the endpoints were seen to be in reasonably good agreement with the nominal values. However, the fitting procedure is clearly an area for improvement. On one hand, more realistic study of how the detector affects the distributions, and in particular the end regions, is called for. On the other hand, further study of the many realisations of the theory curves seems necessary. It is important to find good fit functions for the signal. A central part of such a programme is the incorporation of multiple squark masses at different rates. At a less ambitious scale the theory distributions should be studied for sheer acquaintance. The importance of such an awareness was demonstrated for the $m^{\max}_{ql(\text{high})}$ measurement at (β).

In order to turn the endpoint measurements into particle masses, and understand the resulting errors of this procedure, we considered an ensemble of 10,000 'gedanken' experiments. For each experiment a numerical fit for the particle masses was performed, using the method of least squares, thus appropriately handling the correlation between measurements due to the common jet energy scale error. Where available the analytic expressions for the masses in terms of the endpoints were used to provide starting points for the fits.

The least squares function was found to often have two or even three minima of comparable importance, a consequence of the multiple realisations for many of the endpoints. Without the threshold measurement there are for both scenarios usually two equally good minima, one in the correct region and one in another region, giving different masses. When the threshold endpoint is added, the minimum in the correct region is usually preferred. Still, in a noticeable fraction of experiments there will be more than one solution. Due to less precise measurements this applies more to (β) than to (α).

At (α) the minima of the correct region give masses very close to the nominal ones. The other (incorrect) region gives masses some 10–15 GeV lower. The ensemble distributions are symmetric. At (β) there is one high-mass solution. The more precisely the threshold endpoint is determined, the less important this false minimum becomes. The low-mass solutions, one or two, are closer to the nominal values, but the distributions are skewed. This is a combined effect of the large endpoint uncertainties and the so-called border effect.

The obtained masses of the three lightest particles are found to be very strongly related. Furthermore it was seen that mass differences are better variables, in the sense that they are less correlated than the masses themselves. Due to the form of the endpoint expressions, the LHC will measure mass differences at high precision, but leave the overall scale less certain. A Linear Collider measurement of the LSP mass effectively sets the scale, which is why the precision of the masses improve drastically when the LHC and the Linear Collider measurements are combined.

Acknowledgments

This work has been performed partly within the ATLAS Collaboration, and we thank collaboration members for helpful discussions. We have made use of the physics analysis framework and tools which are the result of collaboration-wide efforts. It is a great

pleasure to thank Giacomo Polesello for his contributions in the early stages of this work, and continued interest and advice. BKG would like to thank Steinar Stapnes for useful discussions. DJM would like to thank Ben Allanach for useful discussions. This research has been supported in part by the Research Council of Norway.

References

[1] S. Weinberg, Phys. Rev. D **13** (1976) 974; Phys. Rev. D **19** (1979) 1277; L. Susskind, Phys. Rev. D **20** (1979) 2619; G. 't Hooft, in *Recent developments in gauge theories*, Proceedings of the NATO Advanced Summer Institute, Cargese 1979, ed. G. 't Hooft *et al.* (Plenum, New York 1980).

[2] P. Fayet and S. Ferrara, Phys. Rept. **32** (1977) 249.

[3] S. Dimopoulos and H. Georgi, Nucl. Phys. B **193** (1981) 150.

[4] H. P. Nilles, Phys. Rept. **110** (1984) 1.

[5] H. E. Haber and G. L. Kane, Phys. Rept. **117** (1985) 75.

[6] R. Haag, J. T. Lopuszanski and M. Sohnius, Nucl. Phys. B **88** (1975) 257.

[7] M. B. Green, J. H. Schwarz and E. Witten, "Superstring Theory. Vol. 1: Introduction," Cambridge University Press (1987) (Cambridge Monographs On Mathematical Physics).

[8] N. Sakai and T. Yanagida, Nucl. Phys. B **197** (1982) 533.

[9] K. Inoue, A. Kakuto, H. Komatsu and S. Takeshita, Prog. Theor. Phys. **68** (1982) 927 [Erratum-ibid. **70** (1983) 330]; Prog. Theor. Phys. **71** (1984) 413.

[10] N. K. Falck, Z. Phys. C **30** (1986) 247.

[11] L. E. Ibanez and G. G. Ross, Phys. Lett. B **110** (1982) 215.

[12] L. E. Ibanez, Phys. Lett. B **118** (1982) 73.

[13] J. R. Ellis, D. V. Nanopoulos and K. Tamvakis, Phys. Lett. B **121** (1983) 123.

[14] L. Alvarez-Gaume, J. Polchinski and M. B. Wise, Nucl. Phys. B **221** (1983) 495.

[15] H. Goldberg, Phys. Rev. Lett. **50** (1983) 1419;
L. M. Krauss, Nucl. Phys. B **227** (1983) 556;
J. R. Ellis, J. S. Hagelin, D. V. Nanopoulos, K. A. Olive and M. Srednicki, Nucl. Phys. B **238** (1984) 453.

[16] F. Gianotti, New J. Phys. **4** (2002) 63.

[17] B. C. Allanach, G. A. Blair, S. Kraml, H. U. Martyn, G. Polesello, W. Porod and P. M. Zerwas, arXiv:hep-ph/0403133.

[18] A. H. Chamseddine, R. Arnowitt and P. Nath, Phys. Rev. Lett. **49** (1982) 970.

[19] V. M. Lobashev *et al.*, Phys. Lett. B **460** (1999) 227.

[20] ATLAS Collaboration, *ATLAS Detector and Physics Performance Technical Design Report 2.* No. CERN-LHCC-99-014 ATLAS-TDR-14. May, 1999.

[21] B. C. Allanach *et al.*, in *Proc. of the APS/DPF/DPB Summer Study on the Future of Particle Physics (Snowmass 2001)* ed. N. Graf, Eur. Phys. J. C **25** (2002) 113 [eConf **C010630** (2001) P125] [arXiv:hep-ph/0202233].

[22] H. Baer, C. h. Chen, F. Paige and X. Tata, Phys. Rev. D **53** (1996) 6241 [arXiv:hep-ph/9512383].

[23] I. Hinchliffe, F. E. Paige, M. D. Shapiro, J. Soderqvist and W. Yao, Phys. Rev. D **55** (1997) 5520 [arXiv:hep-ph/9610544].

[24] I. Hinchliffe, F. E. Paige, E. Nagy, M. D. Shapiro, J. Soderqvist and W. Yao, LBNL-40954

[25] H. Bachacou, I. Hinchliffe and F. E. Paige, Phys. Rev. D **62** (2000) 015009 [arXiv:hep-ph/9907518].

[26] G. Polesello, *Precision SUSY measurements with ATLAS for SUGRA point 5*, ATLAS Internal Note, PHYS-No-111, October 1997.

[27] G. Weiglein *et al.* [LHC / ILC Study Group], arXiv:hep-ph/0410364.

[28] B. K. Gjelsten, E. Lytken, D. J. Miller, P. Osland, G. Polesello, *A detailed analysis of the measurement of SUSY masses with the ATLAS detector at the LHC*, ATL-PHYS-2004-007, Geneva, CERN, Jan 2004.

[29] S. Eidelman *et al.* [Particle Data Group Collaboration], Phys. Lett. B **592** (2004) 1.

[30] H. Baer, F. E. Paige, S. D. Protopopescu and X. Tata, arXiv:hep-ph/9305342, arXiv:hep-ph/0001086.

[31] B. C. Allanach, C. G. Lester, M. A. Parker and B. R. Webber, JHEP **0009** (2000) 004 [arXiv:hep-ph/0007009].

[32] C. G. Lester, *Model independent sparticle mass measurements at ATLAS*, Ph. D. thesis, http://www.slac.stanford.edu/spires/find/hep/www?r=cern-thesis-2004-003

[33] B. K. Gjelsten, D. J. Miller, P. Osland, arXiv:hep-ph/0501033

[34] J. R. Ellis, K. A. Olive and Y. Santoso, New J. Phys. **4** (2002) 32 [arXiv:hep-ph/0202110].

[35] J. R. Ellis, K. A. Olive, Y. Santoso and V. C. Spanos, Phys. Lett. B **565** (2003) 176 [arXiv:hep-ph/0303043].

[36] A. Raklev, presented at "Nordic LHC Workshop", Copenhagen, June 2004, http://hep.nbi.dk/NLHC9-NG7/

[37] J. A. Casas, A. Lleyda and C. Munoz, Nucl. Phys. B **471** (1996) 3 [arXiv:hep-ph/9507294]; S. Abel and T. Falk, Phys. Lett. B **444** (1998) 427 [arXiv:hep-ph/9810297]; D. G. Cerdeno, E. Gabrielli, M. E. Gomez and C. Munoz, JHEP **0306** (2003) 030 [arXiv:hep-ph/0304115].

[38] B. C. Allanach, in *Proc. of the APS/DPF/DPB Summer Study on the Future of Particle Physics (Snowmass 2001)* ed. N. Graf, eConf **C010630** (2001) P319 [arXiv:hep-ph/0110227].

[39] C. L. Bennett *et al.*, Astrophys. J. Suppl. **148** (2003) 1 [arXiv:astro-ph/0302207].

[40] D. N. Spergel *et al.*, Astrophys. J. Suppl. **148** (2003) 175 [arXiv:astro-ph/0302209].

[41] M. M. Nojiri, D. Toya and T. Kobayashi, Phys. Rev. D **62** (2000) 075009 [arXiv:hep-ph/0001267].

[42] B. K. Gjelsten, Ph. D. thesis, University of Oslo, 2004.

[43] P. Richardson, JHEP **0111** (2001) 029 [arXiv:hep-ph/0110108]; A. J. Barr, arXiv:hep-ph/0405052.

[44] T. Sjöstrand, P. Edén, C. Friberg, L. Lönnblad, G. Miu, S. Mrenna, E. Norrbin, Comput. Phys. Commun. 135 (2001) 238; T. Sjostrand, L. Lonnblad and S. Mrenna, "PYTHIA 6.2: Physics and manual", arXiv:hep-ph/0108264.

[45] H. L. Lai *et al.* [CTEQ Collaboration], Eur. Phys. J. C **12** (2000) 375 [arXiv:hep-ph/9903282].

[46] G. Marchesini, B. R. Webber, G. Abbiendi, I. G. Knowles, M. H. Seymour and L. Stanco, Comput. Phys. Commun. 67 (1992) 465;
G. Corcella, I.G. Knowles, G. Marchesini, S. Moretti, K. Odagiri, P. Richardson, M. H. Seymour, B. R. Webber, JHEP **0101** (2001) 010 [arXiv:hep-ph/9912396]

[47] E. Richter-Was, D. Froidevaux and L. Poggioli, "ATLFAST 2.0: a fast simulation package for ATLAS", Tech. Rep. ATL-PHYS-98-131 (1998)

[48] J. A. Aguilar-Saavedra *et al.* [ECFA/DESY LC Physics Working Group Collaboration], "TESLA Technical Design Report Part III: Physics at an e+e- Linear Collider," arXiv:hep-ph/0106315.

[49] T. Abe *et al.* [American Linear Collider Working Group Collaboration], "Linear collider physics resource book for Snowmass 2001. 1: Introduction," in *Proc. of the APS/DPF/DPB Summer Study on the Future of Particle Physics (Snowmass 2001)* ed. N. Graf, SLAC-R-570, arXiv:hep-ex/0106055.

Preprint typeset in JHEP style - HYPER VERSION

ATL-PHYS-2005-001

Measurement of the Gluino Mass via Cascade Decays for SPS 1a

B. K. Gjelsten

Department of Physics, University of Oslo, N-0316 Oslo, Norway
E-mail: B.K.Gjelsten@fys.uio.no

D. J. Miller

Department of Physics and Astronomy, University of Glasgow, Glasgow G12 8QQ, U.K.
E-mail: D.Miller@physics.gla.ac.uk

P. Osland

Department of Physics, University of Bergen, N-5007 Bergen, Norway
E-mail: Per.Osland@ift.uib.no

Abstract: If R-parity conserving supersymmetry is realised with masses below the TeV scale, sparticles will be produced and decay in cascades at the LHC. In the case of a neutral LSP, which will not be detected, decay chains cannot be fully reconstructed, complicating the mass determination of the new particles. In this paper we extend the method of obtaining masses from kinematical endpoints to include a gluino at the head of a five-sparticle decay chain. This represents a non-trivial extension of the corresponding method for the squark decay chain. We calculate the endpoints of the new distributions and assess their applicability by examining the theoretical distributions for a variety of mass scenarios. The precision with which the gluino mass can be determined by this method is investigated for the mSUGRA point SPS 1a. Finally we estimate the improvement obtained from adding a Linear Collider measurement of the LSP mass.

Keywords: SUSY, BSM, MSSM.

Contents

1. Introduction

Supersymmetry [1, 2, 3, 4] provides one of the more popular extensions to the Standard Model at higher energies. It has many attractive features, one of which is a possible solution to the hierarchy problem [5]. For this to be the case supersymmetric particles must exist near the TeV-scale, and may therefore be accessed by the LHC.

Conservation of R-parity means that any interaction vertex must involve an even number of supersymmetric fields. For collider experiments this has two important consequences: sparticles will be produced in pairs, and the decay chain of a sparticle will always end with the lightest supersymmetric particle (LSP). Each SUSY event at the LHC will then result in two decay chains, each giving an undetected LSP together with a number of detectable Standard-Model particles. The escaping LSP's make it difficult to fully reconstruct events. This means that the masses of the sparticles involved in a decay chain cannot be readily reconstructed from the end products. However, even though they do not represent any particular sparticle, the various mass distributions that can be constructed from the detectable particles of the decay do have a sensitivity to the sparticle masses. In particular, the maximum value of each of these distributions can in principle be calculated for any given decay chain, and this maximum value will be determined by the masses involved in the decay. If these kinematical endpoints are measured, it is then possible to obtain the sparticle masses in a numerical fit. This 'endpoint method' has been widely used to determine masses of supersymmetric particles [6, 7, 8, 9, 10, 11]. The decay chain

$$\tilde{q}_L \to \tilde{\chi}_2^0 q_{\rm f} \to \tilde{l}_R l_{\rm n} q_{\rm f} \to \tilde{\chi}_1^0 l_{\rm f} l_{\rm n} q_{\rm f} \tag{1.1}$$

is particularly amenable to this method[1]. In [12] we investigated this decay chain in considerable detail for two points on the SPS 1a line [13]: (α), which is the standard point and often simply referred to as 'the SPS 1a point', and (β), which lies at somewhat higher masses. In this paper we restrict ourselves to the standard SPS 1a point and investigate the situation where a gluino is at the head of the decay chain,

$$\tilde{g} \to \tilde{q}_L q_{\rm n} \to \tilde{\chi}_2^0 q_{\rm f} q_{\rm n} \to \tilde{l}_R l_{\rm n} q_{\rm f} q_{\rm n} \to \tilde{\chi}_1^0 l_{\rm f} l_{\rm n} q_{\rm f} q_{\rm n} \tag{1.2}$$

Seven more distributions become available with the inclusion of $q_{\rm n}$, and their endpoints, if measurable, will enable us to find the gluino mass. For ease of reference the new distributions/endpoints will be called 'gluino distributions/endpoints' as opposed to the 'squark distributions/endpoints' which do not involve the gluino mass.

Although very much in line with the now standard method for the masses involved in (1.1), this way of obtaining the gluino mass is new. At present two other methods are proposed. One is an approximate technique, used for example in [14]. If, in the three-body decay $\tilde{\chi}_2^0 \to \tilde{\chi}_1^0 ll$, we have m_{ll} at its maximum value, $m_{ll} = m_{ll}^{\rm max}$, then $\tilde{\chi}_1^0$ is at rest in the rest frame of $\tilde{\chi}_2^0$. Assuming $m_{\tilde{\chi}_1^0}$ known, the four-vector of $\tilde{\chi}_2^0$ can then be fully

[1] Maintaining the standard convention, the subscripts 'n' for *near* and 'f' for *far* on the leptons and quarks are used to distinguish the order of particle emission in the decay chain. These subscripts will be suppressed if there is no ambiguity.

reconstructed. Next, adding the two quark four-momenta provides us with the complete four-momentum of the gluino (and squark). This allows the mass of the gluino (and the squark) to be found in the more traditional way of plotting the mass peak. Apart from the normal experimental uncertainties this method is exact. However, to get a sizable sample, also events with m_{ll} somewhat below $m_{ll}^{\max}$ must be used. This makes the method approximate and requires a rigorous treatment of the systematic errors induced by the approximation.

For the decay chain (1.2), it is generally not the case that $\tilde{\chi}_1^0$ is at rest in the rest frame of $\tilde{\chi}_2^0$ when $m_{ll} = m_{ll}^{\max}$. Only if $m_{\tilde{l}_R}^2 = m_{\tilde{\chi}_2^0} m_{\tilde{\chi}_1^0}$ is this true, and the more this relation is violated, the less reliable the results will become. To apply this method to (1.2) the following three effects must be controlled: i) the knowledge of $m_{\tilde{\chi}_1^0}$ — this can be assumed known from the standard endpoint analysis of the squark chain, but the appropriate uncertainties must be included, ii) the systematics from the inclusion of events with $m_{ll} < m_{ll}^{\max}$, and iii) the systematics from the violation of $m_{\tilde{l}_R}^2 = m_{\tilde{\chi}_2^0} m_{\tilde{\chi}_1^0}$. A systematic treatment of all these effects is still wanting.

The other method to obtain the gluino mass from (1.2) goes under the name of the 'Mass relation method', and is described in [15]. In a first version the masses of $\tilde{\chi}_1^0$, $\tilde{l}_R$ and $\tilde{\chi}_2^0$ are assumed known, e.g. from the squark-endpoint analysis. For a given gluino-chain event we then have six unknowns: $m_{\tilde{g}}$, $m_{\tilde{q}_L}$ and the four-momentum of $\tilde{\chi}_1^0$. On-shell mass conditions for the five sparticles provide five equations. For *one* such event we are one condition short of determining the system. [If also $m_{\tilde{q}_L}$ is assumed known, the system is solvable.] A second event of the same type will again give 5 equations for 6 unknowns. Two of the unknowns, $m_{\tilde{g}}$ and $m_{\tilde{q}_L}$ are however the same for the two events. In combination one therefore has 10 equations for 10 unknowns. The system can be solved analytically to provide (in some cases multiple) masses for the gluino and the squark. The mass relation method involves no approximations of the type described for the first method, and is in this respect at the same level as the endpoint method we will use here. The mass relation method also has the advantage that it avoids the difficulties related to estimating endpoints, and it can give a measurement even for quite small number of events. On the other hand the uncertainties on the three lighter masses as well as possible correlations between the masses need to be appropriately handled. An extension of the method to take no input masses, and/or include in a consistent way measurements from an endpoint analysis should be feasible and would meet these requirements. For the endpoint method all measurements go into the same fit, so errors and correlations are automatically treated correctly.

The structure of the present paper is as follows. In Sect. 2 we review the calculation of the endpoint of the quark-dilepton invariant mass resulting from squark decay, here denoted $m_{q_t ll}^{\max}$, and present an alternative approach. This new approach is then used to calculate the 'gluino endpoints'. Also, theory distributions are plotted for the gluino distributions, showing some of the variation. Sect. 3 contains an outline of the derivation of one particular kinematical edge, it may be skipped by the reader more interested in the physics results. In Sect. 4 relevant masses, cross-sections and branching ratios of the standard SPS 1a point are given. The ATLAS simulation ending with an estimate for some of the new distributions, is carried through in Sect. 5, where also energy scale errors are

discussed in some detail. In Sect. 6 values for masses and mass differences are found. The effect of adding a Linear Collider measurement is investigated in Sect. 7, while conclusions are made in Sect. 8.

2. Endpoint calculation

2.1 Review of the squark chain

In the case of the squark decay chain (1.1) four mass distributions can in principle be constructed from the three Standard Model end-products: m_{ll}, $m_{q_{\rm f}l_{\rm n}}$, $m_{q_{\rm f}l_{\rm f}}$ and $m_{q_{\rm f}ll}$. The kinematical endpoints of these distributions can be expressed in terms of the sparticle masses involved in the cascade. If these endpoints were measured, one would have four measurements for quantities which involve four unknown masses, and the masses could be determined. In a realistic setting there is however no a priori way of telling which is which of the two leptons. Therefore, not all of these 'primary' distributions can be constructed. While m_{ll} and $m_{q_{\rm f}ll}$ are fine since there is no need for identifying the leptons, $m_{q_{\rm f}l_{\rm n}}$ and $m_{q_{\rm f}l_{\rm f}}$ are not readily usable. Instead two 'secondary' distributions are defined, $m_{q_{\rm f}l({\rm high})}$ and $m_{q_{\rm f}l({\rm low})}$. The first collects on an event by event basis the higher of the two $m_{q_{\rm f}l}$ values available, the second collects the lower. In this way four endpoint measurements are regained, and the four unknown sparticle masses can again be determined. The analytic expressions for the endpoints of the relevant distributions, as given in [10], were confirmed [12] and are included here for completeness and because some of them will be used in the discussion of the gluino endpoints:

$$\left(m_{ll}^{\rm max}\right)^2 = \left(m^2_{\tilde{\chi}^0_2} - m^2_{\tilde{l}_R}\right)\left(m^2_{\tilde{l}_R} - m^2_{\tilde{\chi}^0_1}\right)/m^2_{\tilde{l}_R} \tag{2.1}$$

$$\left(m_{q_{\rm f}ll}^{\rm max}\right)^2 = \left\{ \begin{array}{lll} \frac{\left(m^2_{\tilde{q}_L} - m^2_{\tilde{\chi}^0_2}\right)\left(m^2_{\tilde{\chi}^0_2} - m^2_{\tilde{\chi}^0_1}\right)}{m^2_{\tilde{\chi}^0_2}} & \text{for} \quad \frac{m_{\tilde{q}_L}}{m_{\tilde{\chi}^0_2}} > \frac{m_{\tilde{\chi}^0_2}}{m_{\tilde{l}_R}}\frac{m_{\tilde{l}_R}}{m_{\tilde{\chi}^0_1}} & (1) \\ \frac{\left(m^2_{\tilde{q}_L} m^2_{\tilde{l}_R} - m^2_{\tilde{\chi}^0_2} m^2_{\tilde{\chi}^0_1}\right)\left(m^2_{\tilde{\chi}^0_2} - m^2_{\tilde{l}_R}\right)}{m^2_{\tilde{\chi}^0_2} m^2_{\tilde{l}_R}} & \text{for} \quad \frac{m_{\tilde{\chi}^0_2}}{m_{\tilde{l}_R}} > \frac{m_{\tilde{l}_R}}{m_{\tilde{\chi}^0_1}}\frac{m_{\tilde{q}_L}}{m_{\tilde{\chi}^0_2}} & (2) \\ \frac{\left(m^2_{\tilde{q}_L} - m^2_{\tilde{l}_R}\right)\left(m^2_{\tilde{l}_R} - m^2_{\tilde{\chi}^0_1}\right)}{m^2_{\tilde{l}_R}} & \text{for} \quad \frac{m_{\tilde{l}_R}}{m_{\tilde{\chi}^0_1}} > \frac{m_{\tilde{q}_L}}{m_{\tilde{\chi}^0_2}}\frac{m_{\tilde{\chi}^0_2}}{m_{\tilde{l}_R}} & (3) \\ \left(m_{\tilde{q}_L} - m_{\tilde{\chi}^0_1}\right)^2 & \text{otherwise} & (4) \end{array} \right\} \tag{2.2}$$

$$\left(m_{q_{\rm f}l({\rm low})}^{\rm max}, m_{q_{\rm f}l({\rm high})}^{\rm max}\right) = \left\{ \begin{array}{lll} \left(m_{q_{\rm f}l_{\rm n}}^{\rm max}, m_{q_{\rm f}l_{\rm f}}^{\rm max}\right) & \text{for} \quad 2m^2_{\tilde{l}_R} > m^2_{\tilde{\chi}^0_1} + m^2_{\tilde{\chi}^0_2} > 2m_{\tilde{\chi}^0_1} m_{\tilde{\chi}^0_2} & (1) \\ \left(m_{q_{\rm f}l({\rm eq})}^{\rm max}, m_{q_{\rm f}l_{\rm f}}^{\rm max}\right) & \text{for} \quad m^2_{\tilde{\chi}^0_1} + m^2_{\tilde{\chi}^0_2} > 2m^2_{\tilde{l}_R} > 2m_{\tilde{\chi}^0_1} m_{\tilde{\chi}^0_2} & (2) \\ \left(m_{q_{\rm f}l({\rm eq})}^{\rm max}, m_{q_{\rm f}l_{\rm n}}^{\rm max}\right) & \text{for} \quad m^2_{\tilde{\chi}^0_1} + m^2_{\tilde{\chi}^0_2} > 2m_{\tilde{\chi}^0_1} m_{\tilde{\chi}^0_2} > 2m^2_{\tilde{l}_R} & (3) \end{array} \right\} \tag{2.3}$$

$$\left(m_{q_{\rm f}l_{\rm n}}^{\rm max}\right)^2 = \left(m^2_{\tilde{q}_L} - m^2_{\tilde{\chi}^0_2}\right)\left(m^2_{\tilde{\chi}^0_2} - m^2_{\tilde{l}_R}\right)/m^2_{\tilde{\chi}^0_2} \tag{2.4}$$

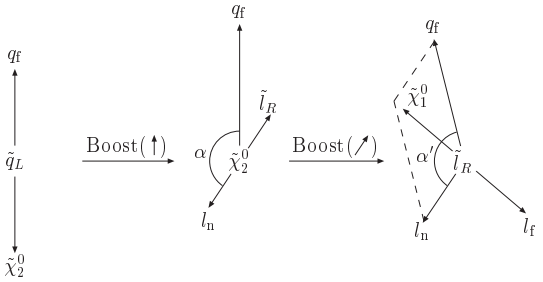

Figure 1: Standard way of calculating $m_{q_{\rm f}ll}^{\rm max}$.

$$\left(m_{q_{\rm f}l_{\rm f}}^{\rm max}\right)^2 = \left(m_{\tilde{q}_L}^2 - m_{\tilde{\chi}_2^0}^2\right)\left(m_{\tilde{l}_R}^2 - m_{\tilde{\chi}_1^0}^2\right)/m_{\tilde{l}_R}^2 \tag{2.5}$$

$$\left(m_{q_{\rm f}l({\rm eq})}^{\rm max}\right)^2 = \left(m_{\tilde{q}_L}^2 - m_{\tilde{\chi}_2^0}^2\right)\left(m_{\tilde{l}_R}^2 - m_{\tilde{\chi}_1^0}^2\right)/\left(2m_{\tilde{l}_R}^2 - m_{\tilde{\chi}_1^0}^2\right) \tag{2.6}$$

2.2 Calculation of $m_{q_{\rm f}ll}^{\rm max}$

When the gluino is added to the head of the chain to give (1.2), new distributions can be constructed and from their endpoints the gluino mass can be determined. To pave the way for the calculations of the endpoints of the new distributions, we first review the calculation of $m_{q_{\rm f}ll}^{\rm max}$, as given in Eq. (2.2). In Fig. 1 the decay of $\tilde{q}_L$ is shown stepwise. Start in the rest frame of $\tilde{q}_L$, and align the coordinate system to its decay products. Next, boost to the rest frame of $\tilde{\chi}_2^0$, which decays such that $l_{\rm n}$ is emitted with an angle α relative to the direction of $q_{\rm f}$. Finally, boost to the rest frame of $\tilde{l}_R$, which in turn decays; for a given α, $m_{q_{\rm f}ll}$ is maximized by choosing $\mathbf{p}_{l_{\rm f}}$ opposite to $\mathbf{p}_{q_{\rm f}} + \mathbf{p}_{l_{\rm n}}$ in the rest frame of $\tilde{l}_R$.

One ends up with an expression for $m_{q_{\rm f}ll}$ in terms of the angle α and the four sparticle masses involved; the task is then to maximize this with respect to α. One must seek the critical points of this constrained $m_{q_{\rm f}ll}$ distribution in the four-dimensional mass space and distinguish whether or not they correspond to a maximum. In the part of mass space where no critical point is found, the endpoints of the domain, $\alpha = [0, \pi]$, must be analysed. In this case, three different expressions are found for three distinct regions in mass space. In total, mass space is thus divided into four regions, each with its specific expression for $m_{q_{\rm f}ll}^{\rm max}$, see Eq. (2.2).

The above calculation becomes fairly involved, and is preferably performed with the aid of a computer program. An alternative approach is possible, where a geometrical understanding of the decay is more emphasised. The four-vector of the sum of the end products; the two leptons, the quark and the LSP, equals the four-vector of the squark. We therefore have

$$m_{\tilde{q}_L}^2 = (p_{q_{\rm f}ll} + p_{\tilde{\chi}_1^0})^2 = m_{q_{\rm f}ll}^2 + m_{\tilde{\chi}_1^0}^2 + 2p_{q_{\rm f}ll} \cdot p_{\tilde{\chi}_1^0} \tag{2.7}$$

where $p_{q_{\rm f}ll}$ is the sum of the four-vectors of the two leptons and the (far) quark. In the

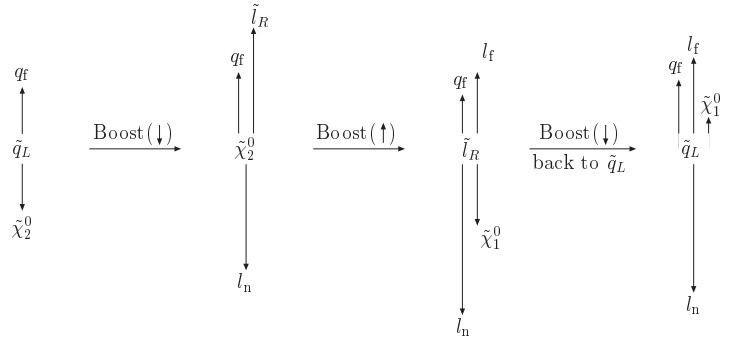

Figure 2: One of three 'dominance regions' for $m_{q_{\rm f}ll}^{\rm max}$

rest frame of $\tilde{q}_L$ we have

$$\mathbf{p}_{q_{\rm f}ll} = -\mathbf{p}_{\tilde{\chi}_1^0}, \quad E_{q_{\rm f}ll} = m_{\tilde{q}_L} - E_{\tilde{\chi}_1^0} \tag{2.8}$$

which gives

$$m_{q_{\rm f}ll}^2 = m_{\tilde{q}_L}^2 - m_{\tilde{\chi}_1^0}^2 - 2\big(m_{\tilde{q}_L}\sqrt{m_{\tilde{\chi}_1^0}^2 + \mathbf{p}_{\tilde{\chi}_1^0}^2} - m_{\tilde{\chi}_1^0}^2\big) \tag{2.9}$$

The smaller the momentum of the LSP is in the rest frame of the initial squark, the larger $m_{q_{\rm f}ll}$ is, which agrees with one's intuition. At the extreme, if the LSP is brought to rest in the squark rest frame, $m_{q_{\rm f}ll}$ will attain its largest value, $m_{\tilde{q}_L} - m_{\tilde{\chi}_1^0}$, which corresponds to the critical-point solution of the more formal approach described earlier. In some regions of mass space it is however not possible to have $\tilde{\chi}_1^0$ at rest in the rest frame of $\tilde{q}_L$. In these regions, one of the intermediate sparticles is sent off with so high momentum that not even optimal choices of directions for the other two decays can bring $\tilde{\chi}_1^0$ to rest (in the rest frame of $\tilde{q}_L$). The LSP will, for the decay which gives the maximum value of $m_{q_{\rm f}ll}$, have a non-zero momentum in the same direction as the sparticle sent out from the 'hardest' decay. There are three separate 'dominance regions' in mass space where this happens, one for each sparticle decay in the cascade.

Consider the case where the second decay, that of $\tilde{\chi}_2^0$, is dominant. If $\tilde{\chi}_1^0$ cannot be brought to rest in the rest frame of $\tilde{q}_L$, the maximum value is obtained for the optimized case where $q_{\rm f}$ and $l_{\rm f}$ fly off in one direction and $l_{\rm n}$ in the opposite, see Fig. 2. In the last step of the figure all momenta are boosted back to the rest frame of $\tilde{q}_L$. If we are inside the dominance region, $\tilde{\chi}_1^0$ ends up with a momentum pointing 'upwards' in the rest frame of $\tilde{q}_L$, as in the figure. In this case the defining criterion of the region takes the form,

$$|\mathbf{p}_{l_{\rm n}}| > |\mathbf{p}_q + \mathbf{p}_{l_{\rm f}}| \quad \Rightarrow \quad \frac{m_{\tilde{\chi}_2^0}}{m_{\tilde{l}_R}} > \frac{m_{\tilde{l}_R}}{m_{\tilde{\chi}_1^0}} \frac{m_{\tilde{q}_L}}{m_{\tilde{\chi}_2^0}} \tag{2.10}$$

where the three-momenta are taken in the rest frame of $\tilde{q}_L$. Note the form of the constraint in terms of *ratios of the masses of nearest neighbours in the decay chain*. The dominant

ratio is the one which corresponds to the decay of $\tilde{\chi}_2^0$. The expression for $m_{q_{\rm f}ll}^{\rm max}$ in this region is then found by simply combining the four-momenta of the three Standard-Model particles for the given configuration.

The defining inequality of the other two dominance regions and the resulting expressions for $m_{q_{\rm f}ll}^{\rm max}$ are found by similar approaches. The general result is given in Eq. (2.2). Note the systematic pattern of inequalities which define the dominance regions. Although in cases *(1)* and *(3)* the right-hand side of the inequalities can be simplified, this has not been done in order to emphasise the structure of the constraints.

The approach described above has some clear advantages over the more formal approach. It is visual in that each region is 'understood' in terms of a dominant decay, here in the sense that the mass ratio is larger than the product of the other two, together with minimum momentum of $\tilde{\chi}_1^0$ in the rest frame of $\tilde{q}_L$. No angle α is needed. Only cascade decays 'on a line' need be considered, which allows the entire calculation to be performed on a few sheets of paper. Furthermore, and this is the most celebrated quality here, the approach is easily extendable to an arbitrary number of particles.

2.3 Gluino endpoints

Using the above method we obtain the maximum value of m_{qqll} for the five-sparticle gluino chain:

$$\left(m_{qqll}^{\rm max}\right)^2 = \left\{ \begin{array}{lll} \dfrac{\left(m_{\tilde{g}}^2 - m_{\tilde{q}_L}^2\right)\left(m_{\tilde{q}_L}^2 - m_{\tilde{\chi}_1^0}^2\right)}{m_{\tilde{q}_L}^2} & \text{for} \quad \dfrac{m_{\tilde{g}}}{m_{\tilde{q}_L}} > \dfrac{m_{\tilde{q}_L}}{m_{\tilde{\chi}_2^0}} \dfrac{m_{\tilde{\chi}_2^0}}{m_{\tilde{l}_R}} \dfrac{m_{\tilde{l}_R}}{m_{\tilde{\chi}_1^0}} & (1) \\ \dfrac{\left(m_{\tilde{g}}^2 m_{\tilde{\chi}_2^0}^2 - m_{\tilde{q}_L}^2 m_{\tilde{\chi}_1^0}^2\right)\left(m_{\tilde{q}_L}^2 - m_{\tilde{\chi}_2^0}^2\right)}{m_{\tilde{q}_L}^2 m_{\tilde{\chi}_2^0}^2} & \text{for} \quad \dfrac{m_{\tilde{q}_L}}{m_{\tilde{\chi}_2^0}} > \dfrac{m_{\tilde{\chi}_2^0}}{m_{\tilde{l}_R}} \dfrac{m_{\tilde{l}_R}}{m_{\tilde{\chi}_1^0}} \dfrac{m_{\tilde{g}}}{m_{\tilde{q}_L}} & (2) \\ \dfrac{\left(m_{\tilde{g}}^2 m_{\tilde{l}_R}^2 - m_{\tilde{\chi}_2^0}^2 m_{\tilde{\chi}_1^0}^2\right)\left(m_{\tilde{\chi}_2^0}^2 - m_{\tilde{l}_R}^2\right)}{m_{\tilde{\chi}_2^0}^2 m_{\tilde{l}_R}^2} & \text{for} \quad \dfrac{m_{\tilde{\chi}_2^0}}{m_{\tilde{l}_R}} > \dfrac{m_{\tilde{l}_R}}{m_{\tilde{\chi}_1^0}} \dfrac{m_{\tilde{g}}}{m_{\tilde{q}_L}} \dfrac{m_{\tilde{q}_L}}{m_{\tilde{\chi}_2^0}} & (3) \\ \dfrac{\left(m_{\tilde{g}}^2 - m_{\tilde{l}_R}^2\right)\left(m_{\tilde{l}_R}^2 - m_{\tilde{\chi}_1^0}^2\right)}{m_{\tilde{l}_R}^2} & \text{for} \quad \dfrac{m_{\tilde{l}_R}}{m_{\tilde{\chi}_1^0}} > \dfrac{m_{\tilde{g}}}{m_{\tilde{q}_L}} \dfrac{m_{\tilde{q}_L}}{m_{\tilde{\chi}_2^0}} \dfrac{m_{\tilde{\chi}_2^0}}{m_{\tilde{l}_R}} & (4) \\ \left(m_{\tilde{g}} - m_{\tilde{\chi}_1^0}\right)^2 & \text{otherwise} & (5) \end{array} \right\} \quad (2.11)$$

Similarly to $m_{q_{\rm f}ll}^{\rm max}$, notice the systematic form of the defining inequalities. Here, we have four dominance regions, each defined in terms of a nearest-neighbour mass ratio dominating the product of the three others. As before, simplifications can be made to these inequalities, but with the undesired consequence of obscuring the neat and systematic structure.

In principle, a measurement of $m_{qqll}^{\rm max}$ would, in combination with the squark endpoints, suffice to provide the gluino mass. The long decay chain does however allow for more distributions to be constructed, from which endpoints can be extracted and compared with analytic expressions. These other available endpoints are useful both as over-constraining measurements and as consistency tests.

The gluino chain has seven primary endpoints which involve $q_{\rm n}$ and thus $m_{\tilde{g}}$. The two-particle primary endpoints $m_{qq}^{\rm max}$, $m_{q_{\rm n}l_{\rm n}}^{\rm max}$, $m_{q_{\rm n}l_{\rm f}}^{\rm max}$ are easily calculated from cascade decays on a line. There is only one realisation for each.

For the three-particle endpoint $m^{\max}_{qql_{\rm n}}$, the particles involved are neigbours in the decay chain, giving a situation similar to $m^{\max}_{q_{\rm f}ll}$. The solution can be found from Eq. (2.2) via the substitutions

$$(m_{\tilde{q}_L}, m_{\tilde{\chi}^0_2}, m_{\tilde{l}_R}, m_{\tilde{\chi}^0_1}) \to (m_{\tilde{g}}, m_{\tilde{q}_L}, m_{\tilde{\chi}^0_2}, m_{\tilde{l}_R}) \tag{2.12}$$

in both the endpoint expressions and the inequalities.

The two other three-particle endpoints $m^{\max}_{q_{\rm n}ll}$ and $m^{\max}_{qql_{\rm f}}$ are more difficult to find because the particles involved are not all nearest neighbours in the decay chain. However, it is possible to transform the problem into one which involves only nearest neighbours. Let us first consider $m^{\max}_{q_{\rm n}ll}$. The initial point of difficulty is the orientation of the $\tilde{q}_L$ decay, where the unused $q_{\rm f}$ is emitted. Will the orientation which gives the largest $m_{q_{\rm n}ll}$ depend on the mass scenario? To answer this question, boost to the rest frame of $\tilde{\chi}^0_2$. Whatever the details of the two steps prior to the creation of $\tilde{\chi}^0_2$, at this stage the only quantity of relevance to $m_{q_{\rm n}ll}$ is $|\mathbf{p}_{q_{\rm n}}|$. The larger the momentum is, the larger $m_{q_{\rm n}ll}$ can become. Thus, independent of masses, for maximum values of $m_{q_{\rm n}ll}$, the orientation of the $\tilde{q}_L$ decay is always the one that maximizes $|\mathbf{p}_{q_{\rm n}}|$ in the rest frame of $\tilde{\chi}^0_2$. This means sending $\tilde{\chi}^0_2$ in the opposite direction of $q_{\rm n}$, and the configuration which gives $m^{\max}_{q_{\rm n}ll}$ therefore has $\mathbf{p}_{q_{\rm n}}$ parallel to $\mathbf{p}_{q_{\rm f}}$.

With this point settled, the situation can be transformed into a nearest-neighbour decay, for which we know the solution. To do this we introduce a pseudo-particle: as seen from the rest frame of $\tilde{\chi}^0_2$ the momentum of $q_{\rm n}$ corresponds to the decay of a pseudo-particle $Y \to \tilde{\chi}^0_2 q_{\rm n}$ with mass $m^2_Y = m^2_{\tilde{g}} - m^2_{\tilde{q}_L} + m^2_{\tilde{\chi}^0_2}$. In such a picture all particles are nearest neighbours, and the solution (2.2) applies with appropriate substitution:

$$m_{\tilde{q}_L} \to m_Y = \sqrt{m^2_{\tilde{g}} - m^2_{\tilde{q}_L} + m^2_{\tilde{\chi}^0_2}} \tag{2.13}$$

For $m^{\max}_{qql_{\rm f}}$ the orientation of the $\tilde{\chi}^0_2$ decay is fixed to maximize $|\mathbf{p}_{l_{\rm f}}|$ in the rest frame of $\tilde{\chi}^0_2$, analogous to the argument above. Another pseudo-particle is then defined at the end of the decay chain, $\tilde{\chi}^0_2 \to Yl_{\rm f}$ where $m_Y = m_{\tilde{\chi}^0_1} m_{\tilde{\chi}^0_2}/m_{\tilde{l}_R}$. Again, the problem has been reformulated in terms of nearest neighbours, so solution (2.2) applies. The appropriate substitutions are

$$(m_{\tilde{q}_L}, m_{\tilde{\chi}^0_2}, m_{\tilde{l}_R}, m_{\tilde{\chi}^0_1}) \to (m_{\tilde{g}}, m_{\tilde{q}_L}, m_{\tilde{\chi}^0_2}, m_{\tilde{\chi}^0_1} m_{\tilde{\chi}^0_2}/m_{\tilde{l}_R}) \tag{2.14}$$

As was discussed for the squark chain, primary distributions based on distinguishing the two leptons can in practice not be constructed. Instead of the distributions $m_{q_{\rm n}l_{\rm n}}$, $m_{q_{\rm n}l_{\rm f}}$, $m_{qql_{\rm n}}$ and $m_{qql_{\rm f}}$ one can construct $m_{q_{\rm n}l(\text{high})}$, $m_{q_{\rm n}l(\text{low})}$, $m_{qql(\text{high})}$ and $m_{qql(\text{low})}$. While the endpoint of a 'high' distribution is simply the maximum of the two primary endpoints for the given mass scenario, further considerations are needed for the 'low' distributions. For $m_{q_{\rm n}l(\text{low})}$ these considerations are quite manageable, but for the three-particle distribution $m_{qql(\text{low})}$ they become rather involved. The general solution for the latter is given in Sect. 3.2.

The endpoint expressions are summarized below. Together with Eq. (2.11), the six first ones, Eqs. (2.15)–(2.20), correspond to the distributions which are usable in that they

do not rely on distinguishing the two leptons:

$$\left(m_{qq}^{\max}\right)^2 = \left(m_{\tilde{g}}^2 - m_{\tilde{q}_L}^2\right)\left(m_{\tilde{q}_L}^2 - m_{\tilde{\chi}_2^0}^2\right)/m_{\tilde{q}_L}^2 \tag{2.15}$$

$$m_{qql(\mathrm{low})}^{\max} \ : \text{ see Sect. 3.2} \tag{2.16}$$

$$m_{qql(\mathrm{high})}^{\max} = \max(m_{qql_\mathrm{n}}^{\max}, m_{qql_\mathrm{f}}^{\max}) \tag{2.17}$$

$$m_{q_\mathrm{n}ll}^{\max} \ : \text{ Eq. (2.2) with } m_{\tilde{q}_L} \to \sqrt{m_{\tilde{g}}^2 - m_{\tilde{q}_L}^2 + m_{\tilde{\chi}_2^0}^2} \tag{2.18}$$

$$m_{q_\mathrm{n}l(\mathrm{low})}^{\max} = \max(m_{q_\mathrm{n}l_\mathrm{n}}^{\max}, m_{q_\mathrm{n}l(\mathrm{eq})}^{\max}) \tag{2.19}$$

$$m_{q_\mathrm{n}l(\mathrm{high})}^{\max} = \max(m_{q_\mathrm{n}l_\mathrm{n}}^{\max}, m_{q_\mathrm{n}l_\mathrm{f}}^{\max}) \tag{2.20}$$

$$\left(m_{q_\mathrm{n}l_\mathrm{n}}^{\max}\right)^2 = \left(m_{\tilde{g}}^2 - m_{\tilde{q}_L}^2\right)\left(m_{\tilde{\chi}_2^0}^2 - m_{\tilde{l}_R}^2\right)/m_{\tilde{\chi}_2^0}^2 \tag{2.21}$$

$$\left(m_{q_\mathrm{n}l_\mathrm{f}}^{\max}\right)^2 = \left(m_{\tilde{g}}^2 - m_{\tilde{q}_L}^2\right)\left(m_{\tilde{l}_R}^2 - m_{\tilde{\chi}_1^0}^2\right)/m_{\tilde{l}_R}^2 \tag{2.22}$$

$$\left(m_{q_\mathrm{n}l(\mathrm{eq})}^{\max}\right)^2 = \left(m_{\tilde{g}}^2 - m_{\tilde{q}_L}^2\right)\left(m_{\tilde{l}_R}^2 - m_{\tilde{\chi}_1^0}^2\right)/(2m_{\tilde{l}_R}^2 - m_{\tilde{\chi}_1^0}^2) \tag{2.23}$$

$$m_{qql_\mathrm{n}}^{\max} \ : \text{ Eq. (2.2) with } (m_{\tilde{q}_L}, m_{\tilde{\chi}_2^0}, m_{\tilde{l}_R}, m_{\tilde{\chi}_1^0}) \to (m_{\tilde{g}}, m_{\tilde{q}_L}, m_{\tilde{\chi}_2^0}, m_{\tilde{l}_R}) \tag{2.24}$$

$$m_{qql_\mathrm{f}}^{\max} \ : \text{ Eq. (2.2) with } (m_{\tilde{q}_L}, m_{\tilde{\chi}_2^0}, m_{\tilde{l}_R}, m_{\tilde{\chi}_1^0}) \to (m_{\tilde{g}}, m_{\tilde{q}_L}, m_{\tilde{\chi}_2^0}, m_{\tilde{\chi}_1^0} m_{\tilde{\chi}_2^0}/m_{\tilde{l}_R}) \tag{2.25}$$

2.4 Quark ambiguity

Adding a gluino to the cascade introduces an additional ambiguity: how does one distinguish between the jet initiated by the gluino decay and that initiated by the squark decay? Initially we will assume that the two correct jets of a signal event are selected, and discuss the difficulties associated with this assumption later. In this case, one can seek to distinguish the two quark jets kinematically, by, for example, their transverse momenta, p_T. If $m_{\tilde{g}}^2 - m_{\tilde{q}_L}^2$ is very different from $m_{\tilde{q}_L}^2 - m_{\tilde{\chi}_2^0}^2$, the two quarks will be emitted with noticeably different energies, and a p_T comparison will, with a certain purity, serve to distinguish between the jets. However, one cannot, a priori, know which jet is to be assigned to q_n or q_f, i.e. whether it is q_n or q_f which gives rise to the hardest jet, and one must instead turn to the differences in production rates. Only when a gluino sits on top of the chain is q_n produced, and often, the ratio of directly versus indirectly produced squarks is sufficient to determine the average behaviour of q_f. This then allows statements on the average behaviour of q_n and q_f to be made, which may be used to construct samples where the quark identity is required, Eqs. (2.18)–(2.20), as well as the squark distributions $m_{q_\mathrm{f}ll}$, $m_{q_\mathrm{f}l(\mathrm{low})}$ and $m_{q_\mathrm{f}l(\mathrm{high})}$. Such a separation of q_n and q_f will always introduce impurities; whether these are manageable or not will depend on the given SUSY scenario.

To be fully general one might consider constructing new secondary distributions in which there is no need to distinguish the jets. The distributions m_{ll}, m_{qq}, m_{qqll}, $m_{qql(\mathrm{low})}$ and $m_{qql(\mathrm{high})}$ would remain unaffected, but instead of $m_{q_\mathrm{f}ll}$ and $m_{q_\mathrm{n}ll}$, one should construct new distributions $m_{qll(\mathrm{high})}$ and $m_{qll(\mathrm{low})}$. The endpoint expression of the former is readily available, but not of the latter. The complexity of the calculation and the resulting expression for $m^{\mathrm{max}}_{qll(\mathrm{low})}$ can be expected to be similar to that of $m^{\mathrm{max}}_{qql(\mathrm{low})}$ shown in Sect. 3.2. Furthermore, for the four m_{ql} distributions one can collect four new distributions based on the order of the four values per event. Only the endpoint of the $m_{ql(\mathrm{high})}$ distribution is readily available, while the other three endpoints become very difficult to calculate. A programme to calculate the new endpoints where quarks are not distinguished, has so far not been started.

The above discussion shows that as a second jet is added, the complexity of the situation increases significantly. In return many more endpoints become available, allowing for thorough consistency checks. In Sect. 5 we will return to these issues in the context of a simulation at the standard SPS 1a point.

2.5 Theory distributions

In order for the endpoint method to be useful, not only must the analytic expressions for the endpoints be available, it must also be possible to determine these endpoints from the experimental mass distributions. A first criterion for this is that the edges of the distributions 'point' unambiguously towards the exact endpoints. If the shape of a distribution is sufficiently concave at high values, the endpoint will most likely be underestimated and large systematic uncertainties must be added. In general the shapes of the mass distributions vary if the sparticle masses are varied. To investigate the range of possible shapes for each distribution, the full cascade has been generated for many mass scenarios, and the resulting theoretical mass distributions studied.

A representative selection of mass scenarios, showing some of the shape variety of the gluino distributions, is shown in Fig. 3. In generating these decays, quarks and leptons are assumed to be massless, which in the worst case (b-quark) leads to a perfectly acceptable error of $\mathcal{O}$(MeV). Furthermore, only decay phase space has been used, without the associated matrix elements. In principle, this ignores possible spin correlations between leptons and/or quarks. However, since the distributions used here are summed over lepton charge, no spin effects are expected [16]. A similar investigation for the squark distributions was performed in [12]. See also [17].

Since m_{qq} is constructed from two nearest neighbours in the decay chain, the shape is triangular for any masses, similar to m_{ll}. Its endpoint can thus in principle be determined quite accurately. The shape of the m_{qqll} distribution depends on the masses, but in practically all scenarios the edge is well described by a linear descent towards the theoretical endpoint. This should guarantee its determination experimentally if the background is sufficiently low. For most scenarios this is also true for $m_{qql(\mathrm{low})}$, although the distribution can take on other shapes.

The three 'high' distributions, $m_{qql(\mathrm{high})}$, $m_{q_\mathrm{f}l(\mathrm{high})}$ and $m_{q_\mathrm{n}l(\mathrm{high})}$, show a large variety of forms. The $m_{q_\mathrm{f}l(\mathrm{high})}$ distribution is very similar to the $m_{q_\mathrm{n}l(\mathrm{high})}$ distribution and is not

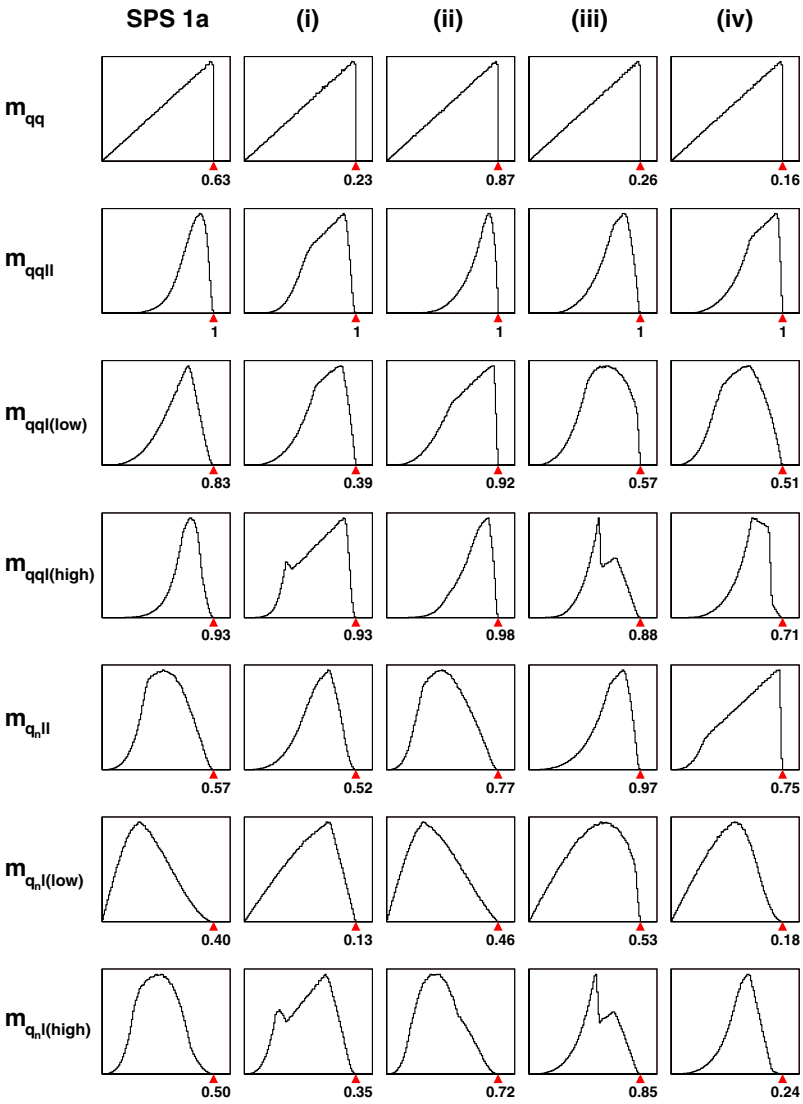

Figure 3: Theory distributions for SPS 1a and four other mass scenarios, showing some of the shape variety. Only gluino distributions are shown. Kinematic endpoints are marked with a triangle and given in units of $m_{qqll}^{\max}$, the largest of the endpoints.

reproduced here (see [12]). A common feature of these distributions is the danger of not noticing the 'foot', seen, for example, in $m_{qql(\mathrm{high})}$, scenario (iv), where the true maximum

value may be obscured by backgrounds.

The last of the three-particle distributions, $m_{q_{\rm n}ll}$, also has an extensive variety of shapes. The behaviour of the edge is usually reasonable, but with a certain danger of foot-like structures, as in scenario (i). Finally, the two $m_{q_{\rm n}l}$ distributions are often unreliable in that the edges are concave. It may therefore be difficult to get good estimates of the endpoints.

In summary, from the distributions of Fig. 3 we can then conclude that m_{qq} and m_{qqll} point reliably towards the endpoint for any mass scenario. Somewhat less reliable are the endpoint estimates found from the three-particle distributions. Lastly even less reliable endpoint estimates can be obtained from the two $m_{q_{\rm n}l}$ distributions. In Sect. 5 we will see how these statements change for a 'realistic' experimental setup.

3. Determination of $m^{\rm max}_{qql({\rm low})}$

This section presents some technical details on the derivation of $m^{\rm max}_{qql({\rm low})}$. It can be skipped by the reader interested in the physics only.

3.1 $m^{\rm max}_{ql({\rm low})}$

In preparation for the calculation of $m^{\rm max}_{qql({\rm low})}$ we here show how to obtain the general solution for $m^{\rm max}_{q_{\rm f}l({\rm low})}$. As both are 'low'-endpoints, many of the considerations are similar, only significantly more difficult to carry through for $m^{\rm max}_{qql({\rm low})}$.

Let us first recall that since there are two leptons, two invariant masses can be constructed, one of which will be higher than the other. These will be denoted the 'high' and 'low' distributions, each of which will have a maximum, denoted 'max'. Thus, the difficulty lies in identifying whether 'high' and 'low' correspond to the 'near' ($l_{\rm n}$) and 'far' ($l_{\rm f}$) leptons, or vice versa. The $m_{q_{\rm f}l({\rm high})}$ and $m_{q_{\rm f}l({\rm low})}$ distributions are constructed from the highest/lowest of $m_{q_{\rm f}l_{\rm n}}$ and $m_{q_{\rm f}l_{\rm f}}$ on an event by event basis. (We here assume that the correct jet has been selected.) Since the $m_{q_{\rm f}l}$ value which gives the absolute maximum must necessarily be the higher of $m_{q_{\rm f}l_{\rm n}}$ and $m_{q_{\rm f}l_{\rm f}}$ for the given configuration, we simply have $m^{\rm max}_{q_{\rm f}l({\rm high})} = \max(m^{\rm max}_{q_{\rm f}l_{\rm n}}, m^{\rm max}_{q_{\rm f}l_{\rm f}})$. For $m^{\rm max}_{q_{\rm f}l({\rm low})}$ the situation is more complicated; we need to look for the maximum value of the *lower* of $m_{q_{\rm f}l_{\rm n}}$ and $m_{q_{\rm f}l_{\rm f}}$. This conditional maximisation requires that both $m_{q_{\rm f}l}$ values are compared for the given configuration: under no circumstance can the endpoint be higher than the lower of the two maxima, $m^{\rm max}_{q_{\rm f}l({\rm low})} \leq \min(m^{\rm max}_{q_{\rm f}l_{\rm n}}, m^{\rm max}_{q_{\rm f}l_{\rm f}})$.

Let us first assume a mass scenario where $m^{\rm max}_{q_{\rm f}l_{\rm n}} < m^{\rm max}_{q_{\rm f}l_{\rm f}}$, which directly corresponds to the condition

$$m^2_{\tilde{l}_R} > m_{\tilde{\chi}^0_1} m_{\tilde{\chi}^0_2}. \tag{3.1}$$

This is manifest in regions *(1)* and *(2)* of Eq. (2.3). Now, let us further assume that we have a decay configuration where $m_{q_{\rm f}l_{\rm n}}$ takes on its maximum value, $m_{q_{\rm f}l_{\rm n}} = m^{\rm max}_{q_{\rm f}l_{\rm n}}$, so that $q_{\rm f}$ and $l_{\rm n}$ are back-to-back in the rest frame of $\tilde{\chi}^0_2$. If it is possible to choose an orientation of $\mathbf{p}_{l_{\rm f}}$ such that $m_{q_{\rm f}l_{\rm f}} > m_{q_{\rm f}l_{\rm n}}$, then $m_{q_{\rm f}l_{\rm n}}$ can be a 'low'-value, and we will have $m^{\rm max}_{q_{\rm f}l({\rm low})} = m^{\rm max}_{q_{\rm f}l_{\rm n}}$. Specifically, this occurs when $m_{q_{\rm f}l_{\rm f}}$ takes on its maximum value, with

$\mathbf{p}_{l_f}$ in the opposite direction to $\mathbf{p}_{q_f}$ (and parallel to $\mathbf{p}_{l_n}$). This special case occurs for

$$2m^2_{\tilde{l}_R} > m^2_{\tilde{\chi}^0_1} + m^2_{\tilde{\chi}^0_2}, \tag{3.2}$$

i.e. region *(1)* of Eq. (2.3).

If this mass constraint is not satisfied, $m_{q_f l_n}$ will be the 'high'-value for any configuration which has $m_{q_f l_n} = m^{\max}_{q_f l_n}$ and $m_{q_f l_f}$ will be the 'low' value. To find the configuration which gives $m^{\max}_{q_f l(\mathrm{low})}$ in this case, consider the more general situation where the angle α between $\mathbf{p}_{q_f}$ and $\mathbf{p}_{l_n}$ (in the rest frame of $\tilde{\chi}^0_2$) is reduced. The maximum value of $m_{q_f l_f}$ for this case is denoted $m^{\max}_{q_f l_f}(\alpha)$. [It will occur when $\mathbf{p}_{q_f}$ and $\mathbf{p}_{l_f}$ are back to back in the $\tilde{l}_R$ rest frame since $|\mathbf{p}_{l_f}|$ obviously is independent of orientation in this particular frame.] If α is reduced (starting from π), $m_{q_f l_n}(\alpha)$ will decrease and $m^{\max}_{q_f l_f}(\alpha)$ will increase. As α decreases, the 'high'-value decreases and the 'low'-value increases, and for some angle α_{eq} they become equal: $m_{q_f l_n}(\alpha_{\mathrm{eq}}) = m^{\max}_{q_f l_f}(\alpha_{\mathrm{eq}})$. If α is reduced below α_{eq}, $m_{q_n l_n}$ will become the 'low'-value, and as it decreases with α the 'low'-value will decrease. Hence, α_{eq} gives the optimal configuration, $m^{\max}_{q_f l(\mathrm{low})} = m_{q_f l_n}(\alpha_{\mathrm{eq}}) \equiv m^{\max}_{q_f l(\mathrm{eq})}$. A simple calculation gives (2.6), and is valid for

$$m^2_{\tilde{\chi}^0_1} + m^2_{\tilde{\chi}^0_2} > 2m^2_{\tilde{l}_R}, \tag{3.3}$$

i.e. regions *(2)* and *(3)* of Eq. (2.3).

One might expect to also find a separate solution for $m_{q_f l_f} < m_{q_f l_n}$ and $m_{q_f l_f} = m^{\max}_{q_f l_f}$, in analogy with the first solution obtained above. The situation is however not symmetric with respect to the two leptons. Maximisation of $m_{q_f l_f}$ necessarily fixes $m_{q_f l_n}$ at zero, so there is no third possibility, and once again $m^{\max}_{q_f l(\mathrm{low})} = m^{\max}_{q_f l(\mathrm{eq})}$. The general solution for $m^{\max}_{q_f l(\mathrm{low})}$ is then given by two expressions, $m^{\max}_{q_f l_n}$ and $m^{\max}_{q_f l(\mathrm{eq})}$, in the mass regions derived above, see (2.3). (Below, we will see that a third possibility is relevant for $m^{\max}_{qql(\mathrm{low})}$.)

3.2 $m^{\max}_{qql(\mathrm{low})}$

For a three-particle endpoint, the *configurations* which give the maximum values $m^{\max}_{qql_n}$ and $m^{\max}_{qql_f}$, as well as the endpoint expressions themselves, will be mass dependent [contrary to the situation for $m^{\max}_{q_f l_n}$ and $m^{\max}_{q_f l_f}$]. In particular, we see from (2.2), (2.24) and (2.25) that there are four different cases (mass regions) for each. This increases the number of situations to consider, as well as the complexity for each.

To calculate $m^{\max}_{qql(\mathrm{low})}$ we use the same strategy as above. We will first investigate the situation $m_{qql_n} < m_{qql_f}$ with $m_{qql_n} = m^{\max}_{qql_n}$ (Sect. 3.2.1) and find the appropriate conditions on the masses corresponding to $m^{\max}_{qql(\mathrm{low})} = m^{\max}_{qql_n}$. Then we will investigate the 'opposite' situation, $m_{qql_f} < m_{qql_n}$ with $m_{qql_f} = m^{\max}_{qql_f}$ (Sect. 3.2.2), and find the mass conditions for the solution $m^{\max}_{qql(\mathrm{low})} = m^{\max}_{qql_f}$. This differs from $m^{\max}_{q_f l(\mathrm{low})}$, where no such solution was available. Finally an 'equal'-solution will be sought (Sect. 3.2.3). It will consist of a critical-point solution and boundary solutions (at the boundary of a two-dimensional parameter space). The calculation of the 'equal'-solution is cumbersome and preferably performed with the aid of a computer program.

The resulting expressions for the full solution are not very complicated, but many. Care should be taken in the implementation.

In the rest frame of $\tilde{\chi}_2^0$ the quark sector and the lepton sector can be described without reference to each other. This makes the $\tilde{\chi}_2^0$ rest frame particularly convenient to use. Unless stated otherwise, momenta and energies are given in this rest frame. The coordinate system will be chosen such that the combined momentum of the two quarks, $\mathbf{p}_{qq}$ will point upwards (along +z). The x and y components are not required, allowing the four-vectors to be given solely by the energy and the momentum in the z-direction.

3.2.1 $m^{\max}_{qql(\mathrm{low})} = m^{\max}_{qql_{\mathrm{n}}}$

We here investigate the situation $m_{qql_{\mathrm{n}}} < m_{qql_{\mathrm{f}}}$ with $m_{qql_{\mathrm{n}}} = m^{\max}_{qql_{\mathrm{n}}}$. The possible configurations with a maximised $m_{qql_{\mathrm{n}}}$ are given in Table 1. The four rows correspond to the four different regions of mass-space appropriate to Eq. (2.24) (i.e. Eq. (2.2) with the substitution of Eq. (2.24)), as labeled by the first column. The second column shows the corresponding 'region condition'. The third and fourth column show the directions of the quark and lepton momenta, from left to right as in the decay chain. The combined momentum of the quarks is always upwards (in the rest frame of $\tilde{\chi}_2^0$). The direction of $\mathbf{p}_{l_{\mathrm{n}}}$ is always downwards, while the direction of $\mathbf{p}_{l_{\mathrm{f}}}$ is upwards for configuration 1, downwards for configuration 2. Notice that in region *(4)*, configurations which correspond to a maximum of $m_{qql(\mathrm{low})}$ do *not* have the quarks aligned in the $\tilde{\chi}_2^0$ rest frame. There are four mass regions and two directions for $\mathbf{p}_{l_{\mathrm{f}}}$, giving in total eight possibilities. Each must be considered.

$m^{\max}_{qql_{\mathrm{n}}}$	region condition	config. 1 $q_{\mathrm{n}}q_{\mathrm{f}}$ $l_{\mathrm{n}}l_{\mathrm{f}}$	config. 2 $q_{\mathrm{n}}q_{\mathrm{f}}$ $l_{\mathrm{n}}l_{\mathrm{f}}$
region *(1)*	$\frac{m_{\tilde{q}}}{m_{\tilde{q}_L}} > \frac{m_{\tilde{q}_L}}{m_{\tilde{\chi}_2^0}} \frac{m_{\tilde{\chi}_2^0}}{m_{\tilde{l}_R}}$	$\uparrow\downarrow$ $\downarrow\uparrow$ superfluous	$\uparrow\downarrow$ $\downarrow\downarrow$ trivial
region *(2)*	$\frac{m_{\tilde{q}_L}}{m_{\tilde{\chi}_2^0}} > \frac{m_{\tilde{\chi}_2^0}}{m_{\tilde{l}_R}} \frac{m_{\tilde{q}}}{m_{\tilde{q}_L}}$	$\downarrow\uparrow$ $\downarrow\uparrow$ superfluous	$\downarrow\uparrow$ $\downarrow\downarrow$ trivial
region *(3)*	$\frac{m_{\tilde{\chi}_2^0}}{m_{\tilde{l}_R}} > \frac{m_{\tilde{q}}}{m_{\tilde{q}_L}} \frac{m_{\tilde{q}_L}}{m_{\tilde{\chi}_2^0}}$	$\uparrow\uparrow$ $\downarrow\uparrow$ no solution	$\uparrow\uparrow$ $\downarrow\downarrow$ trivial
region *(4)*	otherwise	$\nwarrow\!\!\nearrow$ $\downarrow\uparrow$ superfluous	$\nwarrow\!\!\nearrow$ $\downarrow\downarrow$ trivial

Table 1: Possible configurations for $m^{\max}_{qql_{\mathrm{n}}}$. See the text for details.

The comments 'trivial', 'no solution' and 'superfluous' give the conclusion of the investigations. Some of these are seen right away: in region *(3)*, configuration 1 the value of $m_{qql_{\mathrm{f}}}$ evidently vanishes since the three particles go in the same direction, hence $m_{qql_{\mathrm{f}}}$ must always be smaller than $m_{qql_{\mathrm{n}}}$ and there is 'no solution'. For configuration 2, in all four regions the condition $m_{qql_{\mathrm{n}}} < m_{qql_{\mathrm{f}}}$ is simply $|\mathbf{p}_{l_{\mathrm{n}}}| < |\mathbf{p}_{l_{\mathrm{f}}}|$, which 'trivially' corresponds to

$$m^2_{\tilde{\chi}_1^0} + m^2_{\tilde{\chi}_2^0} < 2m^2_{\tilde{l}_R}. \tag{3.4}$$

The three regions of configuration 1 which are marked 'superfluous' give mass conditions which turn out to be subsets of the corresponding ('trivial') mass condition of configuration 2 [when the appropriate region condition is also imposed]. This means that

if the ('superfluous') configuration 1 is possible, then also configuration 2 is possible. The conclusion of this subsection will therefore be that $m^{\max}_{qll(\mathrm{low})} = m^{\max}_{qql_{\mathrm{n}}}$ if and only if the trivial condition (3.4) is satisfied. The rest of the subsection is dedicated to proving that the superfluous conditions are indeed contained in the trivial one.

For each of the three regions we must first find the mass condition by requiring $m_{qql_{\mathrm{n}}} < m_{qql_{\mathrm{f}}}$. The proofs that these conditions are already contained in the trivial condition [given that the appropriate region conditions are also imposed], are carried through by combining these with the 'anti-trivial' condition, $m^2_{\tilde{\chi}^0_1} + m^2_{\tilde{\chi}^0_2} > 2m^2_{\tilde{l}_R}$, and see that this leads to contradictions. For regions *(1)* and *(2)* the proofs are fairly straightforward, but less so for region *(4)* due to the complicated nature of the region condition and the non-aligned quarks. Below we first find the mass conditions of the three regions, then show the proof for one of them. The proofs of the two others are similar.

Regions *(1)* **and** *(2)*

In the rest frame of $\tilde{\chi}^0_2$ the relevant four-vectors of configuration 1 are:

$$p_{qq} = (E_{qq},\ |\mathbf{p}_{qq}|), \quad p_{l_{\mathrm{n}}} = (|\mathbf{p}_{l_{\mathrm{n}}}|,\ -|\mathbf{p}_{l_{\mathrm{n}}}|), \quad p_{l_{\mathrm{f}}} = (|\mathbf{p}_{l_{\mathrm{f}}}|,\ |\mathbf{p}_{l_{\mathrm{f}}}|) \tag{3.5}$$

where each entry is given in the form $(E,\ p_z)$. The condition we need to satisfy is then:

$$\begin{aligned} m_{qql_{\mathrm{n}}} < m_{qql_{\mathrm{f}}} &\Leftrightarrow (p_{qq} + p_{l_{\mathrm{n}}})^2 < (p_{qq} + p_{l_{\mathrm{f}}})^2 \Leftrightarrow p_{qq} \cdot p_{l_{\mathrm{n}}} < p_{qq} \cdot p_{l_{\mathrm{f}}} \\ &\Leftrightarrow (E_{qq} + |\mathbf{p}_{qq}|)|\mathbf{p}_{l_{\mathrm{n}}}| < (E_{qq} - |\mathbf{p}_{qq}|)|\mathbf{p}_{l_{\mathrm{f}}}| \end{aligned} \tag{3.6}$$

The lepton three-momenta have the magnitude:

$$|\mathbf{p}_{l_{\mathrm{n}}}| = \frac{(m^2_{\tilde{\chi}^0_2} - m^2_{\tilde{l}_R})}{2m_{\tilde{\chi}^0_2}}, \quad |\mathbf{p}_{l_{\mathrm{f}}}| = \frac{(m^2_{\tilde{l}_R} - m^2_{\tilde{\chi}^0_1})m_{\tilde{\chi}^0_2}}{2m^2_{\tilde{l}_R}} \tag{3.7}$$

For region *(1)* the quark sector gives

$$E_{qq} = |\mathbf{p}_{q_{\mathrm{n}}}| + |\mathbf{p}_{q_{\mathrm{f}}}|, \qquad |\mathbf{p}_{qq}| = |\mathbf{p}_{q_{\mathrm{n}}}| - |\mathbf{p}_{q_{\mathrm{f}}}| \tag{3.8}$$

$$E_{qq} + |\mathbf{p}_{qq}| = 2|\mathbf{p}_{q_{\mathrm{n}}}| = \frac{(m^2_{\tilde{g}} - m^2_{\tilde{q}_L})m_{\tilde{\chi}^0_2}}{m^2_{\tilde{q}_L}}, \qquad E_{qq} - |\mathbf{p}_{qq}| = 2|\mathbf{p}_{q_{\mathrm{f}}}| = \frac{(m^2_{\tilde{q}_L} - m^2_{\tilde{\chi}^0_2})}{m_{\tilde{\chi}^0_2}} \tag{3.9}$$

For region *(2)*, the only difference is the expression for $|\mathbf{p}_{qq}|$, which differs by an overall sign ($|\mathbf{p}_{qq}| = |\mathbf{p}_{q_{\mathrm{f}}}| - |\mathbf{p}_{q_{\mathrm{n}}}|$), and amounts to interchanging the two expressions in (3.9). If the expressions for regions *(1)* and *(2)* are inserted into (3.6), the following mass conditions are found:

$$\text{region } (1): \qquad m^2_{\tilde{l}_R}(m^2_{\tilde{g}} - m^2_{\tilde{q}_L})(m^2_{\tilde{\chi}^0_2} - m^2_{\tilde{l}_R}) < m^2_{\tilde{q}_L}(m^2_{\tilde{q}_L} - m^2_{\tilde{\chi}^0_2})(m^2_{\tilde{l}_R} - m^2_{\tilde{\chi}^0_1}) \tag{3.10}$$

$$\text{region } (2): \quad m^2_{\tilde{q}_L} m^2_{\tilde{l}_R}(m^2_{\tilde{q}_L} - m^2_{\tilde{\chi}^0_2})(m^2_{\tilde{\chi}^0_2} - m^2_{\tilde{l}_R}) < m^4_{\tilde{\chi}^0_2}(m^2_{\tilde{g}} - m^2_{\tilde{q}_L})(m^2_{\tilde{l}_R} - m^2_{\tilde{\chi}^0_1}) \tag{3.11}$$

If (3.10) or (3.11) is satisfied, together with the appropriate region condition (Table 1, second column), then we have $m^{\max}_{qql(\mathrm{low})} = m^{\max}_{qql_{\mathrm{n}}}$.

Region *(4)*

In region *(4)* the quarks are not sent out 'on a line' (parallel/antiparallel). We must instead find p_{qq} in the rest frame of $\tilde{\chi}_2^0$ using the following equations:

$$(m_{\tilde{g}} - m_{\tilde{l}_R})^2 = p_{qql_n}^2 = p_{qq}^2 + 2p_{qq} \cdot p_{l_n} = E_{qq}^2 - \mathbf{p}_{qq}^2 + 2(E_{qq} + |\mathbf{p}_{qq}|)|\mathbf{p}_{l_n}| \tag{3.12}$$

$$m_{\tilde{g}}^2 = p_{qq\tilde{\chi}_2^0}^2 = p_{qq}^2 + m_{\tilde{\chi}_2^0}^2 + 2p_{\tilde{\chi}_2^0} \cdot p_{qq} = E_{qq}^2 - \mathbf{p}_{qq}^2 + m_{\tilde{\chi}_2^0}^2 + 2m_{\tilde{\chi}_2^0} E_{qq} \tag{3.13}$$

The first equation uses the expression for $m_{qql_n}^{\max}$ found in Eq. (2.24). From these we find p_{qq}:

$$E_{qq} = \frac{m_{\tilde{g}}(m_{\tilde{\chi}_2^0}^2 + m_{\tilde{l}_R}^2) - 2m_{\tilde{\chi}_2^0}^2 m_{\tilde{l}_R}}{2m_{\tilde{\chi}_2^0} m_{\tilde{l}_R}}, \quad |\mathbf{p}_{qq}| = \frac{m_{\tilde{g}}(m_{\tilde{\chi}_2^0}^2 - m_{\tilde{l}_R}^2)}{2m_{\tilde{\chi}_2^0} m_{\tilde{l}_R}} \tag{3.14}$$

$$E_{qq} + |\mathbf{p}_{qq}| = \frac{m_{\tilde{\chi}_2^0}(m_{\tilde{g}} - m_{\tilde{l}_R})}{m_{\tilde{l}_R}}, \quad E_{qq} - |\mathbf{p}_{qq}| = \frac{(m_{\tilde{g}} m_{\tilde{l}_R} - m_{\tilde{\chi}_2^0}^2)}{m_{\tilde{\chi}_2^0}} \tag{3.15}$$

Insertion of these expressions into (3.6) gives the condition for region *(4)*:

$$m_{\tilde{l}_R}(m_{\tilde{g}} - m_{\tilde{l}_R})(m_{\tilde{\chi}_2^0}^2 - m_{\tilde{l}_R}^2) < (m_{\tilde{g}} m_{\tilde{l}_R} - m_{\tilde{\chi}_2^0}^2)(m_{\tilde{l}_R}^2 - m_{\tilde{\chi}_1^0}^2) \tag{3.16}$$

If this is satisfied together with the corresponding region condition in the second column of Table 1, then $m_{qql(\mathrm{low})}^{\max} = m_{qql_n}^{\max}$.

However, as stated earlier the mass conditions (3.10), (3.11) and (3.16) are 'superfluous'. Below this is proved for region *(1)*. From the region condition and the 'anti-trivial' condition, we have the following inequalities:

$$\frac{m_{\tilde{g}}}{m_{\tilde{q}_L}} > \frac{m_{\tilde{q}_L}}{m_{\tilde{\chi}_2^0}} \frac{m_{\tilde{\chi}_2^0}}{m_{\tilde{l}_R}} \Leftrightarrow m_{\tilde{l}_R}^2(m_{\tilde{g}}^2 - m_{\tilde{q}_L}^2) > m_{\tilde{q}_L}^2(m_{\tilde{q}_L}^2 - m_{\tilde{l}_R}^2) \tag{3.17}$$

$$m_{\tilde{\chi}_1^0}^2 + m_{\tilde{\chi}_2^0}^2 > 2m_{\tilde{l}_R}^2 \Leftrightarrow (m_{\tilde{\chi}_2^0}^2 - m_{\tilde{l}_R}^2) > (m_{\tilde{l}_R}^2 - m_{\tilde{\chi}_1^0}^2) \tag{3.18}$$

Starting from (3.10) and using (3.17)–(3.18) we can then write

$$\begin{aligned} m_{\tilde{q}_L}^2(m_{\tilde{q}_L}^2 - m_{\tilde{\chi}_2^0}^2)(m_{\tilde{l}_R}^2 - m_{\tilde{\chi}_1^0}^2) &> m_{\tilde{l}_R}^2(m_{\tilde{g}}^2 - m_{\tilde{q}_L}^2)(m_{\tilde{\chi}_2^0}^2 - m_{\tilde{l}_R}^2) \\ &> m_{\tilde{q}_L}^2(m_{\tilde{q}_L}^2 - m_{\tilde{l}_R}^2)(m_{\tilde{\chi}_2^0}^2 - m_{\tilde{l}_R}^2) \\ &> m_{\tilde{q}_L}^2(m_{\tilde{q}_L}^2 - m_{\tilde{l}_R}^2)(m_{\tilde{l}_R}^2 - m_{\tilde{\chi}_1^0}^2) \\ &\Rightarrow m_{\tilde{l}_R} > m_{\tilde{\chi}_2^0} \end{aligned} \tag{3.19}$$

which is clearly wrong. Hence, given the correct region condition, the mass condition (3.10) is in contradiction to the anti-trivial condition, meaning that it must be contained in the trivial condition. Similar proofs apply for the two other superfluous cases.

We therefore have the following conclusion, as already stated: if (3.4) is satisfied, then $m_{qll(\mathrm{low})}^{\max} = m_{qql_n}^{\max}$.

3.2.2 $m^{\max}_{qql(\mathrm{low})} = m^{\max}_{qql_\mathrm{f}}$

Here we investigate the situation $m_{qql_\mathrm{f}} < m_{qql_\mathrm{n}}$ with $m_{qql_\mathrm{f}} = m^{\max}_{qql_\mathrm{f}}$. The possible configurations with a maximised m_{qql_f} are given in Table 2 (in contrast to Table 1 where m_{qql_n} was maximized). As before we consider the rest frame of $\tilde{\chi}^0_2$ and align the coordinate system such as to have $\mathbf{p}_{qq}$ pointing upwards. The maximum value for m_{qql_f} is found for the decay configuration of $\tilde{\chi}^0_2$ and $\tilde{l}_R$ which maximises $\mathbf{p}_{l_\mathrm{f}}$ downwards (in the rest frame of $\tilde{\chi}^0_2$). This is achieved if first $\tilde{l}_R$, then l_f, are emitted downwards. Since this necessarily fixes $\mathbf{p}_{l_\mathrm{n}}$ upwards, there is only one configuration in Table 2. The mass ratios in the quark sector are the same for $m^{\max}_{qql_\mathrm{f}}$ as for $m^{\max}_{qql_\mathrm{n}}$, but in the lepton sector the relevant ratio is now $m_{\tilde{\chi}^0_2}/(m_{\tilde{\chi}^0_1} m_{\tilde{\chi}^0_2}/m_{\tilde{l}_R}) = m_{\tilde{l}_R}/m_{\tilde{\chi}^0_1}$, see (2.24) and (2.25), which changes the region conditions in column 2 as compared to those of Table 1.

$m^{\max}_{qql_\mathrm{f}}$	region condition	config. 1 $q_\mathrm{n} q_\mathrm{f}$ $l_\mathrm{n} l_\mathrm{f}$
region *(1)*	$\frac{m_{\tilde{g}}}{m_{\tilde{q}_L}} > \frac{m_{\tilde{q}_L}}{m_{\tilde{\chi}^0_2}} \frac{m_{\tilde{l}_R}}{m_{\tilde{\chi}^0_1}}$	$\uparrow\downarrow$ $\uparrow\downarrow$ unique
region *(2)*	$\frac{m_{\tilde{q}_L}}{m_{\tilde{\chi}^0_2}} > \frac{m_{\tilde{l}_R}}{m_{\tilde{\chi}^0_1}} \frac{m_{\tilde{g}}}{m_{\tilde{q}_L}}$	$\downarrow\uparrow$ $\uparrow\downarrow$ unique
region *(3)*	$\frac{m_{\tilde{l}_R}}{m_{\tilde{\chi}^0_1}} > \frac{m_{\tilde{g}}}{m_{\tilde{q}_L}} \frac{m_{\tilde{q}_L}}{m_{\tilde{\chi}^0_2}}$	$\uparrow\uparrow$ $\uparrow\downarrow$ no solution
region *(4)*	otherwise	$\nwarrow\!\!\uparrow$ $\uparrow\downarrow$ unique

Table 2: Possible configurations for $m^{\max}_{qql_\mathrm{f}}$. See the text for details.

Region *(3)* has no solution since m_{qql_n} vanishes and therefore cannot be the 'high'-value. In the three other regions there are unique mass conditions for the solution $m^{\max}_{qql(\mathrm{low})} = m^{\max}_{qql_\mathrm{f}}$, which is what we seek here. The calculations follow the exact same path as in the previous subsection.

Regions *(1)* and *(2)*

In the rest frame of $\tilde{\chi}^0_2$ the relevant four-vectors are [compare with (3.5)]:

$$p_{qq} = (E_{qq},\ |\mathbf{p}_{qq}|), \quad p_{l_\mathrm{n}} = (|\mathbf{p}_{l_\mathrm{n}}|,\ |\mathbf{p}_{l_\mathrm{n}}|), \quad p_{l_\mathrm{f}} = (|\mathbf{p}_{l_\mathrm{f}}|,\ -|\mathbf{p}_{l_\mathrm{f}}|) \tag{3.20}$$

The condition we need to satisfy is now:

$$\begin{aligned} m_{qql_\mathrm{f}} < m_{qql_\mathrm{n}} &\Leftrightarrow (p_{qq} + p_{l_\mathrm{f}})^2 < (p_{qq} + p_{l_\mathrm{n}})^2 \Leftrightarrow p_{qq} \cdot p_{l_\mathrm{f}} < p_{qq} \cdot p_{l_\mathrm{n}} \\ &\Leftrightarrow (E_{qq} + |\mathbf{p}_{qq}|)|\mathbf{p}_{l_\mathrm{f}}| < (E_{qq} - |\mathbf{p}_{qq}|)|\mathbf{p}_{l_\mathrm{n}}| \end{aligned} \tag{3.21}$$

The lepton momenta are still given by (3.7). The energy and momentum of the quarks are the same as in the previous subsection: Eq. (3.9) for region *(1)*, the expressions interchanged for region *(2)*.

When these expressions are inserted into (3.21), we find the following mass conditions:

$$\text{region } (1): \quad m^4_{\tilde{\chi}^0_2}(m^2_{\tilde{g}} - m^2_{\tilde{q}_L})(m^2_{\tilde{l}_R} - m^2_{\tilde{\chi}^0_1}) < m^2_{\tilde{q}_L} m^2_{\tilde{l}_R}(m^2_{\tilde{q}_L} - m^2_{\tilde{\chi}^0_2})(m^2_{\tilde{\chi}^0_2} - m^2_{\tilde{l}_R}) \quad (3.22)$$

$$\text{region } (2): \quad m^2_{\tilde{q}_L}(m^2_{\tilde{q}_L} - m^2_{\tilde{\chi}^0_2})(m^2_{\tilde{l}_R} - m^2_{\tilde{\chi}^0_1}) < m^2_{\tilde{l}_R}(m^2_{\tilde{g}} - m^2_{\tilde{q}_L})(m^2_{\tilde{\chi}^0_2} - m^2_{\tilde{l}_R}) \quad (3.23)$$

If (3.22) or (3.23) is satisfied, together with the appropriate region condition (Table 2, second column), then we have $m^{\max}_{qql(\text{low})} = m^{\max}_{qql_f}$.

Region *(4)*

In region *(4)* the combination of

$$(m_{\tilde{g}} - m_{\tilde{\chi}^0_1} m_{\tilde{\chi}^0_2}/m_{\tilde{l}_R})^2 = p^2_{qql_f} = p^2_{qq} + 2p_{qq}\cdot p_{l_f} = E^2_{qq} - \mathbf{p}^2_{qq} + 2(E_{qq} + |\mathbf{p}_{qq}|)|\mathbf{p}_{l_f}| \quad (3.24)$$

[equivalent to (3.12)] with (3.13) results in:

$$E_{qq} = \frac{m_{\tilde{g}}(m^2_{\tilde{l}_R} + m^2_{\tilde{\chi}^0_1}) - 2m_{\tilde{\chi}^0_2} m_{\tilde{l}_R} m_{\tilde{\chi}^0_1}}{2m_{\tilde{l}_R} m_{\tilde{\chi}^0_1}}, \quad |\mathbf{p}_{qq}| = \frac{m_{\tilde{g}}(m^2_{\tilde{l}_R} - m^2_{\tilde{\chi}^0_1})}{2m_{\tilde{l}_R} m_{\tilde{\chi}^0_1}} \quad (3.25)$$

$$E_{qq} + |\mathbf{p}_{qq}| = \frac{(m_{\tilde{g}} m_{\tilde{l}_R} - m_{\tilde{\chi}^0_2} m_{\tilde{\chi}^0_1})}{m_{\tilde{\chi}^0_1}}, \quad E_{qq} - |\mathbf{p}_{qq}| = \frac{(m_{\tilde{g}} m_{\tilde{\chi}^0_1} - m_{\tilde{\chi}^0_2} m_{\tilde{l}_R})}{m_{\tilde{l}_R}} \quad (3.26)$$

Insertion of these expressions into (3.21) gives the condition for region *(4)*:

$$m^2_{\tilde{\chi}^0_2}(m_{\tilde{g}} m_{\tilde{l}_R} - m_{\tilde{\chi}^0_2} m_{\tilde{\chi}^0_1})(m^2_{\tilde{l}_R} - m^2_{\tilde{\chi}^0_1}) < m_{\tilde{l}_R} m_{\tilde{\chi}^0_1}(m_{\tilde{g}} m_{\tilde{\chi}^0_1} - m_{\tilde{\chi}^0_2} m_{\tilde{l}_R})(m^2_{\tilde{\chi}^0_2} - m^2_{\tilde{l}_R}) \quad (3.27)$$

If this is satisfied together with the corresponding region condition, then $m^{\max}_{qql(\text{low})} = m^{\max}_{qql_f}$.

This result completes the special-case solutions of $m^{\max}_{qql(\text{low})}$.

3.2.3 $m^{\max}_{qql(\text{low})} = m^{\max}_{qql(\text{eq})}$

If none of the above mass conditions are fulfilled, the maximum of $m_{qql(\text{low})}$ will in general be reached in an 'equal-solution' decay configuration, where $m_{qql_n} = m_{qql_f}$.

The relevant information on the two first steps of the cascade decay is contained in the value of $|\mathbf{p}_{qq}|$. (We stay in the rest frame of $\tilde{\chi}^0_2$.) Its maximum value is attained if q_n and q_f are sent off in the same direction, and is given by,

$$|\mathbf{p}^{\uparrow\uparrow}_{qq}| = \frac{m^2_{\tilde{g}} - m^2_{\tilde{\chi}^0_2}}{2m_{\tilde{\chi}^0_2}} \quad (3.28)$$

If sent off in opposite directions, $|\mathbf{p}_{qq}|$ is at its minimum,

$$|\mathbf{p}^{\uparrow\downarrow}_{qq}| = \frac{|m^2_{\tilde{g}} m^2_{\tilde{\chi}^0_2} - m^4_{\tilde{q}_L}|}{2m^2_{\tilde{q}_L} m_{\tilde{\chi}^0_2}} \quad (3.29)$$

In the following we let $|\mathbf{p}_{qq}|$ be a free variable and only later impose the physical constraint $|\mathbf{p}_{qq}| \in [|\mathbf{p}^{\uparrow\downarrow}_{qq}|, |\mathbf{p}^{\uparrow\uparrow}_{qq}|]$.

As before, we align the coordinate system to have $\mathbf{p}_{qq}$ along +z. The first lepton, l_n, is emitted at an angle α relative to $\mathbf{p}_{qq}$. The direction of the second lepton, l_f, is chosen

to maximize $m_{qql_{\rm f}}$ for the given α, allowing the notation $m^{\max}_{qql_{\rm f}}(\alpha)$. We have this freedom since we are interested in the maximum, not just any $m_{qql(\rm eq)}$ value. At this stage the decay is parametrised in terms of two variables, $|\mathbf{p}_{qq}|$ and α. By requiring $m_{qql_{\rm n}}(\alpha) = m^{\max}_{qql_{\rm f}}(\alpha)$, the angle can be expressed in terms of $|\mathbf{p}_{qq}|$:

$$\cos\alpha_{\rm eq} = \frac{m^2_{\tilde{l}_R}\left(m^2_{\tilde{\chi}^0_1} + m^2_{\tilde{\chi}^0_2} - 2m^2_{\tilde{l}_R}\right)\left(\sqrt{m^2_{\tilde{g}} + |\mathbf{p}_{qq}|^2} - m_{\tilde{\chi}^0_2}\right) - m_{\tilde{\chi}^0_2}\left(m^2_{\tilde{l}_R} - m^2_{\tilde{\chi}^0_1}\right)\varphi(|\mathbf{p}_{qq}|)}{\left(m^2_{\tilde{\chi}^0_2} - m^2_{\tilde{l}_R}\right)\left(2m^2_{\tilde{l}_R} - m^2_{\tilde{\chi}^0_1}\right)|\mathbf{p}_{qq}|} \tag{3.30}$$

where $\varphi(|\mathbf{p}_{qq}|)$ is given by

$$\varphi(|\mathbf{p}_{qq}|) = \left[m^2_{\tilde{\chi}^0_2}|\mathbf{p}_{qq}|^2 + \left(m^2_{\tilde{\chi}^0_1} + m^2_{\tilde{\chi}^0_2} - 2m^2_{\tilde{l}_R}\right)\left(m^2_{\tilde{g}} + m^2_{\tilde{\chi}^0_2} - 2m_{\tilde{\chi}^0_2}\sqrt{m^2_{\tilde{g}} + |\mathbf{p}_{qq}|^2}\right)\right]^{1/2} \tag{3.31}$$

[Later we will need to ensure that $|\cos\alpha_{\rm eq}| \leq 1$.] Insertion of this solution into $m_{qql_{\rm n}}(\alpha)$ [or $m^{\max}_{qql_{\rm f}}(\alpha)$] returns an expression for $m_{qql(\rm eq)}$ in terms of $|\mathbf{p}_{qq}|$ only. Since we are interested in a maximum value we now search for the critical point of $m_{qql(\rm eq)}$, and find an expression for the critical momentum,

$$|\mathbf{p}^{\rm crit}_{qq}| = \left[\left(2m_{\tilde{l}_R}(m^2_{\tilde{\chi}^0_1} + m^2_{\tilde{\chi}^0_2} - 2m^2_{\tilde{l}_R}) + (3m^2_{\tilde{l}_R} - m^2_{\tilde{\chi}^0_1})\sqrt{m^2_{\tilde{g}} + 2m^2_{\tilde{l}_R} - m^2_{\tilde{\chi}^0_1} - m^2_{\tilde{\chi}^0_2}}\right)^2 - 4m^2_{\tilde{g}}m^2_{\tilde{\chi}^0_2}m^2_{\tilde{l}_R}\right]^{\frac{1}{2}} \frac{1}{2m_{\tilde{\chi}^0_2}m_{\tilde{l}_R}} \tag{3.32}$$

Inserting this back into $m_{qql(\rm eq)}$ gives an expression for the critical point solution,

$$\left(m^{\rm crit}_{qql(\rm eq)}\right)^2 = m^2_{\tilde{g}} - \left[m_{\tilde{\chi}^0_2}(3m^2_{\tilde{l}_R} - m^2_{\tilde{\chi}^0_1})\sqrt{|\mathbf{p}^{\rm crit}_{qq}|^2 + m^2_{\tilde{g}}} - m^2_{\tilde{\chi}^0_2}m^2_{\tilde{l}_R} - (m^2_{\tilde{l}_R} - m^2_{\tilde{\chi}^0_1})\varphi(|\mathbf{p}^{\rm crit}_{qq}|)\right] / (2m^2_{\tilde{l}_R} - m^2_{\tilde{\chi}^0_1}) \tag{3.33}$$

All expressions found from the procedure above are formal. In order for them to be physical, the momentum and the angle α of the critical solution must lie in the allowed regions:

$$|\mathbf{p}^{\rm crit}_{qq}| \in [|\mathbf{p}^{\uparrow\downarrow}_{qq}|, |\mathbf{p}^{\uparrow\uparrow}_{qq}|] \tag{3.34}$$

$$\cos\alpha_{\rm eq}(|\mathbf{p}^{\rm crit}_{qq}|) \in [-1, 1] \tag{3.35}$$

For a given set of masses Eqs. (3.34) and (3.35) must be tested numerically for the resulting $|\mathbf{p}^{\rm crit}_{qq}|$.

If the critical solution is *not* physical, the maximum must lie on the boundary of the two-dimensional domain defined by Eqs. (3.34) and (3.35). For $\cos\alpha_{\rm eq} = \pm 1$ the appropriate $|\mathbf{p}_{qq}|$ can be found by redoing the procedure leading to (3.33) but with α fixed at 0 or π. This gives the following expression for $|\mathbf{p}_{qq}|$:

$$|\mathbf{p}^{\cos\alpha=\pm1}_{qq}| = \frac{\pm(m^2_{\tilde{\chi}^0_1}m^2_{\tilde{\chi}^0_2} - m^4_{\tilde{l}_R})}{4m_{\tilde{\chi}^0_2}m^2_{\tilde{l}_R}(m^2_{\tilde{\chi}^0_2} - m^2_{\tilde{l}_R})(m^2_{\tilde{l}_R} - m^2_{\tilde{\chi}^0_1})}\Big[- (2m^2_{\tilde{\chi}^0_2}m^2_{\tilde{l}_R} - m^2_{\tilde{\chi}^0_1}m^2_{\tilde{\chi}^0_2} - m^4_{\tilde{l}_R})$$

$$+\sqrt{(m^2_{\tilde{\chi}^0_1}m^2_{\tilde{\chi}^0_2}-m^4_{\tilde{l}_R})^2+4m^2_{\tilde{g}}m^2_{\tilde{l}_R}(m^2_{\tilde{\chi}^0_2}-m^2_{\tilde{l}_R})(m^2_{\tilde{l}_R}-m^2_{\tilde{\chi}^0_1})}\Big] \tag{3.36}$$

The invariant mass can then be found straightforward by taking $m^2_{qql_{\rm n}}=(p_{qq}+p_{l_{\rm n}})^2$ and using (3.13). This gives

$$\begin{aligned}\left(m^{\cos\alpha=\pm1}_{qql(\rm eq)}\right)^2 = &\Big[(m^2_{\tilde{g}}+m^2_{\tilde{l}_R})m_{\tilde{\chi}^0_2}-(m^2_{\tilde{\chi}^0_2}+m^2_{\tilde{l}_R})\sqrt{|\mathbf{p}^{\cos\alpha=\pm1}_{qq}|^2+m^2_{\tilde{g}}}\\ &\mp(m^2_{\tilde{\chi}^0_2}-m^2_{\tilde{l}_R})|\mathbf{p}^{\cos\alpha=\pm1}_{qq}|\Big]/m_{\tilde{\chi}^0_2}\end{aligned} \tag{3.37}$$

The boundary solutions at maximum and minimum $|\mathbf{p}_{qq}|$ are most easily found by inserting the boundary values (3.28)–(3.29) into the general solution (3.33). This gives

$$\left(m^{\uparrow\uparrow}_{qql(\rm eq)}\right)^2 = (m^2_{\tilde{g}}-m^2_{\tilde{\chi}^0_2})(m^2_{\tilde{l}_R}-m^2_{\tilde{\chi}^0_1})/(2m^2_{\tilde{l}_R}-m^2_{\tilde{\chi}^0_1}) \tag{3.38}$$

$$\begin{aligned}\left(m^{\uparrow\downarrow}_{qql(\rm eq)}\right)^2 = &\big[-(3m^2_{\tilde{l}_R}-m^2_{\tilde{\chi}^0_1})(m^2_{\tilde{g}}m^2_{\tilde{\chi}^0_2}+m^4_{\tilde{q}_L})+2m^2_{\tilde{q}_L}[m^2_{\tilde{g}}(2m^2_{\tilde{l}_R}-m^2_{\tilde{\chi}^0_1})+m^2_{\tilde{\chi}^0_2}m^2_{\tilde{l}_R}]\\ &+2m^2_{\tilde{q}_L}(m^2_{\tilde{l}_R}-m^2_{\tilde{\chi}^0_1})\varphi(|\mathbf{p}^{\uparrow\downarrow}_{qq}|)\big]/[2m^2_{\tilde{q}_L}(2m^2_{\tilde{l}_R}-m^2_{\tilde{\chi}^0_1})]\end{aligned} \tag{3.39}$$

All expressions (3.37)–(3.39) are formal. For a given set of masses one must explicitly (numerically) impose the one of Eqs. (3.34) and (3.35) which is not satisfied by construction.

3.2.4 General solution

Putting all this together, the fully general solution for $m^{\max}_{qql(\rm low)}$ is given by

$$m^{\max}_{qql(\rm low)}=\begin{cases} m^{\max}_{qql_{\rm n}} & \text{for} \quad m^2_{\tilde{\chi}^0_1}+m^2_{\tilde{\chi}^0_2}<2m^2_{\tilde{l}_R}\\ m^{\max}_{qql_{\rm f}} & \text{for} \quad \langle\text{cut1}\rangle\\ m^{\max}_{qql(\rm eq)} & \text{otherwise}\end{cases} \tag{3.40}$$

where

$$\begin{aligned}\langle\text{cut1}\rangle \;=\; &\left[\frac{m_{\tilde{g}}}{m_{\tilde{q}_L}}>\frac{m_{\tilde{q}_L}}{m_{\tilde{\chi}^0_2}}\frac{m_{\tilde{l}_R}}{m_{\tilde{\chi}^0_1}}\;\bigwedge\;\frac{m^4_{\tilde{\chi}^0_2}\left(m^2_{\tilde{g}}-m^2_{\tilde{q}_L}\right)\left(m^2_{\tilde{l}_R}-m^2_{\tilde{\chi}^0_1}\right)}{m^2_{\tilde{q}_L}m^2_{\tilde{l}_R}\left(m^2_{\tilde{q}_L}-m^2_{\tilde{\chi}^0_2}\right)\left(m^2_{\tilde{\chi}^0_2}-m^2_{\tilde{l}_R}\right)}<1\right]\\ \bigvee\;&\left[\frac{m_{\tilde{q}_L}}{m_{\tilde{\chi}^0_2}}>\frac{m_{\tilde{l}_R}}{m_{\tilde{\chi}^0_1}}\frac{m_{\tilde{g}}}{m_{\tilde{q}_L}}\;\bigwedge\;\frac{m^2_{\tilde{q}_L}\left(m^2_{\tilde{q}_L}-m^2_{\tilde{\chi}^0_2}\right)\left(m^2_{\tilde{l}_R}-m^2_{\tilde{\chi}^0_1}\right)}{m^2_{\tilde{l}_R}\left(m^2_{\tilde{g}}-m^2_{\tilde{q}_L}\right)\left(m^2_{\tilde{\chi}^0_2}-m^2_{\tilde{l}_R}\right)}<1\right]\\ \bigvee\;&\left[\frac{m_{\tilde{g}}}{m_{\tilde{q}_L}}<\frac{m_{\tilde{q}_L}}{m_{\tilde{\chi}^0_2}}\frac{m_{\tilde{l}_R}}{m_{\tilde{\chi}^0_1}}\;\bigwedge\;\frac{m_{\tilde{q}_L}}{m_{\tilde{\chi}^0_2}}<\frac{m_{\tilde{l}_R}}{m_{\tilde{\chi}^0_1}}\frac{m_{\tilde{g}}}{m_{\tilde{q}_L}}\bigwedge\frac{m_{\tilde{l}_R}}{m_{\tilde{\chi}^0_1}}<\frac{m_{\tilde{g}}}{m_{\tilde{q}_L}}\frac{m_{\tilde{q}_L}}{m_{\tilde{\chi}^0_2}}\right.\\ &\left.\bigwedge\;\frac{m^2_{\tilde{\chi}^0_2}\left(m_{\tilde{g}}m_{\tilde{l}_R}-m_{\tilde{\chi}^0_2}m_{\tilde{\chi}^0_1}\right)\left(m^2_{\tilde{l}_R}-m^2_{\tilde{\chi}^0_1}\right)}{m_{\tilde{l}_R}m_{\tilde{\chi}^0_1}\left(m_{\tilde{g}}m_{\tilde{\chi}^0_1}-m_{\tilde{\chi}^0_2}m_{\tilde{l}_R}\right)\left(m^2_{\tilde{\chi}^0_2}-m^2_{\tilde{l}_R}\right)}<1\right]\end{aligned} \tag{3.41}$$

is constructed from (3.22), (3.23) and (3.27) together with the appropriate region conditions. Expressions for $m^{\max}_{qql_{\rm n}}$ and $m^{\max}_{qql_{\rm f}}$ are given in Eqs. (2.24) and (2.25) respectively, and $m^{\max}_{qql(\rm eq)}$ is given by

$$m^{\max}_{qql(\rm eq)}=\max\left(m^{\rm crit}_{qql(\rm eq)},m^{\cos\alpha=\pm1}_{qql(\rm eq)},m^{\uparrow\uparrow}_{qql(\rm eq)},m^{\uparrow\downarrow}_{qql(\rm eq)}\right) \tag{3.42}$$

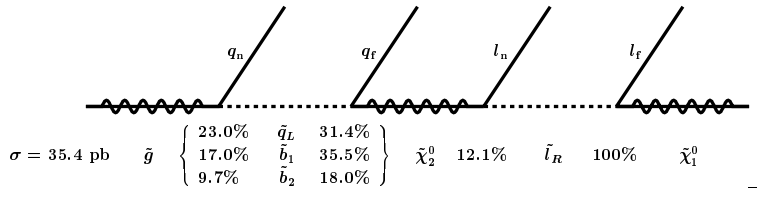

Figure 4: SPS 1a cascade decay with branching ratios and cross-sections.

which uses (3.33) and (3.37)–(3.39).

4. SPS 1a

The 'basic' SPS 1a point is defined by the following mSUGRA GUT-scale parameter values,

$$m_{1/2} = 250 \text{ GeV}, \ m_0 = -A_0 = 100 \text{ GeV}, \ \tan\beta = 10, \ \mu > 0 \tag{4.1}$$

evolved down to the electroweak scale by version 7.58 of `ISAJET` [18]. Table 3 shows the masses at the electroweak scale. The masses which enter the signal chain are shown in boldface.

$\tilde{g}$	$\tilde{d}_L$	$\tilde{d}_R$	$\tilde{u}_L$	$\tilde{u}_R$	$\tilde{b}_2$	$\tilde{b}_1$	$\tilde{t}_2$	$\tilde{t}_1$
595.2	**543.0**	520.1	**537.2**	520.5	**524.6**	**491.9**	574.6	379.1
$\tilde{e}_L$	$\tilde{e}_R$	$\tilde{\tau}_2$	$\tilde{\tau}_1$	$\tilde{\nu}_{e_L}$	$\tilde{\nu}_{\tau_L}$		$H^\pm$	A
202.1	**143.0**	206.0	133.4	185.1	185.1		401.8	393.6
$\tilde{\chi}_4^0$	$\tilde{\chi}_3^0$	$\tilde{\chi}_2^0$	$\tilde{\chi}_1^0$	$\tilde{\chi}_2^\pm$	$\tilde{\chi}_1^\pm$		H	h
377.8	358.8	**176.8**	**96.1**	378.2	176.4		394.2	114.0

Table 3: Masses [GeV] for the SPS 1a point.

Fig. 4 shows the signal chain with the relevant branching ratios. To the left the production rate of gluinos is shown, followed by the branching ratios of a gluino into left-handed squarks and both sbottom states. Since the mass difference between $\tilde{b}_1$ and the other squarks is comparable to the mass difference between the gluino and the squarks, phase space effects become significant, resulting in a noticeably enhanced decay rate into $\tilde{b}_1$. All the relevant squarks have a large branching ratio into $\tilde{\chi}_2^0$. The dominant decay of $\tilde{\chi}_2^0$ is into staus, but selectrons plus smuons take an important 12%, which is still sufficient. Due to the reconstruction problems of taus, the much smaller electron plus muon sample is strongly preferable to the tau sample.[2] Finally, the right-handed slepton decays with full rate into the LSP.

[2]For convenience of notation we will for the rest of the paper use 'lepton'/'slepton' for the two first generations and 'tau'/'stau' for the third generation.

	$\Sigma(\tilde{g})$	$\Sigma(\tilde{q}_L)$	$\Sigma(\tilde{q}_R)$	$\Sigma(\tilde{b}_1)$	$\Sigma(\tilde{b}_2)$	$\Sigma(\tilde{t}_1)$	$\Sigma(\tilde{\chi}_2^0)$
Direct	35.4	24.6	25.8	1.4	0.9	3.4	1.8
Indirect	-	8.2	14.6	6.3	3.5	5.6	16.0
Total	35.4	32.8	40.4	7.7	4.3	9.0	17.8

Table 4: Selected sparticle production rates in pb.

Table 4 shows 'sparticle production rates' of the most relevant sparticles. Rather than ordinary cross-sections these are rates of single sparticle production, so, for example, an event $gg \to \tilde{g}\tilde{g}$ counts twice for the gluino production rate. Direct production, where the sparticle is produced in the initial collision, and indirect production, where the sparticle is produced by a decay, are separated. Since the gluino is the heaviest sparticle, it is only produced directly. For squarks the indirect production from gluino decay is significant, especially for flavours of low abundance in the proton.

5. Data analysis

For the purpose of studying the feasibility of extracting the gluino mass from kinematical endpoints, we have investigated various distributions, as they might appear at the LHC.

5.1 Event generation and Standard Model rejection

Signal and background are generated for 300 fb^{-1}, which corresponds to three years at design luminosity of 10^{34} cm^{-2}s^{-1}. The simulation setup is identical to the one used for the squark-endpoint analysis. GUT-scale parameters are evolved to low-energy by ISAJET 7.58 [18] and passed, via the standard interface, to PYTHIA 6.2 [19] which calculates the decay widths and the LHC cross-sections by use of CTEQ 5L [20] PDF's. Finally ATLFAST 2.60 [21] performs a parametrised fast simulation of the ATLAS detector. See Sect. 5.1 of [12] for further details. In that study the squark kinematical endpoints were measured, so we focus here only on the gluino distributions.

The signature of a signal event is two opposite-sign same-flavour (SF) leptons, considerable missing p_T from the escaping LSPs, and at least three quite hard jets, two from the signal chain and one from the decay of the squark nearly always present in the other decay chain. (Only one of the chains is reconstructed, even if the other chain should contain the signal as well.) The most important Standard-Model process to have features similar to the signal is $t\bar{t}$ production. An extra jet is needed, but a hadron collider usually provides additional jets.

Also W/Z together with jets, one of which is a b-jet, can mimic the signal, and in combination with the underlying event, pile-up and detector effects, other processes will also now and then result in the given signature. Together with $t\bar{t}$ we therefore include QCD, Z/W+jet as well as $ZZ/ZW/WW$ production. No K-factors have been used.

The precuts (not tuned) used to isolate the chain are the following:

- At least four jets, satisfying: $p_T^{\text{jet}} > 150, 100, 50, 20$ GeV

- $E_{T,\mathrm{miss}} > \max(100\ \mathrm{GeV}, 0.2M_{\mathrm{eff}})$ with $M_{\mathrm{eff}} \equiv E_{T,\mathrm{miss}} + \sum_{i=1}^{4} p_{T,i}^{\mathrm{jet}}$
- Two isolated opposite-sign same-flavour (SF) leptons satisfying $p_T^{\mathrm{lep}} > 20, 10$ GeV

The QCD background is cut away by the requirement of two leptons and of considerable missing p_T. For the processes involving Z and W the requirement of high hadronic activity together with the missing p_T removes nearly all events. After the rather hard cuts listed above, the Standard-Model background consists of approximately 95% $t\bar{t}$. However, because of the large SUSY cross-section for this scenario, the main background comes from other SUSY processes.

5.2 Three background types

It is convenient to divide the background into three different parts, 'lepton-uncorrelated', 'lepton-correlated' and 'combinatorial'. The two first consist of events which do not contain the signal chain. In the *lepton-uncorrelated* background two leptons are produced, but in different parts of the decay and therefore independently. With the assumption of lepton universality and neglecting the mass difference between electrons and muons, which is very reasonable for the energies involved, this background type will produce the same amount of each of e^+e^-, $\mu^+\mu^-$, $e^+\mu^-$ and μ^+e^-. On a statistical basis these four event types, and in particular the same-flavour versus the different-flavour events, will in no way differ in number of jets, hardness, event shape, etc. If otherwise satisfying the precuts, the lepton-uncorrelated same-flavour events will be part of and contaminate our sample. While it is of course not possible to know on an event by event basis which of the selected events are lepton-uncorrelated, we do know that their distribution is identical to the different-flavour distribution. Thus, by collecting the different-flavour sample (with the same precuts) and subtracting this from the same-flavour sample, the contribution of the lepton-uncorrelated events is canceled. The cost is an increased statistical error per histogram bin, $\sigma^2_{\mathrm{SF-DF}} = \sigma^2_{\mathrm{SF}} + \sigma^2_{\mathrm{DF}}$. In addition to lepton universality, for this 'different-flavour-subtraction' procedure to work perfectly, the acceptance of electrons and muons must be identical, and the reconstruction of same-flavour events and different-flavour events must have the same efficiencies. If these conditions are not met, corrections are needed. In this study we have assumed perfect working conditions, although it is known that the fast simulation does not treat nearby same-flavour and different-flavour leptons on an equal footing, see Sect. 5.2 of [12].

For the *lepton-correlated* background, the leptons are always same-flavour, so no different-flavour sample is available to show its distribution. These events typically come from the decay of Z, in which case they can to some degree be controlled, or from sleptonic decay of neutralinos. In the latter case no particular signature, e.g. in the m_{ll} distribution, is available to discriminate this background from the signal. In particular much of this background will come from $\tilde{\chi}_2^0$'s decaying sleptonically, but which are not part of our signal chain. For the analysis of the squark chain, as done in [12], one important criterion is that the $\tilde{\chi}_2^0$'s produced from squarks make up a good fraction of the total $\tilde{\chi}_2^0$ production. Events with $\tilde{\chi}_2^0$'s not originating from the relevant squarks usually still contain jets and constitute

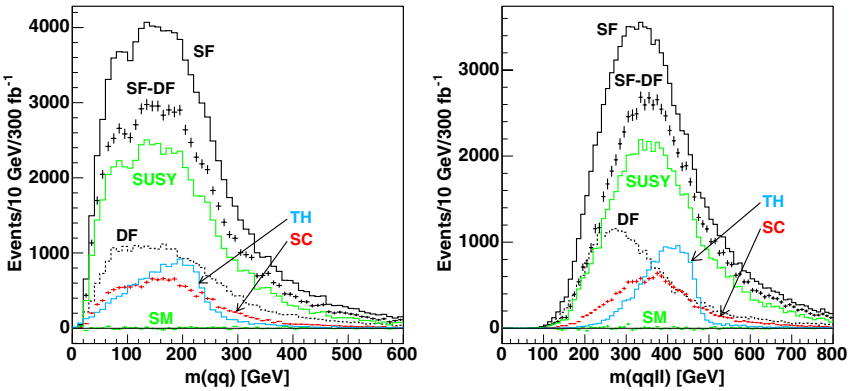

Figure 5: Invariant mass distributions for non-b-tagged events. Endpoints not detectable. See the text for details.

a large part of the background. As the signal chain grows longer, this background increases relative to the signal. In the case of the whole gluino chain what is important is that the $\tilde{\chi}_2^0$'s with a gluino grandparent are not severely outnumbered by the total $\tilde{\chi}_2^0$ production, for the events selected. This is a stricter criterion, and we will find that the flavour of the intermediate squark, whether it is $\tilde{q}_L$ or $\tilde{b}$, will be crucial for the isolation of the signal.

The third background type, combinatorial background, is a result of our inability to know which of the jets correspond to the quark sent out from the gluino ($q_{\rm n}$) and from the squark ($q_{\rm f}$). In most analyses one assumes that the quark from a squark decay can on average be distinguished from the quark from a gluino decay on the basis of hardness. In most mSUGRA scenarios this is viable, as $\tilde{\chi}_2^0$ is so much lighter than the squark. Since two squarks are expected in nearly all events, assuming here $m_{\tilde{g}} > m_{\tilde{q}}$, one can then attribute the two hardest jets to the decay of the two squarks. Remaining jets can then be attributed to gluino decays, other quarks in the event, e.g. from the decay of t or W, and/or the underlying event. The exact jet selection algorithms used in this study are based on these assumptions, and will be detailed in the subsections below.

In more general SUSY scenarios it need not be the case that $q_{\rm f}$ is harder than $q_{\rm n}$. In general, given an unknown SUSY scenario, the appropriate jet selection procedure must be the result of a careful study. For this also the mass hierarchy of the gluino and the squarks must be established. A systematic study of how such information can be obtained is lacking but would be very valuable.

5.3 Non-b-tagged distributions

In Fig. 5 two of the non-b-tagged distributions, m_{qq} and m_{qqll}, are shown. The black solid and dashed curves show the same-flavour ('SF') and different-flavour ('DF') distributions. In black with error bars their difference, the different-flavour-subtracted distribution ('SF-DF') is shown. Solid green shows the SUSY background ('SUSY'). Its shape is given by the lepton-correlated part, but the lepton-uncorrelated part is also significant and increases

the random fluctuations. Dashed green shows the negligible Standard Model background ('SM'). For both backgrounds different-flavour subtraction is performed. The blue curve shows the parton-level distribution of the selected events ('TH'), while the red points with error bars show the part of the different-flavour-subtracted sample which contains the correct signal chain ('SC'), also referred to as the 'signal-chain distribution'. Any discrepancy between these two distributions is mostly due to combinatorial background, i.e. from picking the wrong jets.

For these distributions it was assumed that $q_{\rm f}$ is one of the two hardest jets while $q_{\rm n}$ is selected among number 3 and 4 in p_T-hardness. This is in line with the mass assumptions usually valid in mSUGRA scenarios, as described above. The jet selection used for the distributions plotted is, on an event-by-event basis, the one out of four possible combinations which gave the smallest m_{qqll} value. Other selection algorithms were also tried. In addition we require that neither of the involved jets is b-tagged.

It is clear that the positions of the endpoints, which are seen in the parton-level distributions (solid blue), are not easily detectable from the different-flavour-subtracted sample. This is mainly due to the size of the lepton-correlated part of the SUSY background (solid green), which makes up $\sim 80\%$ of the total sample. Structures in the signal part of the sample are therefore not easily identified. This result can be anticipated from Table 4, which shows that only $8.2/32.8 = 25\%$ of $\tilde{q}_L$'s originate from a gluino. The ratio of gluino-induced $\tilde{\chi}_2^0$'s becomes therefore quite small.

Another difficulty is the combinatorial background. The red points with errors, which include signal events only, do not at all point to the nominal endpoints at 242 GeV and 490 GeV (for $\tilde{u}_L$). This is because the jet pair selected is often not the correct one.

Other jet selection algorithms of this simple type have been tried, but none allows any edge structure caused by the kinematics of the decay chain to be recognised. This is also true for the other five gluino distributions (not shown). One must therefore conclude that the endpoints of the non-b-tagged gluino distributions are not experimentally obtainable by looking at one distribution at a time. If instead correlations between mass distributions were investigated it might be possible to identify endpoint-related edge structures.

5.4 b-tagged distributions

The distributions of the b-tagged samples are shown in Figs. 6–7. The curves follow the colour code of Fig. 5, but the same-flavour and different-flavour distributions are not shown separately, only their difference. For the b-tagged distributions the different-flavour distribution is $\sim 40\%$ of the same-flavour distribution, which is somewhat larger than for the non-b-tagged distribution where the ratio is $\sim 25\%$. In both cases the different-flavour distribution favours lower mass values and does not interfere very much with the edge structure, as seen in Fig. 5 for the non-b-tagged distribution.

Contrary to the previous case, the b-tagged distributions have clear edge structures which provide values for the endpoints. The main reason for this is that the different-flavour-subtracted SUSY background (solid green) now makes up a manageable 35%, to be compared with 80% for the non-b-tagged sample. This reduction is due to the fact that *the majority of $\tilde{b}$'s are produced indirectly from gluino decay* [because of the low b-content

of the proton], see Table 4, in combination with a jet selection requirement of exactly two b-tagged jets. Although the total production of $\tilde{\chi}_2^0$ is 6–7 times larger (see Fig. 4 and Table 4) than the production which starts out from $\tilde{g} \to \tilde{b}b$, two b-jets are also needed, which reduces considerably the number of selected background events. (For background events the b's are usually produced in the other chain, typically from the same $\tilde{g} \to \tilde{b}b$, or from $\tilde{g} \to \tilde{t}_1 t$ in either of the chains, which also produces multiple b's.) Since the rate of b-jets is considerably smaller than the rate of light jets, also in SUSY events, we are likely not to have additional b-jets in a signal event. The combinatorial background is therefore small, as is clear from the good correspondence between the parton-level distribution ('TH') and the signal-chain distribution ('SC').

The exact jet-selection used here is in line with the previous assumption that $b_{\rm f}$ is harder than $b_{\rm n}$. The first is searched for among the two p_T-hardest, the second among number three and four. Only events which have one b-jet among the two hardest and one among the two next were selected. (In a more realistic study where emphasis is put on issues like fitting techniques, impact on the distributions from the precuts etc., it would be natural to investigate the effect of also including events which have their two b-tagged jets as number 1 and 2 or as number 3 and 4.)

For the distributions in Fig. 7 no endpoint estimation is attempted. The two $m_{b_{\rm n}l}$ distributions are distrusted since they do not usually 'point' towards the maximum value, as shown in Fig. 3. The phase space corresponding to the largest values is very small, leaving only an experimentally undetectable tail to mark the endpoint. These distributions are furthermore made less useful by the need to distinguish $b_{\rm n}$ from $b_{\rm f}$. For the distributions of Fig. 6 this is not an issue because both b's were used. At SPS 1a the endpoints involving $b_{\rm n}$ have smaller nominal value than the corresponding endpoints with $b_{\rm f}$. Consequently, if we are not able to cleanly distinguish $b_{\rm n}$ from $b_{\rm f}$, all distributions which have $b_{\rm n}$ as the only quark will get a contamination which stretches beyond the endpoints. If this contamination is substantial, and here it is, the $b_{\rm n}$ endpoints will be washed out. The combination of these two effects seems to disable these three distributions. The nominal endpoints are $m^{\rm max}_{b_{\rm n}ll} = 281$ GeV, $m^{\rm max}_{b_{\rm n}l({\rm low})} = 197$ GeV and $m^{\rm max}_{b_{\rm n}l({\rm high})} = 248$ GeV, which are clearly not obtainable from the distributions in Fig. 7. To cope with the problem of distinguishing $b_{\rm n}$ and $b_{\rm f}$ more general distributions could be constructed, as was discussed in Sect. 2.4.

For m_{bb} the fit values are a considerable 25 GeV higher than the nominal value, and are not really accounted for by the errors. It is not completely understood why the discrepancy is so large; whether it is a statistical fluctuation or some other effect. Since the reconstruction resolution is much worse for jets than for leptons, one should expect that a mass distribution constructed from jets alone will be more smeared and therefore give worse endpoint determination than one which also involves leptons. This is probably part of the reason.

To extract the endpoints from the distribution, signal and background hypotheses are needed. Usually, at this level of detail, a straight line is used for the signal in the edge region. We see from the theory distribution of Fig. 3 that the straight-line hypothesis in the edge region is normally quite well supported for the four distributions of Fig. 6. (The

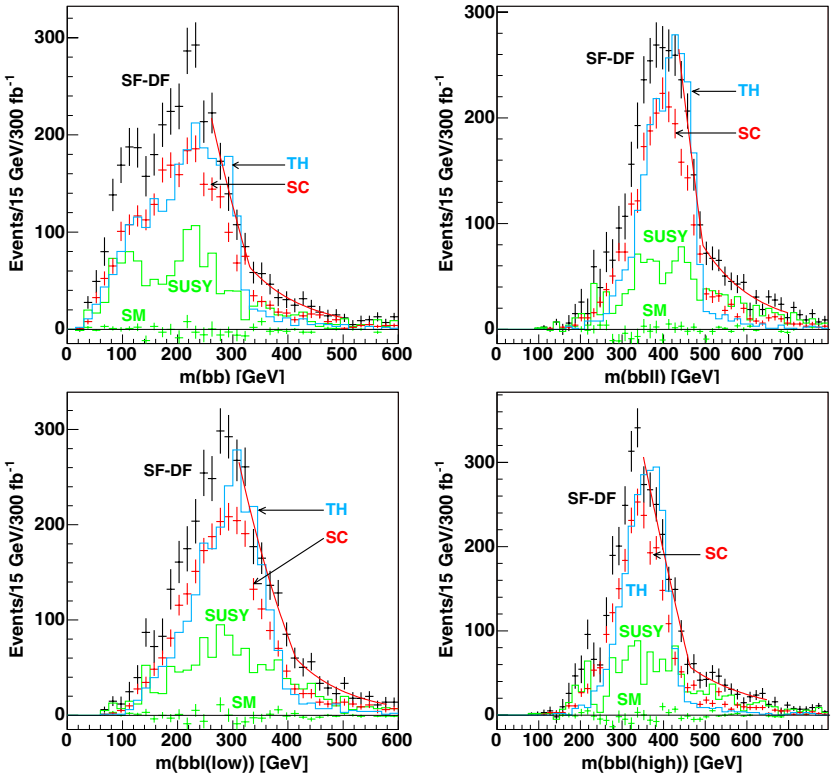

Figure 6: Four good b-tagged invariant mass distributions. See the text for details.

exception is $m_{qql(\text{high})}$, which in some cases might have a dangerous foot at the very last part of the edge.)

Which background hypothesis to use is less clear. The background is here mainly from other SUSY processes, and therefore in principle unknown. One attempt to sketch the shape of the background, is by combining the lepton and the jet sectors of different events into a mixed-event sample, as described in Sect. 5 of [12]. The shapes of the mixed-event distributions are then used as background hypotheses. Another way is to simply select for the background some appropriate function, based on the distribution slightly beyond the edge, where only background resides. An exponential or a polynomial usually gives a fair description. Whatever the signal and background hypotheses, systematics are introduced which may not always be easy to estimate.

For the plots of Fig. 6 the signal was fitted with a straight line, while the background was modeled by both an exponential and a mixed-event sample. A four/three-parameter fit was then performed by use of MINUIT [22] for exponential/mixed-event background hypothesis and several different histogram binnings and fit ranges. Each distribution gives

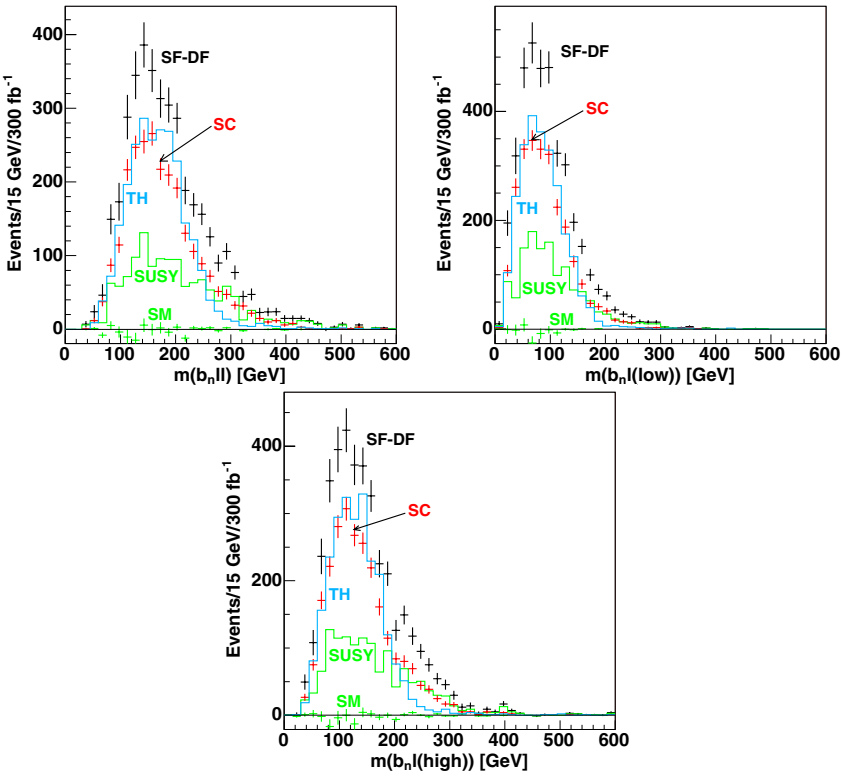

Figure 7: Three bad b-tagged invariant mass distributions. See the text for details.

fit values and statistical errors within a fairly narrow interval, indicative of the systematic uncertainty in the fitting procedure. The results of the fits are summarized in Table 5 at the end of this section, after the discussion of energy scale errors.

5.5 Propagation of energy scale errors

In ATLAS it is expected that the absolute energy scale of jets and leptons will be known to 1% and 0.1%, respectively, see Ch. 12 of [23]. This energy scale uncertainty translates into an uncertainty, or 'error', for any mass constructed from jets and/or leptons. In particular, the masses which go into our distributions have such an error in addition to the statistical error.

Invariant masses which are constructed from jets alone or leptons alone, will inherit their uncertainties of 1% or 0.1%, respectively. For an invariant mass made from one lepton and one jet, the energy scale error is at 0.5%. For masses constructed from more than two jets and leptons, the energy scale error is not constant, but varies within a given calculable

interval, depending on whether it is the jet(s) or the lepton(s) which dominate the mass for the given event.

To find appropriate energy scale errors, we must investigate m_{qqll}, m_{qql} and m_{qll}. The overall masses can be expressed in terms of two-particle masses, which have a constant energy scale error:

$$m^2_{qqll} = m^2_{qq} + m^2_{q_{\rm n}l_{\rm n}} + m^2_{q_{\rm n}l_{\rm f}} + m^2_{q_{\rm f}l_{\rm n}} + m^2_{q_{\rm f}l_{\rm f}} + m^2_{ll} \tag{5.1}$$

$$m^2_{qql} = m^2_{qq} + m^2_{q_{\rm n}l} + m^2_{q_{\rm f}l} \tag{5.2}$$

$$m^2_{qll} = m^2_{ql_{\rm n}} + m^2_{ql_{\rm f}} + m^2_{ll} \tag{5.3}$$

Absolute lower/upper limits for the energy scale error of the quantities on the left-hand side can then be found by assuming that the right-hand side is totally dominated by the term which has the smallest/largest energy scale error. This results in

$$\frac{\sigma(m_{qqll})}{m_{qqll}} \in (0.1, 1)\%, \quad \frac{\sigma(m_{qql})}{m_{qql}} \in (0.5, 1)\%, \quad \frac{\sigma(m_{qll})}{m_{qll}} \in (0.1, 0.5)\% \tag{5.4}$$

where σ denotes the energy scale error. These are absolute limits valid for any mass scenario. To find the relevant numbers for SPS 1a, all accepted events were reexamined; scaling the jet momenta of each event by 1.01 and taking the ratio of the new and the old invariant mass. We then find the following average and root-mean-square values (in parentheses) of the relevant energy scale errors,

$$\begin{aligned} \frac{\sigma(m_{bbll})}{m_{bbll}} &= 0.66(0.10)\%, & \frac{\sigma(m_{bbl(\rm low)})}{m_{bbl(\rm low)}} &= 0.80(0.11)\% \\ \frac{\sigma(m_{bbl(\rm high)})}{m_{bbl(\rm high)}} &= 0.71(0.10)\%, & \frac{\sigma(m_{b_{\rm n}ll})}{m_{b_{\rm n}ll}} &= 0.42(0.02)\% \end{aligned} \tag{5.5}$$

Inclusion of the lepton energy scale will give a small correction to these numbers. For $m_{b_{\rm n}ll}$, which we will not be using, the energy scale is nearly constant. For the three other distributions, the errors lie between approximately 0.5% and 1%, and fairly uniformly distributed, as is reflected in the root-mean-square values. For the fitting, only the energy scale error for masses which lie in the edge region is relevant. However, it turns out that at SPS 1a and for these distributions, the error is almost the same for low as for high invariant mass values. Although the error of each distribution is found to lie in a fairly broad interval rather than being constant for all events, we have here used the average values, Eq. (5.5), as a basis for the energy scale errors in Table 5.

An alternative approach could be to scale the jet momenta up/down as done above, then redo the entire fitting process on the new distributions and from this extract the effect of the energy scale error. For this to work one would have to disentangle the effect of the scaling from the yet uncontrolled systematics of the fitting procedure. At the present stage of fitting competence the gain from using a more correct procedure is probably lost in the increased complexity.

Edge	Nominal Value [GeV]	Fit Value [GeV]	Energy Scale Error ($\sigma^{\rm scale}$) [GeV]	Statistical Error ($\sigma^{\rm stat}$) [GeV]
$m_{bb}^{\rm max}$	312.7	335–339	3.4	6–10
$m_{bbll}^{\rm max}$	496.3	494–500	3.3	5–7
$m_{bbl({\rm low})}^{\rm max}$	413.2	407–417	3.3	8–12
$m_{bbl({\rm high})}^{\rm max}$	461.9	454–462	3.3	5–7

Table 5: Endpoint values found from fitting the edges in Fig. 6, for 300 fb^{-1}. The nominal values correspond to the mass of $\tilde{b}_1$ which is produced at significantly higher rates than the heavier $\tilde{b}_2$. The energy scale errors are based on the discussion in Sect. 5.5. No values are given for the three distributions in Fig. 7.

6. Masses from endpoints

6.1 10,000 ATLAS experiments

The precision with which the sparticle masses can be obtained at the LHC, is found from the endpoint-measurement values of Table 5. For this we do not use the specific fit values of the simulation undertaken in the previous section, but instead generate an ensemble of LHC experiments, constructed from the estimated *errors* found in the previous section, as done in [10]. An ensemble of 10,000 experiments is generated, where endpoint fit values are generated by assuming a Gaussian distribution around the nominal values. The width of the Gaussians are given by $\sigma^{\rm scale}$ and $\sigma^{\rm stat}$. Within one experiment the $\sigma^{\rm scale}$ errors of the endpoints are correlated, as they originate from the common jet and lepton energy scale uncertainty.

For each experiment the endpoint values $\mathbf{E}^{\rm exp}$ are combined with the general endpoint expressions $\mathbf{E}^{\rm th}$ in a least-square function Σ,

$$\Sigma = [\mathbf{E}^{\rm exp} - \mathbf{E}^{\rm th}(\mathbf{m})]^T \mathbf{W} [\mathbf{E}^{\rm exp} - \mathbf{E}^{\rm th}(\mathbf{m})] \tag{6.1}$$

The weight matrix $\mathbf{W}$ is the inverse of the covariance matrix which is constructed from the endpoint errors and appropriately handles the endpoint correlations due to the energy scale error. The minimisation of Σ then yields the masses. Due to the composite nature of the endpoint expressions, there are usually several competing Σ minima for a given set of endpoints. If these minima are close in Σ value, they must all be considered, opening the way for multiple mass solutions. Finally, ensemble distributions for the masses can be plotted and studied, and are to be interpreted as probability distributions for the masses which can be obtained at the LHC. We will be interested in the mean and width of these ensemble distributions. For more details of the procedure, see [12].

6.2 Mass estimation

In total six sparticles are involved in our decay chains: $\tilde{\chi}_1^0$, $\tilde{l}_R$, $\tilde{\chi}_2^0$, $\tilde{q}_L$, $\tilde{b}_1$ and $\tilde{g}$. The masses of the first five of these could already be obtained from the squark endpoints alone, as was done in [12]. The gluino mass is accessed by the gluino endpoints which add (at

present) three more usable measurements, those of Table 5, excluding $m_{b\bar{b}}^{\max}$. Since the gluino endpoints also involve the other masses (except $m_{\tilde{q}_L}$), the six squark endpoints and the three gluino endpoints are combined in a single fit where all the masses are free parameters. The squark-endpoint measurements are given in Table 4 (upper part) of [12]. The values of the right-most column, 'Syst. Fit Error' are not used. For the gluino endpoints of Table 5 (in the present paper) the statistical error is given as an interval. We take here the midpoint of the interval, and also assume that the systematics of the fit values (also given by intervals) will be settled, or at least dominated by the statistical errors. This assumption might be somewhat optimistic, and should be kept in mind when contemplating the results obtained below. Furthermore, we have decided to use only three out of seven gluino distributions. In particular the choice of excluding $m_{b\bar{b}}^{\max}$ was made after consultation with the Monte Carlo truth at our specific SUSY scenario, which is not a viable strategy in a realistic setting. More study could however promote this result into a generic one.

If we start from the squark endpoints and add only *one* of the gluino endpoints in the numerical fit, the gluino mass will be determined and all the other masses will remain unchanged. This is so because there is exactly one new measurement for one new mass. The gluino mass returned from the fit is the one which gives zero for the new terms added to Σ, so there is no increase in the Σ-value. Also, the number of minima remains unchanged by adding one more measurement for one more mass. This situation is similar to the determination of $m_{\tilde{b}_1}$ in [12]. Only one endpoint involves $\tilde{b}_1$, so its inclusion has no effect on the other masses or number of minima.

When more gluino endpoints are added, the gluino sector becomes over-determined, and the position of the minima will change, i.e. the other masses will be affected. Since the gluino endpoints have somewhat larger errors than the squark endpoints, large effects are not expected, except perhaps for $\tilde{b}_1$. Below, results are given for the case when all three gluino endpoints are used.

For the current precision of the endpoint measurements, the numerical fit nearly always returns two minima, one in mass region *(1,1)*, which is the region of the nominal masses at SPS 1a, and one in mass region *(1,2)*. If the minima are close in Σ-value, both must be considered. Table 6 shows the probability of having more than one solution in an experiment. The cut on $\Delta\Sigma$, the distance to the global minimum, gives the quality of the second minimum. In most cases the *(1,1)* minimum is the selected one. These numbers are very similar to the numbers obtained without the gluino endpoints, Table 5 of [12], where a more detailed description can also be found.

	# Minima	*(1,1)*	*(1,2)*
$\Delta\Sigma \leq 0$	1.00	91%	9%
$\Delta\Sigma \leq 1$	1.11	95%	16%
$\Delta\Sigma \leq 3$	1.30	98%	32%
$\Delta\Sigma \leq 99$	1.87	99%	87%

Table 6: Number of minima for various $\Delta\Sigma$ cuts and their whereabouts.

The masses are given in Table 7 for minima which satisfy $\Delta\Sigma \leq 1$. These results are very close to the results obtained without the gluino endpoints, see Table 6 of [12]. Only $\tilde{b}_1$ is affected, as was expected.

The gluino mass is quite well determined. The ensemble mean is at the nominal value,

		(1,1)		*(1,2)*	
	Nom	Mean	RMS	Mean	RMS
$m_{\tilde{\chi}_1^0}$	96.1	96.3	3.7	85.5	3.4
$m_{\tilde{l}_R}$	143.0	143.2	3.7	130.6	3.8
$m_{\tilde{\chi}_2^0}$	176.8	177.0	3.6	165.7	3.5
$m_{\tilde{q}_L}$	537.2	537.5	6.0	523.5	5.0
$m_{\tilde{b}_1}$	491.9	492.2	12.5	471.8	12.6
$m_{\tilde{g}}$	595.2	595.5	7.2	582.5	6.8
$m_{\tilde{l}_R} - m_{\tilde{\chi}_1^0}$	46.92	46.93	0.28	45.11	0.72
$m_{\tilde{\chi}_2^0} - m_{\tilde{\chi}_1^0}$	80.77	80.77	0.18	80.19	0.29
$m_{\tilde{q}_L} - m_{\tilde{\chi}_1^0}$	441.2	441.2	3.1	438.0	2.8
$m_{\tilde{b}_1} - m_{\tilde{\chi}_1^0}$	395.9	396.0	11.2	386.3	11.2
$m_{\tilde{g}} - m_{\tilde{\chi}_1^0}$	499.1	499.2	5.6	497.0	5.4
$m_{\tilde{g}} - m_{\tilde{b}_1}$	103.3	103.3	9.1	110.7	9.5

Table 7: Masses (Mean) and root-mean-square deviations from the mean (RMS) of minima in regions *(1,1)* and *(1,2)*, for $\Delta\Sigma \leq 1$. The nominal masses (Nom) are given in the second column. All values in GeV. See the text for more details.

and the root-mean-square deviation from the mean is 7.2 GeV, only a GeV more than for $m_{\tilde{q}_L}$. For the other masses, especially the lighter ones, mass differences are much more accurately determined than the masses themselves. This is also the case for the gluino, although to a lesser degree, as is seen from the smaller root-mean-square value for $m_{\tilde{g}} - m_{\tilde{\chi}_1^0}$ of 5.6/5.4 GeV. When the correlation to $\tilde{\chi}_1^0$ is taken into account, as in mass differences, $\tilde{q}_L$ is better determined than $\tilde{g}$, as it naively should be from the smaller squark endpoint errors. Since the gluino endpoints involve the sbottom mass, one might expect that the masses of $\tilde{g}$ and $\tilde{b}_1$ have a considerable correlation. Some correlation is found, as can be seen from comparing the root-mean-square value of $m_{\tilde{g}} - m_{\tilde{b}_1}$ with that of $m_{\tilde{b}_1}$ alone.

The ensemble distributions summarized in Table 7, i.e. for $\Delta\Sigma \leq 1$, are shown in Fig. 8. The unfilled distributions in black show from left to right $m_{\tilde{\chi}_1^0}$, $m_{\tilde{l}_R}$, $m_{\tilde{\chi}_2^0}$, $m_{\tilde{b}_1}$, $m_{\tilde{q}_L}$ and $m_{\tilde{g}}$ for solutions in the nominal region *(1,1)*. We will have such a solution in 95% of the experiments, see Table 6. The unfilled distributions in blue (grey) show the same masses for solutions in region *(1,2)*. Such a solution occurs in 16% of the experiments. (For $\Delta\Sigma \leq 1$ there is an 11% chance of having both solution types.) The smaller rate of the *(1,2)* solutions is reflected in the smaller area under the blue curves. The *(1,2)* solutions return slightly lower masses, so these distributions are positioned 'down' (due to the lower rate) and slightly to the left of the *(1,1)* distributions. The filled distributions show from left to right $m_{\tilde{l}_R} - m_{\tilde{\chi}_1^0}$, $m_{\tilde{\chi}_2^0} - m_{\tilde{\chi}_1^0}$, $m_{\tilde{g}} - m_{\tilde{b}_1}$, $m_{\tilde{b}_1} - m_{\tilde{\chi}_1^0}$, $m_{\tilde{q}_L} - m_{\tilde{\chi}_1^0}$ and $m_{\tilde{g}} - m_{\tilde{\chi}_1^0}$. Again, the most populated distributions (black curves) are for solutions in region *(1,1)*, the least populated (blue curves) for *(1,2)* solutions. For mass *differences* there is more overlap between the *(1,1)* and *(1,2)* solutions, in particular for $m_{\tilde{l}_R} - m_{\tilde{\chi}_1^0}$ and $m_{\tilde{\chi}_2^0} - m_{\tilde{\chi}_1^0}$, of which only the lower parts of the distributions are visible. Mass differences are better determined than the masses themselves, reflected here by the narrower distributions of the former. In

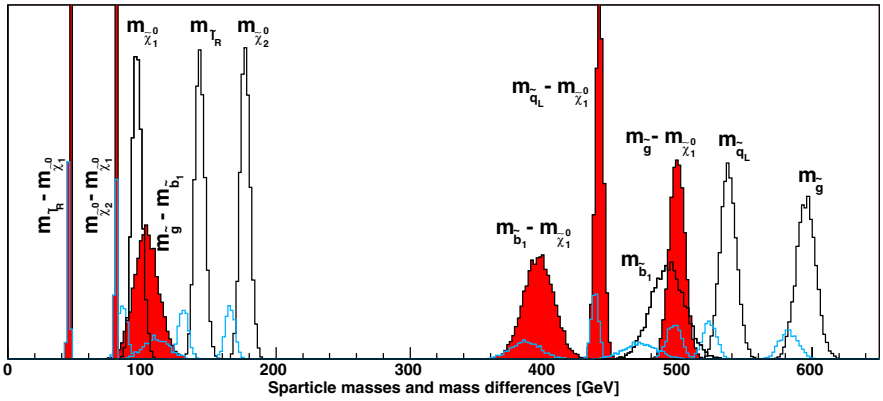

Figure 8: Sparticle masses and mass differences for solutions with $\Delta\Sigma \leq 1$. See the text for details.

the case of $\tilde{b}_1$ this effect is clear for $m_{\tilde{g}} - m_{\tilde{b}_1}$, much less so for $m_{\tilde{b}_1} - m_{\tilde{\chi}_1^0}$, which points to the fact that $\tilde{b}_1$ largely decouples from $\tilde{\chi}_1^0$,

6.3 Edge sensitivities

It may seem a puzzle that $m_{\tilde{g}}$ is determined with much higher precision than $m_{\tilde{b}_1}$. Both masses enter the three new gluino endpoints, but $m_{\tilde{b}_1}$ has in addition the $m^{\min}_{b_f l l(\theta > \frac{\pi}{2})}$ measurement. Naively one might therefore expect the $\tilde{b}_1$ mass to be more precisely determined.

In order to better see how masses are constrained by the endpoint formulas, consider the part of the least-square function Σ which involves one given endpoint and one given mass only. For simplicity of argument, assume that the endpoint measurement is at the nominal value, as are the masses. Changing the given mass away from the nominal value by an amount Δm will give an increase of our selected Σ part by

$$\Big(\frac{E(m+\Delta m) - E^{\rm exp}}{\sigma_E}\Big)^2 \approx \Big(\frac{E(m) + (\partial E/\partial m)\Delta m - E^{\rm exp}}{\sigma_E}\Big)^2 = \Big(\frac{(\partial E/\partial m)\Delta m}{\sigma_E}\Big)^2 \quad (6.2)$$

where E is the value of a particular kinematical endpoint. The value of Δm which gives an increase of Σ by 1 (from this term only), is then given by

$$\Delta m = \frac{\sigma_E}{(\partial E/\partial m)} \quad (6.3)$$

Since the shift in mass also induces changes to other contributions to Σ, the interpretation of Δm is not straight-forward in terms of mass error. Still, Δm does combine the precision of the endpoint, given by the endpoint error σ_E, with the response of the endpoint to the mass, which are the two important quantities. The same relation could be derived in a mathematically more intuitive way,

$$\Delta m = \Big(\frac{\partial m}{\partial E}\Big)\Delta E = \frac{\sigma_E}{(\partial E/\partial m)} \quad (6.4)$$

where the endpoint variation ΔE is set equal to the experimental error σ_E.

Inclusion of the endpoint error opens for comparison between different endpoints, even if only in a semi-quantitative way which does not take correlations into account. The importance of the different endpoints in constraining a given mass can then be studied. In Table 8, values for $\partial E/\partial m$ and Δm are given for both the squark and the gluino endpoints. For the three gluino endpoints of Fig 7, where no fit was made and hence no σ is available, Δm is not given.

	$\tilde{\chi}_1^0$		$\tilde{l}_R$		$\tilde{\chi}_2^0$		$\tilde{q}_L$		$\tilde{b}_1$		$\tilde{g}$	
	$\frac{\partial E}{\partial m}$	Δm	$\frac{\partial E}{\partial m}$	Δm	$\frac{\partial E}{\partial m}$	Δm	$\frac{\partial E}{\partial m}$	Δm	$\frac{\partial E}{\partial m}$	Δm	$\frac{\partial E}{\partial m}$	Δm
$m_{ll}^{\max}$	-0.7	-0.1	-0.6	-0.2	1.3	0.1	-	-	-	-	-	-
$m_{q_f ll}^{\max}$	-1.9	-1.2	-	-	0.7	3.2	0.9	2.6	-	-	-	-
$m_{q_f ll(\theta>\frac{\pi}{2})}^{\min}$	-0.8	-3.2	-1.6	-1.5	1.7	1.4	0.4	6.2	-	-	-	-
$m_{q_f l(\mathrm{low})}^{\max}$	-	-	-3.9	-0.4	3.0	0.6	0.6	2.8	-	-	-	-
$m_{q_f l(\mathrm{high})}^{\max}$	-3.2	-0.7	2.2	1.0	-0.3	-8.2	0.8	2.7	-	-	-	-
$m_{b_f ll(\theta>\frac{\pi}{2})}^{\min}$	-0.7	-6.5	-1.5	-3.1	1.5	3.0	-	-	0.4	11.8	-	-
$m_{bb}^{\max}$	-	-	-	-	-0.3	-39.6	-	-	-1.3	-8.1	1.7	6.3
$m_{bbll}^{\max}$	-1.3	-5.2	-	-	0.3	23.4	-	-	-0.1	-65.1	1.0	6.5
$m_{bbl(\mathrm{low})}^{\max}$	-	-	-2.3	-4.5	1.5	6.8	-	-	-0.6	-19.0	1.3	8.4
$m_{bbl(\mathrm{high})}^{\max}$	-2.1	-3.2	1.4	4.7	-0.4	-17.6	-	-	-0.3	-24.5	1.1	6.1
$m_{b_n ll}^{\max}$	-1.2	-	-	-	0.7	-	-	-	-1.2	-	1.5	-
$m_{b_n l(\mathrm{low})}^{\max}$	-	-	-2.6	-	2.1	-	-	-	-0.9	-	1.0	-
$m_{b_n l(\mathrm{high})}^{\max}$	-2.1	-	1.4	-	-	-	-	-	-1.1	-	1.3	-

Table 8: Partial derivatives of endpoints with respect to masses at the nominal mass values. The larger the partial derivative $\partial E/\partial m$ is, the more sensitive the given endpoint is to the given mass. The quantity Δm [GeV] is defined by $\sigma_E/(\partial E/\partial m)$, where σ_E is the combined statistical and energy scale error of the endpoint. See the text for more details.

These numbers show immediately that the three gluino endpoints included in the numerical fit have a strong sensitivity to the gluino mass, but only a very moderate sensitivity to the sbottom mass. Also $m_{b_f ll(\theta>\frac{\pi}{2})}^{\min}$ is seen not to constrain $m_{\tilde{b}_1}$ too much. If $m_{bb}^{\max}$ could be used or some of the squark endpoints other than $m_{b_f ll(\theta>\frac{\pi}{2})}^{\min}$ (numbers shown only for $\tilde{q}_L$), then $m_{\tilde{b}_1}$ could be determined more accurately. The table can also be used to understand better which of the endpoints are important in constraining each of the lighter masses.

7. LHC + Linear Collider (LC)

Within the time-frame of the analysis of LHC data, measurements from a Linear Collider may become available. While the LHC is able to measure mass differences at high precision, as documented in the previous section, a Linear Collider will, due to the much cleaner environment, provide precise measurements of the sparticles which are kinematically accessible, in particular $\tilde{\chi}_1^0$. Such a measurement will be the scale fixer which is lacking in

the LHC data, and will in combination with the LHC measurements allow one to also fix the masses of the heavier sparticles not accessible at the Linear Collider.

To estimate the effect of a Linear Collider measurement of $m_{\tilde{\chi}_1^0}$, we add to our least-square function Σ, a term $[(m_{\tilde{\chi}_1^0} - m^{\rm LC}_{\tilde{\chi}_1^0})/\sigma^{\rm LC}_{m_{\tilde{\chi}_1^0}}]^2$, where the quantities with superscript 'LC' are the Linear Collider measurements. Since $\sigma^{\rm LC}_{m_{\tilde{\chi}_1^0}} = 0.05$ GeV [24], this means practically fixing $m_{\tilde{\chi}_1^0}$ at the nominal value.

For the *(1,2)* solutions, which normally return $\tilde{\chi}_1^0$ masses some 10 GeV below the nominal value, this has the dramatic effect of reducing their occurrences to $\sim 1\%$ (for $\Delta\Sigma \leq 3$). These minima can therefore for most purposes be neglected. As a consequence, the probability of having two minima is strongly reduced, to the per mille level. For SPS 1a the Linear Collider measurement thus closes the issue of multiple minima altogether.

		(1,1)	
	Nom	Mean	RMS
$m_{\tilde{\chi}_1^0}$	96.05	96.05	0.05
$m_{\tilde{l}_R}$	142.97	142.97	0.29
$m_{\tilde{\chi}_2^0}$	176.82	176.82	0.17
$m_{\tilde{q}_L}$	537.2	537.2	2.5
$m_{\tilde{b}_1}$	491.9	491.9	10.9
$m_{\tilde{g}}$	595.2	595.2	5.5
$m_{\tilde{g}} - m_{\tilde{b}_1}$	103.3	103.3	9.0

Table 9: Mass values (all in GeV) from LHC+LC. Since the occurrences of *(1,2)* solutions are reduced to $\sim 1\%$, they are left out.

The combined LHC + LC results are shown in Table 9. Comparison with the numbers of Table 7 shows that the mass measurements improve considerably when the LC measurement is included. The root-mean-square values of the masses are now approximately equal to the root-mean-square values of mass differences without the LC measurement. For $m_{\tilde{b}_1}$ the correlation to $m_{\tilde{\chi}_1^0}$ is not dominant. The spread of $m_{\tilde{b}_1}$ is therefore still larger than the spread of $m_{\tilde{g}} - m_{\tilde{b}_1}$, which does not feel the fixing of $m_{\tilde{\chi}_1^0}$. As was the case without the LC measurement, the inclusion of the gluino endpoints in the numerical fit does not affect the other masses. The exception is $m_{\tilde{b}_1}$, for which the root-mean-square value is reduced by $\sim$1 GeV compared to the results in [12].

8. Conclusion

In this paper we have extended the endpoint method of obtaining masses in R-parity conserving SUSY scenarios to also include the gluino mass, given the decay chain (1.2). We first introduced an alternative approach for calculating $m^{\rm max}_{q_{\rm f}ll}$. This approach was then used to calculate $m^{\rm max}_{qqll}$ for all possible cases. The remaining six gluino endpoints were also calculated. Solutions to many of these were obtained from the $m^{\rm max}_{q_{\rm f}ll}$ result via appropriate substitutions. Theory distributions for the seven new distributions were studied for a selection of mass scenarios, revealing that some of the distributions often have little phase space towards higher masses, making them less useful.

An ATLAS simulation of 300 fb^{-1} was performed for the mSUGRA point SPS 1a. While we were not able to detect the gluino edges in the case of an intermediate first or second-generation squark ($\tilde{q}_L$), edges were found and fitted in the case of an intermediate sbottom. This is due to fact that 80% of the $\tilde{b}$'s come from a gluino, together with the jet

selection requirement of having two and only two b-tagged jets, both important background-reducing factors. Not all of the endpoints were used. Energy scale errors were discussed and found to lie in intervals rather than being constant. Yet, they were taken as constants in the analysis.

To estimate the precision with which sparticle masses can be obtained at the LHC, an ensemble of 10,000 'gedanken experiments' were performed, in which for each 'experiment' three of the gluino endpoints were combined with the squark endpoints obtained in [12] in a least-square fit to give the masses. Inherent to the method, mass differences are better determined than the masses themselves. Furthermore, one set of endpoint measurements in general corresponds to several sets of masses. The inclusion of the gluino endpoints affects the number of minima and the masses of $\tilde{\chi}_1^0$, $\tilde{l}_R$, $\tilde{\chi}_2^0$ and $\tilde{q}_L$ only minimally. In the case of $\tilde{b}_1$ there is a noticeable correlation to the gluino. The ensemble distribution of the gluino mass was found to have a root-mean-square value of 7 GeV. The spread for $m_{\tilde{g}} - m_{\tilde{\chi}_1^0}$ was found to be about 1.5 GeV smaller.

Spurred by the lack of significant improvement in the ensemble spread of $m_{\tilde{b}_1}$ compared to the precision obtained for $m_{\tilde{g}}$, even though the new measurements involved both, a sensitivity analysis for all the relevant endpoints was performed. This investigation showed that the three gluino endpoints in use have limited sensitivity to the sbottom mass, thus confirming the different impact they have on the gluino and sbottom masses.

Finally the impact of a joint LHC–LC analysis was estimated. The endpoint measurements from the LHC were combined with a Linear Collider measurement for the LSP mass. This essentially fixes the mass scale. Consequently, in the combined analysis the masses themselves are determined with roughly the same precision as that of mass *differences* determined at the LHC alone.

Acknowledgments

This work has been performed partly within the ATLAS Collaboration, and we thank collaboration members for helpful discussions. We have made use of the physics analysis framework and tools which are the results of collaboration-wide efforts. We are in particular grateful to Giacomo Polesello for numerous discussions. BKG would like to thank Steinar Stapnes for useful discussions. This research has been supported in part by the Research Council of Norway.

References

[1] P. Fayet and S. Ferrara, Phys. Rept. **32** (1977) 249.

[2] S. Dimopoulos and H. Georgi, Nucl. Phys. B **193** (1981) 150.

[3] H. P. Nilles, Phys. Rept. **110** (1984) 1.

[4] H. E. Haber and G. L. Kane, Phys. Rept. **117** (1985) 75.

[5] S. Weinberg, Phys. Rev. D **13** (1976) 974; Phys. Rev. D **19** (1979) 1277; L. Susskind, Phys. Rev. D **20** (1979) 2619; G. 't Hooft, in *Recent developments in gauge theories*, Proceedings

of the NATO Advanced Summer Institute, Cargese 1979, ed. G. 't Hooft *et al.* (Plenum, New York 1980).

[6] I. Hinchliffe, F. E. Paige, M. D. Shapiro, J. Soderqvist and W. Yao, Phys. Rev. D **55** (1997) 5520 [arXiv:hep-ph/9610544].

[7] I. Hinchliffe, F. E. Paige, E. Nagy, M. D. Shapiro, J. Soderqvist and W. Yao, LBNL-40954

[8] H. Bachacou, I. Hinchliffe and F. E. Paige, Phys. Rev. D **62** (2000) 015009 [arXiv:hep-ph/9907518].

[9] G. Polesello, *Precision SUSY measurements with ATLAS for SUGRA point 5*, ATLAS Internal Note, PHYS-No-111, October 1997.

[10] B. C. Allanach, C. G. Lester, M. A. Parker and B. R. Webber, JHEP **0009** (2000) 004 [arXiv:hep-ph/0007009].

[11] C. G. Lester, *Model independent sparticle mass measurements at ATLAS*, Ph. D. thesis, http://www.slac.stanford.edu/spires/find/hep/www?r=cern-thesis-2004-003

[12] B. K. Gjelsten, D. J. Miller, P. Osland, JHEP **12** (2004) 003 [arXiv:hep-ph/0410303].

[13] B. C. Allanach *et al.*, in *Proc. of the APS/DPF/DPB Summer Study on the Future of Particle Physics (Snowmass 2001)* ed. N. Graf, Eur. Phys. J. C **25** (2002) 113 [eConf **C010630** (2001) P125] [arXiv:hep-ph/0202233].

[14] B. K. Gjelsten, E. Lytken, D. J. Miller, P. Osland, G. Polesello, *A detailed analysis of the measurement of SUSY masses with the ATLAS detector at the LHC*, ATL-PHYS-2004-007, Geneva, CERN, Jan 2004; G. Weiglein *et al.* [LHC / ILC Study Group], arXiv:hep-ph/0410364.

[15] M. M. Nojiri, G. Polesello, D.R. Tovey, arXiv:hep-ph/0312317.

[16] P. Richardson, JHEP **0111** (2001) 029 [arXiv:hep-ph/0110108]; A. J. Barr, arXiv:hep-ph/0405052.

[17] B. K. Gjelsten, Ph. D. thesis, University of Oslo, 2005.

[18] H. Baer, F. E. Paige, S. D. Protopopescu and X. Tata, arXiv:hep-ph/9305342, arXiv:hep-ph/0001086.

[19] T. Sjöstrand, P. Edén, C. Friberg, L. Lönnblad, G. Miu, S. Mrenna, E. Norrbin, Comput. Phys. Commun. **135** (2001) 238; T. Sjöstrand, L. Lönnblad and S. Mrenna, "PYTHIA 6.2: Physics and manual", arXiv:hep-ph/0108264.

[20] H. L. Lai *et al.* [CTEQ Collaboration], Eur. Phys. J. C **12** (2000) 375 [arXiv:hep-ph/9903282].

[21] E. Richter-Was, D. Froidevaux and L. Poggioli, "ATLFAST 2.0: a fast simulation package for ATLAS", Tech. Rep. ATL-PHYS-98-131 (1998)

[22] F. James and M. Roos, Comput. Phys. Commun. **10** (1975) 343.

[23] ATLAS Collaboration, *ATLAS Detector and Physics Performance Technical Design Report 2.* No. CERN-LHCC-99-014 ATLAS-TDR-14. May, 1999.

[24] J. A. Aguilar-Saavedra *et al.* [ECFA/DESY LC Physics Working Group Collaboration], "TESLA Technical Design Report Part III: Physics at an e+e- Linear Collider," arXiv:hep-ph/0106315.